Dipl.-Ing. Andreas Klug

Organic Field-Effect Transistors – Process Development, Stability Issues and Sensor Applications

DISSERTATION

zur Erlangung des akademischen Grades
Doktor der technischen Wissenschaften

Doktoratsstudium der technischen Wissenschaften
Technische Physik

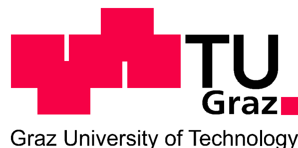

Technische Universität Graz

Betreuer:

Ao. Univ.-Prof. Dipl.-Ing. Dr.techn. Emil J. W. List

Institut für Festkörperphysik

Graz, März 2010

Deutsche Fassung:
Beschluss der Curricula-Kommission für Bachelor-, Master- und Diplomstudien vom 10.11.2008
Genehmigung des Senates am 1.12.2008

EIDESSTATTLICHE ERKLÄRUNG

Ich erkläre an Eides statt, dass ich die vorliegende Arbeit selbstständig verfasst, andere als die angegebenen Quellen/Hilfsmittel nicht benutzt, und die den benutzten Quellen wörtlich und inhaltlich entnommene Stellen als solche kenntlich gemacht habe.

Graz, am …………………………… ………………………………………………..
(Unterschrift)

Englische Fassung:

STATUTORY DECLARATION

I declare that I have authored this thesis independently, that I have not used other than the declared sources / resources, and that I have explicitly marked all material which has been quoted either literally or by content from the used sources.

…………………………… ………………………………………………..
date (signature)

„Aber immer genügt es, wenn ein Werk auch nur einen einzigen Menschen wirklich begeistert, denn jede echte Begeisterung wird selber schöpferisch.“

Stefan Zweig

ACKNOWLEDGEMENT

First of all I would like to thank Prof. Emil List for providing me the opportunity to work in his team on fascinating research projects, for his continuous effort to acquire new ones, for having enabled me to assist him during an exciting startup of a new company, with all its challenges, and for having mentored me for more than six years now.
Furthermore, I am particularly indebted to six persons, who spent innumerable hours with me fabricating, measuring, analyzing and discussing devices: Matthias Baumann, with whom I worked on operational stability of OFETs with various gate dielectrics, Raphael Pfattner, with whom I did first ambient stability investigations on organic semiconductors, Martin Denk, who assisted in the development of the SensFET, Arno Meingast, with whom OFET process development at NTC Weiz was both fun and successful, Gerhild Wurzinger, with whom stability investigations on semiconductors could be greatly enhanced and Alexander Blümel, with whom I developed the MIMIC- and µTP-OFETs and who did all the AFM investigations presented in this work.
Furthermore, I would like to thank Christian Slugovc, Thomas Bauer and Martina Sandholzer for providing the ROM-polymers and for great discussions.
I would also like to thank the group of Prof. Ullrich Scherf, in particular Benjamin Souharce and Michael Forster, for providing us with the polymer semiconductors.
Special thanks go to Stefan Sax for a fruitful relationship both privately and professionally for more than 10 years now. For sure we have spent more time together than a lot of married couples.
I would also like to thank Stefan Gamerith, who induced my enthusiasm for the OFET many years ago and Peter Pacher for great discussions on OFETs.
Furthermore I would like to thank Robert Schennach for support with the IR investigations, Thomas Haber, Meltem Sezen and Werner Grogger for the TEM investigations and Heinz-Georg Flesch and Roland Resel for the XRD measurements.
Of course I would like thank the colleagues and former colleagues at the NTC Weiz for their support and great collaboration, in particular Helmut Wiedenhofer, Rita Eckhard, Sonja Steßl-Mühlbacher, Sigi Psutka, Michael Graf, Andreas Ranz, Gernot Mauthner, Markus Postl, Alfred Neuhold, Stefan Kappaun, Wolfgang Wiedemair, Josef Harrer, Renée Hirschmann, Roman Trattnig, Conny Ranz and Kerstin Schmoltner.
I would also like to thank the colleagues and former colleagues at the Institute of Solid State Physics for their assistance, in particular Harald Plank (also for the great time in San Francisco), Evelin Fisslthaler, Egbert Zojer, Horst Scheiber, Stefan Brandstätter, Thomas Piok, Sabrina Eder and Birgit Kunert.
Special thanks, of course, go to my parents and Birgit for their love and continuous encouragement.
And last but for sure not least I would like to thank Silvia for having supported me so much throughout the last 10 years. Words cannot express how glad I am to have you at my side.

ABSTRACT

Organic electronics is a fascinating future technology and has developed tremendously since the last twenty years, which can be ascribed to the specific properties of electroactive organic compounds. They enable the use of efficient solution-based processing techniques at low temperatures and their chemical, physical and mechanical properties can be easily tailored, thus allowing for the development of new applications such as flexible displays, inkjet-printed electronics or smart sensors, some of which are not far from being commercialized.

This work focused on three central issues related to organic field-effect transistors (OFETs): processing, stability and sensing.

The first one, processing, involved the successful implementation and testing of a completely new modular OFET fabrication line, integrated within a cleanroom environment at the NanoTecCenter Weiz Forschungsgesellschaft mbH, including equipment definition and acquisition, process development and optimization as well as device fabrication and characterization. With this line poly(3-hexylthiophene) (P3HT)- and pentacene-based OFETs with various source/drain-electrode geometries and channel dimensions were prepared and thoroughly investigated with respect to short-channel effects and the implications of dielectric surface modification. Furthermore, well-performing OFETs were developed with solution-processable silver source/drain electrodes structured by two soft-lithographic techniques, namely Micromolding In Capillaries and Microtransfer Printing. Finally, organic field-effect transistors formed on insulating copper wires were fabricated, indicating the potential of combining readily available mass products with solution-processable organic semiconductors.

The issue stability involved a detailed investigation of the ambient and shelf-life stability of OFETs containing various polytriphenylamine-derivatives as organic semiconductors with ionization potentials >5 eV. The influences of oxygen, moisture and dielectric surface modification on the device stability were evaluated and the results were benchmarked against the well-established transistor materials pentacene and P3HT, the latter also investigated with respect to operational stability in combination with an ion-conducting dielectric.

Finally, regarding sensing, a novel OFET-sensor concept was developed, which is based on the application of an analyte-sensitive gate dielectric. It was successfully evaluated with top-gate/bottom-contact OFETs including various solution-processable, pH-sensitive polymer dielectrics, which led to a distinct increase of the channel current upon exposure to ammonia at concentration levels down to 100 ppm. Aside from current-voltage OFET-analysis, also UV/VIS-spectroscopy, Fourier transform infrared spectroscopy and capacitance measurements were used to rationalize the underlying sensor mechanism.

KURZFASSUNG

Organische Elektronik ist eine faszinierende Zukunftstechnologie und hat sich in den letzten zwanzig Jahren ungemein weiterentwickelt, was man den spezifischen Eigenschaften elektroaktiver organischer Materialien zuschreiben kann. Diese ermöglichen die Anwendung effizienter Prozesstechnologien bei niedrigen Temperaturen und ihre chemischen, physikalischen und mechanischen Eigenschaften können maßgeschneidert werden. Dadurch ergeben sich neue Anwendungen wie flexible Displays, tintenstrahlgedruckte Elektronik oder intelligente Sensoren, von denen manche kurz vor ihrer Markteinführung stehen.

Diese Arbeit beschäftigte sich mit drei wichtigen Aspekten von organischen Feldeffekt-Transistoren (OFETs): Prozessierung, Stabilität und Sensorik.

Der erste Punkt, Prozessierung, beinhaltete die erfolgreiche Implementierung und Erprobung einer neuen modularen OFET Fabrikationslinie im Reinraum der NanoTecCenter Weiz Forschungsgesellschaft mbH, inklusive Gerätedefinition und -beschaffung, Prozessentwicklung und -optimierung sowie Bauelementherstellung und -charakterisierung. Mit dieser Linie wurden Poly(3-hexylthiophen) (P3HT)- und Pentacen-basierende OFETs mit verschiedenen Source/Drain-Elektrodengeometrien und Kanaldimensionen hergestellt und bezüglich Kurzkanaleffekten und den Auswirkungen einer Oberflächenmodifikation des Dielektrikums untersucht. Weiters wurden OFETs mit Source/Drain-Elektroden entwickelt, die aus einer Silber-Nanodispersion mittels zweier soft-lithographischer Techniken, „Micromolding In Capillaries“ und „Microtransfer Printing“, hergestellt und strukturiert wurden. Schließlich wurden organische Feldeffekt-Transistoren auf isolierenden Kupferdrähten erzeugt, die das Potential einer Kombination von alltäglichen Massenprodukten mit aus der Lösung verarbeitbaren organischen Halbleitern aufzeigen.

Der Punkt Stabilität involvierte eine detaillierte Analyse der Luftstabilität und Lagerfähigkeit von OFETs mit verschiedenen Polytriphenylamin-Derivaten als organische Halbleiter, die Ionisierungspotentiale >5 eV aufweisen. Die Einflüsse von Sauerstoff, Luftfeuchtigkeit und Oberflächenmodifikation des Dielektrikums auf die Bauelementstabilität wurden bestimmt und die Ergebnisse mit den etablierten Transistormaterialien Pentacen und P3HT verglichen, wobei letzteres auch bezüglich Betriebsstabilität in Kombination mit einem ionen-leitenden Dielektrikum untersucht wurde.

Schließlich, was die Sensorik betrifft, wurde ein neues OFET-Sensorkonzept basierend auf der Anwendung eines sensitiven Dielektrikums entwickelt. Dieses wurde erfolgreich mit Bauelementen evaluiert, die verschiedene, aus der Lösung verarbeitbare, pH-sensitive Polymere als Dielektrika beinhalteten und unter Exposition von gasförmigem Ammoniak bis zu einer Nachweisgrenze von 100 ppm mit einer Zunahme des Kanalstroms sensitiv reagierten. Neben der elektrischen Charakterisierung der OFETs wurden auch spektroskopische Untersuchungen im sichtbaren und infraroten Wellenlängenbereich sowie Kapazitätsmessungen durchgeführt, um den zugrundeliegenden Sensormechanismus zu erkunden.

Table of Contents

1. Introduction 1
1.1. Historical Overview 2
1.2. Scope of this Thesis 4
2. Fundamentals 6
2.1. Organic Semiconductors 7
2.1.1. Chemical Structures and Electronic Configurations 7
2.1.2. Excited States 9
2.1.2.1. Polarons 9
2.1.2.2. Excitons 10
2.1.3. Charge Transport 11
2.1.3.1. Electrical Conductivity and Charge-Carrier Mobility 11
2.1.3.2. General Issues 11
2.1.3.3. Charge Transport in Organic Single Crystals 12
2.1.3.4. Charge Transport in Polycrystalline Materials 13
2.1.3.5. Charge Transport in Disordered Conjugated Polymers 13
2.2. Organic Field-Effect Transistors 15
2.2.1. Architectures and Fabrication Techniques 15
2.2.1.1. Substrates 16
2.2.1.2. Organic Semiconductors 16
2.2.1.3. Gate Dielectrics 17
2.2.1.4. Electrodes (Source/Drain/Gate) 17
2.2.2. Operating Principle, Device Characteristics and Parameters 18
2.2.2.1. Field-Effect Mobility 22
2.2.2.2. Threshold Voltage and Switch-on Voltage 22
2.2.2.3. On/Off-Current Ratio 23
2.2.2.4. Subthreshold Slope 23
2.2.2.5. Contact Resistance 24
2.2.2.6. Short-Channel Effects 26
2.2.3. Device Stability 26
2.2.3.1. Environmental Stability 26
2.2.3.2. Operational Stability 27
2.3. OFET-based Sensors 28
3. OFET Fabrication Techniques and Process Development 30
3.1. Implementation and Testing of a New Modular OFET Fabrication Line 31
3.1.1. Introduction 31
3.1.2. Equipment 31
3.1.3. Process Implementation and Device Fabrication 33
3.1.3.1. Development and Optimization of a Photolithographic Lift-Off Process for Structuring OFET Source/Drain Electrodes 34
3.1.3.2. Process Development and Optimization for Substrate Pre-treatment with HMDS and Evaluation with Contact Angle-, AFM- and XRD-measurements 37
3.1.3.3. Completion of Devices 42

3.1.4. Device Characteristics of OFETs with Various Source/Drain-Electrode Geometries, Channel Dimensions and Substrate Pre-treatments 43
3.1.4.1. OFETs with Ring-Type Source/Drain-Electrode Structures 43
3.1.4.2. OFETs with Interdigital Source/Drain-Electrode Structures 44
3.1.4.3. OFETs with Various Channel Lengths - Short-Channel Effects and Influence of Substrate Pre-treatment with HMDS 46
3.2. Structuring of Silver Source/Drain Electrodes by Micromolding In Capillaries (MIMIC) and Microtransfer Printing (µTP) 55
3.2.1. Introduction 55
3.2.2. Device Fabrication 56
3.2.2.1. Fabrication and Analysis of MIMIC Source/Drain Structures 56
3.2.2.2. Fabrication and Analysis of µTP Source/Drain Structures 58
3.2.2.3. Completion of MIMIC- and µTP-OFETs 60
3.2.3. Device Characteristics of MIMIC- and µTP-OFETs 61
3.2.3.1. OFETs based on MIMIC Source/Drain Electrodes 61
3.2.3.2. OFETs based on µTP Source/Drain Electrodes 64
3.3. WireOFETs 67
3.3.1. Introduction 67
3.3.2. Device Fabrication 68
3.3.3. Device Characteristics of WireOFETS 69
3.4. Summary and Conclusions 71
4. Stability Issues of Organic Field-Effect Transistors 73
4.1. Introduction 74
4.2. Materials 75
4.3. Ambient and Shelf-life Stability 76
4.3.1. First Investigations 76
4.3.1.1. Device Fabrication 77
4.3.1.2. Device Characteristics 77
4.3.2. Influence of Oxygen, Moisture and Surface Modification with HMDS 85
4.3.2.1. Stability Measurement Plant and Probe Chamber 85
4.3.2.2. Device Fabrication 86
4.3.2.3. $PTPA_3$-based OFETs 87
4.3.2.4. rr-P3HT based OFETs 89
4.3.2.5. Pentacene-based OFETs 90
4.4. Operational Stability 92
4.4.1. Polyvinyl Alcohol (PVA) 92
4.4.1.1. Solution Preparation and Dialysis 93
4.4.2. Device Fabrication 93
4.4.3. Device Characteristics 94
4.5. Summary and Conclusions 98
5. OFET-based Sensors with Sensitive Gate Dielectrics used for Low-Concentration Ammonia Detection 99
5.1. Introduction 100
5.2. The SensFET Concept 101

5.3. Applied Dielectric Materials 104
5.3.1. Preparation of ROM-Polymer Solutions 106
5.3.2. UV/VIS-Absorption Spectroscopy 106
5.3.3. FTIR Spectroscopy 109
5.4. Equipment for Electrical Device Characterization 112
5.5. Capacitors based on ROMP Dielectrics 113
5.5.1. Device Fabrication 114
5.5.2. Device Characteristics 115
5.5.2.1. Frequency Dependence 115
5.5.2.2. DC-Bias Dependence 117
5.5.2.3. Exposure to Ammonia 117
5.6. NH_3-SensFETs 120
5.6.1. Preliminary Work - OFETs with Comb-shaped Top-Gate Electrode 120
5.6.2. First OFET-based Sensors 121
5.6.3. Second-Generation SensFETs 124
5.6.3.1. Device Fabrication and Microscope Analysis 124
5.6.3.2. Electrical Characteristics of Sensor-OFETs 127
5.6.4. OFETs based on ROM-Polymers and $PTPA_3$ as Organic Semiconductor 135
5.6.5. Direct Interaction between rr-P3HT and Ammonia 137
5.6.6. Explanation of the Sensor Response 138
5.6.6.1. Qualitative Explanation 138
5.6.6.2. Quantitative Estimations 144
5.7. Summary and Conclusions 147
6. Appendix 149
6.1. List of Publications 150
6.1.1. Jounal Papers 150
6.1.2. Conference Contributions 150
6.1.3. Patent Applications 151
6.2. Bibliography 152

1. INTRODUCTION

Organic electronics is a fascinating future technology and has developed tremendously since the last twenty years, which can be ascribed to the specific properties of electroactive organic compounds. They enable the use of efficient solution-based processing techniques at low temperatures and their chemical, physical and mechanical properties can be easily tailored, thus allowing for the development of new applications such as flexible displays, inkjet-printed electronics or smart sensors, some of which are not far from being commercialized.

This chapter provides a brief historical overview of the major developments in the field of organic electronics and illustrates the scope of this thesis.

1.1. Historical Overview

First investigations on the semiconducting properties of organic materials date back to the late 1940s and beginning 1950s.[1] They focused on the photoconductive behavior of small organic molecules, in particular acenes, in the crystalline state.[2,3]

In 1963 Pope and co-workers were the first to report on electroluminescence in an organic semiconductor, namely single-crystalline anthracene.[4] The applied materials exhibited semi-conducting behavior but with low performance and therefore they were considered to have only little potential for applications.

Molecularly doped polymers appeared in the mid-1960s[5], showing higher semiconducting performance. For these materials small organic pigments are integrated into a matrix polymer, thus combining photoconductive properties with specific mechanical features. Since the 1970s these photoconductors have been employed in xerographic devices.[6]

The discovery of metallic-like behavior of doped polyacetylene by Alan J. Heeger, Alan G. MacDiarmid and Hideki Shirakawa in 1977,[7,8] for which they received the Nobel Prize of Chemistry in 2000,[9] was an important milestone in the field of organic (semi)conductors and has induced a lot of research since then.

Today electroactive organic materials provide great possibilities for new applications. The ability to tailor their electrical, optical and mechanical properties enables the use of low-cost deposition and structuring techniques at low temperatures on large areas of rigid, flexible, organic, inorganic or even biological substrates. Just imagine printing an integrated circuit with your own home-office inkjet printer. This might be possible in the not too distant future. Moreover, this class of materials allows for the development of high-performing sensors, as optimized sensitivity and selectivity with respect to a target analyte can be easily induced.

The successful integration of electroactive organic materials has led to a number of very promising applications and devices. In the late 1980s electroluminescent organic vacuum-evaporated dye films with high performance were demonstrated.[10,11] Moreover, field-effect transistors based on polythiophene[12,13] and on small conjugated oligomers[14,15] were reported. In 1990 Burroughes and co-workers demonstrated the first conjugated polymer LED (PLED).[16]

Aside from organic light-emitting diodes (OLEDs), organic field-effect transistors (OFETs) and corresponding circuits,[17,18,19,20,21,22,23,24,25] also organic solar cells,[26,27] organic photodiodes[28] and organic lasers[29,30] have emerged. "*Plastic electronics*" have become a key word in this regard.

Even flexible displays are not a vision any more[31,32] and first commercial products appear on the market.

This thesis is focusing on organic field-effect transistors. The basic principle of the field-effect transistor (FET) was proposed by Lilienfeld as early as 1925 and patented in 1930.[33] FETs based on inorganic semiconductors such as metal-oxide-semiconductor field-effect transistors (MOSFET) have become workhorses in modern microelectronics both as discrete devices and in integrated circuits.[34,35] The first silicon-based MOSFET was realized in 1960.[36] Compared to bipolar transistors, which, invented in 1947,[37,38] marked the birth of modern microelectronics, field-effect transistors generally operate at significantly smaller amounts of power.

The field effect in *organic* semiconductors was demonstrated for the first time more than three decades ago.[39,40] However, OFETs have been considered as having only little potential for applications until 1987.[12,13] Since then a lot of research has led to a significant increase of the device performance, which is nowadays comparable to that of thin-film transistors based on amorphous hydrogenated silicon (a-Si:H), the latter being mainly applied as display drivers.

However, compared to the latter, OFETs also make use of the advantages associated with electroactive organic materials and will find their application as switching devices in active matrix flat panel displays,[31,41,42,43] as sensors,[44,45,46,47] in radio-frequency identification tags (RFIDs) and low-end smart cards. All-polymer integrated circuits[48] and even organic electronics fabricated on paper[49] have been demonstrated already.

The real challenge for the following years to come will be to integrate organic semiconductor based sensors with organic electronics for fabricating reliable and cheap sensor tags and labels, which will open up new applications with distinct advantages over existing sensor products regarding cost and applicability.

1.2. Scope of this Thesis

This work focused on three main aspects related to organic field-effect transistors: fabrication techniques and processes, ambient and operational stability, OFET-based sensing.

Chapter 2 provides a brief introduction into organic semiconductors and organic field-effect transistors. After describing the chemical structures and electronic configurations of small conjugated molecules and semiconducting polymers, excited states and the various models describing charge transport in such materials will be shortly reviewed. Then OFET architectures and fabrication techniques as well as the operating principle and important device parameters will be described. Finally stability issues and the current developments of OFET-based sensors will be summarized.

Chapter 3 deals with processing issues. At first the implementation and testing of a completely new modular OFET fabrication line, integrated within a cleanroom environment, is described, including equipment definition and acquisition, process development and optimization as well as device fabrication and characterization. In this section rr-P3HT- and pentacene-based OFETs with various source/drain-electrode geometries and channel dimensions, prepared with the newly established line, are investigated with respect to short-channel effects and the implications of dielectric surface modification with hexamethyldisilazane. The next section deals with the fabrication and analysis of well-performing bottom-gate/bottom-contact OFETs based on rr-P3HT with silver source/drain electrodes defined by two soft-lithographic techniques, namely Micromolding In Capillaries and Microtransfer Printing. Finally, organic field-effect transistors formed on insulating copper wires (wireOFETs) are presented, indicating the potential of combing readily available mass products with solution-processable organic semiconductors for the fabrication of smart, textile-compatible, low-cost organic electronics.

Chapter 4 relates to ambient, operational and shelf-life stability of organic field-effect transistors. Bottom-gate/bottom-contact OFETs containing various polytriphenylamine-(PTPA)-derivatives as organic semiconductors with ionization potentials > 5 eV are investigated with respect to their ambient and shelf-life stability. The results are benchmarked against the well-established transistor semiconductors rr-P3HT and pentacene. Although the latter two exhibit larger field-effect mobility values, corresponding OFETs are degraded upon air exposure mainly due to oxygen/moisture-induced doping or charge-carrier trapping.

On the contrary, device parameters of PTPA-OFETs remained rather stable, even after storage under dark ambient conditions for several months. Moreover, when the substrate surface was hydrophobized by HMDS pre-treatment, the stability of the investigated semiconductors was found to be distinctly increased. Finally, also the operational stability of a rr-P3HT-based top-gate OFET with polyvinyl alcohol as gate dielectric is analyzed and the observed channel current drifts upon bias stress are explained by the movement of residual mobile ions within the dielectric.

Chapter 5 deals with OFET-based sensing. A novel OFET-sensor concept is presented, which is based on the application of an analyte-sensitive gate dielectric. In detail, the organic dielectric material is chemically adapted to change its electronic properties upon contact with an analyte for generating a response which is electrically detectable through an OFET. Various solution-processable, pH-sensitive, ring-opening metathesis polymerized dielectric materials were extensively investigated with gaseous ammonia as model analyte using UV/VIS spectroscopy, Fourier transform infrared spectroscopy, capacitance measurements and atomic force microscopy. By employing these materials in bottom-contact OFETs with a meander-shaped top-gate structure, ammonia concentrations as low as 100 ppm could be detected by an irreversible source-to-drain current increase, while devices based on a reference dielectric bearing no pH-sensitive groups showed negligible response. The obtained results support the reaction mechanism proposed at the beginning of this chapter, which is closed by a detailed response explanation, also including calculations based on a standard device model to roughly quantify the interactions.

The appendix at the end of this thesis includes a list of publications and the bibliography.

2. FUNDAMENTALS

This chapter provides a brief introduction into organic semiconductors and organic field-effect transistors. After describing the chemical structures and electronic configurations of small conjugated molecules and semiconducting polymers, excited states and the various models describing charge transport in such materials will be shortly reviewed. Then OFET architectures and fabrication techniques as well as the operating principle and important device parameters will be described. Finally stability issues and the current developments of OFET-based sensors will be summarized.

2.1. Organic Semiconductors

The following sections provide a brief introduction into organic semiconductors, summarizing a more detailed description in [50].

2.1.1. Chemical Structures and Electronic Configurations

Figure 2.1 illustrates the chemical structures of typical organic p-type semiconductors, which are commonly applied for OFET-applications.

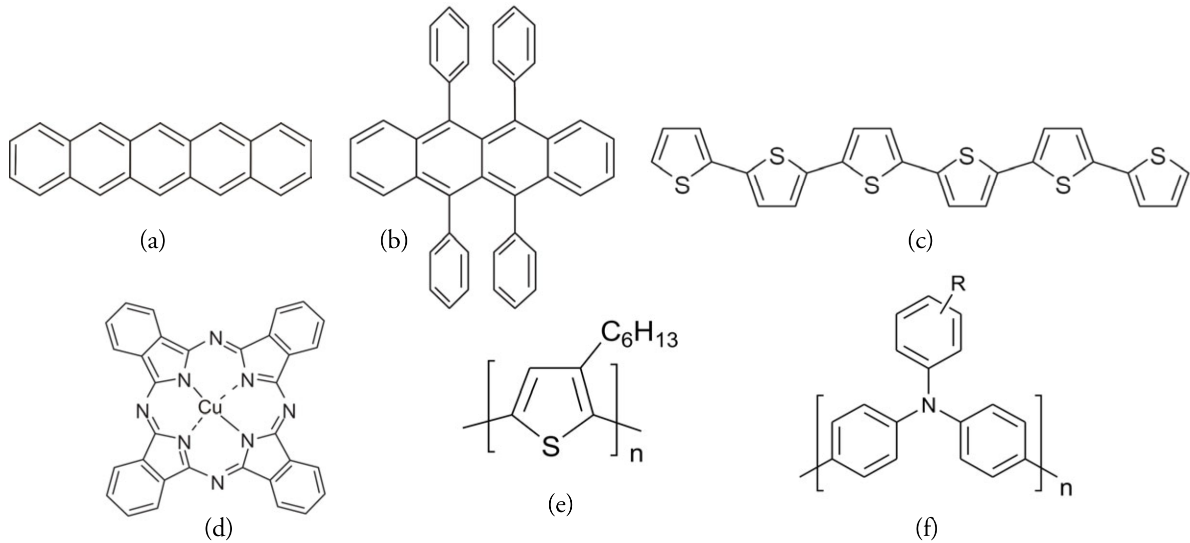

Figure 2.1: Chemical structures of typical organic p-type semiconductors applied in OFETs: a) pentacene; b) rubrene; c) α-sexithiophene (6T); d) copper phthalocyanine (CuPc); e) regioregular poly(3-hexylthiophene) (rr-P3HT); f) polytriphenylamine (PTPA).

The central element of organic materials is carbon.[51] Carbon comprises six electrons and in its ground state it exhibits the electronic configuration $1s^2 2s^2 2p^2$, including two unpaired electrons in the 2p atomic orbitals (Figure 2.2 left). However, due to the low energetic difference between the 2s and 2p states one of the two 2s electrons can easily be promoted to the vacant 2p state, which results in an excited electronic state with the configuration $1s^2 2s^1 2p^3$ (Figure 2.2, middle).

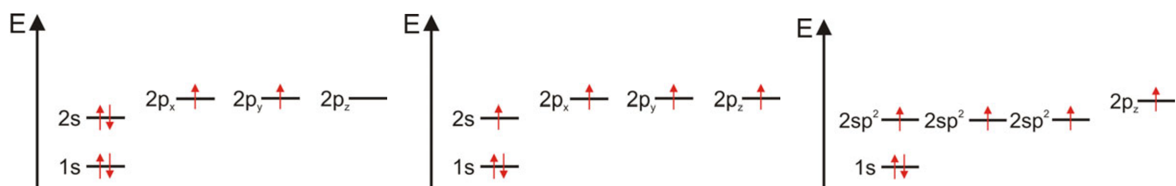

Figure 2.2: Electronic configurations of atomic carbon in the ground state (left), in the excited state (middle) and in sp^2-configuration (right).

This configuration, however, could not explain the experimentally observed regular tetrahedral shape of methane with four equivalent C-H bonds. The problem was solved by L. C. Pauling, who introduced the concept of hybridization.[52] For organic semiconducting molecules and their solids the sp^2 hybridization of carbon is very important, where one s orbital and two p orbitals (e.g. 2s, $2p_x$ and $2p_y$) are linearly combined to three equivalent sp^2 hybrid orbitals, with the third p orbital ($2p_z$) remaining unaltered. Figure 2.2 right shows the corresponding electronic configuration and Figure 2.3 the trigonal planar structure of an sp^2 hybrid orbital.

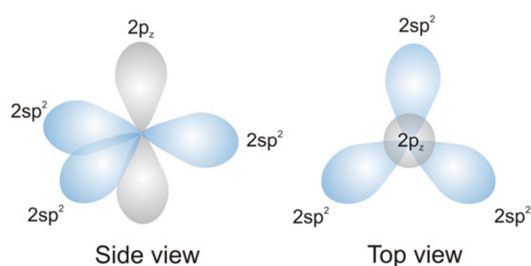

Figure 2.3: Sp^2 hybrid orbital.

In conjugated molecules or polymers[1,9] the sp^2 hybrid orbitals of neighboring atoms form highly localized σ-bonds and the corresponding unmodified p_z orbitals a delocalized π-electron system, which ideally spans the entire molecule. According to a simple band picture using the *Hückel molecular orbital method*, conjugated polymers are expected to exhibit metallic behavior: the *N* $2p_z$ orbitals (unpaired electrons) of the participating carbon atoms lead to *N* π-molecular orbitals. Due to the overlap of the orbitals between neighboring atoms the π-electron wavefunction delocalizes over the chain, resulting in a π-band for high *N*. Since each carbon atom contributes one unpaired electron, the corresponding band is half filled and a metallic behavior is expected. However, experiments revealed that conjugated molecules or polymers are insulating or at best semiconducting. This could be explained by the *Peierls distortion*,[53] which results in the alternation of the bond-length between single (σ-) and double (σ- + π-) bonds[a] and hence in a metal-to-insulator transition with an energy gap between a filled π-band and an empty π^*-band. The energetically highest occupied molecular orbital of the π-band is shortened to *HOMO* and the lowest unoccupied molecular orbital of the π^*-band to *LUMO*.

The interaction between the π-electron system of an organic molecule with those of its neighbors basically leads to the formation of molecular solids, which are held together by weak van der Waals forces.

[a] "Conjugated" refers to the alternating sequence of single and double bonds in a molecule.

2.1.2. Excited States

In order to transport charge and/or emit light the semiconductor has to be excited and for charge transport these excitations have to be mobile as well. There is a large difference between excited states in organic semiconductors and those found in their inorganic counterparts. While the latter exhibit rigid three dimensional lattices formed by strong covalent forces, organic solids are formed by weak van der Waals forces and conjugated polymer chains are rather flexible. Therefore the formation of excited states is associated with structural relaxation and consequently charge localization.[1,9,54] In polymers with a degenerate ground-state[b] such as trans-polyacetylene a *soliton* appears as neutral or charged defect, where two structures of different bond order are combined. For polymers with a non-degenerate ground state, which are most of the applied in organic electronic devices, the participating charge carriers are *polarons* and *bipolarons*.

2.1.2.1. Polarons

When an electron is added to the LUMO of a conjugated polymer or removed from its HOMO, the chain is deformed in the region around the charge and consequently the electronic energy of the added charge is lowered. The extent of the lattice deformation (usually several monomers along the polymer chain) is determined by a minimum of the total system energy, which includes the increased elastic deformation energy and the reduced electronic energy.

This quasi-particle composed of the electron (or hole) and its accompanying local lattice distortion is referred to as negative (or positive) polaron. As polarons are "*self-trapped*" or "*self-localized*" by electron-lattice coupling, they have to overcome an energy activation barrier while moving through the material (thermally activated hopping).

Accordingly, the two energetic states of the polaron are found within the π-π^* gap between the HOMO and the LUMO, exhibit bonding and anti-bonding character, respectively, and can be occupied by zero, one, three or four electrons (Figure 2.4).

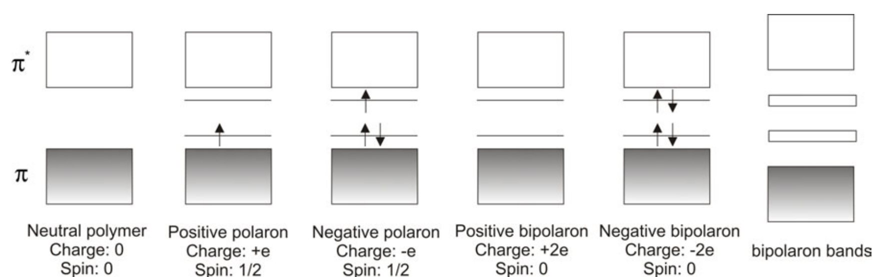

Figure 2.4: Energy levels of the neutral polymer and of various polaronic states in organic semiconductors.

[b] The single and double bonds can be interchanged without altering the total energy of the ground state.

Bipolarons are formed when two electrons are withdrawn from or added to a polymer chain. Accordingly, when more than two electrons are added or removed, bipolaron energy bands arise within the π-π^* gap at the cost of states from the band edges, hence increasing the gap energy.

2.1.2.2. Excitons

Basically, an exciton is an electrically neutral quasi-particle which can move as an entity. It arises, when an electron is removed from the HOMO and placed into its LUMO leaving back a hole. Both, electron and hole are bound to each other due to Coulomb (electron-hole) interaction, forming an exciton. Excitons can be created e.g. by photon absorption or by injection of positive and a negative polarons that meet each other (as used in an OLED). Again the excitation is associated with a structural relaxation of the surrounding molecular geometry. Excitons in organic materials are usually so-called *Frenkel excitons*, which are small-radius excitons and exhibit binding energies in the range of 0.1-0.5 eV. In contrast, more delocalized so-called *Wannier excitons* with smaller binding energies are usually found in inorganic semiconductors. Figure 2.5 schematically illustrates the electronic configurations of the ground state and the excitonic states in organic semiconductors.

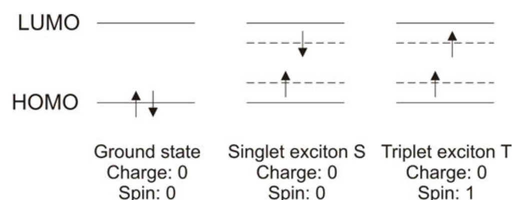

Figure 2.5: Energy levels of the ground state and excitonic states in organic semiconductors.

As electrons and holes exhibit spin ±½, they can combine to a net spin of zero or one. Accordingly *singlet* and *triplet excitons* can be formed. The exciton can be characterized by a wavefunction, which, according to Pauli's principle, has to be antisymmetric with respect to particle exchange. Hence, antisymmetric spatial part implies a symmetric spin part with a net spin of one. This is possible in three different ways $(\uparrow\uparrow)$, $(\downarrow\downarrow)$ and $\frac{1}{\sqrt{2}}\left[(\uparrow\downarrow)+(\downarrow\uparrow)\right]$, leading to triplet excitons. A symmetric spatial part requires an antisymmetric spin part, which is only possible with the configuration $\frac{1}{\sqrt{2}}\left[(\uparrow\downarrow)-(\downarrow\uparrow)\right]$, yielding spin zero and hence a singlet exciton.

The electronic ground state is usually a singlet state. Triplet states are energetically lower compared to the corresponding singlet states due to lower electron-electron repulsion. The migration of excitons mainly is described by energy transfer (Förster-, Dexter-transfer).

Radiative decay of excitons formed by injected polarons is used in OLEDs, dissociation of photo-excited excitons in solar cells and photodetectors. Details about the optical properties and processes in organic semiconductors can be found in [50].

2.1.3. Charge Transport

2.1.3.1. Electrical Conductivity and Charge-Carrier Mobility

Charge transport is associated with the *electrical conductivity* σ of a material, which depends on the density of mobile charge carriers and their mobility. When mobile electrons and holes are present, σ is calculated as:[55]

$$\sigma = en\mu_e + ep\mu_p \tag{2.1}$$

e… elementary charge; *n*/*p*… electron/hole density; μ_e/μ_p… electron/hole mobility.

Accordingly, σ also depends on temperature. While metals exhibit increasing conductivity with decreasing temperature, σ of semiconductors becomes larger upon heating.
One of the most important parameters related to charge transport is charge carrier mobility μ, which at low applied electric fields is defined by:

$$\mu = \frac{|\vec{v}|}{|\vec{E}|} \tag{2.2}$$

$\vec{v}$ … average drift velocity of the charge carriers; $\vec{E}$ … electric field.

The mobility can also be calculated by considering a charge carrier with charge q and effective mass m^*, being scattered after an average time τ:

$$\mu = \frac{q\tau}{m^*} \tag{2.3}$$

Amongst others, the mobility can be determined by Hall measurements, Time-of-Flight (TOF) measurements, Space charge limited current (SCLC) measurements and field-effect measurements.

2.1.3.2. General Issues

Conjugated materials are intrinsically semiconducting[c] with energy gaps in the range of 1-3 eV. Organic semiconductors either show p-type, n-type or ambipolar[56] behavior, with most of them studied so far being p-type.

[c] Due to commonly observed unintential doping they can also be regarded as compensated semiconductors.

N-type materials are more difficult to synthesize and are often unstable under ambient conditions. Moreover, SiO_2 has often been applied as gate dielectric for investigations on the charge transport behavior of organic semiconductors and the polar silanol groups on its surface were found to act as traps for mobile electrons (and also holes).[56]

Due to the formation of polaronic states in conjugated materials charge transport differs significantly from band transport in wide energy bands formed by strong covalent bonds in inorganic single-crystal semiconductors. The latter also exhibit long-range order, thus resulting in high mobility values (e.g. for silicon in the range of ~1000 cm^2/Vs at room temperature).

The degree of order is also strongly associated with the charge transport properties of organic semiconductors. A larger overlap between the π-orbitals of adjacent molecules (π-π stacking) results in larger charge-carrier mobilities and spatial and energetic disorder due to structural defects (twists, kinks, grain boundaries) and chemical impurities lead to charge-carrier trapping and thus reduced mobilities. Several transport models have been developed for single-crystalline, polycrystalline and disordered organic semiconductors, which are, however, often connected to particular systems due to the complexity of these materials and their structures. A detailed review can be found in [50]. Highest charge-carrier mobility values are found with organic single crystals. In naphthalene, for instance, hole mobility values as high as 400 cm^2/Vs at 10K were observed in time-of-flight measurements.[57,58,59,60] In field-effect transistors highest room temperature mobilities are on the order of 15-35 cm^2/Vs and were obtained with rubrene and pentacene single-crystals.[61,62,63,64] In OFETs based on polycrystalline pentacene mobility values are in the range of 1 cm^2/Vs[65,66] and best-performing disordered polymer semiconductors (rr-P3HT) exhibited values on the order of 0.1 cm^2/Vs.[41,67,68,69,70]

2.1.3.3. Charge Transport in Organic Single Crystals

Similar to single crystals based on inorganic semiconductors, the charge carrier mobility in ultra-pure organic molecular crystals was found to increase with decreasing temperature, which can be explained by the theory of polaronic transport.[18,71,72,73,74,75,76] At low temperatures delocalized charge carrier are assumed to move in bands, similar to carrier transport in silicon at room temperature. With increasing temperature electron-phonon interaction becomes stronger and so-called "*large polarons*" are formed, moving in bands with reduced bandwidths of ~0.1 eV. Accordingly, the mobility decreases. Finally, at higher temperatures a small polaron is formed and charge transport is dominated by phonon-assisted hopping between neighboring sites, similar to hopping between impurity states in inorganic semiconductors (see also section 2.1.3.5).[77,78,79,80]

Generally, polaronic models do not account for the presence of disorder (traps), which, however, can strongly affect charge transport in organic semiconductors.

2.1.3.4. Charge Transport in Polycrystalline Materials

Thin films of evaporated small conjugated molecules and oligomers commonly are of polycrystalline nature, in which crystallites (grains) are separated by grain boundaries. Here mobilities usually exhibit a thermally activated behavior and charge transport is mainly described by the multiple thermal trapping and release (MTR) model[81,82] and the grain boundary (GB) model.[83,84,85] The MTR model suggests that charge carriers can move freely in a narrow delocalized band of extended states, but most of them are trapped by localized states (deep or shallow traps) within the energy gap, resulting from homogenously distributed structural and chemical defects. Trapping and thermally activated release of the carriers determines the effective mobility. The MTR model could not account for the temperature-independent mobility at low temperatures observed by various groups.[67,83,86] This led to the GB model, which assumes that carrier traps only reside in grain boundaries and grains are trap-free. At high temperatures carriers overcome the energy barriers at grain boundaries by thermal excitation (thermionic emission). At low temperatures (temperature-independent) tunneling across the grain boundaries becomes the dominant mechanism, while it is thermally activated tunneling at intermediate temperatures.

2.1.3.5. Charge Transport in Disordered Conjugated Polymers

Models describing charge transport in disordered conjugated polymers[87,88,89] focus on the localized states and the shape of their energy distribution, which mirrors the disorder of the system. Charge carriers are believed to move by phonon-induced hopping between localized states (sites) on the same and on neighboring chains, if the corresponding wavefunctions overlap sufficiently.

The hopping model developed by Miller-Abrahams[80] can be used for the charge transport description in π-conjugated polymer systems. Assuming weak electron-phonon coupling (neglect of polaronic effects) and a single-phonon activated charge transport, the transition rate W_{ij} of carriers from an occupied localized state i to an unoccupied localized state j is given by:

$$W_{ij} = \nu_0 \, exp\left(-2\gamma R_{ij}\right) \begin{cases} exp\left(-\frac{\varepsilon_j - \varepsilon_i}{k_B T}\right), & \varepsilon_j > \varepsilon_i \\ 1, & \varepsilon_j < \varepsilon_i \end{cases} \tag{2.4}$$

ν_0… attempt-to-hop (phonon) frequency; γ … inverse of the localization length determined by the wavefunction overlap between the sites; R_{ij}… distance between localized states (sites) i and j; ε_i, ε_j… energy at state i and j, respectively; k_B… Boltzmann constant; T… absolute temperature.

While the first exponential term in eqn. (2.4) represents the tunneling probability between sites and becomes dominant at high temperatures, the second takes into account the probability to absorb a phonon for jumps upward in energy. For a jump downward in energy it is assumed that the charge carrier can always create a phonon to lose its energy. W_{ij} includes the positions and energies of localized states and hence hopping transport strongly depends on structural and energetic disorder.

Other hopping rates including polaronic effects and multi-phonon processes have been developed by Emin[90] and Marcus[91]. The Miller-Abrahams hopping model was further extended to the *variable range hopping (VRH) model* by Sir N. Mott, in which the localized states are assumed to be distributed over the entire energy gap.[92,93,94] Although the VRH model describes well the temperature-dependence of the electrical conductivity in disordered organic semiconductors, it does not account for the empirically observed electric field-dependence of the charge carrier mobility ($\ln \mu \propto \sqrt{E}$).[95,96,97,98,99]

This behavior was first theoretically explained by Bässler[98] in the *Gaussian Disorder Model* (GDM), who applied eqn. (2.4) and performed Monte Carlo simulations, assuming a Gaussian density of localized states[d] and including energetic and positional (spatial) disorder. Later Gartstein and Conwell[100, ,101] extended Bässler's model to the *Correlated Gaussian Disorder Model* (CDM), also including spatial correlations between site energies.

For the description of the temperature- and gate-voltage dependence of the field-effect mobility in disordered organic semiconductors, Vissenberg and Matters[102] developed a percolation model based on Mott's VRH model, in which they assumed an exponential density of states and derived an expression for the electrical conductivity and, accordingly, the field-effect mobility in a transistor as a function of temperature and gate voltage, which was in good agreement with experimental data. It ascribed the gate-voltage dependence of the mobility to increasing carrier concentration, which leads to a filling of the localized states, resulting in an increase of the average energy, thus facilitating the jump to the transport energy.

Later Tanase and co-worker[103] demonstrated that in the energy range in which field-effect transistors operate the exponential DOS is a good approximation of the tail states of the Gaussian DOS, which is used for the charge transport explanation in polymer LEDs.[99] In that way both models for LEDs and FETs based on π-conjugated polymers could be unified.

[d] due to observed Gaussian-shaped absorption spectra of polymer materials.

2.2. Organic Field-Effect Transistors

The following section summarizes the most important issues regarding OFETs. A more detailed introduction is provided in [50].

2.2.1. Architectures and Fabrication Techniques

For organic field-effect transistors[18,19,22,23,24,25] two architectures are mainly applied: the bottom-gate structure (or inverted staggered configuration) and the top-gate structure (or staggered configuration). Figure 2.6 illustrates the differences.

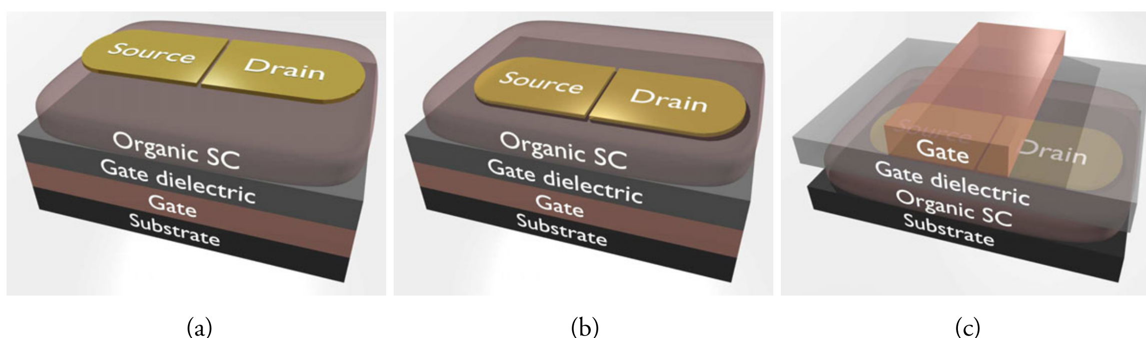

Figure 2.6: a) Bottom-gate/top-contact architecture; b) Bottom-gate/bottom-contact architecture; c) Top-gate/bottom-contact architecture.

For the bottom-gate structure a gate electrode is formed on a substrate, which is then covered by a layer of an appropriate dielectric material and an organic semiconductor forming the active channel layer. Moreover, two electrodes (source and drain) are provided on top (bottom-gate/top-contact configuration, Figure 2.6a) or the organic semiconductor is in fact deposited after the definition of the source/drain electrodes (bottom-gate/bottom-contact configuration, Figure 2.6b). For the top-gate structure source and drain are formed on a substrate, followed by the deposition of the organic semiconducting material, which is then covered by a dielectric. Finally a gate electrode is deposited on top (top-gate/bottom-contact configuration, Figure 2.6c). In another subtype of this architecture, similar to the bottom-gate/top-contact configuration, the organic semiconductor can also be deposited before the definition of the source/drain electrodes (top-gate/top-contact configuration, not shown). Several intermediate layers to promote charge carrier injection or for other purposes can be inserted in both configurations to improve the device performance.

2.2.1.1. Substrates

Considering the solution-processability at low-temperatures of many electroactive organic compounds, substrates may be made of virtually any material type and shape; from rigid to flexible, from flat to cylindrical, everything, even paper, can be applied.[49,104,105,106,107,108]
For investigations on organic semiconductors highly doped silicon wafer pieces with a SiO_2 layer are often used, as the silicon can be applied as gate electrode and SiO_2 as gate dielectric, the latter forming nice interfaces to silicon and exhibiting a rather smooth surface. However, as mentioned, the associated polar silanol groups act as traps for mobile charge carriers.[56]

2.2.1.2. Organic Semiconductors

Semiconductors in OFETs are required to exhibit good charge transport properties, an efficient injection of charge carriers, good processability and environmental stability. Various types of materials can be applied, ranging from small molecules forming single crystals and polycrystalline films to conjugated polymers leading to layers with more or less disordered morphology (see Figure 2.1). In this thesis pentacene, rr-P3HT and polytriphenylamine-derivatives were used.
Single-crystal OFETs are fabricated either by applying an organic crystal, which is grown by the *Physical Vapor Transport (PVT) method*, to OFET structures via electrostatic bonding or by direct fabrication on the crystal surface.[61]
Polycrystalline films are mainly deposited by thermal evaporation in high and ultra-high vacuum units and polymer semiconductors are usually solution-processed by techniques such as spin-coating, drop-casting or inkjet printing. The latter therefore enable the fabrication of all-solution processed devices, for which the solution-compatibility with adjacent layers is an important issue to ensure that an already deposited layer is not dissolved again by subsequent layer deposition. This can be obtained by using orthogonal solvents or an appropriate curing procedure to render the already deposited layer insoluble.
As the charge transport takes place within the first few monolayers close to the interface with the dielectric layer, typical values of the semiconductor layer thickness are 10-50 nm.
Generally, the deposition of the semiconducting film and the corresponding parameters (substrate temperature, deposition rate, base pressure, spin-speed etc.) strongly influence the OFET performance.

2.2.1.3. Gate Dielectrics

Aside from the semiconductor, another important layer material determining the device operation and performance of an organic field-effect transistor is the gate dielectric.[109,110] Within the last years there has been intense research on various kinds of insulating materials, ranging from inorganic oxides and polymeric dielectrics to self-assembled monolayers (SAMs). Generally, polymer dielectrics are interesting, as they enable all-solution processed devices. Just increasing the charge-carrier mobility of the organic semiconductor material does not lead to high-performing devices. Overall performance is determined by the combination of all constituting layer materials, including semiconductor, insulator and electrode metals. Dielectrics with high relative permittivity are suggested for low operating voltages, as upon their use larger charge densities can be induced at lower gate voltage. However, there is still discussion how the relative permittivity influences the field-effect mobility. While some groups found increasing mobility with increasing dielectric constant,[111,112,113] others observed higher μ values with low-k dielectrics.[114] The latter attributed this to increased energetic disorder and enhanced carrier localization at the semiconductor/dielectric interface, when polar (high-k) gate insulators are applied.

It is also well known that the application of ion-conducting (electrolyte) gate dielectrics can lead to a strong reduction of the operating voltage by generating large charge carrier densities ($>10^{14}\,cm^{-2}$) in an OFET channel through ions moving to the interfaces or even into the semiconductor.[115,116,117,118,119,120,121,122] The interactions are mainly ascribed to the formation of electric double layers (EDLs) at the interfaces (leading to very large capacitance values) or to electrochemical doping (oxidation/reduction processes). On the other hand, mobile ions within the dielectric are also responsible for usually undesired hysteresis effects,[109,123,124,125,126,127,128,129,130,131] which, however, if non-volatile, can be used for the fabrication of organic memory elements.[132,133,134]

Moreover, surface modification of the dielectric with self-assembled monolayers based on e.g. silanes (e.g. n-octadecyltrichlorosilane, OTS) or siloxanes (e.g. hexamethyldisilazane, HMDS) was found to have a strong influence on device performance and stability.[135] This will be described in detail in chapters 3 and 4.

2.2.1.4. Electrodes (Source/Drain/Gate)

Typical electrodes in OFETs are made from metals (e.g. gold, silver) or from conducting polymers (e.g. doped poly(ethylenedioxythiophene) (PEDOT:PSS) or polyaniline (PANI)). As mentioned, also highly doped silicon may act as gate.

Proper choice of the electrode material in terms of e.g. work function is fundamental for good charge-carrier injection into and ejection out of the organic semiconductor.[34,35,50,136,137] Basically, charge-carrier injection from a metal into an organic semiconductor can be described as tunneling from (thermally excited) metal states into randomly distributed localized polaronic states of the organic molecule (thermally assisted tunneling, field-assisted thermionic injection).[136] In real contacts dipole layer formation (e.g. by a thin oxide layer) at the interface between metal and organic semiconductor can result in significant energy barriers, even if the metal work function matches to the conduction level of the semiconductor.[138]

Various methods for the fabrication and structuring of source/drain electrodes have been applied, such as vacuum evaporation, sputtering, photolithography, inkjet printing,[50, 139 , 140 , 141 , 142] electrochemical polymerization of monomers,[112] screen printing,[143] photochemical patterning[48] or soft-lithography (see also chapter 3.2). Non-solution-processed techniques typically are more expensive and require sophisticated instrumentation. Moreover, photolithography is difficult to apply for top-contact OFETs, because the electrical properties of the organic semiconductor are often degraded when exposed to corresponding processing solvents and chemicals. Figure 2.7 illustrates examples of OFETs with inkjet-printed source/drain electrodes based on the conductive polymer PEDOT:PSS and a silver-copper nanoparticle dispersion.

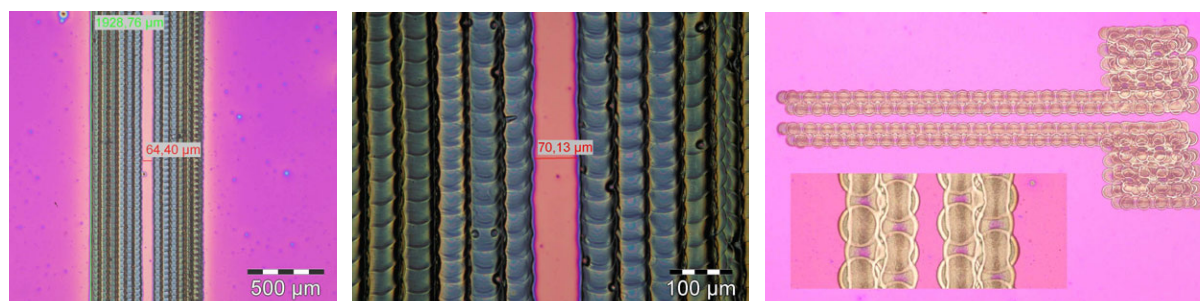

Figure 2.7: Bottom-gate/bottom-contact rr-P3HT-OFETs with inkjet printed PEDOT:PSS- (left and middle) and silver-copper nanoparticle-based source/drain electrodes.[50,139,140]

2.2.2. Operating Principle, Device Characteristics and Parameters

Basically, an OFET resembles a capacitor with one plate providing a conducting channel between two ohmic contacts, the source and the drain electrodes. A voltage applied to the second plate, the gate electrode, modifies the density of charge carriers in the channel. Upon application of a drain voltage these carriers move from the source across the channel into the drain. Hence, just by applying a field across the dielectric layer the device is turned into its "on"- or "off"-state, respectively.

Ideally, no current is needed for switching and so the corresponding power consumption is reduced to - or nearly to - zero. OFETs, like a-Si:H TFTs, operate in the accumulation regime, which means that the charge carriers responsible for the off-current conduction and those accumulated in the channel to yield the on-current are of the same type (positive or negative polarons). Hence, there is no depletion region between the conducting channel and the substrate as found e.g. in MOSFETs and low off currents, which are necessary for high switching abilities, can only be achieved by the low off-conductivity of the organic semiconductor.
Figure 2.8 depicts the two basic operational regimes in an OFET, depending on the applied gate voltage V_G and drain voltage V_D. Roughly speaking, the linear regime is found for $|V_D| < |V_G|$ and the saturation regime for $|V_D| > |V_G|$.

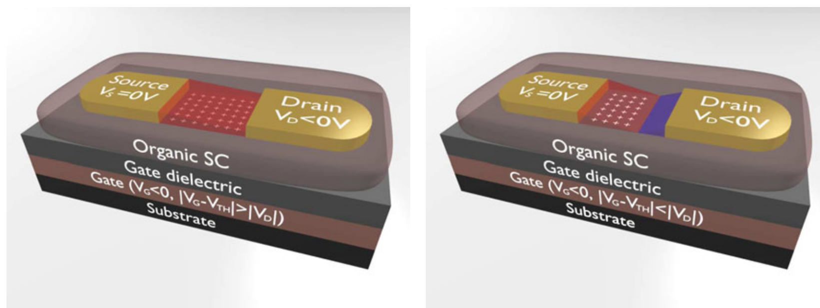

Figure 2.8: Operational regimes in an OFET; left: linear regime; right: saturation regime (red = accumulation region, blue = depletion region).

A comprehensive model for these two regimes was developed by Horowitz and co-workers.[144] Although only drift currents are considered, the presence of parasitic contact resistances is neglected and constant field-effect mobility, not depending on the gate voltages, is assumed, the derived equations are commonly used to quantify the performance of devices.
The model is based on the gradual channel approximation developed by W. Shockley,[34,35] which assumes that the charge density related to the variation of the drain electric field is much smaller then that related to a variation of the gate electric field. Hence, the channel potential is gradually changing with position x along the channel, varying only slightly over distances on the order of the insulator thickness. As the voltages applied to gate and drain electrodes in an OFET are often of the same magnitude, the gradual channel approximation holds when the insulator thickness is much smaller than the channel length.

Neglecting diffusion contributions, the channel current density j_D and the corresponding source-to-drain channel current I_D are given by:

$$j_D = qnv = qn\mu E = qn\mu \frac{dV}{dx} \tag{2.5}$$

$$I_D = qn\mu \frac{dV}{dx} W = |Q(x)|\mu \frac{dV}{dx} W \tag{2.6}$$

q… elementary charge; n… surface charge density; μ… field-effect mobility; E… electric field in x-direction (along the channel); V… channel potential; W… channel width; $Q(x)$… surface charge at position x.

The surface charge $Q(x)$ consists of the charge induced into the accumulation layer $Q_S(x)$ and the charge present in the bulk Q_0 (e.g. due to doping). Assuming that there is no depletion region and that, hence, $Q_S(x)$ spans the complete channel length (corresponding to Figure 2.8 left, $|V_D| < |V_G|$), Q_0 is constant and the surface charge can be calculated according to:

$$Q(x) = Q_S(x) + Q_0 = -C_i\left[V_G - V_{FB} - V_S(x) - V(x)\right] \pm qn_0 d_S \tag{2.7}$$

C_i… insulator capacitance per unit area; V_{FB}… flat band voltage (work function difference between semiconductor and gate-metal); $V_S(x)$… ohmic drop across the semiconductor; $V(x)$… channel potential; n_0… density of free charge carriers at equilibrium; d_S… semiconductor thickness.

The sign of the last term in eqn. (2.7) is related to the majority carriers. For gate voltages larger than a few volts most of the voltage drops across the insulator and $V_S(x)$ can be neglected.[82]
Combining equations (2.6) and (2.7) and integrating from source ($x = 0$, $V = 0$) to drain ($x = L$, $V = V_D$) under the assumption of constant mobility, this leads to the equation for the channel current I_D in the linear regime ($|V_D| < |V_G|$):

$$I_D = \frac{W}{L}\mu C_i\left[\left(V_G - V_{th}\right)V_D - \frac{V_D^2}{2}\right] \tag{2.8}$$

$$V_{th} = \pm\frac{qn_0 d_S}{C_i} + V_{FB} \tag{2.9}$$

The zero voltage or threshold voltage V_{th} results from the non-zero channel current at $V_G = 0$V. The sign in eqn. (2.9) is again related to the majority carriers and inverse to the polarity of V_G.[e]
For small V_D the quadratic term in eqn. (2.8) can be neglected.
When V_D exceeds V_G, a depletion region containing no free charge carriers is formed near the drain electrode beyond the point where $V(x) = V_G$ (corresponding to Figure 2.8 right).
Within this region the effective conductive thickness of the semiconducting film is reduced and the corresponding channel current I_D is given by:

[e] This contradicts to the threshold voltages extracted from experimentally measured OFET characteristics, which usually exhibit the same sign as V_G.

$$I_D = \mu q n_0 \left[d_S - d_{dep}(x) \right] \frac{dV}{dx} W \tag{2.10}$$

$d_{dep}(x)$… thickness of the depletion layer.

Neglecting the flat-band voltage V_{FB}, $d_{dep}(x)$ can be expressed as:[17]

$$d_{dep}(x) = \frac{\varepsilon_S}{C_i} \left[\sqrt{1 + \frac{2C_i^2 \left[V(x) - V_G \right]}{qN\varepsilon_S}} - 1 \right] \tag{2.11}$$

ε_S… permittivity of the semiconductor; N… dopant concentration.

When assuming that the accumulation layer extends from the source ($x = 0$) to a point x where $V(x) = V_G$ and is replaced by a depletion layer beyond this point, the channel current in the saturation regime I_{Dsat} can be calculated as follows:

$$I_{Dsat} = \frac{W}{L} \mu C_i \int_0^{V_G} \left(V_G - V_{th} - V \right) dV + \frac{W}{L} \mu q n_0 \int_{V_G}^{V_{Dsat}} \left[d_S - d_{dep}(x) \right] dV \tag{2.12}$$

Solving the integrals in eqn (2.12), introducing a pinch-off voltage and assuming that the concentration of dopants N is equal to the free charge carrier density at equilibrium n_0, the Horowitz model leads to the following equation for I_{Dsat} ($|V_D| > |V_G|$):

$$I_{Dsat} = \frac{W}{2L} \mu C_i \left(V_G - V_{th} \right)^2 \tag{2.13}$$

Equations (2.8) and (2.13) are the basic formulas describing the linear and the saturation regime observed with OFETs, with the assumptions mentioned above.

The electrical characterization of OFETs usually yields two important sets of curves. The output characteristics are measured by sweeping the drain voltage at various fixed gate voltages. Accordingly, the transfer characteristics are recorded by sweeping the gate voltage at various fixed drain voltages. For determination of the operational stability, a double sweep from low to high values (forward) and back to low values again (reverse sweep) is often performed. Figure 2.9 illustrates typical device characteristics. In particular in the left plot the saturation of the drain current for $|V_D| > |V_G|$ becomes obvious.

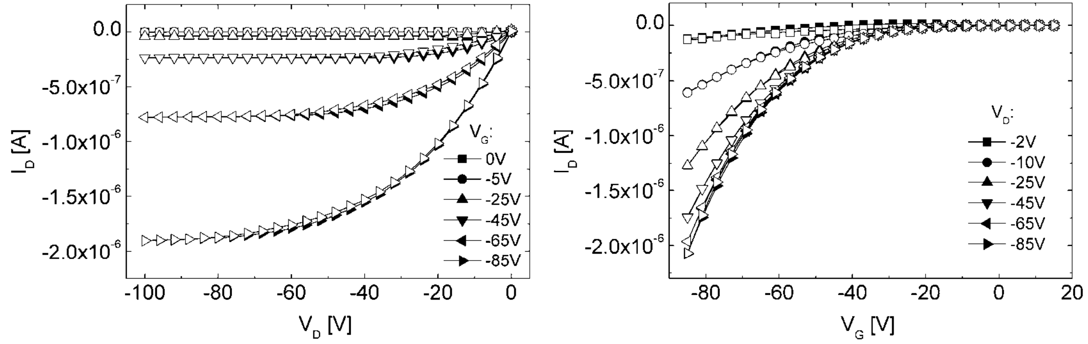

Figure 2.9: Typical output (left) and transfer (right) characteristics of an OFET; filled symbols: sweeps from positive to negative voltages; open symbols: reverse sweep.

2.2.2.1. Field-Effect Mobility

The field-effect mobility μ_{FE} can be derived from the standard equations (2.8) and (2.13) according to:

$$g_m = \left(\frac{\partial I_D}{\partial V_G}\right)_{V_D=const} = \frac{W}{L}\mu_{FE}C_iV_D \qquad \mu_{FE} = \frac{L}{WC_iV_D}\left(\frac{\partial I_D}{\partial V_G}\right)_{V_D=const} \tag{2.14}$$

$$\mu_{FEsat} = \left(\frac{\partial\sqrt{I_{Dsat}}}{\partial V_G}\right)^2_{V_D=const} \cdot \frac{2L}{W \cdot C_i} \tag{2.15}$$

g_m is the so-called transconductance. These equations do not account for a gate-voltage dependent mobility (hence neglecting the existence of traps) and parasitic resistances at the contact.
As mentioned, the gate-voltage dependence of the field-effect mobility is believed to be associated with the induced charge carrier density. Increasing V_G leads to a filling of charge carrier traps within the semiconductor, at the dielectric/semiconductor interface and/or within the dielectric. Consequently the concentration of free charge carriers in the conducting channel is increased, which translates into a higher field-effect mobility.[19] Nevertheless, for a first estimation equations (2.14) and (2.15) are often applied (also within this thesis). Another method to extract μ_{FE}, which also takes into account contact resistance, will be described in chapter 2.2.2.5.

2.2.2.2. Threshold Voltage and Switch-on Voltage

For inorganic metal-insulator-semiconductor-FETs (MISFETs) the threshold voltage is determined by the onset of strong inversion and therefore a physically relevant parameter.[34,35] However, as OFETs operate in the accumulation regime, the parameter has no physical meaning with these devices. Nevertheless it is often extracted from transfer curves by linearly fitting the absolute value (linear regime) or the square root (saturation regime) of the channel current and extrapolating the fit line to zero current, as shown in Figure 2.10.

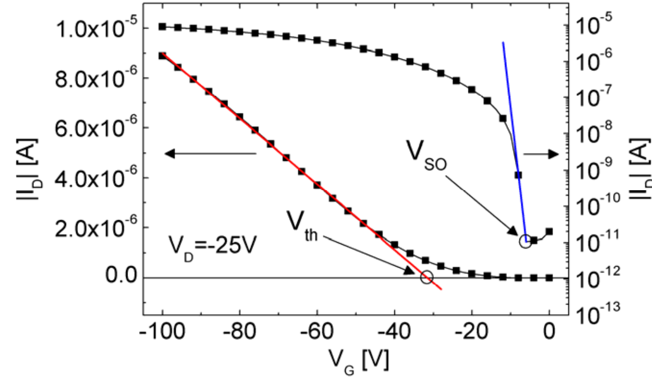

Figure 2.10: Transfer curve (linear and semi-logarithmic) and corresponding fits for the extraction of threshold voltage V_{th}, switch-on voltage V_{SO} and subthreshold slope S.

Due to V_{th} being only a fit parameter, Meijer and co-workers[145] defined a switch-on voltage V_{SO}. Below V_{SO} the variation of the channel current with V_G is zero, while the channel current increases with $V_G > V_{SO}$. Hence, V_{SO} is the gate voltage at which the channel starts to form. For an OFET this parameter is physically more meaningful than V_{th}. The corresponding extraction from the semi-logarithmic transfer curve is also illustrated in Figure 2.10.

Both the switch-on and the threshold voltage are associated with the quality of the semiconductor/dielectric interface and the doping level of the semiconductor. Ideally V_{SO} should be 0V. However, as mentioned, when traps are existing, they are filled by the first injected charge carriers so that for a p-type semiconductor V_{SO} (and accordingly V_{th}) is more negative. On the other hand, when doping increases the bulk charge carrier density, in a p-type OFET V_{SO} and V_{th} shift to more positive values.

2.2.2.3. On/Off-Current Ratio

The on/off-current ratio I_{on}/I_{off} is the ratio of the channel current in the on-state of a transistor (I_{on}), given at a distinct high V_G and V_D (usually in the saturation regime), to the corresponding value in the off-state (I_{off}), given at low V_G (usually $V_G = 0$V) and the same V_D as used for I_{on}. Well-performing OFETs exhibit on/off-current ratios larger than 10^6.

2.2.2.4. Subthreshold Slope

The subthreshold slope S is also an important device parameter, being defined as follows:

$$S = \frac{dV_G}{d(\log I_D)} \tag{2.16}$$

Basically, it is a measure of how much gate voltage has to be applied to increase the channel current by one order of magnitude. Its unit is therefore V/dec.

The subthreshold slope is also associated with the quality of the semiconductor/insulator interface. Accordingly, the maximum number of interface traps $N_{T,max}$ can be derived from S with eqn. (2.17), assuming that the densities of deep bulk states and interface states are independent of energy:[146,147,148]

$$N_{T,max} = \left[\frac{S \cdot log(e)}{kT/q} - 1 \right] \frac{C_i}{q} \tag{2.17}$$

e…Euler's constant; k… Boltzmann constant; T… absolute temperature; q…elementary charge; C_i…insulator capacitance per unit area.

2.2.2.5. Contact Resistance

The presented OFET model for the description of the current-voltage characteristics assumes an ideal device, in which the complete applied drain voltage drops across the channel. As already mentioned, in real devices parasitic resistances related to contacts exist, which often limit the performance of a device, as they might be comparable or even higher than the channel resistance.[34,35,149,150,151,152,153,154,155] The parasitic resistances are associated with the injection barriers at the metal/semiconductor interfaces. Their magnitude is affected by many parameters, including work function difference between metal and semiconductor, interface morphology, trap concentrations, doping levels, interfacial dipole layers, chemical and physical reactions near the interface, temperature and sample geometry. Contact resistance usually increases with decreasing temperature, considering that charges are injected by thermally assisted tunneling across these barriers, Furthermore, its influence on device performance increases with decreasing channel length L.[156] This will be discussed in more detail below.

Contact resistances in an OFET usually depend non-linearly on gate- and drain voltage. Increasing V_G leads to a larger induced carrier density near the metal/semiconductor interfaces, which in turn reduces contact resistance.[f] However, although the absolute value becomes smaller, its relative influence might increase, as the channel resistance also decreases with increasing V_G due to the increasing field-effect mobility. Moreover, the gate-voltage dependence of the contact resistance can also influence the experimentally determined gate-voltage dependence of μ_{FE}.

Basically, when eqn. (2.14) is applied for the determination of the field-effect mobility of OFETs with various channel lengths L, different $\mu_{FE}(V_G)$-curves for different L are obtained,[156] which would imply that mobility is a device parameter rather than a material parameter.

[f] This is similar to contact doping in inorganic semiconductors.

The apparent decrease of μ_{FE} with decreasing L results from parasitic series resistances at the contacts. Compared to long-channel devices, in shorter channels a relatively larger fraction of V_D drops over the parasitic contact resistance R_P (= sum of source and drain contact resistances).
A parameter extraction method which accounts for contact resistance, is the *transfer line method* (TLM),[150,152,153,156] which was originally developed for a-Si TFTs.[157] It enables a separate extraction of the contact resistance R_P and the channel resistance R_{ch}. The device resistance R_{on} can be calculated as the sum of R_{ch} and R_P:

$$R_{on} = \left.\frac{\partial V_D}{\partial I_D}\right|_{V_D \to 0, V_G} = R_{ch}(L) + R_P = \frac{L}{W\mu_{FE}C_i(V_G - V_0)} + R_P \tag{2.18}$$

While the channel resistance R_{ch} is assumed to increase linearly with L, the parasitic contact resistance R_P is independent of the channel length. Consequently, the relative influence of the contact resistance increases as the channel length is reduced.
Plotting R_{on} (=V_D/I_D) as a function of the channel length L for different gate voltages V_G and performing a linear fit to the corresponding curves yields straight lines, the slopes of which reveal the channel resistivity (channel resistance R_{ch} per unit length), while the parasitic contact resistance R_P is obtained by the extrapolation of the fit curves to zero channel length.
The channel conductivity can be calculated as the inverse of the channel resistivity: $\left(\frac{\Delta R_{on}}{\Delta L}\right)^{-1}$.
Deriving this expression with respect to V_G yields the field-effect mobility μ_{FE} corrected for the parasitic series resistance R_P:

$$\frac{\partial\left[\left(\frac{\Delta R_{on}}{\Delta L}\right)^{-1}\right]}{\partial V_G} = \mu_{FE}(V_G)WC_i \tag{2.19}$$

The μ_{FE}-values obtained from (2.19) are higher than those derived from eqn. (2.14), which does not consider contact resistance. Meijer and co-workers,[156] who used this method for OFETs based on conjugated polymers, confirmed that the mobility values derived from equation (2.14) for devices with longer channels are closer to the corrected values, which implies that the influence of R_p is smaller for long-channel OFETs. Further details will be described in chapter 3.
Another, method for the determination of device parameters, which are not affected by parasitic contact resistances, is the 4-probe measurement. Here four electrodes are applied, two for charge injection providing the channel current and two for determining the voltage drop across their distance.

2.2.2.6. Short-Channel Effects

As mentioned, OFETs will also find their application in integrated circuits e.g. for radio-frequency identification tags,[20] which requires operating frequencies in the MHz region and accordingly device miniaturization,[34,35, 158] as the charge carrier mobility in organic semiconductors is low and the relevant cut-off frequency scales with $\mu V_D/L^2$. However, when the channel length is reduced without reducing the dielectric layer thickness, the gradual channel approximation described above is not valid any more and short-channel effects arise, which are well known from inorganic MOSFETs.[34,35,159, 160] Channel-length modulation is one such effect, which is related to an inability of the channel current to saturate for $|V_D| > |V_G|$. This results from the fact that for increasing V_D the width of the depletion region near the drain electrode becomes comparable to the length of the accumulation region (see Figure 2.8 right), which results in a significant reduction of the conductive channel length. According to eqn (2.13) the saturation current I_{Dsat} scales with $1/L$ and therefore becomes dependent on V_D, when the effective L is reduced. Another implication of short-channel effects is a shift of the switch-on voltage (and accordingly also the threshold voltage), transferring a device from enhancement mode (normally off) to depletion mode (normally-on). This can be ascribed to completely depleted channels, in which the channel current enters the space charge limited current (SCLC) regime. The corresponding current density scales with $\mu V_D^2/L^2$, so that I_{Dsat} becomes largely dependent on V_D (non-destructive punch-through).

2.2.3. Device Stability

2.2.3.1. Environmental Stability

In order to yield well-performing low-cost OFETs, essential properties of the applied organic semiconducting materials include solution-processability, high field-effect mobility, compatibility with adjacent layers, in particular with the gate dielectric and the charge-injecting electrodes, and stability with respect to ambient conditions. One of the most common and best-performing polymer-based organic p-type semiconductor materials employed as active layer in OFETs is poly(3-hexylthiophene) (Figure 2.1e), exhibiting nano- or micro-crystalline film morphologies, anisotropic charge transport and a rather large field-effect mobility with highest values on the order of 0.1 cm^2/Vs, the latter usually obtained when the substrate surface was pre-treated with a self-assembled monolayer.[67,109,161,162]

However, when exposed to oxygen, moisture or air, P3HT is not very stable, as has been shown in several reports.[135,163,164,165,166,167,168,169,170,171,172] Due to the rather extensive π-conjugation of

polythiophenes[173] their ionization potential (energy difference between HOMO and vacuum level) is usually rather low (4.4 – 4.8 eV for P3HT)[174,175] and therefore the formation of a reversible charge-transfer complex with oxygen is facilitated (Figure 2.11).[164,165]

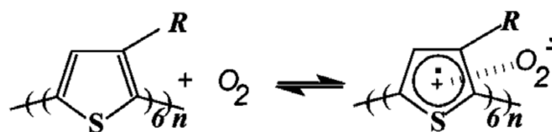

Figure 2.11: Poly(3-alkylthiophen)-oxygen charge transfer complex; figure taken from [165] and modified.

Hence, exposure of P3HT to O_2, in particular in combination with light, leads to an increase of the bulk dopant density and consequently of the hole conductivity of the semiconductor, associated with a decrease of the field-effect mobility.[165,166,168]

Furthermore, adsorbed water molecules (moisture, humidity) have also a strong influence on P3HT-based OFETs.[171] A rather low packing between the polymer chains, a large amount of pinholes and/or many grain boundaries exhibiting wide gaps within the film might facilitate the penetration of oxygen and water molecules thus affecting the charge-transport properties.

In P3HT-based OFETs oxygen- and/or moisture-induced doping typically leads to an increase of the off-current, a decrease of the on-current and, consequently, a decrease of the on/off-current ratio, a reduction of the field-effect mobility, a shift of the switch-on voltage to more positive values and a degradation of the saturation behavior. Also other well-established organic semiconductors such as pentacene degrade under ambient conditions, leading to changes in the device characteristics of corresponding OFETs. Stable air operation therefore involves expensive device encapsulation or a top-gate architecture, where the semiconductor is shielded by an appropriate dielectric material.[176,177] Another possibility is the application of materials with larger ionization potentials. This will described more in detail in chapter 4.

2.2.3.2. Operational Stability

High trap-densities within the semiconducting layer, at the semiconductor/dielectric interface or within the dielectric (Figure 2.12) lead to a reduction of the free charge carrier density within the channel, thus reducing the performance of OFETs.[56,178,179,180,181] These traps mainly arise from chemical and/or structural impurities in the applied materials and are most “efficient” under high applied gate voltage (gate-bias stress).

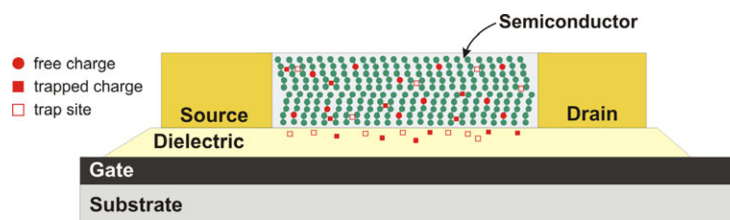

Figure 2.12: Schematic representation of charge trapping in organic semiconductors.

Charge-carrier trapping has several effects on the device characteristics of OFETs. Usually it leads to hysteresis in double sweeps, where the forwardly recorded channel currents are larger than the reversely recorded.[g] Accordingly, for the investigation of the operational stability of an OFET the channel current is often measured at a fixed (high) gate and drain voltage as a function of time. Charge-carrier trapping also causes switch-on voltage (and accordingly threshold voltage) shifts, as an applied gate potential is effectively screened by the build-up of a space charge resulting from trapped carriers. Moreover, gate-bias stress is responsible for the fact that the channel current at a particular V_D and (high) V_G is often larger in the transfer characteristics than in the output characteristics, because a high gate voltage (leading to charge trapping) is longer applied in the latter. Trapped carriers can be released again either upon light exposure (photo-induced de-trapping), by heating or by the application of positive gate-bias stress. When the substrate is pre-treated e.g. with a self-assembled monolayer, the interface trap density can be reduced.

2.3. OFET-based Sensors

OFETs are also believed to find their application as smart (disposable) sensor devices[182] in health-, food- and environmental monitoring, diagnostics and control, ranging from light- and chemical vapor sensors to transducers for ions and biological substances.[183,184,185,186] Such devices are intended to detect miscellaneous analytes like e.g. oxygen, ammonia, alcohol vapors, ions, acids, bases, aromatic compounds or biomolecules. In fact, the drawback of low environmental stability related to some organic semiconductors can be used for sensing ambient gases like oxygen or humidity levels, provided that the material exhibits sufficient selectivity. Nevertheless, ambient stability of the applied materials is generally very important in OFET-sensors. Other requirements include high sensitivity, reproducibility, reliability, robustness and portability. A key target in this field is the establishment of all-solution-processed integrated smart sensor devices. Low switching speeds due to low mobility are not so much an issue for sensing, as response time on the orders of seconds or minutes are often required. Aside from the common aforementioned

[g] The appearance of hysteresis is, however, also strongly influenced by the effective measurement time.

advantages associated with the use of organic semiconductors, OFETs have a number of advantages related to their device architecture. In particular, compared to resistor-based sensors (chemiresistors), field-effect transistors generally have the advantage of being more sensitive due to the inherent amplification of the sensing event. Moreover, they usually exhibit higher response times, higher sensitivity, low power consumption, the ability to implement multi-parameter sensing as well as the possibility to be integrated in complex circuits including signal processing. Several sensors based on the OFET device have been demonstrated already[183,184,185]; for instance, gas- or vapor-sensitive OFETs, mainly of bottom-gate type, for gases like N_2[187], O_2[187], NO_2[188], O_3[189,190] or organic vapors[44,191,192,193,194,195] like alcohols, with the semiconducting layer as sensing layer, where its electrical conductivity is modulated upon direct interaction with an analyte; humidity-sensitive OFETs,[45,196] which show a reduction of the hole mobility by the presence of traps resulting from the polar water molecules; pH-sensitive (or ion-sensitive) OFETs[46,197] based on inorganic dielectrics with an ion-sensitive surface, where the potential drop at the interface between the dielectric and an electrolyte solution is modified when the pH value changes in the latter; biochemical OFET-sensors e.g. for glucose,[197] where a specific enzymatic layer is added to a pH-sensitive OFET; the enzyme leads to the formation of gluconic acid, which, upon dissociation, yields a change in the local pH value. Moreover, organic transistor sensors with a layer of immobilized antibodies or DNA for the detection of the corresponding antigens or complementary target DNA have been proposed, in which direct charge transfer processes or charge displacements induced by complex formation lead to the sensor signal.[47,184]

OFET-sensors were also integrated into arrays for multi-species detection ("E-nose")[44] or into textiles (see chapter 3.3) and they were shown to be applicable for artificial skin applications.[198,199]

3. OFET Fabrication Techniques and Process Development

This chapter at first describes the implementation and testing of a completely new modular OFET fabrication line, integrated within a cleanroom environment, including equipment definition and acquisition, process development and optimization as well as device fabrication and characterization. In this section rr-P3HT- and pentacene-based OFETs with various source/drain-electrode geometries and channel dimensions, prepared with the newly established line, are investigated with respect to short-channel effects and the implications of dielectric surface modification with hexamethyldisilazane. The next section deals with the fabrication and analysis of well-performing bottom-gate/bottom-contact OFETs based on rr-P3HT with silver source/drain electrodes defined by two soft-lithographic techniques, namely Micromolding In Capillaries and Microtransfer Printing. Finally, organic field-effect transistors formed on insulating copper wires (wireOFETs) are presented, indicating the potential of combing readily available mass products with solution-processable organic semiconductors for the fabrication of smart, textile-compatible, low-cost organic electronics.

3.1. Implementation and Testing of a New Modular OFET Fabrication Line

3.1.1. Introduction

During this thesis the startup of a new company, namely the NanoTecCenter Weiz Forschungsgesellschaft mbH,[200] was intensively assisted, in particular with the focus on the setup and testing of a new modular pilot and demonstration fabrication line for the development of organic electronic devices on 1″ x 1″ and 2″ x 2″ substrates up to 4″ wafers. This involved the planning, acquisition, implementation and testing of equipment for substrate pre-treatment, layer deposition, photolithography and device characterization. Furthermore, as the fabrication line was partially set up within a 150 m^2 cleanroom environment,[h] an appropriate cleanroom management had to be implemented, which enabled the certification as ISO class 7 and later even as ISO class 6 cleanroom according to ISO 14644 standards, assuring the preparation of high-quality devices. With the new equipment a photolithographic lift-off process for structuring OFET source/drain electrodes and a process for dielectric surface modification with hexamethyldisilazane (HMDS) was developed, tested and optimized. Finally, well-performing rr-P3HT- and pentacene-based OFETs with various source/drain-electrode geometries and channel dimensions were fabricated with the new line and investigated with respect to short-channel effects and the implications of dielectric surface modification with HMDS.
The data presented in this chapter were obtained in close collaboration with Arno Meingast. Parts of them are therefore also published in his diploma thesis.[201]

3.1.2. Equipment

Figure 3.1 depicts the implemented photolithography equipment. For substrate pre-treatment and solution-based layer deposition a wet bench[202] with laminar flow modules providing an ISO class 5 environment was designed, consisting of a deionized water tap, hand shower and basin, attached to a Millipore Elix 3 deionized water system[203] with a 30 l tank, a heatable ultrasonic basin (Powersonic P1100 D)[204], two Süss[205] Delta 6 RC spincoaters, one SSE[206] Optihot VB20 HMDS hotplate, one Süss[205] Delta 8 HP hotplate and an integrated disposal system for solvents, acids and bases.

[h] Part of the equipment was also implemented in a ~145 m^2 grey room situated adjacent to the cleanroom.

For UV exposure a high-precision EVG 620 top-side mask aligner,[207] equipped with a split-field microscope, a NUV lamp house with a 500 W mercury lamp, a 4″ x 4″ mask holder and a 100 mm wafer chuck was installed, being able to handle soft-, hard-, vacuum-contact and proximity exposure modes for printing resolutions down to 0.6 μm.

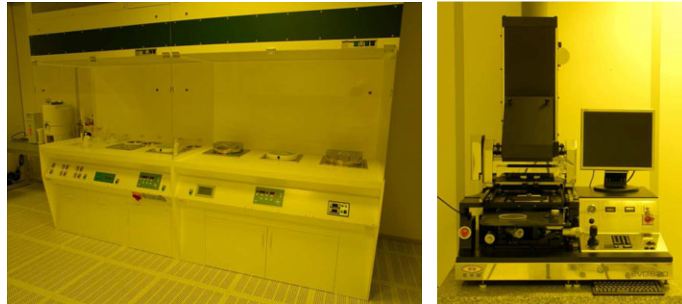

Figure 3.1: Photolithography equipment implemented in an ISO class 6 cleanroom environment, including a custom-made wet bench (left) and an EVG 620 top-side mask aligner (right).

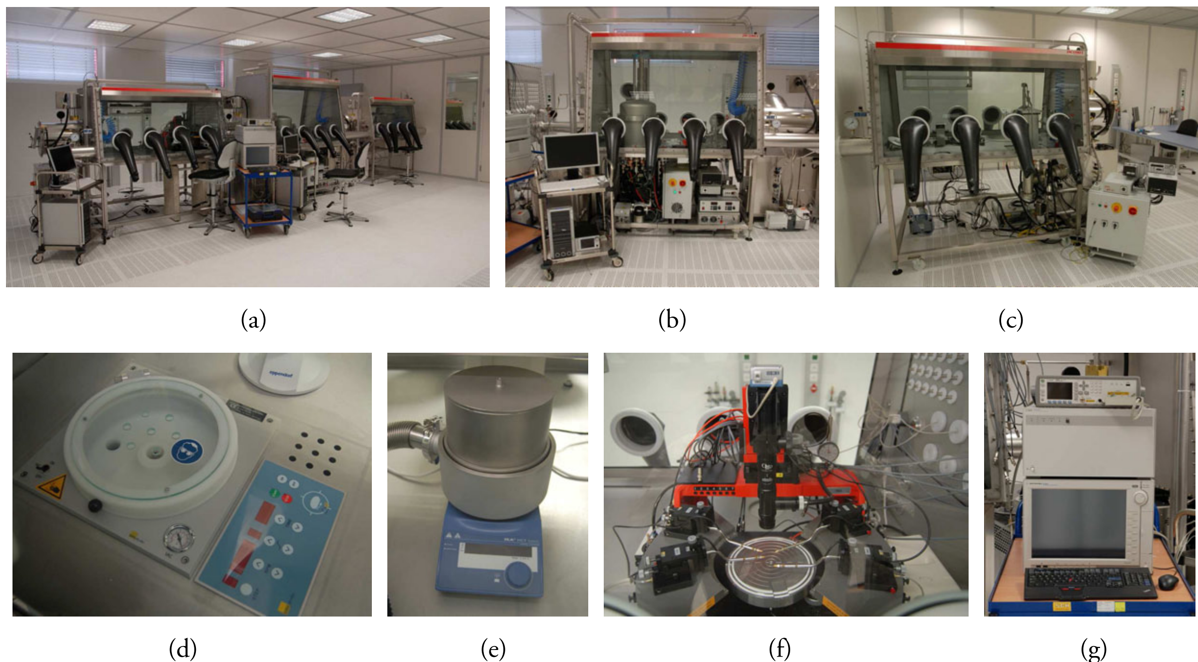

Figure 3.2: a) Argon glove-box cluster for solution-based processing, metallization, small molecule evaporation and device characterization in grey room environment; b) glove-box with fully automated vapor deposition unit;[209] c) glove-box with high vacuum thermal evaporation unit and sputter coater in cleanroom environment; all boxes are connected via locks; d) integrated Süss Delta 6 RC spin-coater; e) high vacuum heating unit; f) Süss PM5 probe station including four triax manipulators, triax chuck, probe-card holder and optical microscope with USB-camera; g) B1500A parameter analyzer, E5250A/E5252A switch matrix and E4980A LCR-meter from Agilent Technologies.

For metallization, polymer solution preparation and processing, small-molecule layer deposition as well as device characterization under inert conditions, a Jacomex[208] glove-box cluster consisting of four connected argon glove-boxes was designed, including sophisticated high vacuum evaporation and heating units,[209] an EMITECH K575X sputter coater,[210] an integrated fridge, a Süss Delta 6 RC spin-coater and a Süss PM5 probe station. Via appropriate feed-through connectors the latter can be connected to a B1500A parameter analyzer with an E5250A/E5252A switch matrix and an E4980A LCR-meter from Agilent Technologies.[i] The pictures in Figure 3.2 give an impression.

Moreover, for substrate surface modification, aside from the mentioned HMDS hotplate, a Femto plasma etch plant from diener electronics[211] with oxygen as process gas was implemented within the cleanroom. For process evaluation and device analysis an Olympus BX51 optical microscope,[212] enabling transmitted light-, reflected light-, bright field-, dark field-, polarization-, Normarski differential interference contrast- and fluorescence microscopy, an Olympus SZX-10 stereo microscope,[212] a Veeco Dimension V Scanning Probe Microscope with a NanoScope V controller[213] and a Krüss DSA 100 contact angle meter[214] were installed.

3.1.3. Process Implementation and Device Fabrication

With the new equipment well-performing bottom-gate/bottom-contact OFETs were to be fabricated, including appropriate device design and process development for substrate pre-treatment, source/drain-electrode definition and organic semiconductor layer deposition. Figure 3.3 shows typical target designs with various types of source/drain-electrode geometries, including structures with variable channel lengths down to 2.5 µm for evaluation of contact effects with the transfer line method (see chapter 2.2.2.5), interdigital structures with a large *W/L*-ratio for high source-to-drain channel currents at low operating voltages and ring-type structures for reduced parasitic leakage currents,[166] which arise when the semiconductor layer is not patterned.

[i] For electrical device characterization further equipment was implemented, such as 2612 dual-channel sourcemeters, 2700 and 2701 DMM/data acquisition systems including multiplexer modules, a 2182A nanovoltmeter, a 6221 AC/DC current source, a 6517A electrometer (all from Keithley) as well as a DSO80204B Infiniium oscilloscope, a 8114A pulse generator and a 33220A function/arbitrary waveform generator (all from Agilent Technologies).

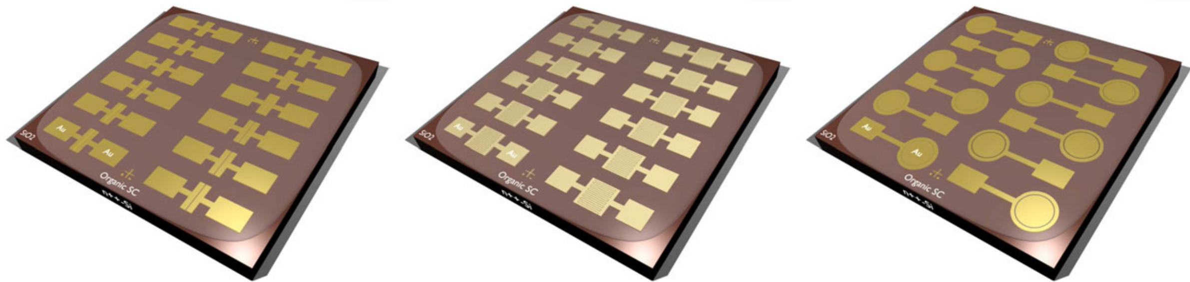

Figure 3.3: Target designs of bottom-gate/bottom-contact OFETs with various types of (gold) source/drain-electrode geometries; left: structures with variable channel lengths; middle: interdigital structures; right: ring-type electrodes.

As substrates for the OFETs, n^{++}-Si wafer pieces (dimensions: 1″ x 1″, resistivity: 3-5 Ωcm) with a 200 nm thick, thermally evaporated SiO_2 layer (capacitance per unit area $C_i \approx 17.3$ nF/cm^2) from austriamicrosystems AG[268] were applied. For the definition of the source/drain electrodes photolithographic lift-off processing[215,216] was chosen, because it involves no wet-chemical etching of metals. Appropriate shadow masks with the target structures were designed with AutoCAD[201] and manufactured by Photronics.[217] Figure 3.4 shows an example.

Figure 3.4: Typical 4″ x 4″ photolithography shadow mask (chrome on quartz glass), divided in 1″ x 1″ sectors with various target structures; critical dimension: 2 µm ± 0.1 µm, no defects/cm^2 > 2 µm.

3.1.3.1. Development and Optimization of a Photolithographic Lift-Off Process for Structuring OFET Source/Drain Electrodes

At first the backside of a wafer piece was scratched with a diamond cutter on several spots to create a contact to the n^{++}-Si acting as common bottom gate. After blowing off with N_2, the substrate was cleaned with acetone and isopropanol, then put into an isopropanol ultrasonic bath for 1-3 min and finally rinsed with deionized water (DI-H_2O). After each cleaning step the wafer piece was dried with N_2 and finally also spin-dried at 4500-5000 rpm for 100 s. Then the lift-off process as schematically depicted in Figure 3.5 was applied using ma-N 1407 photoresist (resolution: 1 µm), ma-D 533/S developer and mr-Rem 660 remover from micro resist technology GmbH.[218]

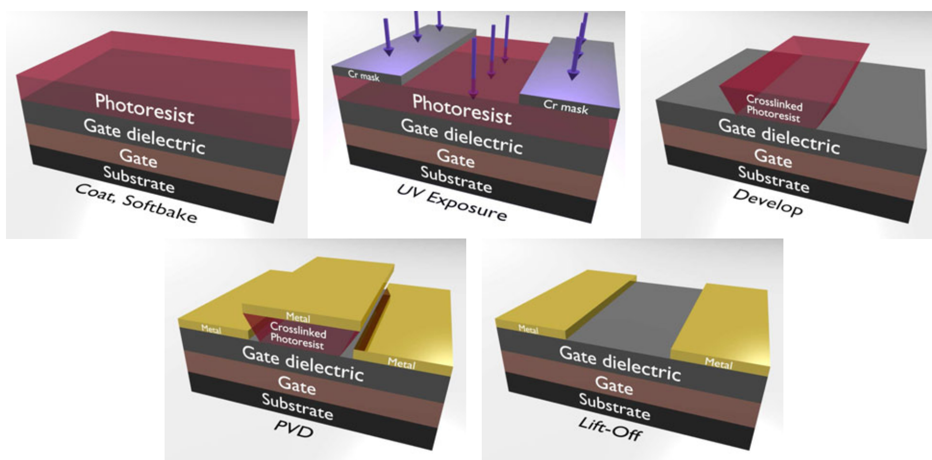

Figure 3.5: Process flow of applied photolithographic lift-off process for structuring OFET source/drain electrodes, including photoresist deposition and softbake, UV exposure through a chrome mask, resist development, metallization and lift-off (removal of resist and metal on resist).

For process optimization several parameters were varied, including spin speed, spin acceleration, softbake time, exposure mode, exposure dose, proximity distance and development time, and the obtained results were evaluated with optical microscopy.[201] The final recipe consisted of the following procedure: after a dehydration bake (200°C, 4 min: 1 min N_2, 2 min vacuum, 1 min N_2) ~400 µl photoresist was spin-cast (3000 rpm, 30 s, nominal thickness: 700 nm), followed by a softbake at 110°C for 60-120 s, an UV exposure (dose: 70-100 mJ/cm^2 at 365 nm (i-line))[j] in proximity mode (2-5 µm)[k] and a dip-development within a developer bath (room temperature, 48 s). After rinsing the sample with DI-H_2O, drying it with N_2 and spin-drying it (5000 rpm, 100 s), a 2 nm chromium layer (deposition rate: 0.2 Å/s) and a 50 nm gold layer (deposition rate: 2 Å/s) were thermally evaporated ($p < 5 \times 10^{-6}$ mbar).[l] Lift-off, i.e. removal of resist and metal on resist, was performed by immersion into an ultrasonic remover bath (50°C, ~5 min), followed by rinsing with DI-H_2O, drying with N_2, spin-drying at 5000 rpm for 100 s and an optical inspection with the Olympus BX51 microscope. Figure 3.6 shows typical results for source/drain structures with variable channel lengths (3 x 2.5 µm, 3 x 10 µm, 3 x 25 µm and 3 x 50 µm). For enabling a fast process evaluation, scale bars were implemented on the photolithography mask with defined line widths and distances (2.5 µm, 5 µm, 10 µm, 20 µm and 40 µm).

[j] corresponding to only 20-30% of manufacturer's recommended dose
[k] Proximity mode, i.e. no contact between mask and substrate, was chosen to reduce mask contamination.
[l] OFETs with source/drain electrodes without chromium as adhesive layer were also fabricated via lift-off. However, as expected, most of the gold was detached during resist stripping.

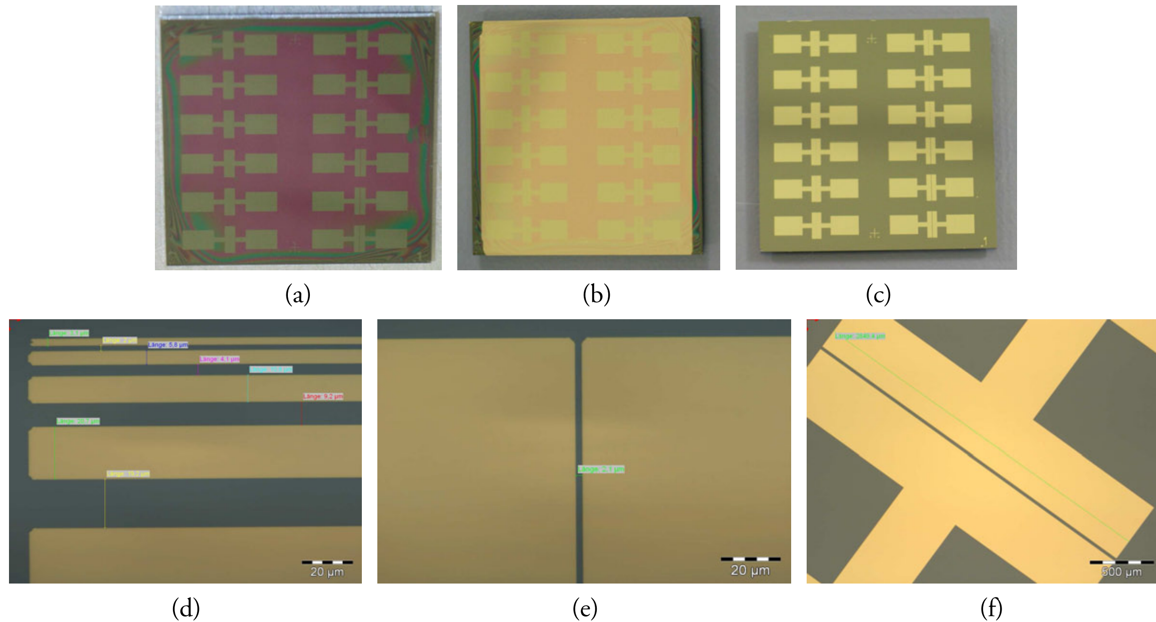

Figure 3.6: Typical sample in various stages during photolithographic structuring of source/drain electrodes with variable channel lengths: a) after exposure and development of photoresist; b) after Cr/Au-evaporation; c) after lift-off; d) scale bars for fast and easy process evaluation; e) source/drain electrodes with $L \approx 2.1$ µm (nominal: 2.5 µm) and $W \approx 2.85$ mm; f) source/drain electrodes with $L \approx 25$ µm and $W \approx 2.85$ mm.

The channel lengths after lift-off were slightly smaller than the resist bars defining L. This is due to the fact that the developed lift-off photoresist exhibits side walls with an undercut profile, which are therefore not covered during metal deposition and thus enable removal of the metal-covered resist (see Figure 3.5). This undercut was also confirmed by analytical transmission electron microscopy (TEM) of a cross-section lamella of a completed top-gate/bottom-contact OFET, fabricated on an n^{++}-Si/SiO_2 substrate with rr-P3HT as organic semiconductor and including PVA as gate dielectric (Figure 3.7). The corresponding preparations and investigations were performed at the FELMI, Graz University of Technology, using a focused ion beam instrument (dual beam NOVA200 nanolab, FEI) and an energy-filtering transmission electron microscope (FEI Tecnai F20 equipped with a Gatan Energy Filter). The trapezoidal form of the gold electrode resulting from the undercut profile of the developed lift-off resist is clearly visible. For analyzing the chemical composition energy-filtering TEM (EFTEM) was used, yielding the spatial distribution of selected elements. The figure below shows a superposition of three differently colored elemental maps (red = carbon, blue = sulfur, green = oxygen). The SiO_2 substrate is identified by its oxygen content (green), the organic semiconductor (rr-P3HT) by its sulfur content (blue) and pure carbon (red) reveals the distribution of the dielectric (PVA).

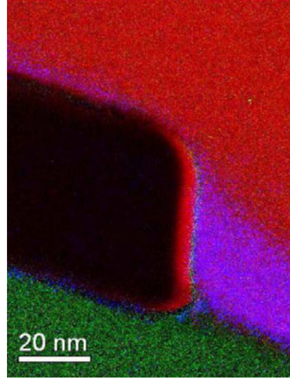

Figure 3.7: EFTEM cross-section (by FELMI, Graz University of Technology) of a top-gate/bottom-contact OFET fabricated on an n^{++}-Si/SiO_2 substrate and including rr-P3HT as organic semiconductor and PVA as gate dielectric; colors correspond to chemical elements (elemental mapping): red = carbon, blue = sulfur, green = oxygen.

3.1.3.2. Process Development and Optimization for Substrate Pre-treatment with HMDS and Evaluation with Contact Angle-, AFM- and XRD-measurements

After the successful implementation of the lift-off process also a procedure for dielectric surface modification with hexamethyldisilazane (HMDS, Figure 3.8) was developed, tested and optimized.

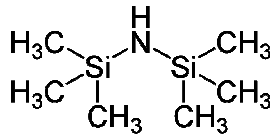

Figure 3.8: Chemical structure of hexamethyldisilazane (HMDS).

Aside from being used as adhesion promoter in photolithography,[219] HMDS can also be applied for improving OFET performance, as it lowers the surface energy of the gate dielectric by removing residual surface water and replacing hydroxyl groups on the SiO_2 surface by apolar methyl groups. The corresponding reaction is as follows:[220,221]

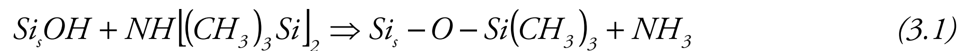

$$Si_sOH + NH\left[(CH_3)_3Si\right]_2 \Rightarrow Si_s - O - Si(CH_3)_3 + NH_3 \qquad (3.1)$$

Generally, the application of self-assembled monolayers (SAMs) such as HMDS before organic semiconductor deposition is assumed to induce structural changes within the semiconductor film, leading to a higher order (surface-mediated molecular ordering).[41,68,222,223] Moreover, as pointed out, OH-groups act as interfacial traps for mobile charge carriers in organic semiconductors and thus removal or coverage of them also enhances charge carrier mobility and even may enable n-type conduction in seemingly p-type semiconductors.[56,224]

Still controversial is the effect of SAMs on the grain size of the semiconductor. Some groups observed the formation of larger grains of e.g. pentacene with SAM-treated or generally more hydrophobic dielectric surfaces, some did not (probably due to the induced roughness), still obtaining a larger mobility with a SAM-treated OFET.[224, 225, 226, 227, 228, 229] However, the morphology in the first few monolayers, where charge transport takes place, might be different from the final film structure often investigated e.g. by AFM or SEM, so that seemingly smaller grain sizes can still yield larger mobility values in OFETs.

For HMDS pre-treatment of our samples the HMDS hotplate shown in Figure 3.9 was applied, which is integrated in the wet bench described above.

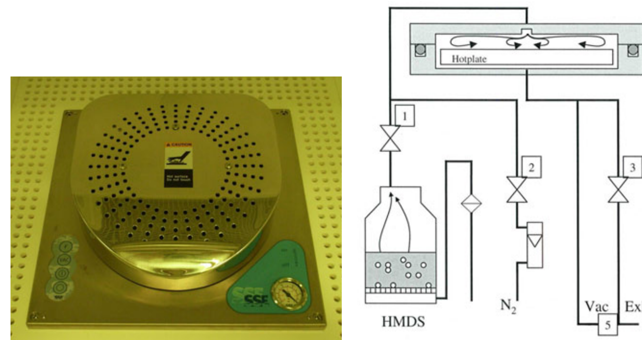

Figure 3.9: Picture of HMDS hotplate (SSE Optihot VB20) and schematic description;[230] 1 = HMDS-supply, 2 = N_2-purge/ventilation, 3 = chamber exhaust, 5 = vacuum supply.

With this hotplate gaseous HMDS, stored in a bubbler in its liquid form, is applied to a substrate surface within a vacuum chamber in a defined manner with air as carrier gas. Vacuum controls the distribution of the vapor and heating the substrate during priming accelerates the hydrophobization, after which HMDS is removed by N_2-purging. Hexamethyldisilazane was purchased from Sigma-Aldrich (Prod. No. 440191, reagent grade, purity ≥ 99%).[231]

Before HMDS application, one substrate was also exposed to oxygen plasma for 10 min ($p(O_2)$: ~$3x10^{-1}$ mbar) to create a hydrophilic substrate surface, which is believed to facilitate the growth of SAMs.[232]

The priming process was evaluated by comparing the static advancing contact angles of DI-H_2O on untreated and pre-treated SiO_2 and glass substrates and also on gold electrodes, applying the sessile drop method. Generally, the contact angle Θ is the angle at which a liquid/vapor interface meets the solid surface (Figure 3.10).[233] It is a measure of the hydrophobicity and determined by the equilibrium of the three interfacial tensions, expressed by Young's equation:

$$\gamma_{sv} = \gamma_{sl} + \gamma_{lv} \cdot cos\,\Theta \tag{3.2}$$

γ_{sv}... solid-vapor surface tension, γ_{sl}... solid-liquid surface tension, γ_{lv}... liquid-vapor surface tension.

Young's equation assumes a perfectly smooth, homogenous and rigid solid surface, not taking into account roughness, impurities, chemical and physical interactions between droplet and solid or droplet evaporation, for which extended models have been developed.[234,235]

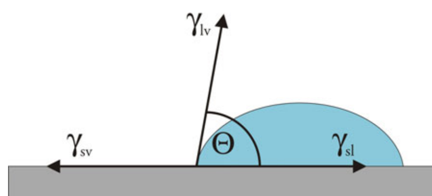

Figure 3.10: Contact angle of a liquid on a solid substrate.

The HMDS process was optimized to obtain DI-H_2O contact angles on pre-treated SiO_2 of at least 90°. Several parameters were varied, including process temperature, duration of HMDS bubbling, priming time and number of priming repetitions.[201]

The final process, performed at a temperature of 120°C, consisted of the following steps:

- Dehydration bake (repeated 3 times): 3 min vacuum, 30 s N_2-purging;
- 1 min vacuum;
- HMDS priming (repeated 3 times): 3 s vacuum + HMDS bubbling; 30 s further HMDS bubbling without vacuum; 20 min priming time (sample left in HMDS atmosphere), 30 s N_2-purging + chamber exhaust; 1 min vacuum;
- Ventilation: 2 min N_2-purging + chamber exhaust; 30 s chamber exhaust only.

Figure 3.11 and Table 1 compare the contact angles of DI-H_2O on SiO_2 and on gold after the lift-off process and a vacuum-bake[m] (120°C, 1 h, $p < 1\text{x}10^{-5}$ mbar) as well as after HMDS-treatment without and with O_2-plasma exposure.

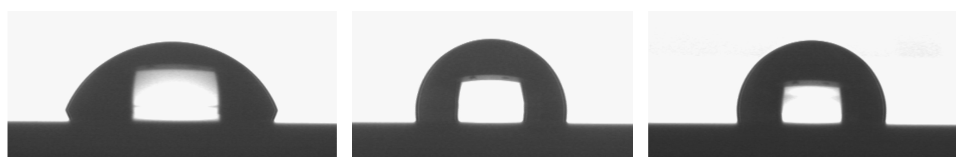

Figure 3.11: Droplet of DI-H_2O on SiO_2 after various pre-treatments for contact angle determination: left: after lift-off and vacuum-bake; middle: after lift-off, HMDS-treatment and vacuum-bake; right: after lift-off, O_2-plasma exposure (10 min), HMDS-treatment and vacuum-bake.

[m] The vacuum-bake was performed to remove residual surface water before deposition of the organic semiconductor.

Table 1: Contact angle values of DI-H_2O on SiO_2 and gold after various pre-treatments determined with a Krüss DSA 100 contact angle meter.

Contact angle on	*Native*	*After lift-off process and vacuum-bake at 120°C for 1 h*	*After lift-off, HMDS treatment and vacuum-bake at 120°C for 1 h*	*After lift-off, O_2 plasma exposure (10 min), HMDS treatment and vacuum-bake at 120°C for 1 h*
SiO_2	*~65°*	*65-70°*	*~90°*	*~90°*
Gold	*~80°*	*~75-80°*	*~80°*	*~80°*

The contact angles of the dielectric increased from ~65° to ~90° upon application of HMDS, proving the successful implementation of the priming process. In contrast, gold seems to be negligibly affected by the surface modification, although exposure to O_2-plasma for 10 min led to a strong reduction of the contact angle not only on SiO_2 (20-25°), but also on gold (~65°). A cleaned glass substrate was also exposed to HMDS with the described process (without O_2-plasma treatment), resulting in an increase of the DI-H_2O contact angle from ~10° to ~70°. The application of the process on a cleaned SiO_2 substrate before photolithographic lift-off structuring led to problems with photoresist adhesion due to over-priming,[216] so that HMDS-treatment was performed only after source/drain-electrode structuring.

Aside from contact angle measurements, the implications of dielectric surface modification on pentacene were investigated with atomic force microscopy. The organic semiconductor was purchased from Sigma-Aldrich with a certified purity ≥ 99.9% and processed without further purification. 30-40 nm thick pentacene layers were evaporated on glass, untreated SiO_2 and HMDS-treated SiO_2 (deposition rate: 0.1 Å/s, $p < 6x10^{-8}$ mbar), with the substrates kept at room temperature. Before semiconductor deposition all substrates were cleaned according to the procedure described in section 3.1.3.1, but no lift-off process was applied.

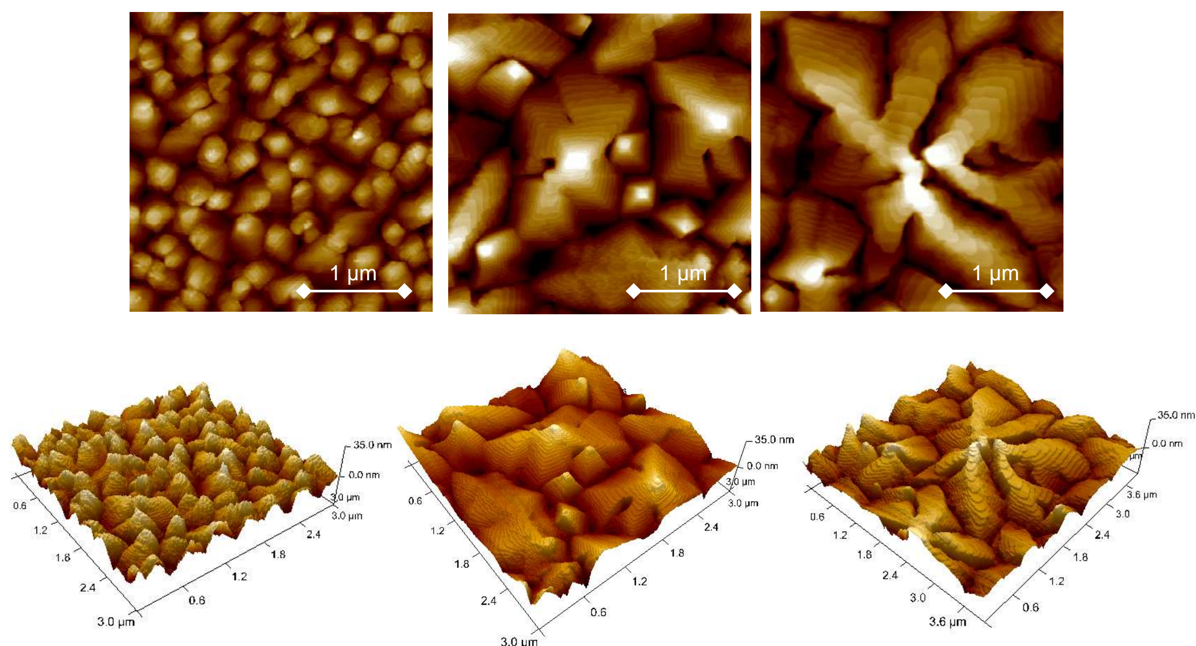

Figure 3.12: Top: AFM-height images of pentacene on glass ($d \approx 41$ nm, $R_{RMS} \approx 7.2$nm, left), on untreated SiO_2 ($d \approx 41$nm, $R_{RMS} \approx 7$ nm, middle) and on HMDS-treated SiO_2 ($d \approx 30$nm, $R_{RMS} \approx 5.4$ nm, right); scan size: 3 µm; color code from black to white corresponds to a z-data range of 50 nm (left), 35 nm (middle) and 30 nm (right); bottom: corresponding 3D AFM-height images.

Figure 3.12 depicts the corresponding AFM-height images, revealing a pentacene layer thickness d between 30 nm and 40 nm and showing mainly dendritic grains, in particular on SiO_2. Obviously, the average size of the pentacene grains increases from a few 100 nm on glass to ~1 µm on untreated SiO_2 and to ~2.5 µm (up to 4 µm) on HMDS-modified SiO_2, correlating well with the contact angle data and suggesting that more hydrophobic substrates lead to a larger grain size. However, during these investigations the surface roughness of the uncoated substrates was not determined, which also has a large influence on the morphology and grain size of organic semiconductors such as pentacene.[236] The lowest RMS-roughness R_{RMS} of the semiconductor film was obtained with the HMDS-treated sample. However, the values are influenced by the homogeneity of the surface and the image right shows only one grain. Therefore they have to be considered with care.

An AFM depth histogram analysis of the pentacene layer on the HMDS-treated SiO_2 revealed a 001 interplanar distance d_{001} of ~15.6 Å, corresponding to the thin-film phase (literature value ~15.4 Å), which is a substrate-induced structure different from the triclinic bulk phase of pentacene with d_{001} ~ 14.4 Å.[178,226,237,238,239,240,241]

This was also confirmed by X-ray diffraction measurements (XRD, Figure 3.13)[n] and is not surprising, since the pentacene bulk phase is known to start beyond a critical film thickness, which depends strongly on the substrate temperature. For a substrate kept at room temperature during deposition this critical thickness is least 100 nm. The XRD measurements did not reveal a significant difference between HMDS-treated and untreated substrates.

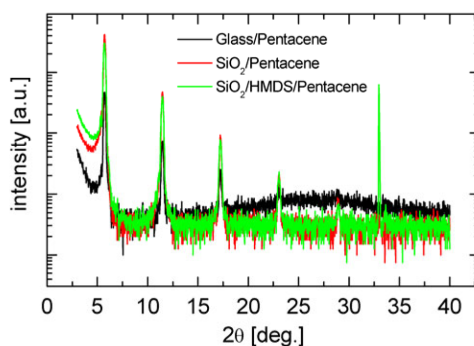

Figure 3.13: X-Ray diffraction spectra of pentacene on various substrates; the peak at 33° is a reflection of silicon.

3.1.3.3. Completion of Devices

After source/drain-electrode definition and an optional HMDS surface treatment, a sample was vacuum-baked ($p < 5x10^{-6}$ mbar) at 120°C for 1 h to reduce residual surface water. Then the organic semiconductor was deposited. For solutions based on regioregular poly(3-hexylthiophene) (M_n: 26900 g/mol; M_w: 37600 g/mol,[o] regio-regularity > 98%, Figure 2.1e), provided by the group of Prof. Scherf,[242] an amount of the material was heated at 120°C in high vacuum for several hours to remove moisture and dedope the semiconductor. Then it was dissolved in spectrally clean chloroform ($CHCl_3$) to a concentration of 2 mg/ml under inert conditions. ~300-350 µl of a solution were spin-cast onto the source/drain structures in argon (1500 rpm, 40 s).[p] Then the film was cured on a hotplate (60°C, 10 min) in argon and dedoped for 1 h at 100-120°C in high vacuum ($p < 5x10^{-6}$ mbar). When, instead, pentacene was applied by thermal evaporation of ~40 nm thick films through a shadow mask (deposition rate: 0.1 Å/s, $p < 6x10^{-8}$ mbar, room temperature), no dedoping bake was performed after semiconductor deposition.

---

[n] The XRD measurements were performed by Heinz-Georg Flesch on a Bruker D8 Discover diffractometer in Bragg Brentano-focusing condition using a copper sealed tube with its characteristic wavelength of 1.5406Å. Primary side slits optics as well as secondary side slits and receiving slit were set to 0.2 mm.

[o] M_n…number average molecular weight, M_w… weight average molecular weight

[p] Sometimes substrates were also cleaned with spectrally clean $CHCl_3$ before solution deposition.

Finally the sample was fixed on a single-sided copper board using conductive silver paste and a frame was scratched within the organic semiconductor layer around every single device in order to reduce parasitic leakage currents. Conductive silver paste was also applied on the source/drain pads for easy contacting and devices were electrically characterized in argon using the equipment shown in Figure 3.2f and g. The corresponding results are presented in the following section.

3.1.4. Device Characteristics of OFETs with Various Source/Drain-Electrode Geometries, Channel Dimensions and Substrate Pre-treatments

3.1.4.1. OFETs with Ring-Type Source/Drain-Electrode Structures

The presented OFETs with ring-type source/drain electrodes were prepared with one of the first non-optimized fabrication routines on a wafer-edge substrate with an UV-exposure dose of 350 mJ/cm^2 and a resist development time of 33 s. Moreover, an older rr-P3HT batch (M_n: 37900 g/mol, M_w: 53700 g/mol) was applied, the semiconductor film was not dedoped by baking and also not patterned, n^{++}-Si was contacted by scratching the SiO_2-layer on top-side, no conductive silver paste was applied on the pads and no HMDS pre-treatment was performed. Still, the results are shortly illustrated to show the influence of the device geometry, when the semiconductor layer is not patterned, in particular regarding parasitic leakage currents.[166] Figure 3.14 includes a sample picture, an optical micrograph of a single OFET and a scheme of the sample architecture. The textured semiconducting layer is attributed to the omitted dedoping bake with this sample, which, when applied, would have led to a smoother film. Figure 3.15 shows the electrical characteristics of a typical device.

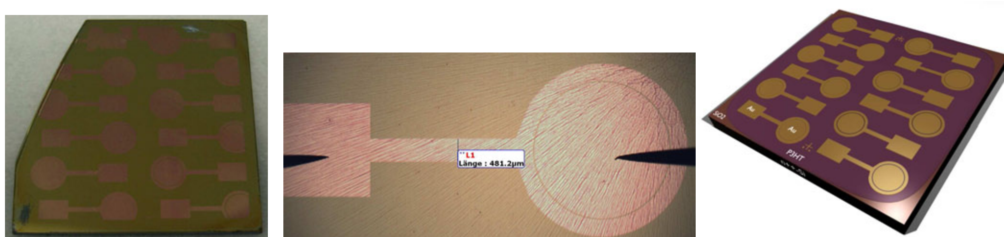

Figure 3.14: Sample with rr-P3HT-based OFETs with ring-type source/drain electrodes (left) and optical micrograph of a single device (middle, $L \approx 25$ µm, $W \approx 9.5$ mm), contacted with manipulator needles; right: scheme of sample architecture.

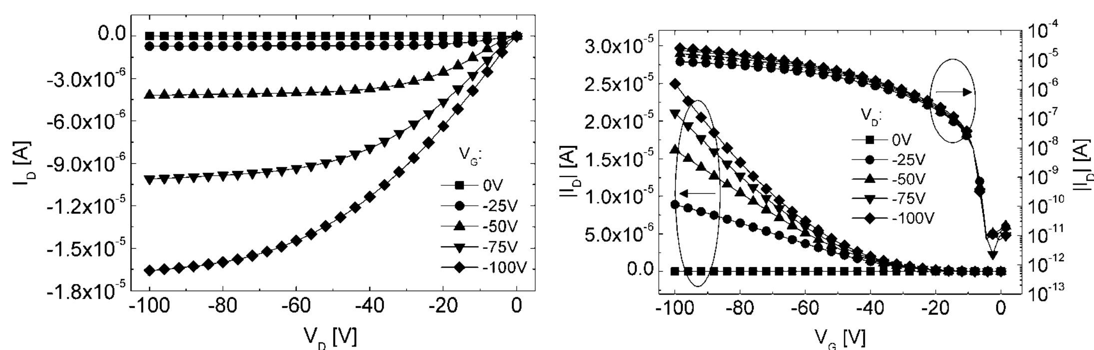

Figure 3.15: Output (left) and transfer (right, linear and semi-logarithmic) characteristics of a typical OFET with ring-type source/drain electrodes ($L \approx 25$ µm, $W \approx 9.5$ mm) measured in argon.

The switch-on voltage V_{SO} was determined to ~-6V and the field-effect mobility was 8.0×10^{-4} cm²/Vs (V_D = -25V, V_G = -80V) in the linear regime and 1.1×10^{-3} cm²/Vs (V_D = -100V, V_G = -80V) in the saturation regime. What is more interesting, however, is the very low off-current of ~10 pA, attributed to the ring-type geometry, which prevents parasitic currents outside the channel region. This led to a very large on/off-current ratio of 2.5×10^{7} (!) for V_D = -85V (I_{on}: V_G = -100V, I_{off}: V_G = 0V), underlining the importance of always considering such parasitic currents, when other geometries are applied and the organic semiconductor is not patterned.

3.1.4.2. OFETs with Interdigital Source/Drain-Electrode Structures

The devices were fabricated according to the description in section 3.1.3 with rr-P3HT as organic semiconductor and without HMDS pre-treatment. Figure 3.16 includes a sample picture, an optical micrograph of a single device and a scheme of the sample architecture. Figure 3.17 illustrates the device characteristics.

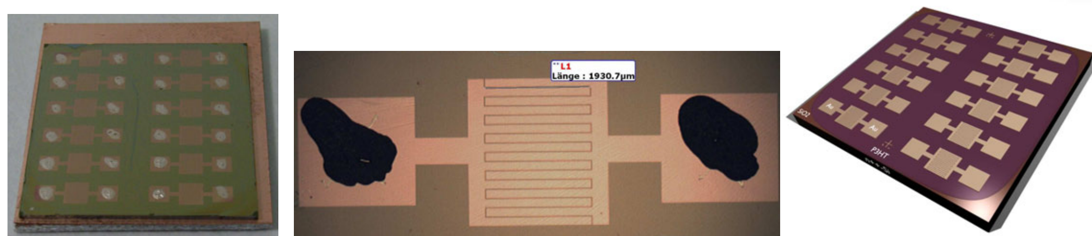

Figure 3.16: Sample with rr-P3HT-based OFETs with interdigital source/drain electrodes (left) and optical micrograph of a single device (middle, $L \approx 25$ µm, $W \approx 32.8$ mm) with drops of conductive silver paste; right: scheme of sample architecture.

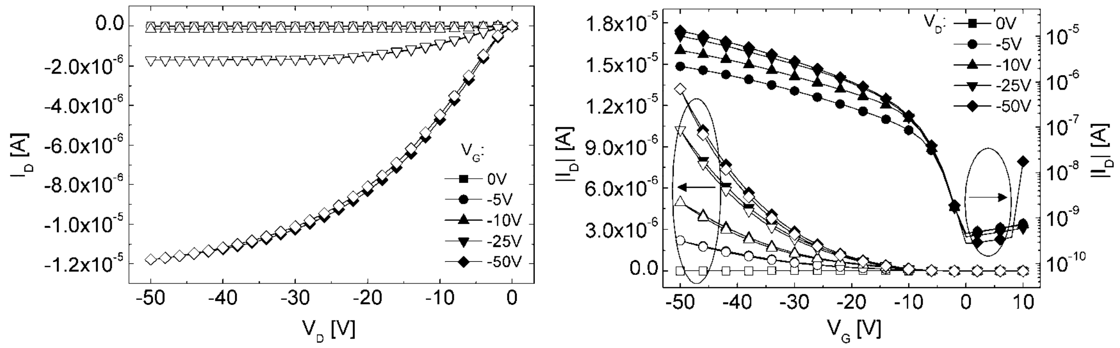

Figure 3.17: Output (left) and transfer (right, linear and semi-logarithmic) characteristics of a typical device with interdigital source/drain electrodes ($L \approx 25$ µm, $W \approx 32.8$ mm) measured in argon; filled symbols: sweeps from positive to negative voltages; open symbols: reverse sweep.

As expected, the large *W/L*-ratio of this geometry leads to high channel currents at low operating voltages. The switch-on voltage was ~0V and the field-effect mobility values were 1.1×10^{-3} cm²/Vs (V_D = -10V, V_G = -50V) in the linear regime and 8.5×10^{-4} cm²/Vs (V_D = -50V, V_G = -40V) in the saturation regime. The on/off-current ratio was 5×10^4 for V_D = -50V (I_{on}: V_G = -50V, I_{off}: V_G = 0V) and gate leakage currents were below 60 nA. Compared to the ring-type OFET in Figure 3.15, the off-currents were ~30 times larger, again emphasizing the implications when choosing for a specific device geometry. Figure 3.18 depicts transfer curves of several devices with interdigital source/drain electrodes, indicating a small device-to-device variation and proving the successful implementation of the lift-off process described above.

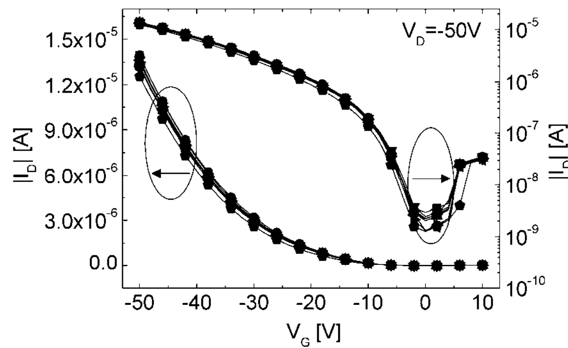

Figure 3.18: Transfer curves (linear and semi-logarithmic) at V_D = -50V of several devices with interdigital source/drain electrodes ($L \approx 25$ µm, $W \approx 32.8$ µm) measured in argon.

3.1.4.3. OFETs with Various Channel Lengths - Short-Channel Effects and Influence of Substrate Pre-treatment with HMDS

a) rr-P3HT-based OFETs

Figure 3.19 illustrates a typical sample with rr-P3HT-based OFETs comprising source/drain-electrodes with variable channel lengths, fabricated according to the description above. The figure also includes an optical micrograph of a single device and a scheme of the sample architecture.

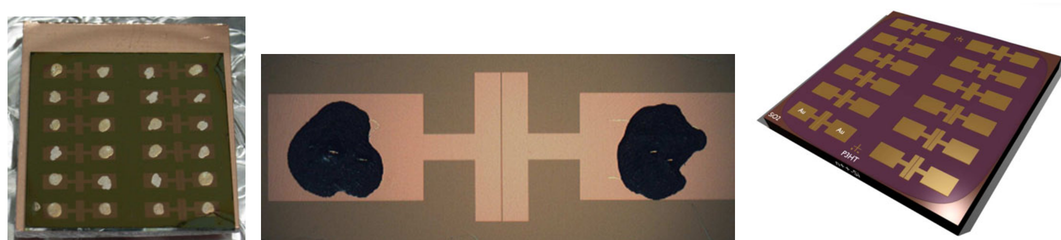

Figure 3.19: Typical sample with rr-P3HT-based OFETs comprising source/drain electrodes with variable channel lengths (left) and optical micrograph of a single device (middle, $L \approx 25$ µm, $W \approx 2.85$ mm) with drops of conductive silver paste; right: scheme of sample architecture.

Figure 3.20 shows AFM-height images of the rr-P3HT film within the channel of OFETs fabricated on untreated SiO_2,[q] on HMDS-treated SiO_2 and on O_2-plasma + HMDS-treated SiO_2. The film thickness was determined to ~16 nm, ~20 nm and ~18 nm, respectively. On the untreated substrate the rr-P3HT average grain size was 50-70 nm and the RMS-roughness ~0.2-0.3 nm. When HMDS was applied, no matter if in combination with O_2-plasma exposure or not, the roughness increased to ~0.5 nm and the grain size was reduced to 20-35 nm (HMDS-treated) and 20-30 nm (O_2-plasma + HMDS-treated).

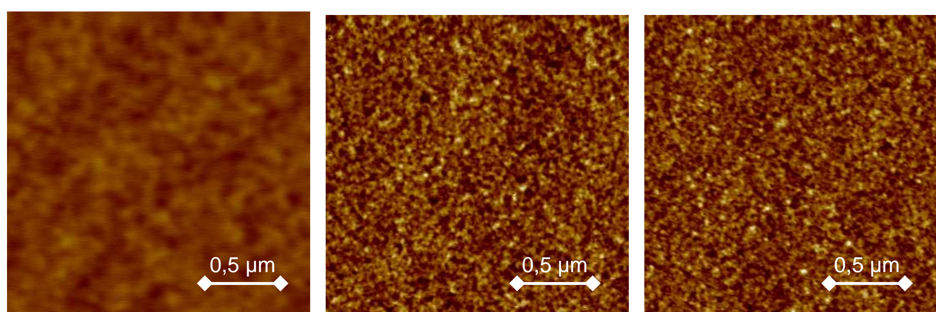

Figure 3.20: AFM-height images of rr-P3HT within the channel of OFETs fabricated on untreated SiO_2 (left), on HMDS-treated SiO_2 (middle) and on O_2-plasma + HMDS-treated SiO_2 (right); scan size: 2 µm; color code from black to white corresponds to a z-data range of 5 nm.

[q] "Untreated" relates only to the application of HMDS.

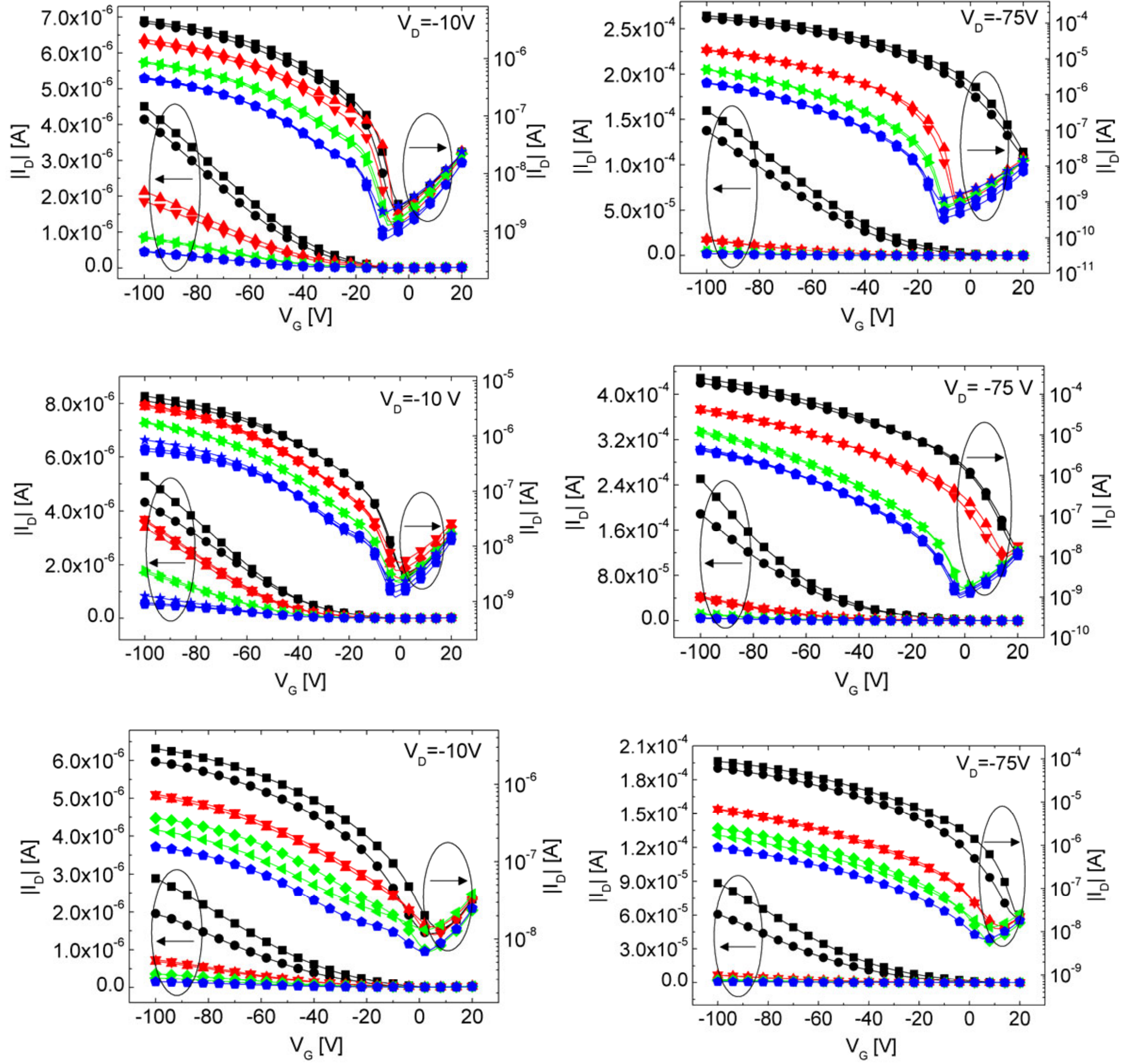

Figure 3.21: Transfer curves (linear and semi-logarithmic) at V_D = -10V (left) and V_D = -75V (right) of several rr-P3HT-based OFETs with channel lengths of ~2.5 µm (black), ~10 µm (red), ~25 µm (green) and ~50 µm (blue), fabricated on untreated SiO_2 (top), on HMDS-treated SiO_2 (middle) and on O_2-plasma + HMDS-treated SiO_2 (bottom); measured in argon.

Figure 3.21 depicts the transfer curves of several devices on the three samples for a low and a high drain voltage V_D. The graphs very well show the appearance of short-channel effects (see chapter 2.2.2.6). The switch on voltage V_{SO}, in particular of devices with small channel lengths ($L \approx 2.5$ µm and $L \approx 10$ µm), becomes apparently dependent on V_D. This is due to the fact that for small L the electric field between source and drain ($E_{SD} = V_D/L$) becomes comparable to the transversal gate field ($E_G = V_G/d_i$), in particular at low V_G, so that the gradual channel approximation is no longer valid. The space charge limited current regime is entered and the source-to-drain channel currents become much larger than the gradual channel approximation predicts, accompanied by the observed shift of V_{SO} to more positive values.

Short-channel effects could be observed for all three samples and become also very obvious in Figure 3.22 and Figure 3.23, where the electrical characteristics of a long- and a short-channel OFET are directly compared. While the device with $L \approx 25$ µm exhibits nice current saturation, the saturation behavior is largely degraded for the OFET with $L \approx 2.5$ µm. As described in chapter 2.2.2.6, this originates from channel-length modulation and non-destructive punch-through.

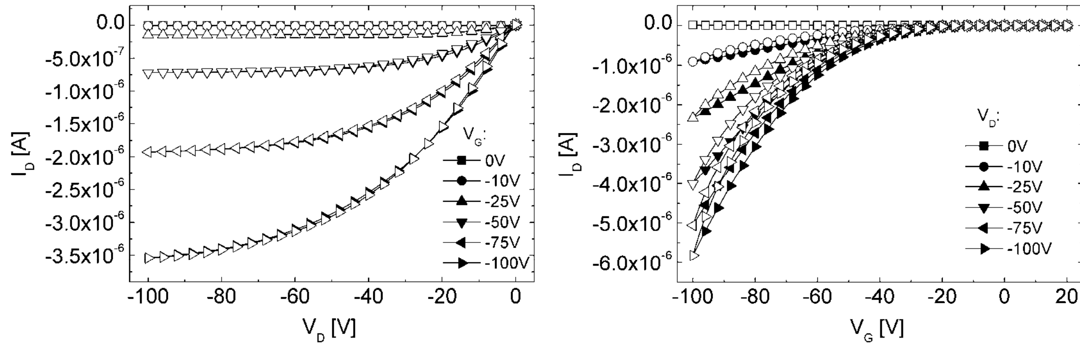

Figure 3.22: Output (left) and transfer (right) characteristics of a typical rr-P3HT-based OFET ($L \approx 25$ µm, $W \approx 2.85$ mm) fabricated on untreated SiO_2 measured in argon; filled symbols: sweeps from positive to negative voltages; open symbols: reverse sweep.

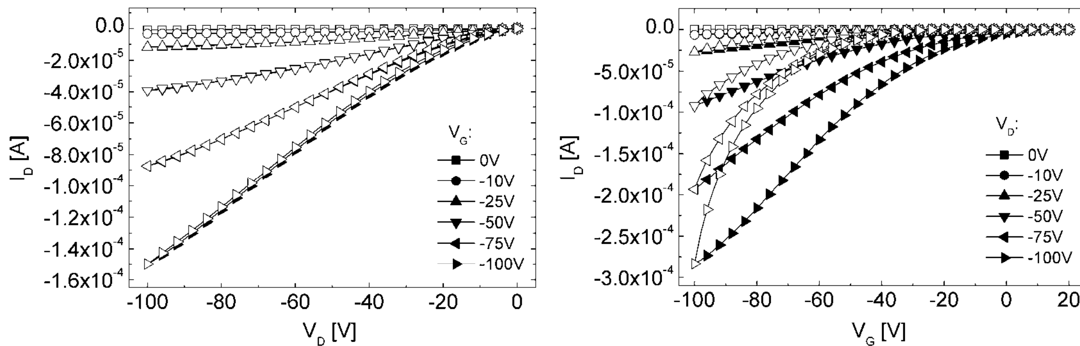

Figure 3.23: Output (left) and transfer (right) characteristics of a typical rr-P3HT-based OFET ($L \approx 2.5$ µm, $W \approx 2.85$ mm) fabricated on untreated SiO_2 measured in argon; filled symbols: sweeps from positive to negative voltages; open symbols: reverse sweep.

Moreover, contact resistance has a relatively larger influence in OFETs with small L, which results in the curvature change of the output curves at low V_D in Figure 3.23 left. Also the hysteresis of the transfer characteristics is largely increased with the short-channel OFET, which is ascribed to charge carrier traps, having a larger influence when channel length is reduced. These effects were observed for all pre-treatments.

When comparing the different substrate pre-treatments (Figure 3.21, Figure 3.24 and Table 2), in particular for larger channel lengths, where short-channel effects are not an issue, obviously the OFETs fabricated on HMDS-treated SiO_2 substrates without O_2-plasma exposure exhibited the best device performance.

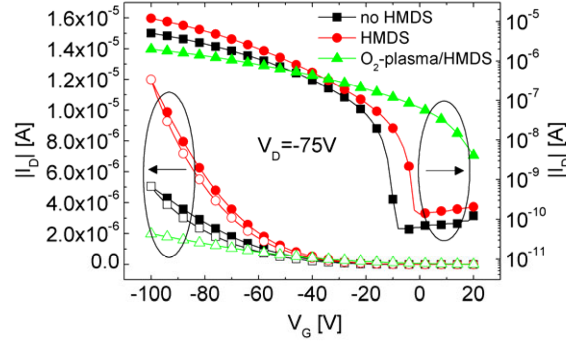

Figure 3.24: Transfer curves (linear and semi-logarithmic) at V_D = -75V of rr-P3HT-based OFETs ($L \approx 25$ µm, $W \approx 2.85$ mm) fabricated on untreated SiO_2, on HMDS-treated SiO_2 and on O_2-plasma + HMDS-treated SiO_2; measured in argon; filled symbols: sweeps from positive to negative voltages; open symbols: reverse sweep.

Table 2: Relevant OFET parameters of typical rr-P3HT-based devices ($L \approx 25$ mm, $W \approx 2.85$ mm) fabricated on SiO_2 with various pre-treatments including also the parameters obtained with the transfer line method; field-effect mobilities μ_{Lin} and μ_{TLM} determined (at V_D = -10V, V_G = -60V) with equations (2.14) and (2.19); switch-on voltage V_{SO}, subthreshold slope S, maximum interfacial trap density $N_{T,max}$ and on/off-current ratio I_{on}/I_{off} (I_{on}: V_G = -100V, I_{off}: V_G = 0V) determined from transfer curve at V_D = -75V; I_{Dmax}(O-T) is percentage of I_D at $V_D = V_G$ = -100V in output characteristics with respect to value in transfer characteristics; L_0 is length of transitional layer between gold electrode and semiconductor; $(R_PW)_0$ is gate-voltage independent part of width-normalized parasitic resistance R_PW; R_PW determined at V_D = -10V, V_G = -70V.

Substrate pre-treatment	V_{SO} [V]	μ_{Lin} [cm²/Vs]	μ_{TLM} [cm²/Vs]	I_{on}/I_{off}	S [V/dec]	$N_{T,max}$ [cm^{-2} eV^{-1}]	I_{Dmax} (O-T) [%]	L_0 [µm]	$(R_PW)_0$ [Ωcm]	R_PW [Ωcm]
No HMDS	-10	$6.5x10^{-4}$	$7.5x10^{-4}$	$4x10^3$	4.9	$8.8x10^{12}$	61	2	$2x10^5$	$6.4x10^5$
HMDS	-2	$1.2x10^{-3}$	$1.4x10^{-3}$	$7x10^3$	5.7	$1.0x10^{13}$	72	3.6	$4x10^4$	$5.0x10^5$
O_2-plasma and HMDS	+8	$1.7x10^{-4}$	$2.3x10^{-4}$	$1x10^2$	13.1	$2.4x10^{13}$	53	1.6	<0	$5.1x10^5$

The on-currents are highest with the HMDS-only treated devices and the switch-on voltages are slightly shifted to more positive values with respect to the untreated devices, accompanied by a small increase of off-current, which is a sign for reduced interfacial trap densities. In contrast, the devices made on substrates exposed to O_2-plasma exhibited positive switch-on voltages, the largest off-currents and the lowest on-currents.

This is ascribed to the fact that plasma-activated polar groups on SiO_2, acting as dopants[232] at lower gate voltages and at the same time as traps[243,244] at higher V_G, were not completely covered by the subsequent HMDS-treatment. The reduced (increased) interfacial trap densities of the HMDS-treated (O_2-plasma + HMDS-treated) sample with respect to the untreated sample are also revealed by the increased (reduced) field-effect mobility. For the HMDS-only treated device this is ascribed to the coverage of silanol groups acting as traps, possibly in combination with a change of the morphology of rr-P3HT close to the interface with the dielectric.[68] Moreover, as mentioned, a large difference between the I_D values at a particular V_D and (high) V_G in the transfer characteristics and output characteristics (corresponding to a small value for I_{Dmax} O-T in Table 2), is also a sign for higher trap densities. The subthreshold slope, from which a corresponding maximum interfacial trap density $N_{T,max}$ according to eqn. (2.17) was extracted, was slightly larger with the HMDS-only treated device. The results are qualitatively in good agreement with similar work performed by other groups.[232] Generally, the performance improvements by HMDS pre-treatment were not as high as might have been expected, which is also ascribed to the applied bottom-contact architecture, exhibiting a lower performance than top-contact devices.

With this device series also the transfer line method (TLM, see chapter 2.2.2.5) was applied in order to evaluate the influence of contact resistance. The important TLM parameters are summarized in Table 2. Figure 3.25 depicts the corresponding device resistance as a function of the channel length for the HMDS-only treated sample. When extrapolating the linear fits, they cross at L_0 = 3.6 µm and $(R_PW)_0$ = 4x10^4 Ωcm. L_0 corresponds to the length of an additional transitional layer between gold electrode and organic semiconductor, adding to the channel length, and $(R_PW)_0$ to the gate-voltage independent part of the contact resistance, being associated with the hole injection barrier. The transitional region seems to be largest for the HMDS-only treated device and smallest for the O_2-plasma + HMDS-treated device. It is known[158,,245,246] that O_2-plasma and UV/ozone treatments of gold lead to the formation of a surface gold oxide layer, which is accompanied by an increase of the surface energy and of the work function of gold, thus resulting in a strong reduction of the contact resistance. This is consistent with the apparently negative value of $(R_PW)_0$, which does not mirror real negative contact resistances, as it is within the standard errors of the linear fits. It just suggests that contact resistance is small. An apparently negative $(R_PW)_0$ was also observed by other groups.[247] Also the contact-angle measurements in chapter 3.1.3.2, which revealed a reduction of the contact angle of gold after O_2-plasma exposure, rendering its surface more hydrophilic, are in accordance with these results.

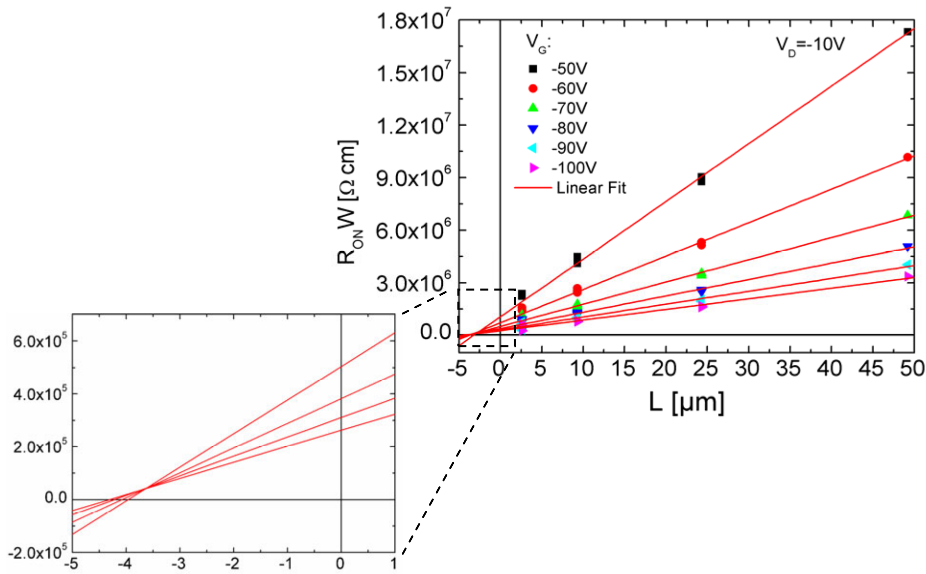

Figure 3.25: TLM-graph of rr-P3HT-based OFETs fabricated on HMDS-treated SiO_2 (in zoomed area only curves V_G=-70V, -80V, -90V and -100V are shown).

Figure 3.26 left shows that the parasitic resistance decreases with increasing gate voltage, which is expected, as charge carriers are more easily injected into the channel when the gate field is increased. Figure 3.26 right compares the field-effect mobility values of the several HMDS-only treated devices with various channel lengths, also including the mobility obtained from TLM. The values of the individual devices were calculated with eqn. (2.14), which does not take into account contact resistance. Due to the fact that contact resistance has a smaller influence in long-channel OFETs (see chapter 2.2.2.5), this neglect results in an apparent increase of mobility with increasing channel length, approaching the TLM mobility corrected for R_P. The graph also shows very well mobility degradation at higher gate voltages for all curves, which results from the fact that with increasing V_G charge carriers gradually concentrate near the semiconductor/insulator interface, where trap densities are higher, hence reducing mobility.[24]

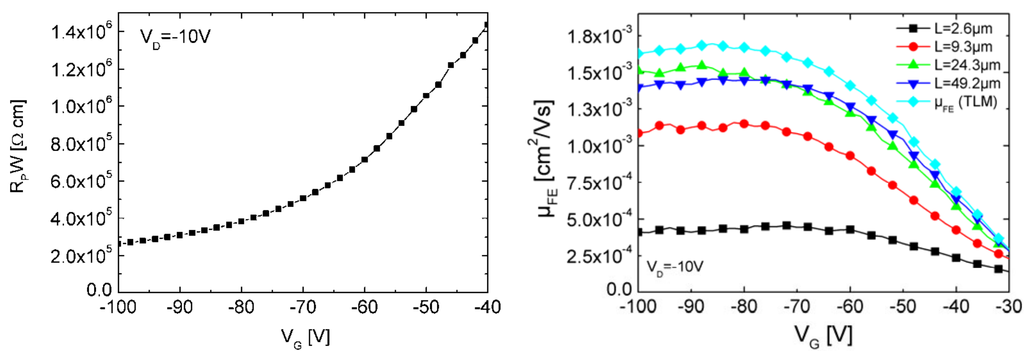

Figure 3.26: Left: width-normalized parasitic resistance obtained from TLM as a function of gate voltage of rr-P3HT-based OFETs fabricated on HMDS-treated SiO_2; right: field-effect mobility of four devices extracted with eqn. (2.14) and from TLM (eqn. (2.19)).

Basically, channel dimensions are targeted to be as small as possible, as the switching speed (cut-off frequency) of an ideal transistor is proportional to $1/L^2$. However, the results presented here confirm that the more the channel length is reduced, the more contact-resistance limited devices become.

b) Pentacene-based OFETs

Also pentacene-based OFETs with variable channel lengths were fabricated on an untreated SiO_2- and a HMDS-only treated SiO_2 substrate according to the procedure described above. No devices were prepared on O_2-plasma+HMDS-treated SiO_2. Figure 3.27 illustrates a typical sample and an optical micrograph of a single device. Clearly observable is the patterned semiconductor layer.

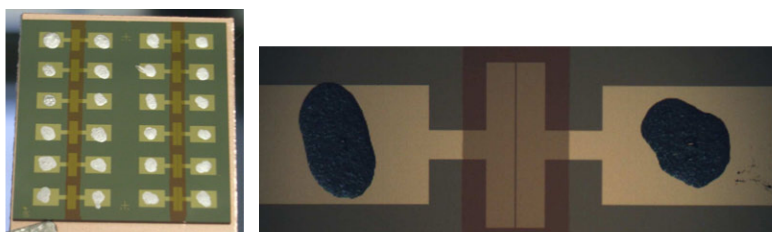

Figure 3.27: Typical sample with pentacene-based OFETs comprising source/drain electrodes with variable channel lengths (left) and optical micrograph of a single device (right, $L \approx 25$ µm, $W \approx 2.85$ mm) with drops of conductive silver paste.

Figure 3.28 includes AFM images of pentacene films in the transitional region between a gold electrode and the channel as well as within the channel of OFETs fabricated on the two differently pre-treated substrates. The average film thicknesses were determined to ~30 nm and ~40 nm, respectively. The average grain size is smaller (< 750 nm) than expected, when taking into account the results in chapter 3.1.3.2. This is attributed to the fact that the samples presented here were processed with the photolithographic lift-off process and hence residuals of the corresponding chemicals might have an impact. Between treated and untreated substrate no significant difference in grain size is observable, corresponding to some reports in literature.[224,225] Furthermore, the amplitude error images clearly illustrate that the average grain size on the electrode is smaller than within the channel, which is well known from literature.[19]

For the untreated substrate the RMS-roughness of the organic semiconductor was ~6.2 nm both within the channel and on the electrode, while it was ~6.3 nm within the channel and ~5.2 nm on the electrode for the HMDS-treated sample. In accordance with the rr-P3HT-based OFETs, the roughness of the semiconductor within the channel is slightly larger, when HMDS surface modification is performed. This was in contrast with the findings in chapter 3.1.3.2, where, however, no lift-off process was applied.

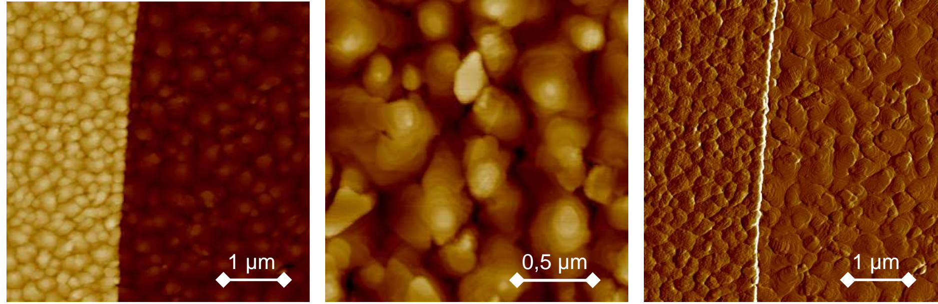

Figure 3.28: AFM-height images of a pentacene film on gold and untreated SiO_2 near the electrode edge (left) and within the transistor channel (middle); right: amplitude error image; scan size: 5 µm (left and right), 2 µm (middle); color code from black to white corresponds to a z-data range of 150 nm, 50 nm and 500 mV, respectively.

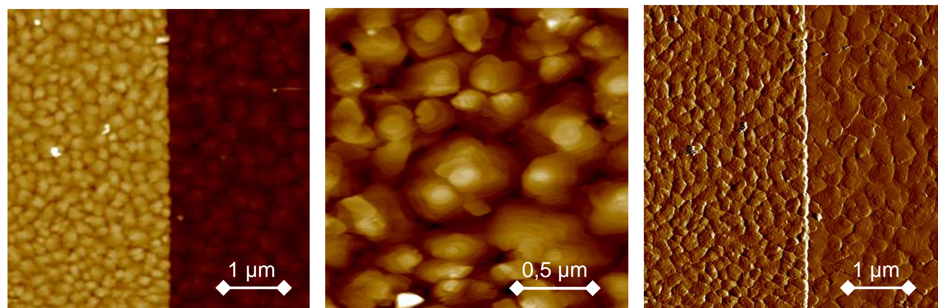

Figure 3.29: AFM-height images of a pentacene film on gold and HMDS-treated SiO_2 near the electrode edge (left) and within the transistor channel (middle); right: amplitude error image; scan size: 5 µm (left and right), 2 µm (middle); color code from black to white corresponds to a z-data range of 150 nm, 50 nm and 500 mV, respectively.

Figure 3.30 shows the transfer curves of several devices on each substrate, exhibiting a low device-to-device variation. Although the shift of the switch-on voltage of short-channel devices is more pronounced with the HMDS-treated sample, short-channel effects also appeared for devices on the untreated SiO_2 substrate at higher V_D (not shown).

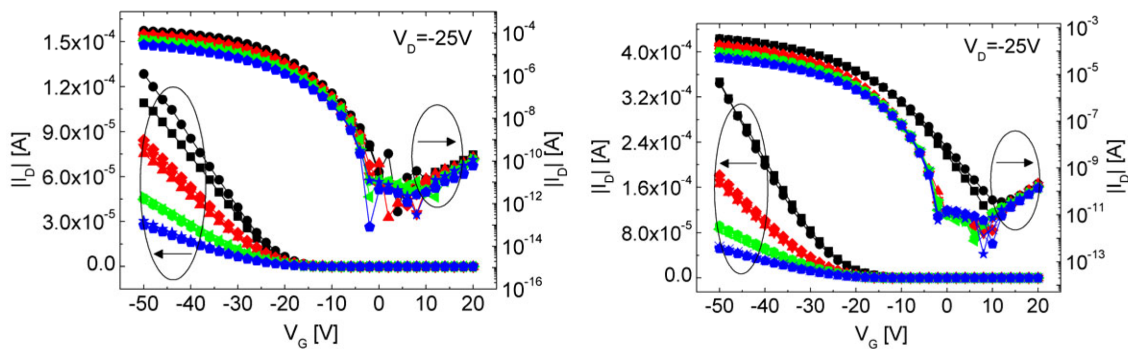

Figure 3.30: Transfer curves (linear and semi-logarithmic) at V_D = -25V of several pentacene-based OFETs with channel lengths of ~2.5 µm (black), ~10 µm (red), ~25 µm (green) and ~50 µm (blue), fabricated on untreated SiO_2 (left) and on HMDS-treated SiO_2 (right); measured in argon.

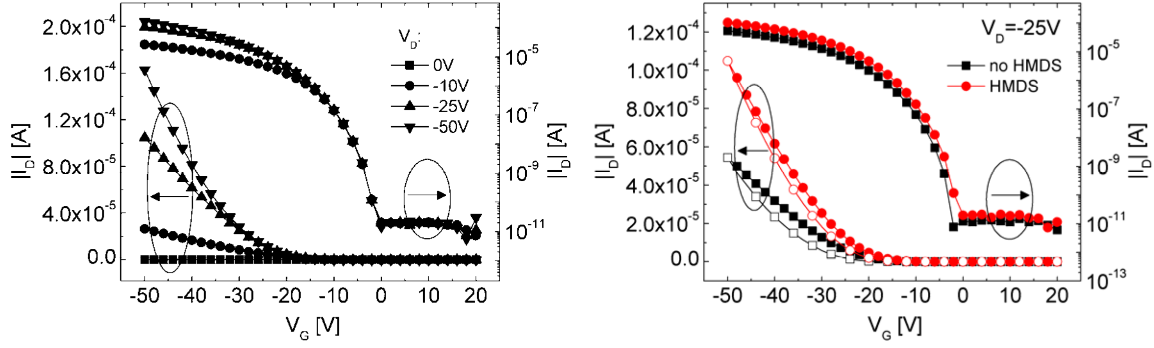

Figure 3.31: Left: transfer characteristics (linear and semi-logarithmic) of a typical pentacene-based OFET ($L \approx 25$ µm, $W \approx 2.85$ mm) fabricated on HMDS-treated SiO_2 measured in argon; right: transfer curves (linear and semi-logarithmic) at V_D = -25V of pentacene-based OFETs ($L \approx 25$ µm, $W \approx 2.85$ mm) fabricated on untreated SiO_2 and on HMDS-treated SiO_2; filled symbols: sweeps from positive to negative voltages; open symbols: reverse sweep.

Figure 3.31 left shows typical transfer characteristics of a HMDS-treated pentacene-OFET. The devices performed reasonably, showing a rather large on/off-current ratio. Similar to the rr-P3HT-based devices, the short-channel OFETs exhibited a larger hysteresis in the transfer characteristics (not shown). Figure 3.31 right and Table 3 compare two devices with and without HMDS-surface modification, showing qualitatively similar tendencies as observed by other groups.[248] HMDS-treatment led to a small positive shift of the switch-on voltage and doubled the field-effect mobility and on/off-current ratio, in accordance with the results of the rr-P3HT-based devices. We didn't observe an off-current reduction by the treatment with HMDS as Yagi et al.,[224] who, however, applied the top-contact architecture. As with the rr-P3HT-based OFETs, performance improvements by HMDS pre-treatment of pentacene-based devices were not as high as might have been expected, which is again ascribed to the applied bottom-contact architecture.

Table 3: Relevant OFET parameters of typical pentacene-based devices ($L \approx 25$ mm, $W \approx 2.85$ mm) fabricated on SiO_2 with and without HMDS-pre-treatment; field-effect mobility μ_{Lin} determined (at V_D = -10V, V_G = -30V) with eqn. (2.14); switch-on voltage V_{SO}, subthreshold slope S, maximum interfacial trap density $N_{T,max}$ and on/off-current ratio I_{on}/I_{off} (I_{on}: V_G = -50V, I_{off}: V_G = 0V) determined from transfer curve at V_D = -25V; I_{Dmax} (O-T) is percentage of I_D at $V_D = V_G$ = -50V in output characteristics with respect to value in transfer characteristics.

Device Parameter	V_{SO} [V]	μ_{Lin} [cm²/Vs]	I_{on}/I_{off}	*S* [V/dec]	$N_{T,max}$ [cm^{-2} eV^{-1}]	I_{Dmax} (O-T) [%]
No HMDS	*-2*	$1.8x10^{-2}$	$4x10^6$	*1.7*	$2.9x10^{12}$	*74*
HMDS	*0*	$3.0x10^{-2}$	$1x10^7$	*1.8*	$3.1x10^{12}$	*82*

3.2. Structuring of Silver Source/Drain Electrodes by Micromolding In Capillaries (MIMIC) and Microtransfer Printing (µTP)

The data presented in this chapter were obtained in close collaboration with Alexander Blümel. Parts are also published in: *Micromolding in capillaries and microtransfer printing of silver nanoparticles as soft-lithographic approach for the fabrication of source/drain electrodes in organic field-effect transistors;* A. Blümel, A. Klug, S. Eder, U. Scherf, E. Moderegger, E. J. W. List, *Org. Electron.* **2007**, *8*, 389.

3.2.1. Introduction

Within the past years there has been much effort in developing and improving new techniques for the processing of advanced functional materials used in promising applications like micro-optics or organic electronics. Much attention has been paid to solution-based techniques, which enable low-cost processing and new possible developments like flexible displays or inkjet-printed electronics. An alternative approach to inkjet printing is soft lithography, which is a collective term for a number of non-photolithographic techniques and has become an important tool for structuring materials on the micro- and nanometer scale.[249,250] In recent years a large number of publications in various fields such as microelectronics (nano-wires[251], OLEDs[252,253], OFETs[31,254,255,256,257,258]) or biology (patterned cell growth[259]) has emphasized its flexibility and applicability in many different areas. There are several soft-lithographic techniques utilizing different principles like capillary action (Micromolding In Capillaries (MIMIC))[260,261,262] or self assembly of molecules (Microcontact Printing (µCP))[263,264]. The use of an elastomeric stamp peeled from a rigid master is the common element of all these techniques. This stamp is used for structuring different materials with processes both similar to and quite different from conventional pattern printing.

Here MIMIC was used for the fabrication of source/drain electrodes based on a solution-processable silver nano-dispersion (CABOT AG-IJ-G-100-S1)[265] in well-performing bottom-gate/bottom-contact OFETs with regioregular poly(3-hexylthiophene) as active layer material. By making use of a system of capillaries between a stamp and a substrate, this technique combines the advantage of solution-processability with high lateral resolution for accurate patterns. Depositing a droplet of the desired material at one end of a capillary makes the liquid enter the microchannel due to capillary action.

In addition, Microtransfer Printing (µTP) was applied, the miniaturized counterpart to conventional letterpress printing, as a means to fabricate OFET source/drain electrodes based on the same silver nano-dispersion as used for the MIMIC-devices.

Here the stamp is set onto an inking pad so that the protruding surfaces of the stamp come into contact with the dispersion. With the inked stamp the silver fluid is directly transferred to the substrate.

3.2.2. Device Fabrication

3.2.2.1. Fabrication and Analysis of MIMIC Source/Drain Structures

For MIMIC stamps spin-cast, exposed and developed photoresist films on pre-cleaned glass pieces cut from microscope slides were used as master structures.[261] Accordingly, a positive photoresist (Microposit S1813 from Shipley[266]) was spun onto the slides at 4000 rpm for 40 s, leading to a nominal film thickness of 1.3 µm, followed by a softbake at 105°C for 210 s. The resist was then exposed to UV light for ~14 s through a chrome mask using an EVG 620 mask aligner[207] with standard settings in a cleanroom and developed in a Microposit 351 developer bath for ~60 s (dilution ratio developer/distilled water: 1/5). Afterwards the master samples were rinsed with distilled water and dried with CO_2. In order to get electrically separated silver electrodes, the resist lines were finally scratched with a needle. Figure 3.32 shows a typical photoresist master.

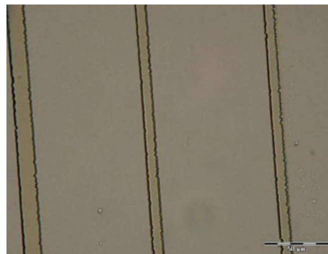

Figure 3.32: Photoresist master for MIMIC stamps.

The stamps themselves were formed from polydimethylsiloxane (PDMS) using Sylgard 184 from Dow Corning.[267] The two-component system, consisting of prepolymer (base) and curing agent, was fabricated with a weight ratio of 10:1 (base : curing agent) and then carefully poured over the master structures. After curing at ~100°C for 1 h, the stamps were peeled from the masters.

As OFET substrates, highly n-doped silicon (n^{++}-Si) wafer pieces (dimensions: 25 mm x 25 mm) with a 247 nm thick, thermally grown silicon dioxide (SiO_2) layer (capacitance per unit area $C_i \approx 14$ nF/cm^2) from austriamicrosystems AG[268] were used. The n^{++}-Si served as common gate electrode, the SiO_2 layer as gate dielectric.

The backside of the substrate was scratched with a diamond cutter on several spots to create a contact to the n^{++}-Si by removing the native oxide. The substrates were then pre-treated with an O_2-plasma in a custom-made plasma chamber for 15 s ($p(O_2)$: $5x10^{-1}$ mbar) and immersed into deionized water to obtain a hydrophilic surface. Afterwards the PDMS stamp was placed onto the substrate to make conformal contact and two droplets of CABOT AG-IJ-G-100-S1[265] silver nano-dispersion were deposited near the open ends of the capillaries. Due to capillary action the channels were filled with the liquid, which is a very slow process depending on geometric parameters of the microchannel as well as dynamic viscosity, surface tension of the carrier fluid and advancing contact angles on both the substrate and the stamp.[261] The sample was stored under ambient conditions until the filling process was completed (~14 h) and after curing at 150°C for 1 h, the stamp was carefully removed. Figure 3.33 schematically depicts the applied MIMIC process flow.

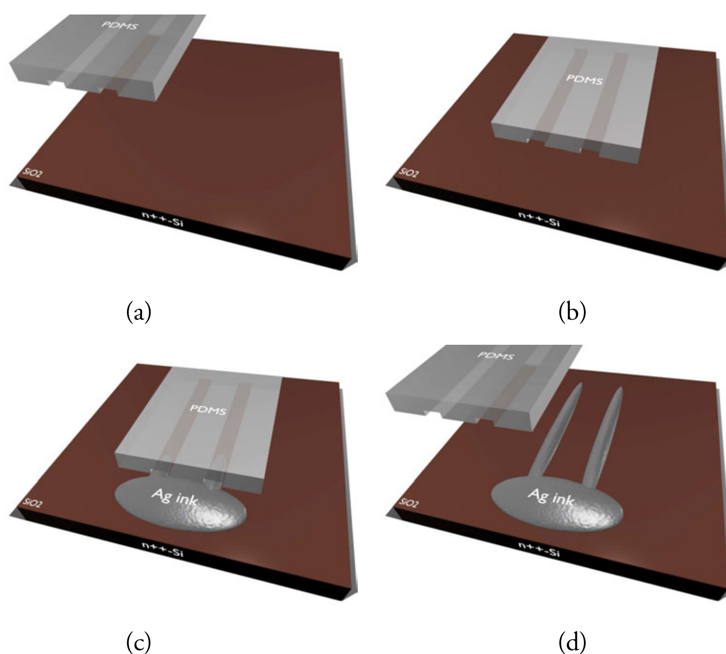

Figure 3.33: Process flow of silver source/drain-electrode structuring by MIMIC: a) PDMS stamp and substrate; b) stamp on substrate; c) silver nano-dispersion entering the microchannels due to capillary action; d) cured silver pattern on the substrate forming source/drain electrodes.

The ready-fabricated MIMIC silver lines were characterized by optical and atomic force microscopy, showing well-defined structures with high lateral resolution (Figure 3.34). The electrode height was determined to approximately 600 nm (for comparison, the capillary height was ~1.3 µm).

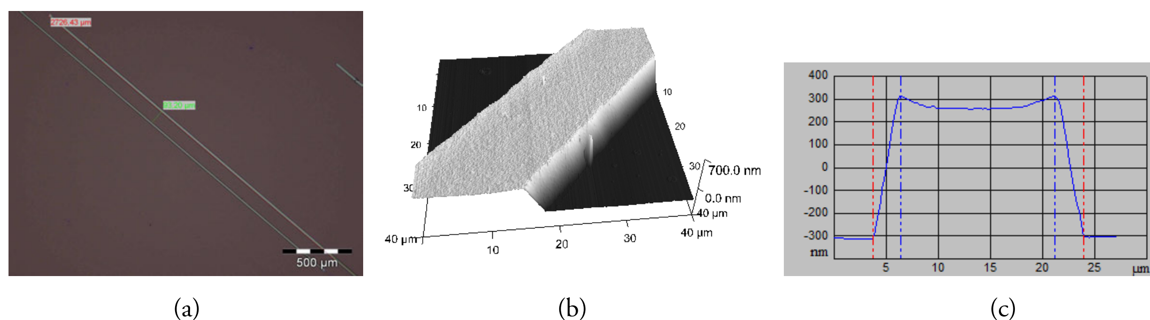

(a) (b) (c)

Figure 3.34: a) Optical micrograph of typical source/drain electrodes fabricated by MIMIC after curing; b) 3D AFM-height image of a silver line; c) cross-sectional shape of a silver line.

The cross-sectional shape differed slightly from the rectangular shape of the master, as the top of the electrodes showed a height depression of 50-60 nm with respect to their edges. This was ascribed both to sagging of the stamp and diffusion of the carrier fluid into the stamp.[269]

Figure 3.35a depicts a single silver MIMIC line between two drops of conductive silver paste. The resistivity of the material was calculated from the current-voltage characteristics of this line (Figure 3.35b right) and its dimensions, the latter being determined by optical microscopy and AFM. Its value was in the range of 15-25 µΩcm, which is significantly above the value of 1.49 µΩcm[55] (1.587 µΩcm)[270] for bulk silver, but well in the range of the specification for the ink (4-32 µΩcm according to CABOT data sheet).

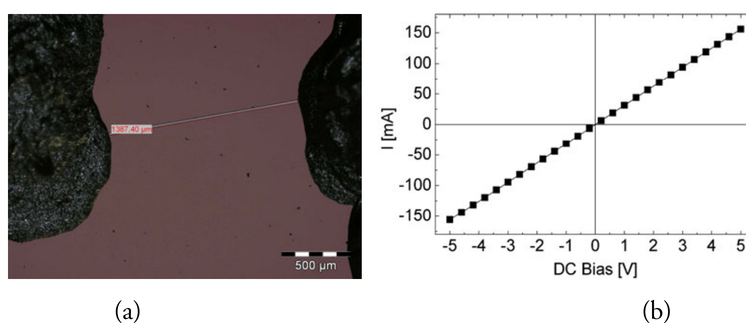

(a) (b)

Figure 3.35: a) Optical micrograph of MIMIC silver line between two drops of conductive silver paste; b) corresponding current-voltage characteristics.

3.2.2.2. Fabrication and Analysis of µTP Source/Drain Structures

As the lateral dimensions of the photoresist masters for MIMIC stamps were too small for the µTP process, µTP master structures were directly printed onto transparency sheets using a conventional 600 dpi office laser printer, yielding a lower lateral resolution (Figure 3.36). The stamps were also fabricated from PDMS using Sylgard 184[267] according to the description above.

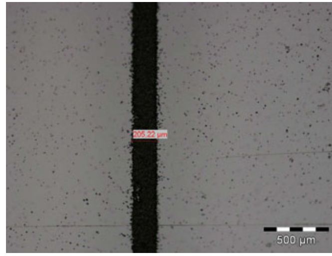

Figure 3.36: Laser-printed master for µTP stamps.

For the “inking pad” a small amount of CABOT AG-IJ-G-100-S1[265] silver nano-dispersion was drop-cast onto a microscope slide. The dispersion spread over a large area due to the hydrophilic glass surface. For more accurate printing the inking pad was stored under ambient conditions for several hours to increase viscosity by evaporation of low-boiling components of the silver nano-dispersion. After inking the stamp, it was put onto a glass slide for several times to get rid of excess ink and obtain well-defined structures. Then the actual printing process was performed either by placing the stamp onto the n^{++}-Si/SiO_2 substrate[r] for ~3 s or leaving it there and baking substrate and stamp for 2 h at 80°C. Both methods typically resulted in defined source/drain electrodes. After removing the stamp, the samples were baked again at 150°C for 1 h. Figure 3.37 schematically illustrates the µTP process flow and Figure 3.38 shows typical source/drain electrodes obtained by µTP. The channel lengths L varied between 140 µm and 190 µm.

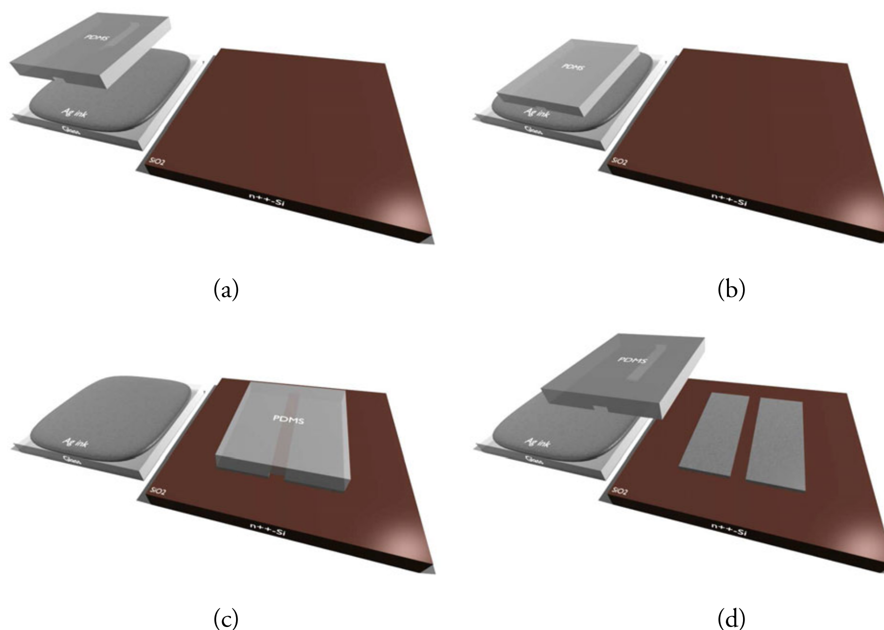

Figure 3.37: Process flow of silver source/drain-electrode structuring by µTP: a) inking pad, substrate and stamp; b) stamp in ink; c) inked stamp transferred onto substrate; d) transferred silver pattern forming source/drain electrodes.

[r] The substrates for µTP-OFETs were not pre-treated with O_2-plasma and deionized water.

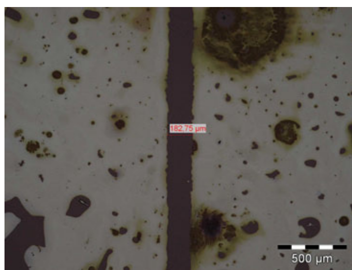

Figure 3.38: Optical micrograph of typical source/drain electrodes fabricated by µTP after curing.

The structures exhibited regions of incomplete pattern transfer. The rather high edge roughness is attributed to the different approach in master production. Moreover, the applied nano-dispersion was optimized for inkjet printing and hence exhibited a too low dynamic viscosity to yield well-defined µTP structures. Nevertheless, one major advantage of Microtransfer Printing is that electrode structuring is performed in a single and fast step, while MIMIC is a very time-consuming procedure related to capillary action.[260,261]

3.2.2.3. Completion of MIMIC- and µTP-OFETs

As organic semiconductor rr-P3HT (M_n = 37900 g/mol, M_w = 53700 g/mol) from the Scherf group[242] was applied. The preparation of the corresponding $CHCl_3$ solutions (2 mg/ml) was similar as described in chapter 3.1.3.3. The substrates with the pre-defined MIMIC and µTP source/drain structures were baked at 110°C in vacuum for 1 h to remove surface water and afterwards the semiconductor solution was deposited under inert conditions by drop-casting (MIMIC structures) and spin-casting (µTP structures, spin parameters: ~1500 rpm, 40 s), respectively.[s] After a drying step at 50°C for 10 min the substrates were fixed on a single-sided copper board using conductive silver paste. A frame was scratched around every single device within the rr-P3HT layer, thus isolating each OFET on a substrate in order to reduce parasitic leakage currents across the gate dielectric and within the organic semiconducting layer. Finally a baking step was performed at 180°C for 1.5 h under high vacuum to dedope the rr-P3HT film even more. Before and after device separation as well as after the baking procedure the OFETs were electrically characterized under argon atmosphere with an E5262A parameter analyzer from Agilent Technologies.

[s] Due to the hydrophilization of the substrates in the MIMIC process spin-coating of rr-P3HT did not yield homogenous films. Therefore drop-casting was applied for MIMIC-devices and spin-casting only for µTP-OFETs.

3.2.3. Device Characteristics of MIMIC- and µTP-OFETs

3.2.3.1. OFETs based on MIMIC Source/Drain Electrodes

Figure 3.39 depicts the output characteristics of a well-performing MIMIC-OFET before and after device separation. By isolating the devices from each other, gate-leakage currents could be reduced by more than one order of magnitude (e.g. from 4.9×10^{-7} A to 3.1×10^{-8} A at V_D = -2V, V_G = -85V), which in particular is observable at high potential difference between gate voltage V_G and drain voltage V_D (note e.g. the crossing output curves at V_D = 0V in Figure 3.39 left). The off-current (I_D at V_G = 0V) was slightly reduced as well.

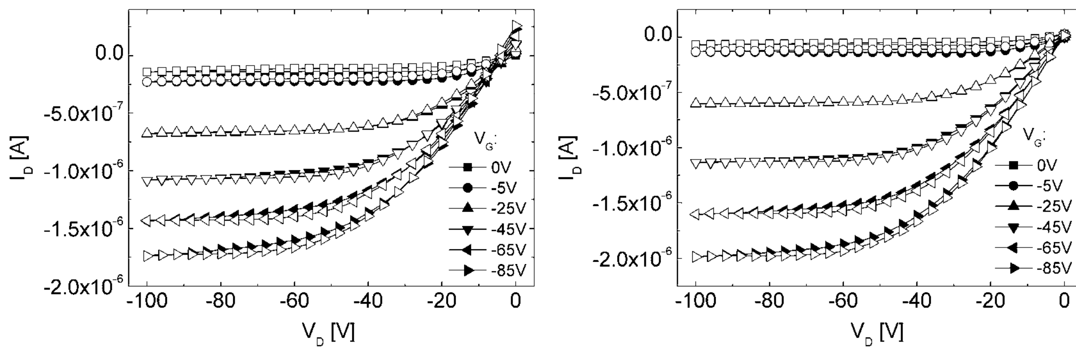

Figure 3.39: Output characteristics of a MIMIC-OFET ($L \approx 94$ µm, $W \approx 1920$ µm) before (left) and after (right) device separation measured in argon; filled symbols: sweeps from positive to negative voltages; open symbols: reverse sweep.

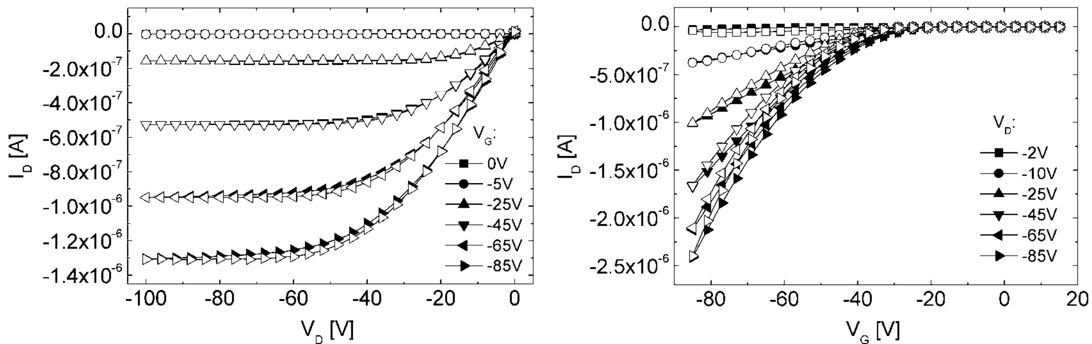

Figure 3.40: Output (left) and transfer (right) characteristics of a MIMIC-OFET ($L \approx 94$ µm, $W \approx 1920$ µm) after baking at ~180°C for 90 min measured in argon; filled symbols: sweeps from positive to negative voltages; open symbols: reverse sweep.

Figure 3.40 depicts the corresponding electrical characteristics after the baking procedure in order to dedope the semiconductor film, which had no influence on parasitic leakage currents.

In particular the output characteristics clearly do not reveal a quadratic behavior of the source-to-drain current I_D with respect to V_G in the saturation regime, which would be expected according to eqn. (2.13). This is ascribed to the inhomogeneous rr-P3HT layer obtained by drop-casting and the hydrophilization of the substrate, which both result in high trap-densities and hence in a pronounced gate-bias induced carrier trapping (see chapter 2.2.3.2). Gate-bias stress is also responsible for the fact the I_D values at a particular V_D and (high) V_G are larger in the transfer characteristics (e.g. I_D at $V_D = V_G$ = -85V in Figure 3.40 left is only ~54% of the corresponding value in Figure 3.40 right). Moreover, trapping of charge carriers is revealed by the hysteresis in the transfer characteristics above.

The rather linear behavior of I_D at low drain voltages and the well-defined current saturation suggest that contact resistance is small in these devices so that charges are assumed to be well injected from the silver MIMIC electrodes into the rr-P3HT. However, in OFETs with larger channel lengths (here $L \approx 94$ µm) the influence of contact resistance generally is reduced due to the larger channel resistance (see chapter 2.2.2.5).

Figure 3.41 compares the transfer curves at V_D = -85V and the field-effect mobility values μ_{Sat} in the saturation regime (determined with eqn. (2.15)) before and after device separation as well as after the baking procedure and Table 4 summarizes important device parameters extracted at the various fabrication stages.

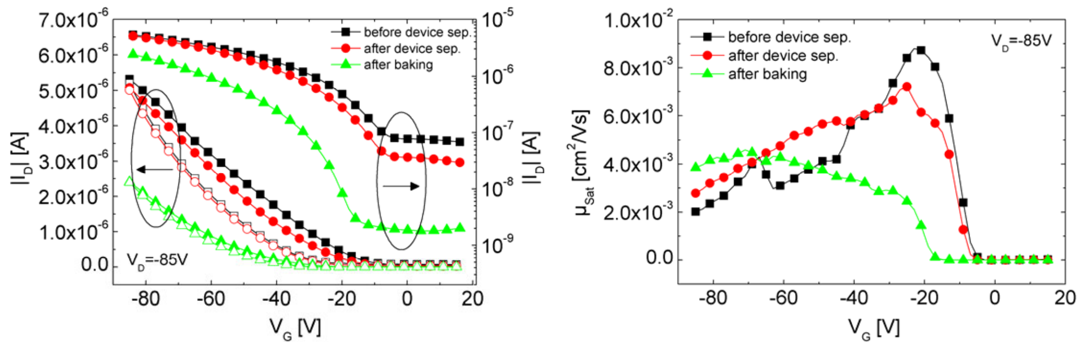

Figure 3.41: Left: transfer curves (linear and semi-logarithmic) at V_D = -85V of a MIMIC-OFET ($L \approx 94$ µm, $W \approx 1920$ µm) before device separation, after device separation and after baking at ~180°C for 90 min measured in argon; filled symbols: sweeps from positive to negative voltages; open symbols: reverse sweep; right: corresponding field-effect mobility in the saturation regime.

Table 4: Device parameters of a MIMIC-OFET ($L \approx 94$ µm, $W \approx 1920$ µm) based on rr-P3HT at various fabrication stages; switch-on voltage V_{SO} and on/off-current ratio I_{on}/I_{off} determined from semi-logarithmic transfer curves at V_D = -85V (I_{on}: V_G = -85V, I_{off}: V_G = 0V); field-effect mobility μ_{Sat} (at V_D = -85V, V_G = -60V) extracted from transfer curves using eqn. (2.15).

Fabrication stage	V_{SO} [V]	I_{off} [A]	I_{on} [A]	I_{on}/I_{off}	μ_{Sat} [cm²/Vs]
Before device separation	~ -5	7.7×10^{-8}	5.3×10^{-6}	7×10^{1}	3.2×10^{-3}
After device separation	~ -7	3.6×10^{-8}	5.1×10^{-6}	1×10^{2}	4.9×10^{-3}
After baking	~ -15	1.9×10^{-9}	2.4×10^{-6}	1×10^{3}	4.2×10^{-3}

While device separation mainly affected the gate-leakage currents, baking obviously led to a strong reduction of the off-current I_{off} and hence an increased on/off-current ratio[t] due to dedoping of the semiconductor film (see chapter 2.2.3.1). As a consequence traps at the semiconductor/dielectric interface became a larger influence, resulting in a shift of switch-on voltage V_{SO} to more negative values. However, after device baking the magnitude of hysteresis was strongly reduced (Figure 3.41 left), which might be attributed to a better morphology of the rr-P3HT layer, leading to a reduced trap density within the semiconductor film and possibly an increased π-π stacking of the polymer chains. Gate-leakage currents and the high doping level (high bulk conductivity) due to the thick drop-cast semiconductor layer are also responsible for the peak of μ_{Sat} at low V_G in Figure 3.41 right, which becomes less pronounced after device separation and even more so after baking. Generally, the obtained mobility values were well in the range expected for disordered rr-P3HT without any substrate pre-treatment.

Figure 3.42 shows the time dependence of the channel current at fixed V_G = -85V and V_D = -100V of a MIMIC-OFET after various bias-stress conditions, investigating the operational device stability. Obviously, applying a negative gate voltage led to a reduction of I_D with time, because mobile positive charge carriers were trapped within the dielectric or at the dielectric/semiconductor interface. On the application of a positive V_G the trapped charge carriers were released again and accordingly the subsequent time measurement revealed a strong increase of I_D (compare red and green curve). Finally, after applying zero gate and drain voltage for 100 s, with this device nearly the pristine $I_D(t)$-characteristics was obtained again. Such measurements performed after film-dedoping by baking revealed a smaller decrease of I_D with time at fixed V_G and V_D (not shown), which is also an indication of a reduced trap density within the active layer.

[t] Also the on-current I_{on} was reduced after baking, but relatively less than the off-current.

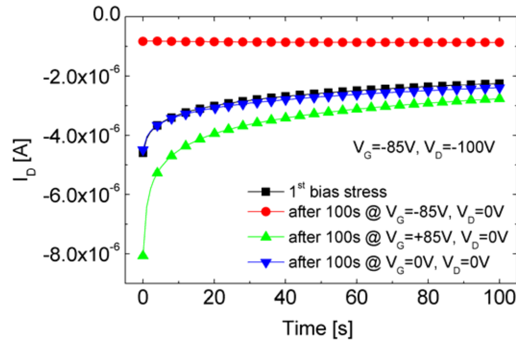

Figure 3.42: Source-to-drain channel current I_D at V_G = -85V and V_D = -100V as a function of time of a MIMIC-OFET ($L \approx 94$ µm, $W \approx 1920$ µm) after various bias-stress conditions measured in argon after device separation.

3.2.3.2. OFETs based on µTP Source/Drain Electrodes

Figure 3.43 shows a typical sample with several µTP-OFETs fixed on a single-sided copper board. The regions of incomplete pattern transfer are clearly visible on the µTP source/drain electrodes.

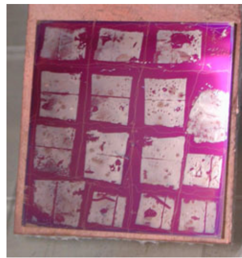

Figure 3.43: Sample with several µTP-OFETs fixed on a single-sided copper board.

As with the MIMIC-OFETs, the reduction of parasitic leakage currents due to device isolation becomes obvious by comparing the output characteristics of a µTP-OFET before and after device separation (Figure 3.44).

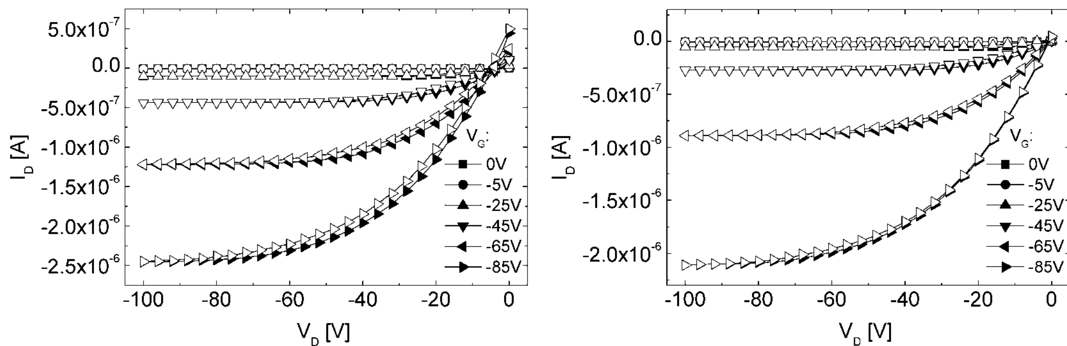

Figure 3.44: Output characteristics of a µTP-OFET ($L \approx 159$ µm, $W \approx 5814$ µm) before (left) and after (right) device separation measured in argon; filled symbols: sweeps from positive to negative voltages; open symbols: reverse sweep.

In fact, isolating the µTP-device shown above also decreased gate-leakage currents by more than one order of magnitude (e.g. from 1.1x10^{-6} A to 6.0x10^{-8} A at V_D = -2V, V_G = -85V) and was accompanied by a small reduction of off-current.

Figure 3.45 shows the corresponding device characteristics after dedoping the semiconductor film by baking, which again had no influence on the parasitic leakage currents.

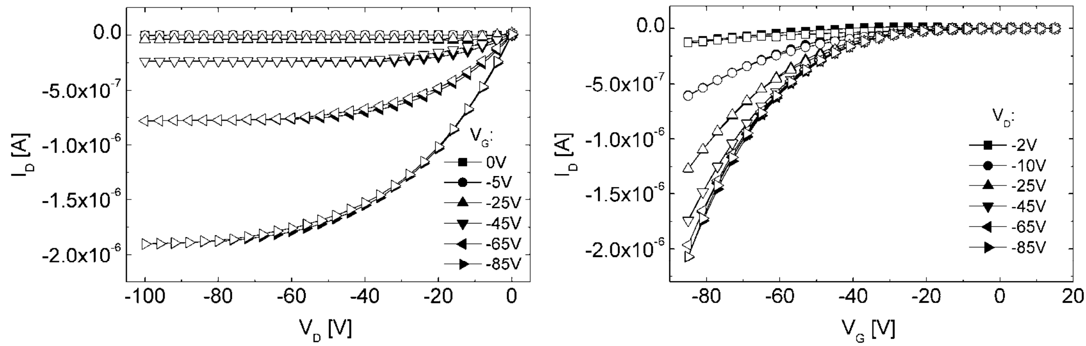

Figure 3.45: Output (left) and transfer (right) characteristics of a µTP-OFET ($L \approx 159$ µm, $W \approx 5814$ µm) after baking at ~180°C for 90 min measured in argon; filled symbols: sweeps from positive to negative voltages; open symbols: reverse sweep.

Similar to the MIMIC-OFETs, the channel current saturates well for $|V_D| > |V_G|$. However, in contrast to the device characteristics shown in Figure 3.40, the µTP-OFETs exhibited a super-quadratic behavior of I_D with respect to V_G in the saturation regime. This is expected when trap densities are rather low and when the field-effect mobility increases with gate bias, as commonly observed with organic small molecule and polymeric semiconductors. The lower trap densities are ascribed both to the spin-casting process (more homogeneous, thinner films than drop-casting) and the absence of the substrate hydrophilization. They are also reflected by the smaller difference of I_D values in the output and transfer characteristics at a particular working point (e.g. I_D at $V_D = V_G$ = -85V in Figure 3.45 left is ~91% of the corresponding value in Figure 3.45 right), by the smaller magnitude of hysteresis in the transfer characteristics (same measurement speed as with the MIMIC-OFETs) and by the lower absolute values of the switch-on voltage (see Figure 3.46 and Table 5). Similar to the MIMIC-OFETs, the linear behavior of I_D at low drain voltages and the well-observable current saturation suggest low contact resistance between the silver µTP electrodes and the rr-P3HT. Still, the influence of contact resistance on device characteristics is rather low compared to channel resistance when channel lengths are large (here $L \approx 159$ µm).

Figure 3.46 left and Table 5 compare the transfer curves at V_D = -85V at the various fabrication stages and the corresponding device parameters, respectively. Figure 3.46 right shows the device-to-device variation of several µTP-OFETs.

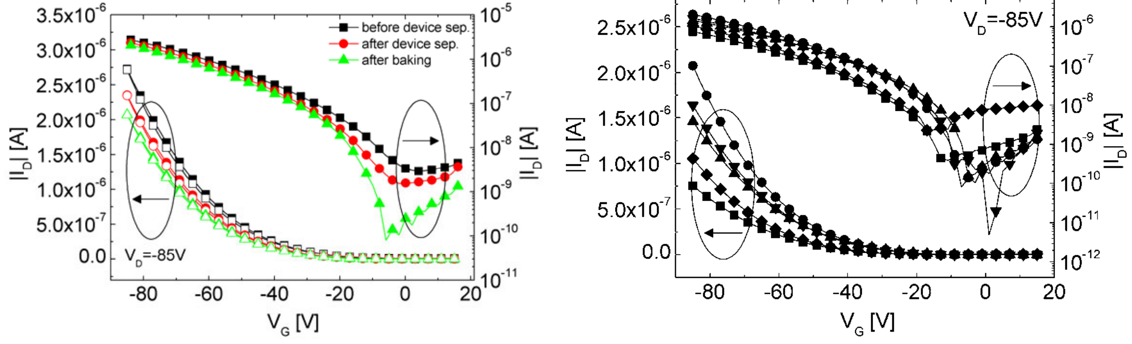

Figure 3.46: Left: transfer curves (linear and semi-logarithmic) at V_D = -85V of a µTP-OFET ($L \approx$ 159 µm, $W \approx$ 5814 µm) before device separation, after device separation and after baking at ~180°C for 90 min measured in argon; filled symbols: sweeps from positive to negative voltages; open symbols: reverse sweep; right: transfer curves (linear and semi-logarithmic) of several µTP-devices after baking with W/L-ratios between 19 and 36.

Table 5: Device parameters of a µTP-OFET ($L \approx$ 159 µm, $W \approx$ 5814 µm) based on rr-P3HT at various fabrication stages; switch-on voltage V_{SO} and on/off-current ratio I_{on}/I_{off} determined from semi-logarithmic transfer curves at V_D = -85V (I_{on}: V_G = -85V, I_{off}: V_G = 0V); field-effect mobility μ_{Sat} (at V_D = -85V, V_G = -60V) extracted from transfer curves using eqn. (2.15).

Fabrication stage	V_{SO} [V]	I_{off} [A]	I_{on} [A]	I_{on}/I_{off}	μ_{Sat} [cm²/Vs]
Before device separation	~+1	$3.2x10^{-9}$	$2.7x10^{-6}$	$8x10^{2}$	$2.6x10^{-3}$
After device separation	~-3	$1.6x10^{-9}$	$2.4x10^{-6}$	$1.5x10^{3}$	$2.3x10^{-3}$
After baking	~-7	$2.1x10^{-10}$	$2.1x10^{-6}$	$1x10^{4}$	$2.0x10^{-3}$

Compared to the MIMIC-OFETs, the more homogenous and thinner semiconductor film of the µTP-devices resulted in a lower doping level and thus a smaller bulk conductivity, which explains the about one order of magnitude smaller off-currents and the correspondingly larger on/off-current ratios. As expected, baking the devices led to an increase of the on/off-current ratio due to dedoping of rr-P3HT, an effect which was, however, less pronounced than observed with the MIMIC-OFETs. The slightly lower field-effect mobility values are also ascribed to the lower doping level.

Figure 3.47 shows the time dependence of the channel current at fixed V_G = -85V and V_D = -100V of a µTP-OFET after various bias-stress conditions, which also revealed charge trapping behavior. Compared to the MIMIC-OFET (Figure 3.42), the µTP-device exhibited a much smaller relative decrease of I_D with time (e.g. in the first bias-stress measurement (black curve) ~23% versus ~52% for the MIMIC-device), which also reflects the lower trap density within the more homogeneous rr-P3HT layer formed by spin-casting.

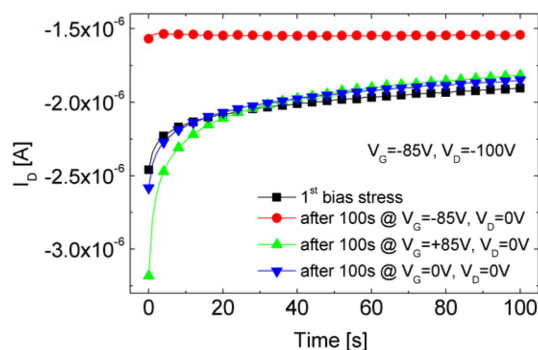

Figure 3.47: Source-to-drain channel current I_D at V_G = -85V and V_D = -100V as a function of time of a µTP-OFET ($L \approx$ 159 µm, $W \approx$ 5814 µm) after various bias-stress conditions measured in argon after device separation.

3.3. WireOFETs

3.3.1. Introduction

Electroactive organic materials are also becoming more and more interesting in the field of electronic textiles (e-textiles),[271] which involves embedding circuitry, sensor systems and electronic devices directly on or into fabric, possibly even during its manufacturing, for the development of e.g. smart clothing. Several e-textile products are already commercially available, featuring either embedded sensors for acquiring physiological parameters, textile control panels on jackets for electronic devices like MP3-players or integrated LEDs and displays.[272] Most of these applications are, however, based on the incorporation of conventional planar silicon-based components into garment, partly also implementing conducting fiber networks.

Due to their specific electrical and mechanical properties, electroactive organic materials provide new opportunities within this field as well. In particular, they allow for cost-effective processing at low temperatures, exhibit low weight, high elasticity and mechanical flexibility and can be easily tailored, also enabling the implementation of sensing functionalities.

So far only few organic electronic devices on fibers or wires have been demonstrated, including OFETs,[106,107,108] an organic wire electrochemical transistor[273] and an organic solar cell.[274] The main challenge is to develop cheap structuring processes and technologies compatible with textile fabrication, in particular with cylindrical substrates. A simple transfer of the manufacturing techniques used for device fabrication on planar substrates (photolithography, inkjet printing, spin-casting, etc.) is obviously very difficult. Most of the OFETs on fibers presented so far applied the bottom-gate/top-contact architecture and were fabricated on metal wires, which were coated with a dielectric layer, followed by organic semiconductor deposition (usually pentacene)

and source/drain-electrode definition via evaporation through crossing wires as shadow masks or via a soft lithographic process.

Within this thesis a readily available mass product, namely an enameled copper wire, i.e. a wire covered with a thin insulation layer, was tested in combination with a solution-processable organic semiconductor for the fabrication of low-cost bottom-gate/bottom-contact OFETs, in the following termed "wireOFETs", which are compatible with fabric manufacturing. Generally, such insulating wires are used for the construction of e.g. transformers, inductors, electric motors or electromagnets. When applied in an OFET, the copper wire can be employed as gate electrode and the insulating material as gate dielectric, both together acting as mechanical support at the same time. Figure 3.48 schematically depicts the corresponding architecture.

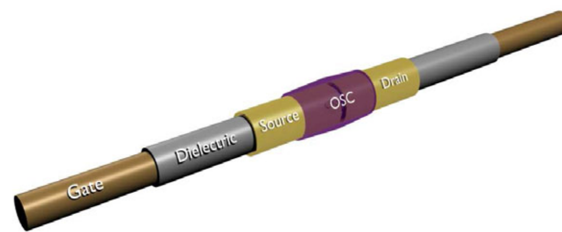

Figure 3.48: WireOFET architecture with copper wire as gate electrode and insulation layer as gate dielectric; OSC… organic semiconductor.

3.3.2. Device Fabrication

Enameled copper wires (conductor diameter: 125 µm, 99.9% purity, product index: CU005895) from Goodfellow,[275] featuring a 2 µm thick insulating polyesterimide layer, were fixed onto a microscope slide acting as support with hot-melt adhesive. At the wire ends the dielectric was removed with a scalpel and the uncovered copper acting as gate was contacted with conductive silver paste. In order to isolate the devices on a single wire, stripes of scotch tape were also fixed onto the glass support. As shadow masks thin crossing wires with a diameter of ~80 µm were applied. Gold source/drain electrodes with a nominal thickness of ~130 nm were thermally evaporated ($p < 1 \times 10^{-6}$ mbar) in a custom-made evaporation plant without rotating the insulating wires during deposition, leading to a non-uniform metal coverage. Assuming that half of a wire was covered with gold, a channel width W of ~200 µm was estimated from the wire diameter. For preventing parasitic leakage currents or shorts between the devices, a piece of transparency sheet was fixed between glass support and wires before gold evaporation.

Figure 3.49 shows corresponding pictures of a sample before and after metal deposition. Figure 3.50 depicts optical micrographs of typical source/drain electrodes before and after removal of a crossing wire acting as shadow mask.

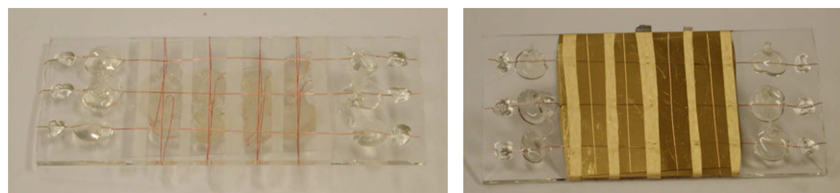

Figure 3.49: Three enameled copper wires fixed on a microscope slide together with crossing wires acting as shadow masks before (left) and after (right) gold evaporation.

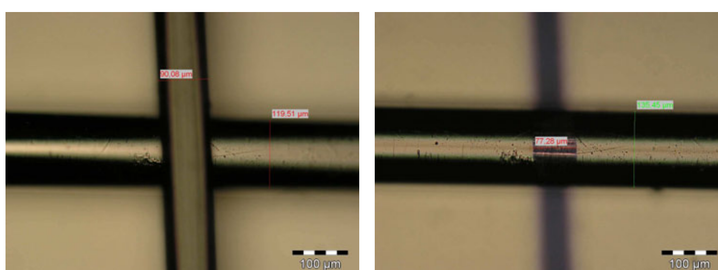

Figure 3.50: Optical micrograph of typical gold source/drain electrodes on an enameled copper wire before (left) and after (right) removal of a crossing wire acting as shadow mask.

As organic semiconductor the same rr-P3HT as for the MIMIC- and µTP-OFETs was used and the corresponding $CHCl_3$-based solution (1 mg/ml) was prepared similarly. The wires with defined source/drain structures were baked under high vacuum at 110°C for 1.5 h to remove surface water and then the semiconductor solution was drop-cast onto the channel area of each device in argon, followed by a film drying step at 50°C for 10 min. After replacing the gold- and rr-P3HT-contaminated transparency sheet by a new one, the individual wireOFETs were contacted with conductive silver paste. They were then baked at ~160°C for ~2 h in high vacuum to dedope the organic semiconductor. Electrical characterization in argon was performed with an Agilent E5262A parameter analyzer before and after baking.

3.3.3. Device Characteristics of WireOFETS

Figure 3.51 shows the output and transfer characteristics of a typical wireOFET before dedoping the rr-P3HT film by baking. Clearly, the measured source-to-drain channel current exhibits a pronounced ohmic behavior due to the inhomogeneous drop-cast semiconductor film, leading to a large bulk conductivity and hence a suppressed field-effect. When subtracting I_{off} at V_G = 0V, the latter becomes more obvious.

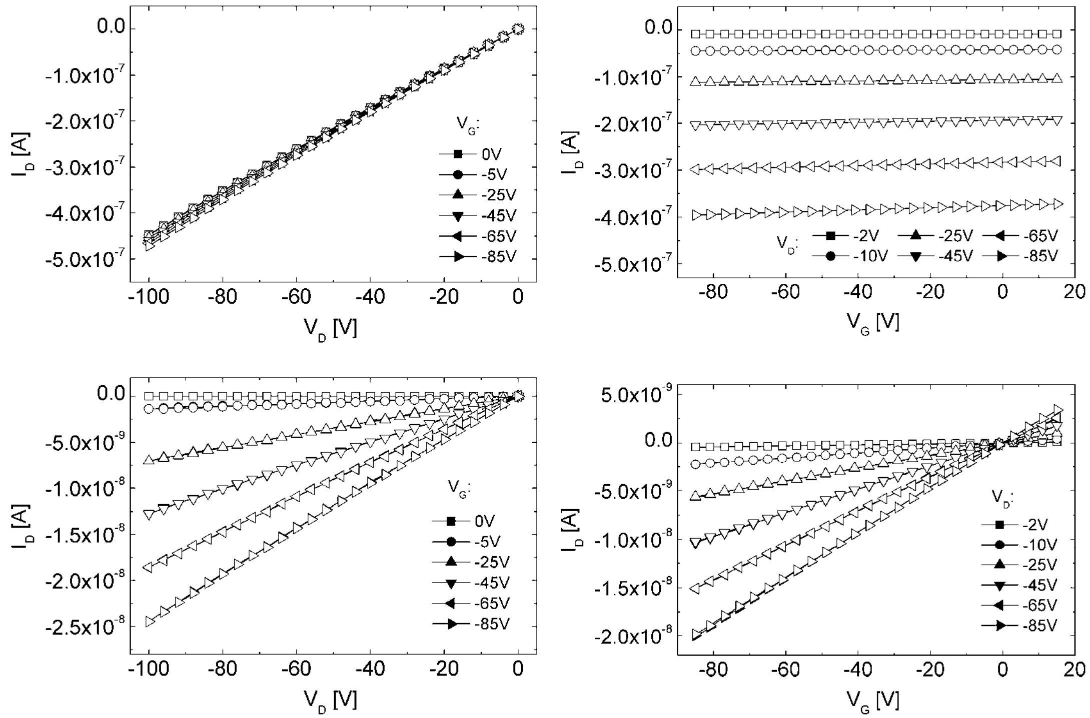

Figure 3.51: Output (left) and transfer (right) characteristics of a wireOFET ($L \approx 65$ µm, $W \approx 200$ µm) before baking at ~160°C for 2 h measured in argon; top: as measured; bottom: after subtracting I_{off} at V_G = 0V; filled symbols: sweeps from positive to negative voltages; open symbols: reverse sweep.

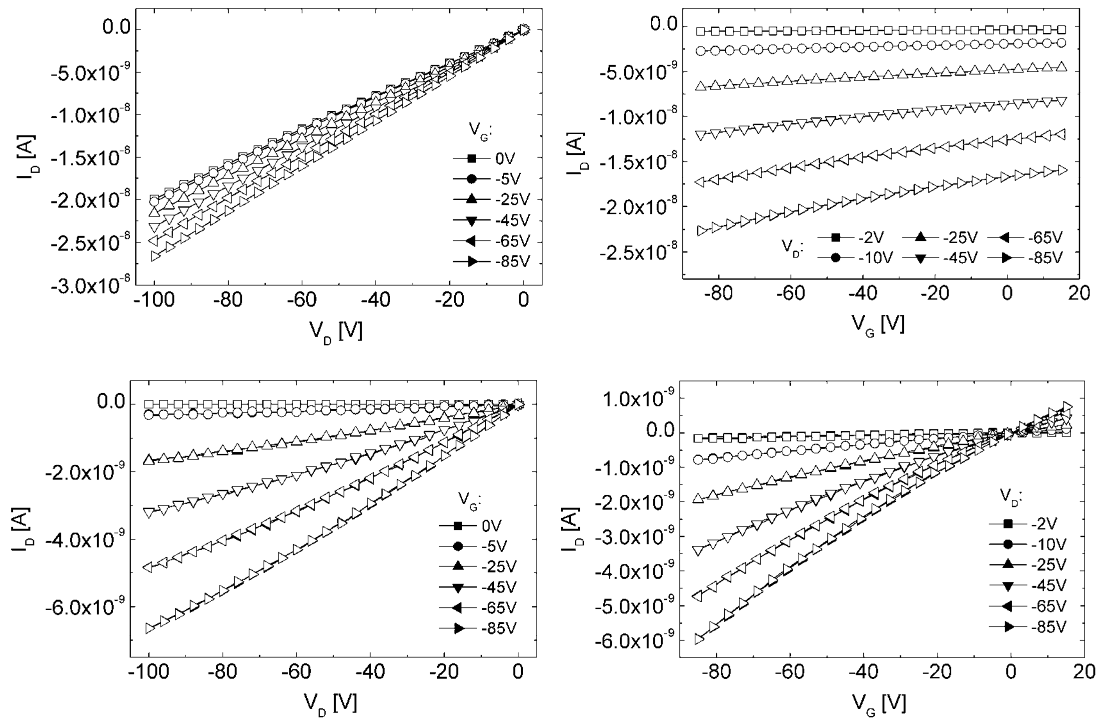

Figure 3.52: Output (left) and transfer (right) characteristics of a wireOFET ($L \approx 65$ µm, $W \approx 200$ µm) after baking at ~160°C for 2 h measured in argon; top: as measured; bottom: after subtracting I_{off} at V_G = 0V; filled symbols: sweeps from positive to negative voltages; open symbols: reverse sweep.

Generally, gate-leakage currents were found to be below 200 pA. As with the MIMIC-OFETs, baking the devices led to a strong reduction of the off- and on-current due to semiconductor dedoping and the field-effect behavior became more pronounced (Figure 3.52).
However, overall device performance was rather low and therefore no detailed device analysis and no further device testing regarding e.g. mechanical flexibility, dielectric reliability and operational stability was performed. For sure material selection, deposition processes and operating voltages of the presented wireOFETs are far from being optimized for e-textile fabrication. Nevertheless, the results indicate the potential of combining readily available mass products with solution-processable organic semiconductors for the textile-compatible fabrication of low-cost organic electronics.

3.4. Summary and Conclusions

In summary, this chapter thoroughly described the development and optimization of several OFET fabrication techniques and processes as well as their effects on the performance of corresponding devices. A new OFET fabrication line was successfully implemented and tested within a cleanroom environment, yielding highly reproducible and well-performing OFETs with low device-to-device variation. Within this section important geometric issues were emphasized, also taking into account their effects on parasitic leakage currents and operating voltages. The implications of SiO_2 surface modification with HMDS were thoroughly investigated by contact angle measurements, atomic force microscopy and OFET-device characterization, exhibiting a distinct performance increase for rr-P3HT- and pentacene-based OFETs. Also the appearance of short-channel effects was analyzed in detail. Although a large part of the results and conclusions in this section is common knowledge, it does not only prove the successful realization of a new fabrication line, but also emphasizes important issues for a successful design and processing of organic field-effect transistors and hopefully contributes to a commercialization of these wonderful devices.
Moreover, it was shown that the soft-lithographic techniques Micromolding In Capillaries and Microtransfer Printing can be applied for the structuring of solution-processable silver source/drain electrodes in OFETs. The attained performance was comparable with OFETs based on commonly used gold source/drain electrodes. Tuning of the ink parameters such as solid content, dynamic viscosity and surface tension will improve the process flow, decrease the process time and yield more accurate and smaller structures, which altogether will be crucial for industrial scale applications. In addition, after the deposition of the electrodes with MIMIC the substrate should be hydrophobized, for instance, by applying a non-polar self-assembled monolayer such as

HMDS, which would facilitate the applicability of spin-casting for better film morphology. With these improvements, MIMIC and μTP could become standard methods in OFET fabrication.
Finally, wireOFETs formed on cheap enameled copper wires were presented, with the copper applied as gate electrode and the insulation layer as gate dielectric. Although the performance of the presented devices was rather low compared to the other OFETs fabricated within this thesis, the results still indicate the potential of combining readily available mass products with solution-processable organic semiconductors for the fabrication of smart low-cost organic electronics being compatible with textile manufacturing.

4. Stability Issues of Organic Field-Effect Transistors

Ambient, operational and shelf-life stability are important prerequisites for low-cost applications based on organic field-effect transistors. Aside from device encapsulation, another approach to obtain air-stable OFETs is the use of organic semiconductors with large ionization potentials. In this chapter bottom-gate/bottom-contact OFETs containing various polytriphenylamine-(PTPA)-derivatives as organic semiconductors with ionization potentials > 5 eV are investigated with respect to their ambient and shelf-life stability. The results are benchmarked against the well-established transistor semiconductors rr-P3HT and pentacene. Although the latter two exhibit larger field-effect mobility values, corresponding OFETs are degraded upon air exposure mainly due to oxygen/moisture-induced doping or charge-carrier trapping. On the contrary, device parameters of PTPA-OFETs remained rather stable, even after storage under dark ambient conditions for several months. Moreover, when the substrate surface was hydrophobized by HMDS pre-treatment, the stability of the investigated semiconductors was found to be distinctly increased. Finally, also the operational stability of a rr-P3HT-based top-gate OFET with polyvinyl alcohol as gate dielectric is analyzed and the observed channel current drifts upon bias stress are explained by the movement of residual mobile ions within the dielectric.

4.1. Introduction

As pointed out in chapter 2.2.3, for well-performing low-cost organic field-effect transistors stable device parameters under ambient conditions and operational stability are very important issues. Aside from encapsulation of the organic semiconductor, another possibility to induce air-stability is the application of semiconducting materials, which exhibit ionization potentials larger than 5 eV, thus preventing or at least reducing doping effects.[175,276,277] An interesting class of such materials is the one of hole-transporting polytriphenylamines (PTPAs).[22,109,114,278,279,280,281,282,283,284,285]

Various types of oligomeric and polymeric triarylamine-derivatives have already been used in xerographic applications,[286] in OLEDs[287,288,289,290,291] and in organic solar cells[287,288,292,293,294,295] due to their photo-conducting properties and their large hole mobilities, resulting - amongst others - from the easy oxidizability of the involved nitrogen atom (= electron donating).

Besides being rather stable with respect to air and moisture, most chemical modifications of PTPAs exhibit good solubility properties and corresponding films show an amorphous morphology, which both enables easy processing with low-cost deposition and structuring techniques including inkjet printing, as morphology effects can largely be neglected and charge transport is regarded isotropic. This makes these materials interesting for the application in all-solution processed OFETs, even if they are known to exhibit lower field-effect mobilities (due to their amorphous nature) compared to well-established semiconductors such as rr-P3HT. Veres and co-workers were the first to apply such nitrogen-containing aromatic polymers as organic semiconductors in OFETs and investigated their performance also in combination with low-k dielectrics.[109,114,278,279]

Within this work four different PTPA-derivatives were compared in bottom-gate/bottom-contact OFETs, being extensively tested with respect to their ambient and shelf-life stability and benchmarked against rr-P3HT and pentacene. The best performing among them was investigated in more detail with respect to influences of oxygen and moisture after the implementation of a new stability measurement plant. Moreover, the effects of substrate surface modification with HMDS on the ambient stability of OFETs containing various organic semiconductors were evaluated. Finally, rr-P3HT was employed and investigated in top-gate/bottom-contact devices with polyvinyl alcohol (PVA) as gate dielectric, which is known to contain residual ions remaining in the material after saponification.

Most of the work presented in this chapter was performed in close collaboration with Raphael Pfattner, Gerhild Wurzinger and Matthias Baumann. Accordingly, some of the data are also

published in their diploma theses.[105, 296, 297] Moreover, a corresponding publication is in preparation.

4.2. Materials

The chemical structures of the employed PTPA-derivatives are depicted in Figure 4.1. They were synthesized by the group of Prof. Scherf in two major steps:[298] at first functionalized dibromo triarylamine monomers with different substituent on the side phenyl group were obtained by Buchwald-Hartwig-type palladium-catalyzed amination of two equivalents of 1-bromo-4-iodobenzene by the corresponding aniline compound. Then functionalized monomers were accordingly polymerized via a Yamamoto-type aryl-aryl coupling polymerization reaction.
The substituent on the side phenyl groups was varied in order to investigate its influence on the processability, stability and general performance of corresponding field-effect transistors. $PTPA_1$ and $PTPA_2$ have already been applied by Veres and co-workers.[109,114,278,279]

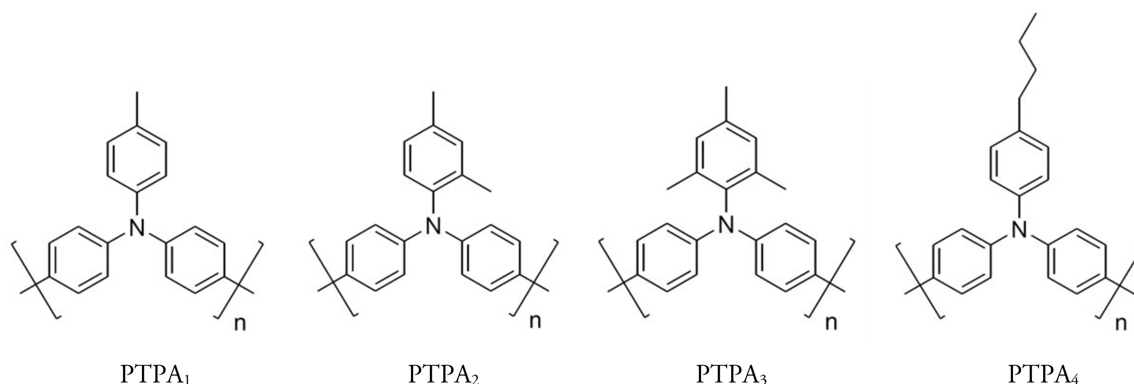

$PTPA_1$ $PTPA_2$ $PTPA_3$ $PTPA_4$

Figure 4.1: Chemical structures of applied polytriphenylamines.

The molecular weights, the band-gap energies and the energetic position of the HOMO levels, determined by the Scherf group[298] with gel permeation chromatography, UV/VIS-absorption spectroscopy and UV photoelectron spectroscopy, respectively, are listed in Table 6, in comparison with corresponding values of rr-P3HT and pentacene. Poly(3-hexylthiophene) was also synthesized by Prof. Scherf's team via the Grignard metathesis polymerization.[299] Pentacene was purchased from Sigma Aldrich with a certified purity ≥ 99.9% and processed without further purification. The UV/VIS-spectroscopy[105,298] of both solutions (with $CHCl_3$ as solvent) and films revealed similar broad and unstructured absorption bands for all PTPA-materials with maxima centered between 370 nm and 390 nm, hence confirming the amorphous nature of the materials and implying that the substituent of the side phenyl groups has no large influence on the optical properties.

The photoluminescence spectra were rather unstructured as well and exhibited emission maxima centered in the range between 420 nm and 430 nm for films and solutions.

Table 6: Relevant material parameters of applied organic semiconductors: M_n... number average molecular weight, M_w… weight average molecular weight, *PDI*… polydispersity index; data for PTPAs obtained from the group of Prof. Scherf:[298] M_n, M_w determined with gel permeation chromatography, HOMO levels measured with an AC-2 surface analyzer from Riken Keiki Co.; band-gap energies determined from onsets of UV/VIS-absorption bands; data for P3HT and pentacene (M_w is here molecular weight) taken from literature.[56,138,174,175,276,300,301,302]

Organic semiconductor	*M_n [g/mol]*	*M_w [g/mol]*	*PDI*	*Bandgap [eV]*	*HOMO (eV)*
$PTPA_1$	*3500*	*6500*	*1.9*	*3.22*	*5.13*
$PTPA_2$	*5000*	*26200*	*5.2*	*3.17*	*5.10*
$PTPA_3$ (top = batch 1, bottom = batch 2)	*38000* *15300*	*69000* *71200*	*1.8* *4.7*	*3.21*	*5.06*
$PTPA_4$	*8800*	*21400*	*2.4*	*3.20*	*5.12*
rr-P3HT (regio-reg. > 98%; top = batch 1, bottom = batch 2)	*37900* *26900*	*53700* *37600*	*1.4* *1.4*	*2.1-2.3*	*4.4-4.9*
Pentacene	-	*278.35*	-	*1.9-2.2*	*4.9-5.2*

The values for the HOMO levels have to be considered with care, when estimating contact resistances between the organic semiconductor and the source/drain electrodes. As mentioned in chapter 2.2.1.4, dipole layers formed at the interface can lead significant energy barriers, even if the metal work function matches to the HOMO level.[138]

4.3. Ambient and Shelf-life Stability

4.3.1. First Investigations

For the first series of bottom-gate/bottom-contact OFETs fabricated for ambient stability investigations at the Graz University of Technology all polymers including rr-P3HT (batch 1) were dissolved in spectrally clean chloroform (2-3 mg/ml) under *ambient conditions* without previously heating the polymer for dedoping. Figure 4.2 depicts the sample architecture and a typical realization including an optical micrograph of a single source/drain structure.

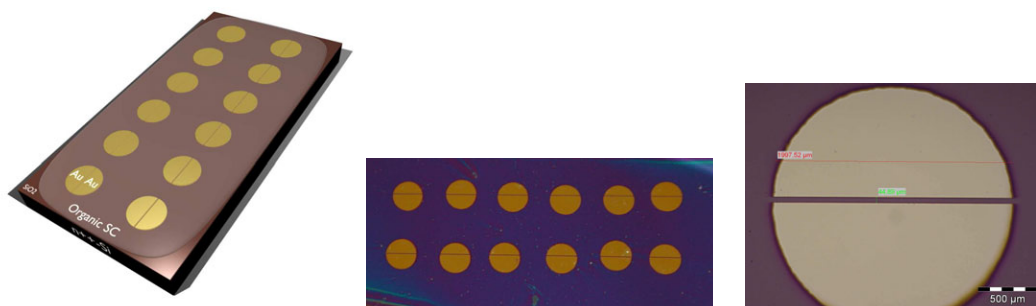

Figure 4.2: Left: sample architecture of first series of bottom-gate/bottom-contact OFETs for stability investigations; middle: typical realization; right: optical micrograph of a single source/drain structure.

4.3.1.1. Device Fabrication

Devices were fabricated on n^{++}-Si wafer pieces (dimensions: ~12.5 mm x 25 mm, 25 mm x 25 mm) with a thermally grown 247 nm thick SiO_2 layer ($C_i \approx 14$ nF/cm^2) provided by austriamicrosystems AG.[268] After removing the native oxide on the substrate backside with a diamond cutter to create contact to the n^{++}-Si acting as common bottom gate, ~80 nm thick gold source/drain electrodes ($L \approx$ 10-50 µm, $W \approx$ 2 mm) were thermally evaporated ($p < 3\text{x}10^{-6}$ mbar) through a shadow mask, which was equipped with tungsten wires of 13-50 µm diameter defining the channel lengths. The samples were baked at 110-120°C for ~1.5-3 h in vacuum to remove residual surface water and then cleaned with CO_2 and pure $CHCl_3$, followed by organic semiconductor deposition via spin-casting *under ambient conditions* (~1500 rpm, 40 s). After transfer into an argon glove box they were attached to a single-sided copper board with conductive silver paste and devices were isolated by scratching the semiconducting layer to reduce parasitic leakage currents. Electrical device characterization was performed with an Agilent E5262A parameter analyzer.

4.3.1.2. Device Characteristics

The OFETs were consecutively characterized under argon atmosphere, in air, after storage in air and darkness for 1-2 weeks and after storage in air and ambient light for ~1 week.[u]

Figure 4.3 contains plots with transfer curves at V_D = -25V of several PTPA-devices on each sample, measured in air and ambient light. All materials revealed field-effect behavior, but device-to-device variation for some samples was rather large. This was ascribed to channel-length variations, resulting from varying under-evaporation of the wires defining the channel.

[u] Measurements were performed at room temperature and ambient relative humidity levels between 30% and 60%.

The largest on-currents were obtained with the $PTPA_3$-based OFETs. $PTPA_4$-devices exhibited the lowest performance (in term of field-effect mobility). The rather high negative switch-on voltages of the OFETs around -30V are probably due to residual surface water and/or SiOH groups on the SiO_2 (semiconductors were spin-cast in air), influencing the film-forming properties of the semiconductor and acting as charge-carrier traps.

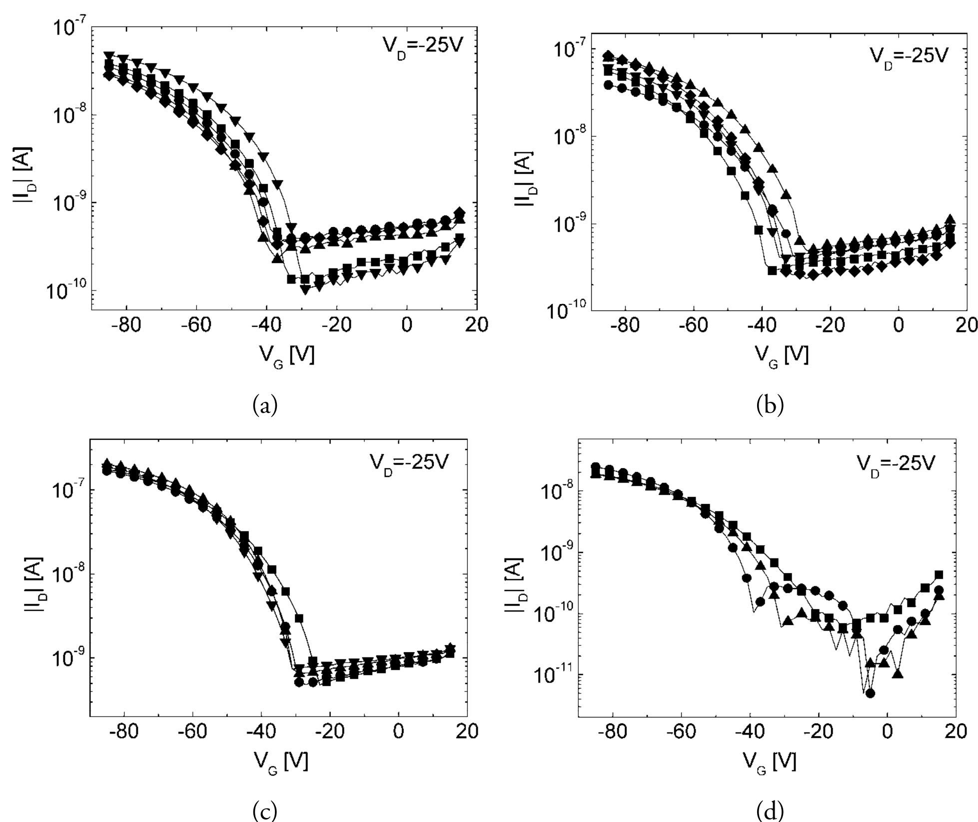

Figure 4.3: Semi-logarithmic transfer curves at V_D = -25V of several PTPA-based OFETs measured in air and ambient light: a) $PTPA_1$ ($L \approx$ 35-50 μm, $W \approx$ 2 mm); b) $PTPA_2$ ($L \approx$ 30-35 μm, $W \approx$ 2 mm); c) $PTPA_3$ ($L \approx$ 41-46 μm, $W \approx$ 2 mm, batch 1); d) $PTPA_4$ ($L \approx$ 15-22 μm, $W \approx$ 2 mm).

Figure 4.4 shows the electrical device characteristics of a single device on each sample before and after storage in air and darkness for 1-2 weeks. Except for the $PTPA_4$-based OFET, all other devices exhibited a small channel-current increase after storage. Still, they can be regarded as rather stable compared to OFETs based on rr-P3HT or pentacene (see below). Due to the low I_D values, in particular observed with $PTPA_1$ and $PTPA_4$, gate-leakage currents had a relatively larger influence, as can be seen by the crossing output curves around V_D = 0V and by the upward bending of the transfer curves at low V_D.

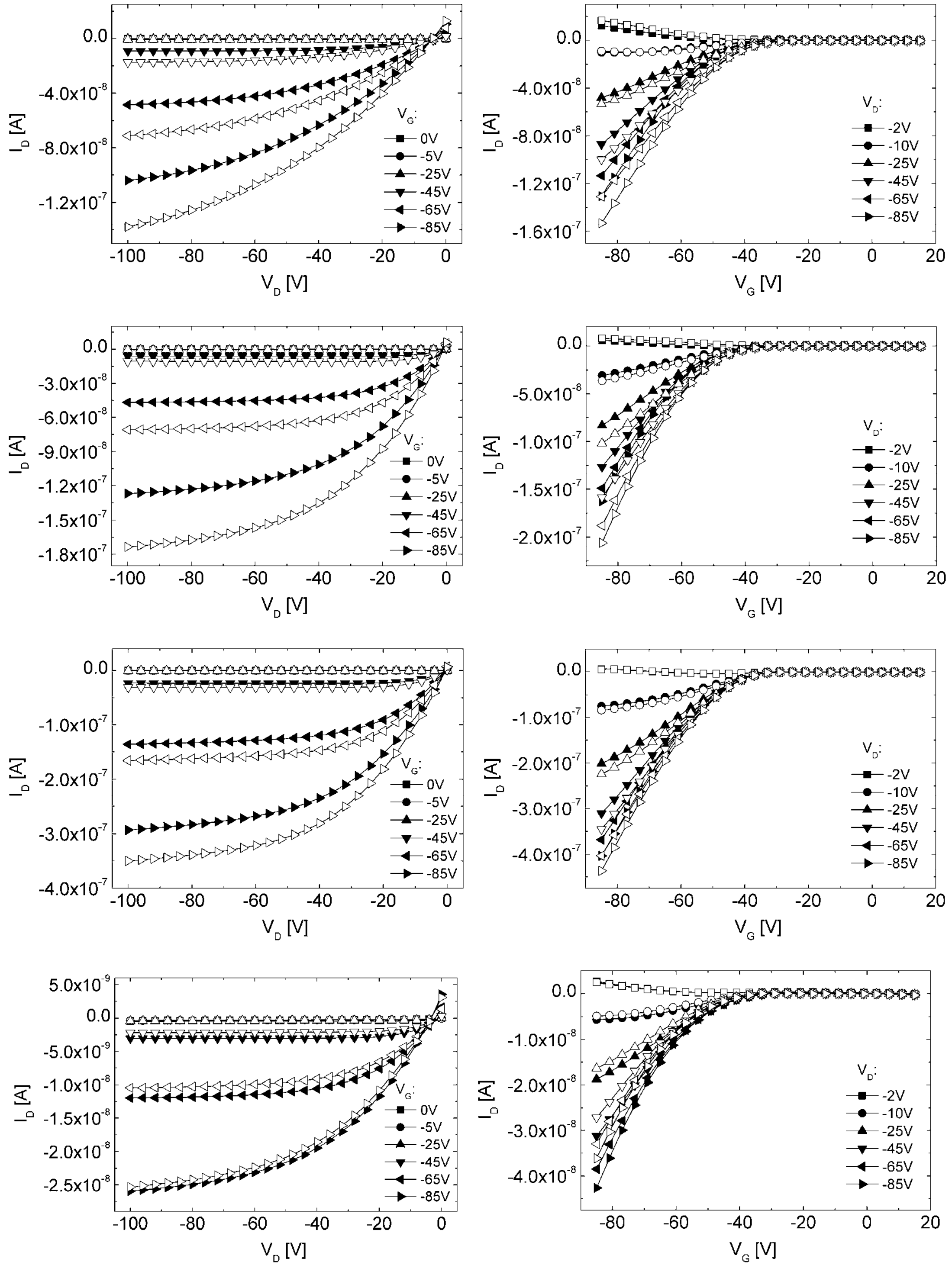

Figure 4.4: Output (left) and transfer (right) characteristics of a PTPA-based OFET on each sample measured in air and ambient light before (filled symbols) and after (open symbols) storage in air and darkness ($PTPA_1$: ~2 weeks, others: ~1 week); from top to bottom: $PTPA_1$ ($L \approx 43$ µm, $W \approx 2$ mm); $PTPA_2$ ($L \approx 35$ µm, $W \approx 2$ mm); $PTPA_3$ ($L \approx 46$ µm, $W \approx 2$ mm, batch 1); $PTPA_4$ ($L \approx 20$ µm, $W \approx 2$ mm).

Stable operation of PTPA-based OFETs after storage in air and darkness is also proven by the graphs shown in Figure 4.5. While $PTPA_3$- and $PTPA_4$-devices had similar transfer curves before and after storage, their $PTPA_1$- and $PTPA_2$-counterparts exhibited a small shift of the switch-on voltages and a small increase of on- and off-currents, which might be ascribed to the lower shielding of oxygen and moisture by the side group substituents of the latter. Also a less dense packing of the polymer chains might be involved. And the presumably slightly thicker film of $PTPA_1$ and $PTPA_2$, which were deposited from a 3 mg/ml chloroform solution ($PTPA_3$ and $PTPA_4$ from 2 mg/ml), might also have an influence on that behavior.

Taking into account performance in terms of both field-effect mobility and ambient stability, clearly $PTPA_3$ is the "winner" material, followed by $PTPA_2$. $PTPA_1$ and $PTPA_4$ share the 3rd place, with the former exhibiting larger field-effect mobility and the latter higher ambient stability. Table 7 below summarizes the corresponding device parameters.

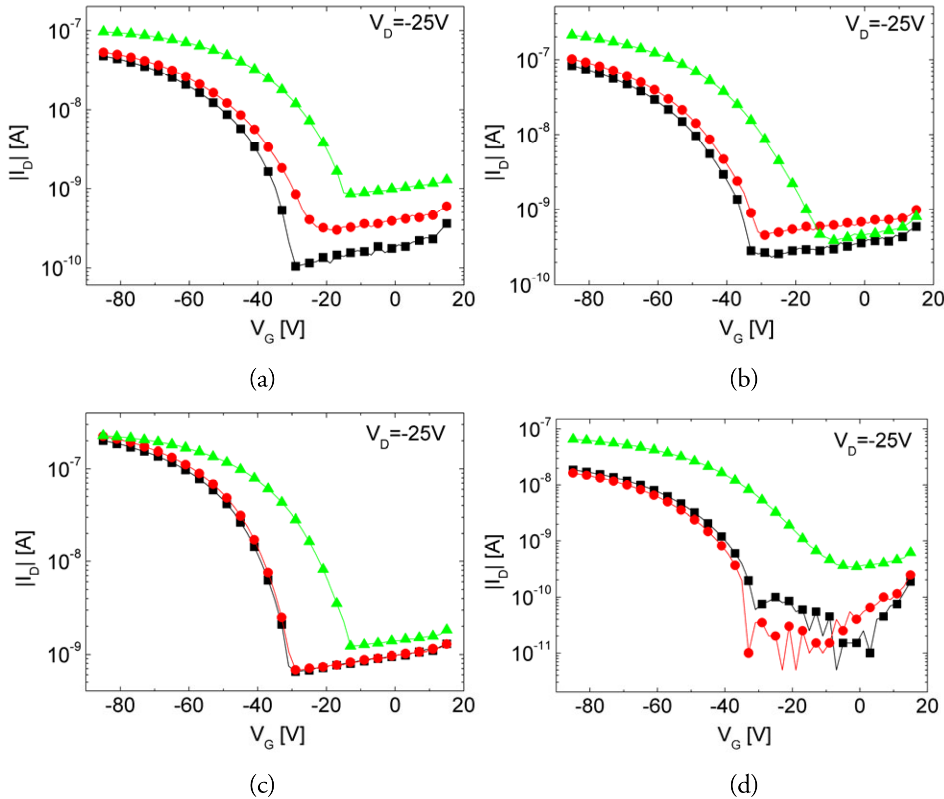

Figure 4.5: Semi-logarithmic transfer curves at V_D = -25V of a PTPA-based OFET on each sample measured in air and ambient light (black), after storage in air and darkness ($PTPA_1$: ~2 weeks, others: ~1 week, red) and after further storage in air and ambient light for ~1 week (green); a) $PTPA_1$ ($L \approx 43$ µm, $W \approx 2$ mm); b) $PTPA_2$ ($L \approx 35$ µm, $W \approx 2$ mm, batch 1); c) $PTPA_3$ ($L \approx 46$ µm, $W \approx 2$ mm, batch 1); d) $PTPA_4$ ($L \approx 20$ µm, $W \approx 2$ mm).

Interestingly, when devices were stored in air and ambient light for several days, they reveal a more distinct change of their electrical characteristics, including a shift of V_{SO} to more positive values and increased on- and off-currents. This is most probably due to the violet and UV portions of ambient light that create photo-excited states, in particular when considering the mentioned absorption maxima of the PTPAs centered at 370 nm-390 nm. In addition, it may well be the case that exposure to ambient light for a longer time induces the release of charge carriers trapped within the semiconductor or at the semiconductor/dielectric interface. Accordingly, after storage for several days or even weeks under *dark* inert conditions, the first transfer curves measured in air generally showed more negative switch-on voltages and reduced on- and off-currents compared to those measured in argon and ambient light before storage (see Table 7). Most likely mobile charge-carrier, which had been created by photo-induced de-trapping during measurements in argon and ambient light, relaxed or were trapped again during storage in argon and darkness. This behavior was also observed for investigated rr-P3HT-based OFETs.

Table 7: Relevant OFET parameters of typical devices based on PTPAs and rr-P3HT measured in air and ambient light; field-effect mobilities μ_{Lin} (at V_D = -10V, V_G = -60V) and μ_{Sat} (at V_D = -85V, V_G = -60V) extracted from transfer curves with equations (2.14) and (2.15), switch-on voltages V_{SO} determined from transfer curve at V_D = -25V; on/off-current ratio I_{on}/I_{off} (I_{on}: V_G = -85V, I_{off}: V_G = 0V) determined from transfer curve at V_D = -85V; values measured in argon and ambient light (1st value) and in air and ambient light (for PTPAs after several minutes in air = 2nd value, for rr-P3HT after 5 min = 2nd value and after 50 min = 3rd value) after storage in argon and darkness.

Organic Semiconductor	*L [μm]*	*W [μm]*	μ_{Lin} *[cm²/Vs]*	μ_{Sat} *[cm²/Vs]*	V_{SO} *[V]*	I_{on}/I_{off}
PTPA₁	43	1950	$4.1x10^{-5}$ $4.7x10^{-5}$	$1.6x10^{-4}$ $1.8x10^{-4}$	-29 -29	$1x10^{3}$ $1x10^{4}$
PTPA₂	35	1950	$8.4x10^{-5}$ $9.2x10^{-5}$	$2.1x10^{-4}$ $1.9x10^{-4}$	-25 -33	$8x10^{2}$ $3x10^{3}$
PTPA₃	46	2000	$2.4x10^{-4}$ $2.7x10^{-4}$	$4.8x10^{-4}$ $5.0x10^{-4}$	-13 -31	$5x10^{2}$ $1x10^{3}$
PTPA₄	20	1860	$7.0x10^{-6}$ $1.1x10^{-5}$	$2.5x10^{-5}$ $2.5x10^{-5}$	-25 -31	$2x10^{2}$ $2x10^{3}$
rr-P3HT	40	2000	$1.3x10^{-4}$ $7.4x10^{-6}$ $2.0x10^{-5}$	$1.9x10^{-4}$ $6.6x10^{-5}$ $3.1x10^{-5}$	-31 -23 +11	$7x10^{2}$ $3x10^{2}$ $2x10^{1}$

With these results the best performing material, $PTPA_3$, was investigated in more detail in OFETs and compared with the stability properties of rr-P3HT-based devices, also including electrical characterization after storage in air and darkness for ~4 months.[v] The applied semiconductors were still from batch 1.

Figure 4.6 depicts a transfer curve of a $PTPA_3$- and a rr-P3HT-based OFET at V_D = -85 V and its transformation during device exposure to air and ambient light for 50 min.

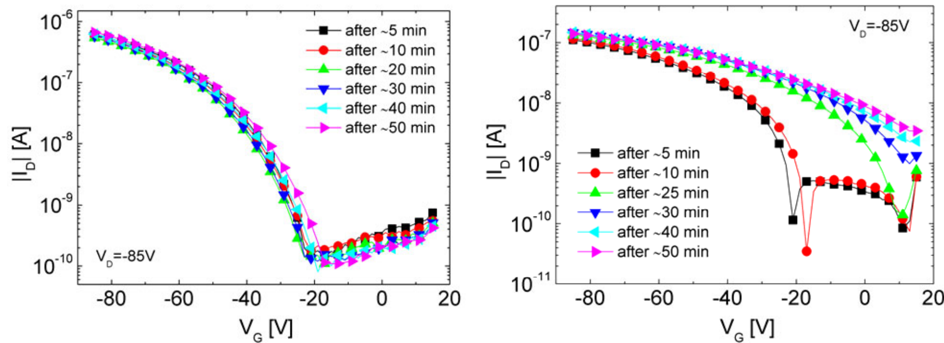

Figure 4.6: Time evolution of a transfer curve at V_D = -85V of a $PTPA_3$-based (left, $L \approx 11$ µm, $W \approx 2$ mm) and a rr-P3HT-based (right, $L \approx 40$ µm, $W \approx 2$ mm) OFET measured in air and ambient light.

While the rr-P3HT-OFET showed a rather strong increase of the off-current (I_D at V_G = 0V) from ~350 pA to ~9 nA and a strong positive shift of the switch-on voltage from -21V to +13 V, ascribed to oxygen- and/or moisture-induced doping (see chapter 2.2.3.1), the corresponding values of the $PTPA_3$-device remained rather constant ($I_{off} \approx$ 200-300 pA, $V_{SO} \approx$ -20 V). Accordingly, the on/off-current ratio of the latter didn't change much (2-3x10^3), while I_{on}/I_{off} of the rr-P3HT-OFET reduced from ~300 to ~20 within the first 50 min in air and ambient light. The saturation field-effect mobility of the presented devices at V_D = -85 V and V_G = -60 V, derived from eqn. (2.15), also remained constant for $PTPA_3$ at ~2x10^{-4} cm^2/Vs, while it was reduced from 6.6 x 10^{-5} cm^2/Vs to 3.1 x 10^{-5} cm^2/Vs with the rr-P3HT-device. Moreover, the amount of hysteresis became much larger with the latter (Figure 4.7), which resembles the increased charge-trapping due to oxygen and moisture. The large hysteresis of the $PTPA_3$-OFET is ascribed to its short channel length (see also chapter 3.1.4.3), but it remains constant during air exposure.

[v] The samples were also exposed to a white LED light, which, however, had no significant effect on the PTPAs, because its emission spectrum was not in the range of the corresponding absorption maxima of the materials. Therefore the results are not shown.

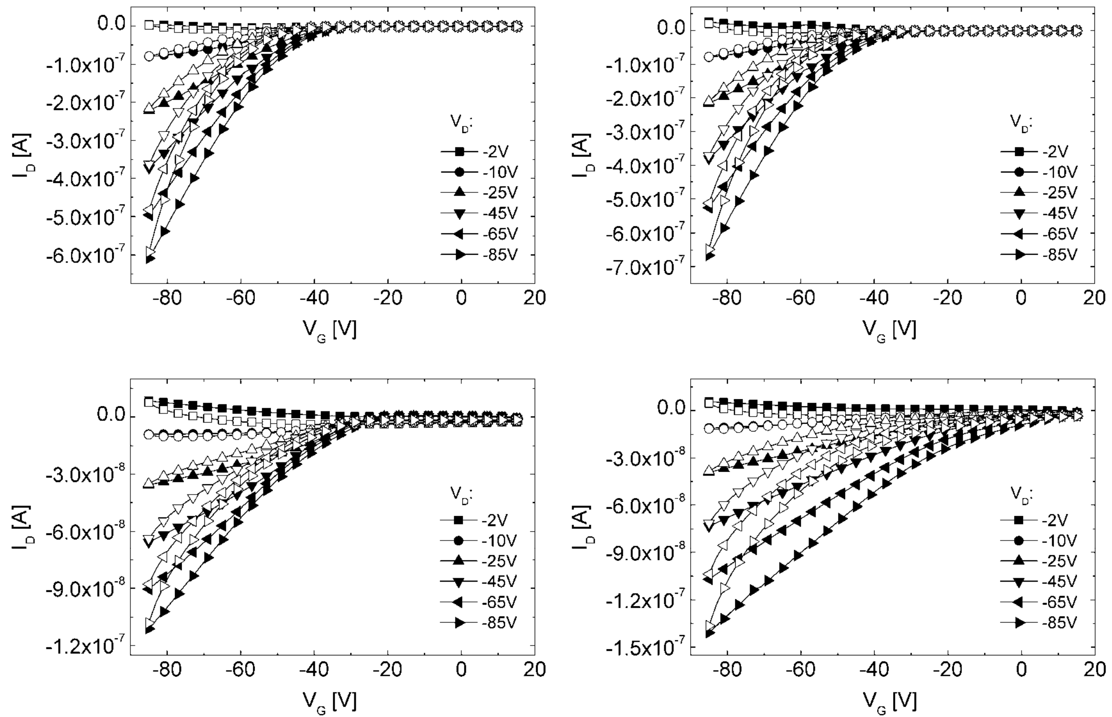

Figure 4.7: Transfer characteristics of an OFET based on $PTPA_3$ (top, $L \approx 11$ µm, $W \approx 2$ mm) and rr-P3HT (bottom, $L \approx 40$ µm, $W \approx 2$ mm) measured in air and ambient light after 5 min (left) and after 50 min (right); filled symbols: forward sweep, open symbols: reverse sweep.

The graphs in Figure 4.8 correspond to those in Figure 4.5 and compare the shelf-life stability of a $PTPA_3$- and a rr-P3HT-OFET, proving the rather stable properties of the nitrogen-containing aromatic polymer even after storage in air and darkness for ~4 months, although this device seems to have "remembered" its storage in air and ambient light. In Figure 4.8 right also the first transfer curve measured in air after 5 min is included (black, open symbols) to emphasize the degradation of rr-P3HT upon air exposure. The corresponding reduction of on- and off-currents and the negative shift of V_{SO} after storage in air and darkness is ascribed to the mentioned relaxation or trapping of photo-induced mobile charge carriers created in the measurement before.

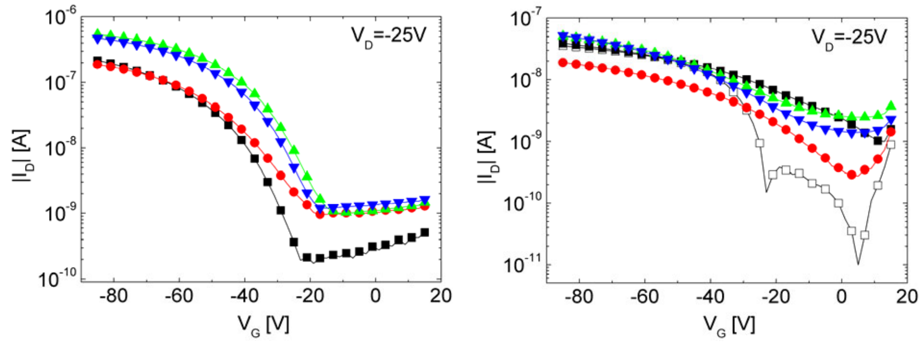

Figure 4.8: Semi-logarithmic transfer curves at V_D = -25V of a $PTPA_3$-based (left, $L \approx 11$ µm, $W \approx 2$ mm) and a rr-P3HT-based OFET (right, $L \approx 40$ µm, $W \approx 2$ mm) measured in air and ambient light (black, open symbols: after ~5 min, filled symbols: after ~50 min), after storage in air and darkness for ~1 week (red), after further storage in air and ambient light for ~1 week (green) and after further storage in air and darkness for ~4 months (blue).[v]

The plots in Figure 4.9 underline the results above, showing the development of the OFET parameters under various conditions and also providing a good performance comparison of the investigated materials, with the main message that PTPA-derivatives are rather stable, except when stored in argon and ambient light, and rr-P3HT clearly degrades upon air exposure, exhibiting a reduced on/off-current ratio and field-effect mobility and a more positive switch-on voltage due to oxygen- and/or moisture-induced doping. The distinct increase of I_{on}/I_{off} (in particular for $PTPA_1$) and the more negative V_{SO} (in particular for $PTPA_3$) of the PTPA-devices after storage in argon and darkness for several weeks is ascribed to the mentioned relaxation of photo-excited charge-carriers created during the measurement in argon and ambient light.

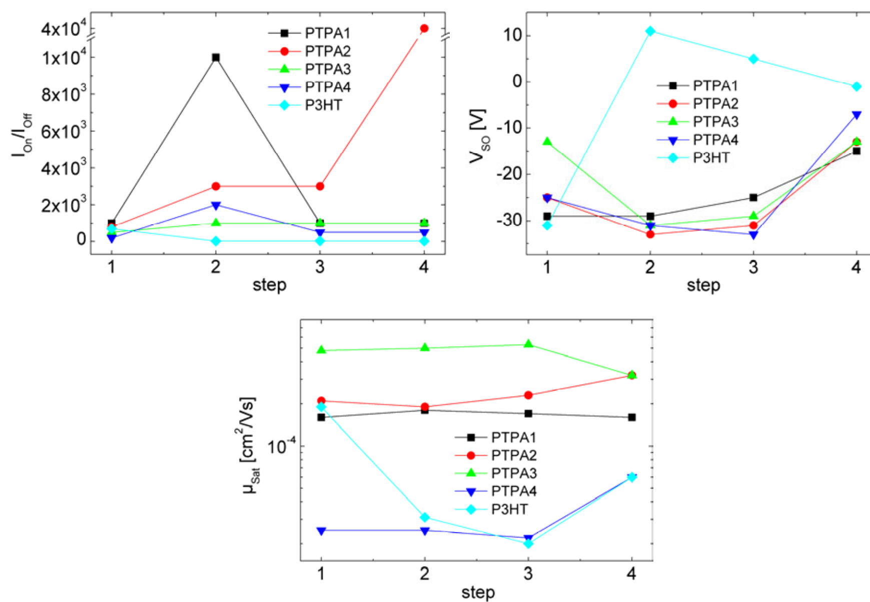

Figure 4.9: Development of device parameters of various OFETs based on PTPAs and rr-P3HT; step 1: argon and ambient light; step 2: air and ambient light after several minutes in air; step 3: after storage in air and darkness for 1-2 weeks; step 4: after storage in air and ambient light for ~1 week; rr-P3HT-OFET had two more steps (exposure to white LED) between 1-2 and 2-3.

The presented results are in good agreement with those of other groups that have performed similar investigations.[282]

4.3.2. Influence of Oxygen, Moisture and Surface Modification with HMDS

After the implementation of the new fabrication line at NTC Weiz also a new stability measurement plant was integrated in the grey room and thus the tested organic semiconductor materials were employed in the newly established OFET structures and their stability properties were investigated even more in detail, differentiating between the influences of oxygen and humidity. Moreover, the implications of substrate pre-treatment with HMDS on the ambient stability of devices were analyzed. The main results will be summarized in the following sections.

4.3.2.1. Stability Measurement Plant and Probe Chamber

Figure 4.10 depicts a scheme of the stability measurement plant, which was installed for testing organic field-effect transistors and other devices under various environmental conditions, including air, oxygen and humidity.[297] Humidity is generated by bubbling gaseous N_2 through hot deionized water. Before exposing the device under test (DUT) in the probe chamber to moisture, the relative humidity values are first set in a reference jar. Ambient air is sucked through the chamber by a membrane vacuum pump and devices can be reset to their pristine state by evacuation with a high vacuum pumping station, consisting of a rotary vane pump and a turbomolecular pump.

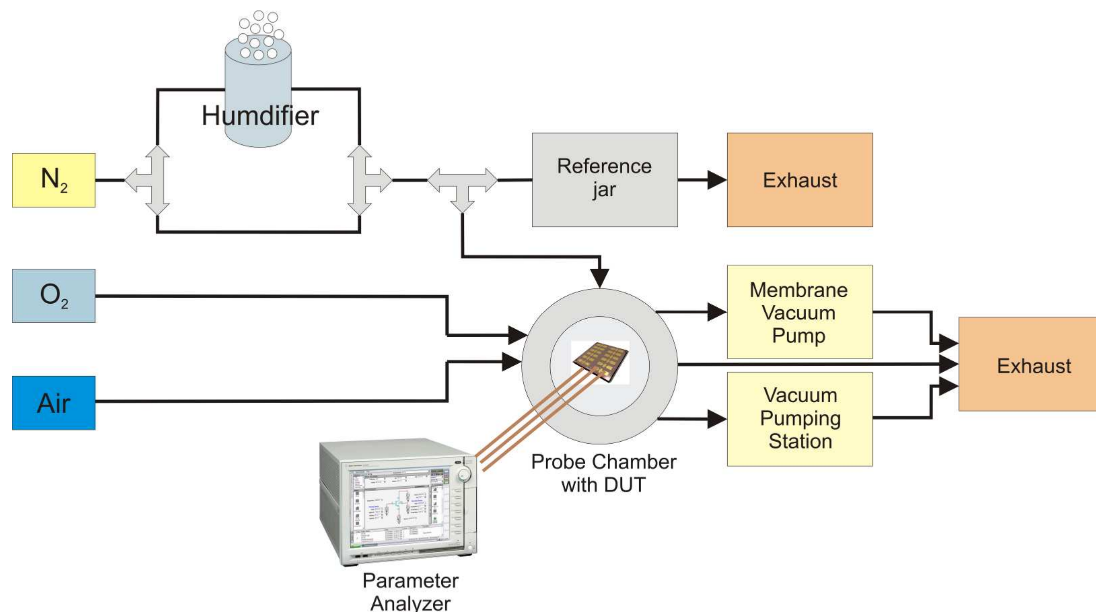

Figure 4.10: Scheme of new stability measurement plant implemented in the grey room at NTC Weiz.

Figure 4.11 depicts the corresponding probe chamber[297] made from stainless steel. For device testing under ambient light a quartz glass was integrated, which can be covered for measurements in the darkness. Gas in- and outlets consist of ¼″ tubes and two stainless steel Parker 3-way ball valves. Tightness with respect to air was verified with compressed air and evacuation. The dimensions were chosen to ensure that the chamber could be transferred into argon glove boxes via the corresponding locks with a diameter of ~15 cm. With this limitation, samples with dimensions of ~1″ x 1″ can be assembled in the chamber. For electrically connecting devices, feed-through connectors were integrated, each consisting of twelve contacts, and fixed with an epoxy resin to ensure air-tightness. The corresponding probe head was made from PMMA and consists of 30 pogo pins for device contacting. OFETs are connected to the parameter analyzer and individually switched via an appropriate switch box with BNC-connectors. For temperature and humidity measurements, a Peltier element, a Pt-100 sensor and a Sensirion SHT15 sensor[303] was implemented with corresponding plugs in the switch box.

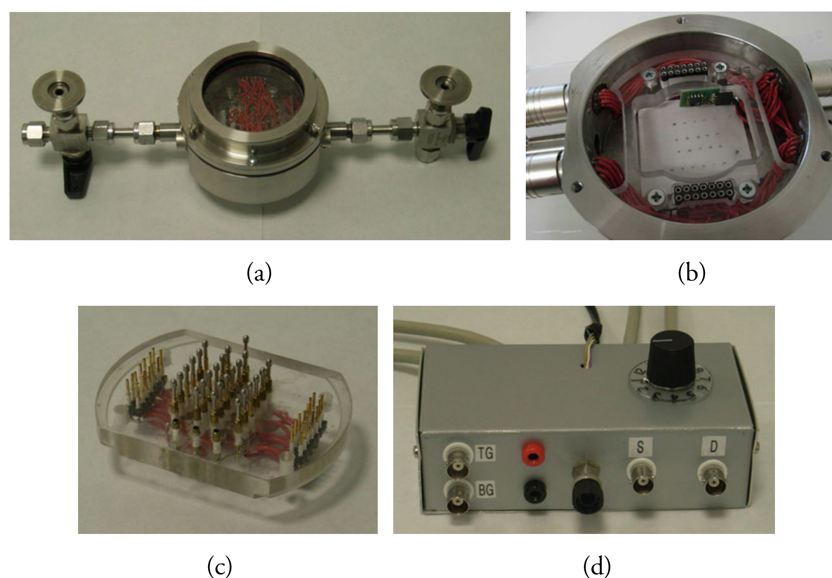

(a) (b)

(c) (d)

Figure 4.11: a) Sealable probe chamber for electrical characterization of OFETs under various environmental conditions; b) interior with Peltier element and humidity and temperature sensors; c) probe head with pogo pins for device contacting; d) switch box for connecting the devices to be tested with a parameter analyzer.

4.3.2.2. Device Fabrication

This setup was applied for the characterization of PTPA-, rr-P3HT (both from batch 2 in Table 6) and pentacene-based devices under various conditions. In contrast to the first series described in chapter 4.3.1, the semiconductor solutions ($CHCl_3$, 2 mg/ml) for this series were prepared *under inert conditions*, including a dedoping bake both of the raw material and the later deposited semiconductor film for 1-2 h at 100-120°C in high vacuum.

Evaporation of pentacene and device fabrication in other respects was performed as described in chapter 3.1.3, using the OFET geometry with variable channel lengths (Figure 3.3 left). For investigating the influence of surface modification on stability, both untreated and HMDS-treated substrates were applied. Electrical characterization was performed with an Agilent B1500A parameter analyzer in argon, vacuum (the latter as reference), under air flow (room temperature, relative humidity ~35%), in oxygen atmosphere and upon exposure to dry and humidified N_2 at various relative humidity levels. In between the samples were more or less reset to their pristine states by evacuation for several hours.

4.3.2.3. $PTPA_3$-based OFETs

Figure 4.12 compares the transfer characteristics of a $PTPA_3$-based OFET ($L \approx 25$ µm, $W \approx 2.85$ mm) fabricated on untreated SiO_2 and on HMDS-treated SiO_2 measured in vacuum.

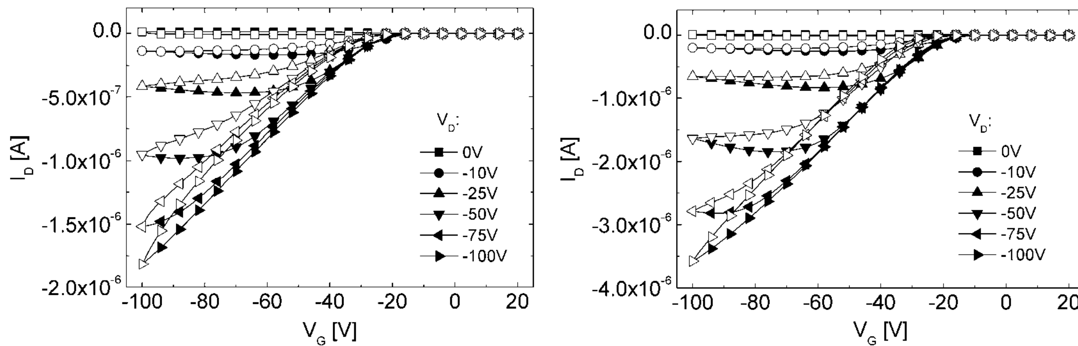

Figure 4.12: Transfer characteristics of a $PTPA_3$-based OFET ($L \approx 25$ µm, $W \approx 2.85$ mm) fabricated on untreated SiO_2 (left) and on HMDS-treated SiO_2 (right) measured in vacuum; filled symbols: sweeps from positive to negative voltages; open symbols: reverse sweep.

As with the rr-P3HT and pentacene-based devices presented in chapter 3.1.4.3, pre-treating the SiO_2-surface with HMDS doubled the saturation field-effect mobility from 3.7×10^{-4} cm^2/Vs to 7.2×10^{-4} cm^2/Vs (at V_D = -75V, V_G = -40V) and the on/off-current ratio from 1.7×10^3 to 3.3×10^3 (at V_D = -75V; I_{on}: V_G = -100V, I_{off}: V_G = 0V). Moreover, the switch-on voltage was reduced from -14V to -8V (at V_D = -75V) due to covering of interfacial traps by HMDS and the subthreshold slope was slightly increased from 4.8 V/dec to 5.74 V/dec.

The plots in Figure 4.13 include transfer curves of the two devices recorded in various environments. As expected, when exposed to air, both devices with and without HMDS pre-treatment were rather stable during the first 80-90 min, exhibiting only a slight increase of hysteresis in combination with a small reduction of the on-current, which confirmed the results of the first stability investigations. Oxygen seemed to have no large influence on both OFETs, either.

More interesting is the behavior of the devices when exposed to humidified N_2. Generally, both OFETs exhibited a shift of the switch-on voltage to more negative values, an increase of the amount of hysteresis and a reduction of the on-current with increasing relative humidity levels. However, these changes were much more significant with the $PTPA_3$-OFET fabricated on the untreated sample. They most likely are ascribed to moisture-induced charge-carrier traps formed within the semiconducting layer or at semiconductor/dielectric interface and as the HMDS-treated substrate was much more hydrophobic than the untreated one, the influence of moisture was reduced and corresponding devices were more stable.

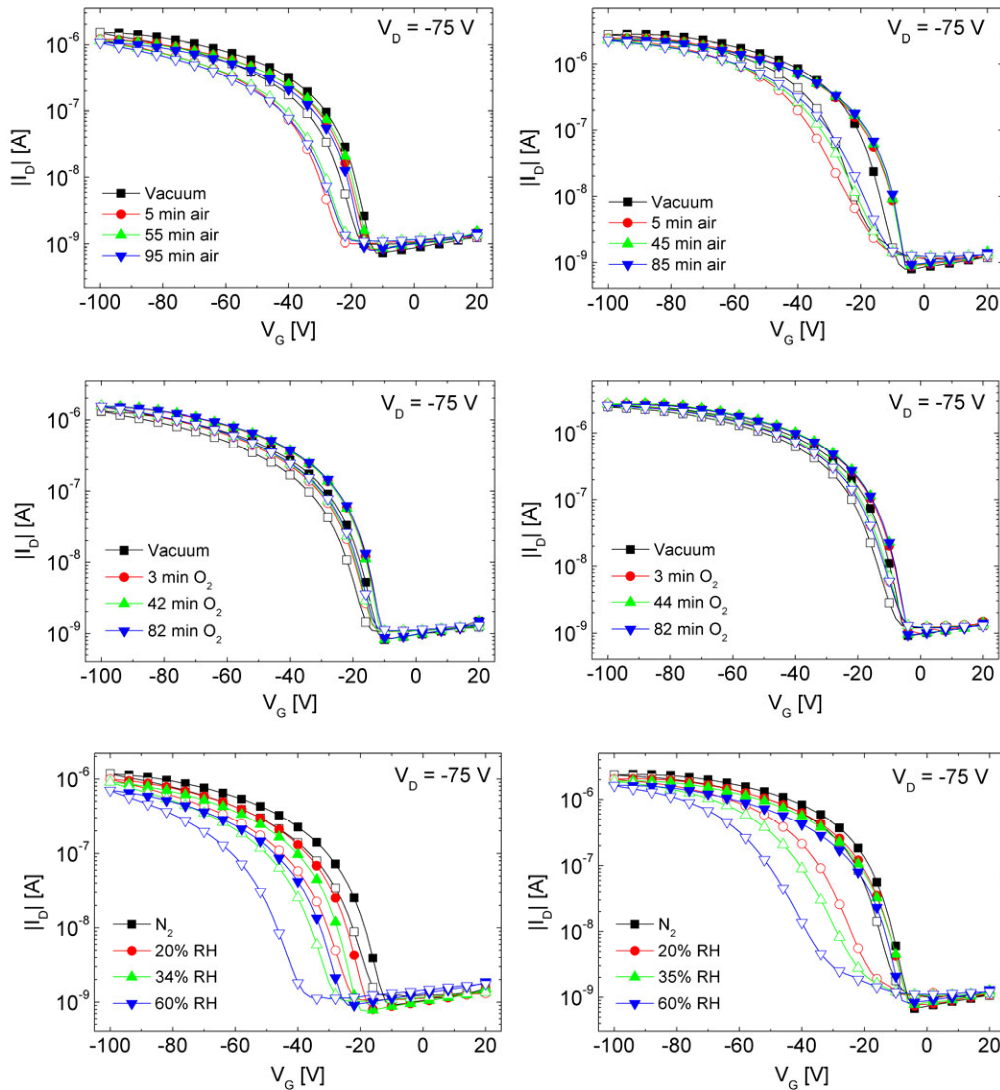

Figure 4.13: Semi-logarithmic transfer curves at V_D = -75V of a $PTPA_3$-based OFET ($L \approx 25$ µm, $W \approx 2.85$ mm) fabricated on untreated SiO_2 (left) and on HMDS-treated SiO_2 (right) measured under various conditions in ambient light; filled symbols: sweeps from positive to negative voltages; open symbols: reverse sweep.

HMDS-treatment of devices based on $PTPA_1$ had similar effects, but in accordance with the results above, corresponding OFETs showed lower mobility and stability. Long-term stability measurements of the new devices also confirmed the findings of the first OFET series.[297]

4.3.2.4. rr-P3HT based OFETs

The effect of HMDS-treatment on device stability was even more pronounced with OFETs containing rr-P3HT as organic semiconductor, as can be seen in Figure 4.14, where again the transfer curves of an untreated device and a HMDS-modified OFET are shown. As expected, these devices were unstable in air, no matter if HMDS-pretreatment was applied or not.

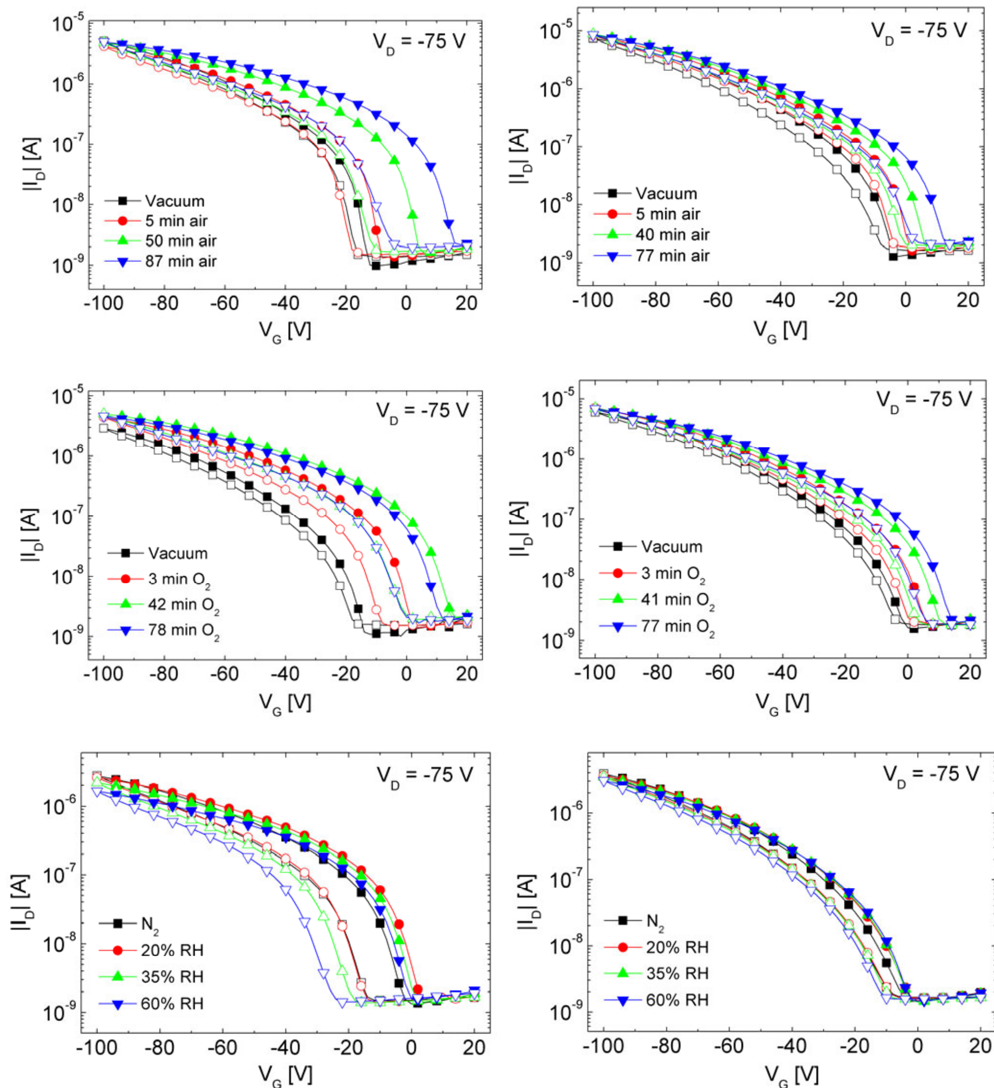

Figure 4.14: Semi-logarithmic transfer curves at V_D = -75V of a rr-P3HT-based OFET ($L \approx$ 25 µm, $W \approx$ 2.85 mm) fabricated on untreated SiO_2 (left) and on HMDS-treated SiO_2 (right) measured under various conditions in ambient light; filled symbols: sweeps from positive to negative voltages; open symbols: reverse sweep.

However, oxygen seems to be the major factor determining stability (at least under ambient light), as the changes observed in air such as positive switch-on voltage shifts and increase of on- and off-currents were found in a similar manner upon oxygen exposure and not so much under humidified N_2, in accordance with results of other groups.[168,172] Nevertheless, the HMDS-treated device was generally more stable than the untreated one (at least found in the short-term stability investigations), which may be ascribed to a more compact packing of the polymer chains and a more hydrophobic surface, both aggravating the penetration of oxygen and moisture into the semiconductor or to the semiconductor/dielectric interface. These results were corresponding to those found by Majewski and co-workers.[135] In particular they correlate higher stability with lower RMS surface roughness and their more stable devices exhibited similar RMS surface roughness values as ours on the order of ~0.5 nm (Figure 3.20).

4.3.2.5. Pentacene-based OFETs

Finally, the new OFET fabrication line was also applied in combination with the implemented stability measurement plant to investigate the ambient stability of pentacene-based devices on untreated and HMDS-treated n^{++}-Si/SiO_2 substrates. Generally, as shown in Figure 4.15, devices exhibited a behavior expected already from literature results.[45,304,305,306,307,308,309] The decrease of on-current and increase of hysteresis upon air exposure can be ascribed to moisture-induced formation of charge-carriers traps mainly in the region of the grain boundaries and near the semiconductor/dielectric interface,[45,,304,306] effects, which were also proposed to be used for humidity sensing. The shift of the switch-on voltage to more positive values, associated with an increase of the off-current, is ascribed to photo-induced oxygen-doping (formation of acceptor-like states)[304,307,308] and possibly also water-induced doping.[305]

Exposure to air of the untreated sample led to a more pronounced decrease of the on-current and a lower positive shift of the switch-on voltage (and thus a smaller increase of the off-current) than observed for the corresponding rr-P3HT-based OFET. Accordingly, while rr-P3HT seems to be more sensitive to oxygen, pentacene is more sensitive to humidity, which is also confirmed when looking at the behavior upon exposure to O_2 and moisture. Again, the SAM-treated pentacene-OFET was more stable than the untreated[309] and even showed no significant degradation when exposed to oxygen, which can be ascribed to a more dense packing of the small molecules in combination with the water-repelling surface properties. Moreover, Wang and co-workers have shown that ambient gases also have an influence on the contact resistance of a device,[310] which, considering our results, might be reduced by surface modification with HMDS.

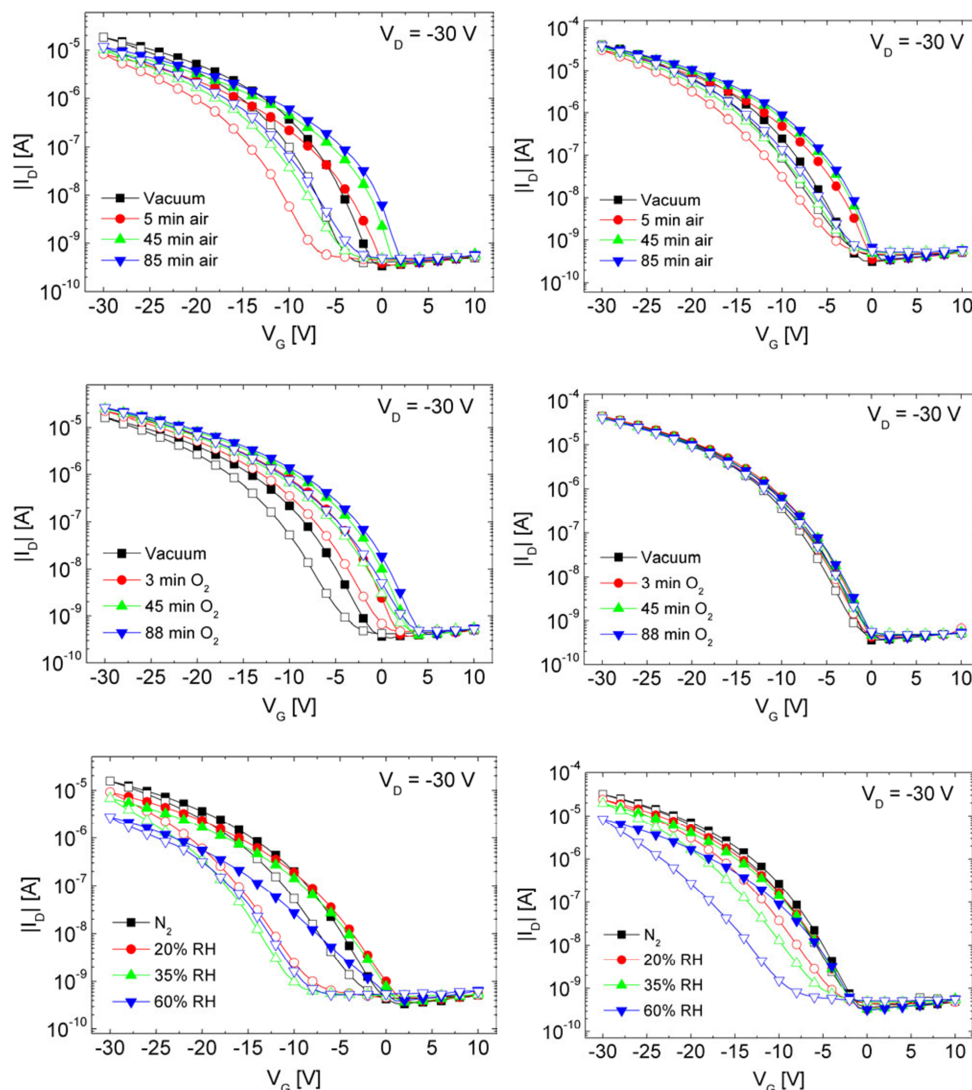

Figure 4.15: Semi-logarithmic transfer curves at V_D = -75V of a pentacene-based OFET ($L \approx 25$ µm, $W \approx 2.85$ mm) fabricated on untreated SiO_2 (left) and on HMDS-treated SiO_2 (right) measured under various conditions in ambient light; filled symbols: sweeps from positive to negative voltages; open symbols: reverse sweep.

Although AFM investigations revealed no large difference in the morphology of both untreated and HMDS-treated samples (Figure 3.28, Figure 3.29, at least in the final film structure), the results described in this section and in chapter 3.1.4.3 prove that surface modification with HMDS does not only improve device performance by covering the amount of interfacial traps on SiO_2, but also increases ambient stability of a device. Nevertheless, neither rr-P3HT- nor pentacene-based OFETs were as stable under ambient conditions as $PTPA_3$.

4.4. Operational Stability

As pointed out in chapter 2.2.1.3, aside from the semiconductor another important layer material determining device performance and device stability of an OFET is the gate dielectric.
The following section illustrates operational device instabilities caused by the movement of mobile impurities in a rr-P3HT-based top-gate OFET with polyvinyl alcohol (PVA) as gate dielectric.

4.4.1. Polyvinyl Alcohol (PVA)

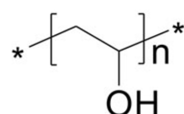

Figure 4.16: Chemical structure of polyvinyl alcohol (PVA)

Figure 4.16 depicts the chemical structure of PVA. The polymer is synthesized by saponification (hydrolysis), where basically poly(vinyl acetate) dissolved in methanol is converted into PVA with sodium hydroxide (NaOH) as catalyst. The content of residual vinyl acetate after saponification, which is influenced by the catalyst concentration, reaction temperature and reaction time, defines the grade of hydrolysis.[311] PVA has several properties, which makes it interesting as gate dielectric in OFETs. It is soluble in water and highly resistant against organic solvents, hence being compatible with many well-established polymeric organic semiconductors that can only be dissolved in organic solvents. It forms smooth homogenous films that are impermeable to gases such as oxygen, nitrogen and carbon dioxide. Moreover, it can be polymerized to exhibit low viscosity, which enables deposition via spin-coating or inkjet printing at considerable solid content.[140] Furthermore, it exhibits a rather large dielectric constant between 6 and 10,[111,112,113] leading to reduced operating voltages. However, PVA films also absorb moisture, which causes swelling and affects the film properties. Basically, the water resistance can be increased by heat-treatment, cross-linking (e.g. with glyoxal[312]) or by UV irradiation.
Another disadvantage of PVA is its content of mobile ions, which, if not removed, lead to hysteresis and operational drift. These ions were identified by us[123,124] and others[129] to originate mainly from sodium acetate, a by-product of saponification. By dialysis, which is mainly based on the diffusion of low-molecular weight solutes across a semi-permeable membrane due to a concentration gradient, the salt content can be largely reduced.

4.4.1.1. Solution Preparation and Dialysis

PVA with the brand name Mowiol (5-88)[w] from Clariant[313] was chosen for its high solubility, low viscosity and low surface tension of water solutions. The PVA granules were dissolved in bi-distilled or de-ionized water to a concentration of 15-20 wt%, while being stirred and heated up to 90°C. Purification was performed by dialyzing the solution for several times in bi-distilled or deionized water using an 18 mm dialysis tube (Part No. 132720) from Spectra/Por[314] with a molecular weight cut-off of 3500 dalton. Dialysis reduced the solid content to 8-9 wt%, which for some devices was later increased up to 12 wt% by slow evaporation of water.

4.4.2. Device Fabrication

Figure 4.17 schematically illustrates the sample architecture, together with a picture of a typical realization on an n^{++}-Si/SiO_2 substrate (oxide thickness: 247 nm, dimensions: ~12.5 mm x ~25 mm). Such devices are actually dual-gate OFETs. Either the top-gate electrode (aluminum) can be used in combination with PVA as gate dielectric (top-gate mode) or n^{++}-Si is biased in combination with SiO_2 as gate dielectric (bottom-gate mode).

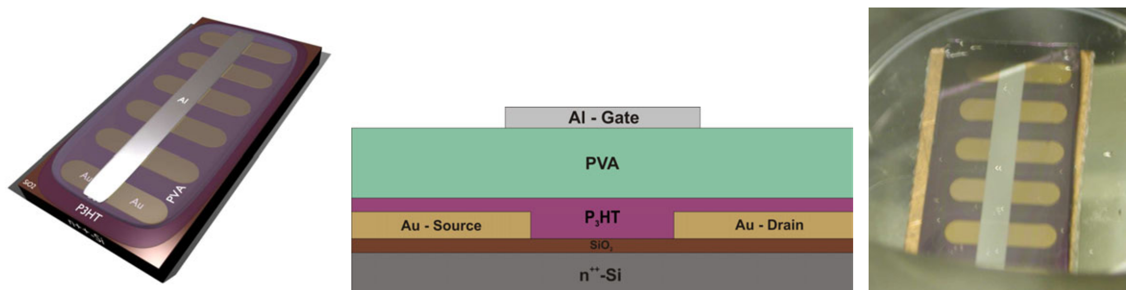

Figure 4.17: Sample architecture, cross-section of a device and typical realization.

After scratching the substrate backside with a diamond cutter and cleaning with CO_2, ~80 nm thick gold source/drain electrodes were thermally evaporated (p < 5x10^{-6} mbar) through a shadow mask equipped with tungsten wires defining the channel lengths.

After heating the sample in high vacuum at 110°C for 1 h to remove residual surface water and cleaning with pure $CHCl_3$, rr-P3HT (batch 1 in Table 6) was spin-cast (~1500 rpm, 40 s) in argon from a $CHCl_3$ solution (2 mg/ml) and then dried (50°C, 5 min). Devices were separated to reduce parasitic leakage currents and the semiconductor film was dedoped in high vacuum for several hours.

---

[w] According to datasheet: molar mass M_w: 37000 g/mol; degree of hydrolysis: 87.7 mol%; residual acetyl content: 10.8 wt%; maximum ash content (Na_2O): 0.5%.

PVA was spin-cast (~900 rpm, 60 s) from a dialyzed hydrogel (12 wt%, $d_i \approx 1$ μm) in air and dried in argon at ~110°C for 1 h and afterwards in high vacuum at ~60°C overnight. Finally, a ~150 nm thick aluminum top-gate electrode, thermally evaporated ($p < 5x10^{-6}$ mbar) through a shadow mask, completed the OFETs. Electrical characterization was performed with an Agilent E5262A parameter analyzer in argon.

4.4.3. Device Characteristics

Figure 4.18 depicts the electrical characteristics of a device operated in top-gate and bottom-gate mode, respectively. Both modes yield about the same maximum channel currents in the output graphs, which, however, is not the case in the transfer characteristics, already indicating the presence of mobile ions within the dielectric. Generally, when bias-induced charge-carrier trapping is the predominant effect in an OFET, for the measurement routines applied within this thesis the transfer characteristics usually exhibit larger I_D values (at the same working point), because a high negative gate voltage is longer applied in the output characteristics. In Figure 4.18 this is observable for bottom-gate operation mode and corresponds to the direction of the hysteresis in the transfer characteristics, exhibiting lower currents in the reverse sweep.

However, when mobile ions are present, they move to the different interfaces depending on the applied voltage difference between drain and gate. During the recording of the first output curves V_D is generally more negative than V_G for a longer time so that positive ions move to the drain electrode. Only in the last two output curves (V_G = -65V and V_G = -85V) V_G becomes more negative than V_D for a longer time, but the short timescale of the drain-voltage sweep and the finite mobility of the ions “confine” them near the drain electrode. The opposite holds for the transfer curves, where positive ions are more pushed away from the drain electrode during their recordings. As a consequence, interactions between mobile ions and rr-P3HT are more pronounced in the output characteristics, leading to larger channel currents at the same working point. Moreover, the hysteresis in top-gate mode, exhibiting higher channel currents in the reverse sweep, also indicates the presence of mobile ions.

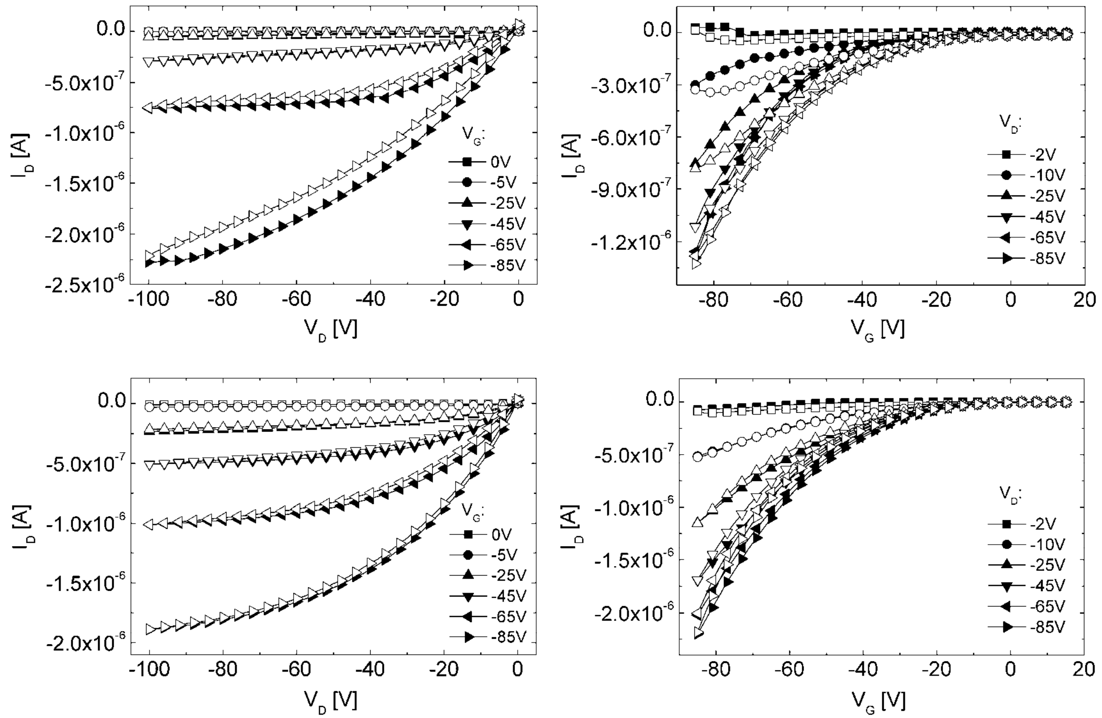

Figure 4.18: Output (left) and transfer (right) characteristics of a rr-P3HT-based OFET ($L \approx 43$ µm, $W \approx 2$ mm) with dialyzed PVA as gate dielectric, operated in top-gate mode (top) and bottom-gate mode (bottom); filled symbols: sweeps from positive to negative voltages; open symbols: reverse sweep; measured in argon.

To investigate this behavior in more detail, bias stress measurements were performed, where the channel current at fixed gate and drain voltage was monitored as a function of time after various bias-stress conditions, similar as in chapter 3.2.3. Figure 4.19 depicts the corresponding graphs, recorded in top- and bottom-gate operation mode.

In bottom-gate operation (n^{++}-Si as common gate and SiO_2 as gate dielectric) I_D (at fixed V_G and V_D) clearly decreased with time, indicating the expected charge-trapping behavior. Due to gate-bias stress mobile carriers are trapped by chemical and/or structural impurities within the semiconductor bulk, at the rr-P3HT/SiO_2-interface and/or within SiO_2 (see chapter 2.2.3.2).

In top-gate operation mode the situation is different. In accordance with the direction of the hysteresis in the transfer characteristics, the channel current (at fixed V_D and V_G) was increasing with time. Moreover, it exhibits larger currents after negative gate-bias stress, which are decreasing with time, and smaller currents after positive gate-bias stress, which are more rapidly increasing with time.

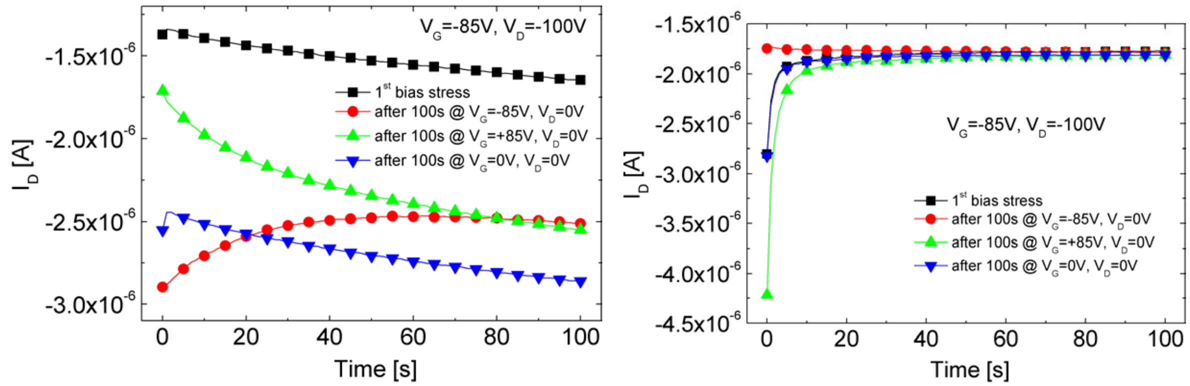

Figure 4.19: Source-to-drain channel current I_D at V_G = -85V and V_D = -100V as a function of time of a rr-P3HT-based OFET ($L \approx 43$ µm, $W \approx 2$ mm) with dialyzed PVA as gate dielectric after various bias-stress conditions measured in argon in top-gate operation (left) and in bottom-gate operation (right).

Figure 4.20 gives a possible explanation, assuming positive mobile ions and negative (less mobile) counter-ions, which is reasonable, as we and others identified mobile Na^+ ions to be the main cause for hysteresis.[123,124,129] Upon stressing the device at V_G = -85V and V_D = -100V the Na^+ ions within PVA are assumed to move to the drain electrode, where they most likely reduce the contact resistance by electrochemical contact doping and influence the pinch-off region. Rep and co-workers also ascribed device instabilities of P3HT-based OFETs on glass substrates to the electric field redistribution of Na^+ ions during operation, causing changes of the bulk and contact resistances.[315] The ions were identified to originate from the glass substrate. Edman and co-workers reported on an electrochemical method to improve charge injection by implementing mobile ions in the semiconductor, which form electric double layers at the source/drain electrodes increasing the on-current.[316] These findings support the proposed mechanism in our devices. On the source side, negative less mobile counter-ions possibly lead to a space-charge polarization, thereby enhancing the gate field. They might also reduce the injection barrier, form an electric double layer at the interface to rr-P3HT and/or dope the semiconductor via electrochemical doping. All these effects can lead to the observed small but distinct channel-current increase with time (black curve). When the device is stressed at V_G = -85V and V_D = 0V, the Na^+ ions move to the gate electrode and negatively charged (mobile or immobile) counter-ions reside near the interface or within the semiconductor layer. As a consequence, during the next measurement step (red curve), the positive polarons in the channel still "feel" the space charge of the negative ions, enhancing the gate-field and/or forming an electric double layer, which explains the larger channel current at the beginning of the curve. However, I_D is reduced with time, as Na^+ ions move to the drain compensating the negative charge of the counter-ions. When the ions have rearranged, channel current increases again.

When applying V_G = +85V and V_D = 0V for 100 s, mobile positive ions are forced to move to the PVA/rr-P3HT interface or into the semiconductor without channel-current flowing. Therefore in the following measurement (green) I_D is lower at the beginning, as positive polarons feel the positive space charge of the ions, hindering their injection and aggravating channel formation. But as ions seem to rearrange rapidly, I_D increases rather fast. The application of V_G = V_D = 0V for 100 s has, as expected, no effect on the ion distribution and therefore the channel current in the subsequent measurement (blue curve) starts at about the same value at which the green curve stopped.

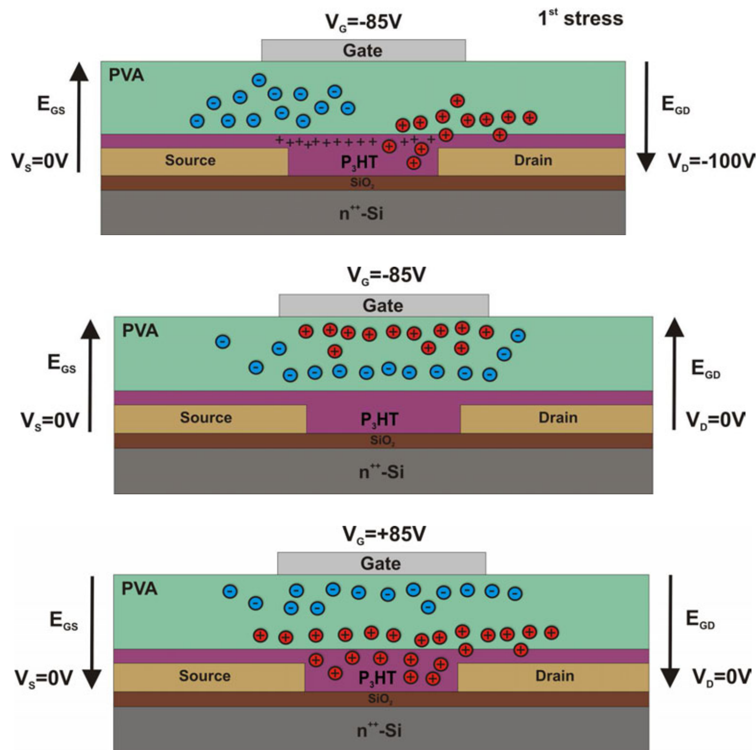

Figure 4.20: Possible explanation for operational drift of a rr-P3HT-based OFET with dialyzed PVA as gate dielectric operated and stressed in top-gate mode.

Generally, also negative mobile ions within the gate dielectric resulting form residual water might have an influence.[126,130,317]

The results above show that although hysteresis is much reduced by dialysis, not all ions can be removed from the dielectric, leading to a small but distinct operational drift. Similar results were obtained with rr-P3HT in combination with water-based gum arabic as gate dielectric.[296] The instabilities, however, seem to be reduced, when combining PVA or gum arabic with $PTPA_3$, which might be associated with the higher ionization potential of $PTPA_3$. Further investigations are ongoing.

4.5. Summary and Conclusions

In conclusion, the ambient and shelf-life stability of bottom-gate/bottom-contact OFETs based on various organic semiconductor materials was extensively investigated. PTPA-based OFETs were found to exhibit lower field-effect mobilities compared to their rr-P3HT-based (and, as expected, also their pentacene-based) counterparts. However, when exposed to air, PTPA-devices are much more stable with respect to switch-on voltage shifts and on-current-, off-current- and field-effect mobility changes. In contrast to rr-P3HT and pentacene, moisture/oxygen-induced doping has a minor influence on PTPA, ascribed to the larger ionization potential, which makes expensive device encapsulation unnecessary. Among the PTPA-derivatives $PTPA_3$ was the best-performing, probably due to its specific substituent on the side phenyl group, aggravating the interaction with oxygen and moisture very effectively.

The detailed analysis of the influences of oxygen, moisture and HMDS pre-treatment on device stability confirmed that rr-P3HT-based OFETs are more sensitive to oxygen, while pentacene-based counterparts exhibit larger response to moisture. High relative humidity levels also had an impact on $PTPA_3$. However, when the substrate was pre-treated with HMDS, all investigated semiconductors exhibited improved stability, which most likely is due to the hydrophobic surface properties in combination with a more dense packing of molecules, aggravating the penetration of water and oxygen into the semiconductor and to the semiconductor/dielectric interface.

The last section in this chapter illustrated the implications of moving ionic impurities within a PVA-based dielectric on the operational stability of rr-P3HT-based top-gate OFETs, including a possible explanation for the observed channel-current drifts under gate-bias stress.

The results presented in this chapter have clearly demonstrated that a lot of issues have to be considered, when selecting materials for OFET fabrication. The realization of well-performing, air- and operationally stable, all-solution processed OFETs without device encapsulation is, for sure, possible. However, to reach this aim further research both in material chemistry and device physics will be needed.

5. OFET-BASED SENSORS WITH SENSITIVE GATE DIELECTRICS USED FOR LOW-CONCENTRATION AMMONIA DETECTION

Aside from other target applications, organic field-effect transistors are also promising devices for sensing various kinds of analytes. In this chapter a novel OFET-sensor concept is presented, which is based on the application of an analyte-sensitive gate dielectric. In detail, the organic dielectric material is chemically adapted to change its electronic properties upon contact with an analyte for generating a response which is electrically detectable through an OFET. Various solution-processable, pH-sensitive, ring-opening metathesis polymerized dielectric materials were extensively investigated with gaseous ammonia as model analyte using UV/VIS spectroscopy, Fourier transform infrared spectroscopy, capacitance measurements and atomic force microscopy. By employing these materials in bottom-contact OFETs with a meander-shaped top-gate structure, ammonia concentrations as low as 100 ppm could be detected by an irreversible source-to-drain current increase, while devices based on a reference dielectric bearing no pH-sensitive groups showed negligible response. The obtained results support the reaction mechanism proposed at the beginning of this chapter, which is closed by a detailed response explanation, also including calculations based on a standard device model to roughly quantify the interactions.

5.1. Introduction

As discussed in chapter 2, the chemical and physical properties of electroactive organic materials can be easily tailored in order to enable, increase or optimize sensitivity and selectivity with respect to an analyte of interest. This, in combination with the possibility to use advanced low-cost solution-based processing techniques such as inkjet printing, has led to the fact that organic-based devices like OFETs are also promising candidates as smart (disposable) sensor elements.

So far sensor approaches involving organic field-effect transistors have been mainly based on the following principles:

- using the semiconducting layer (channel) as sensing part, with its electrical conductivity being modulated upon direct interaction with an analyte;
- providing a reactive dielectric surface e.g. in contact with an electrolyte for pH measurements (change of voltage drop near dielectric/electrolyte interface upon pH change);
- providing an additional specific detection layer comprising e.g. enzymes, antibodies or DNA for bio-sensing, usually on top of the dielectric;
- using the gate electrode as sensitive part.

Within this thesis a novel OFET-sensor concept based on the top-gate/bottom-contact architecture was developed and tested with ammonia (NH_3) as alkaline gaseous analyte. Sensing of ammonia is relevant e.g. for analysis of environmental conditions, for the automotive and chemical industry as well as for medical diagnostics. Moreover, ammonia is a marker for fish freshness and meat spoilage.[318,319,320] A detailed introduction into ammonia sensors and their applications and requirements is given by Timmer and co-workers.[321] Organic field-effect transistors in combination with NH_3 have already been investigated by some groups.[162,322,323] They either focused on the direct interaction between NH_3 and the organic semiconductor or integrated reactive self-assembled monolayers into OFETs, which chemically dedoped the adjacent semiconducting layer upon NH_3 exposure.

The work presented in this chapter was performed under assistance of Martin Denk. Accordingly, parts of the presented data were also published in his diploma thesis.[324] Furthermore, a corresponding patent application (*OFET-based Sensor for Detecting an Analyte*; E. J. W. List, A. Klug, C. Slugovc, M. Denk, UK patent application No. 0906204.3, **2009**) was submitted and a publication (*Organic field-effect transistor based sensors with sensitive gate dielectrics used for low-concentration ammonia detection*; Andreas Klug, Martin Denk, Thomas Bauer, Martina Sandholzer, Ullrich Scherf, Christian Slugovc, Emil J. W. List) is in preparation.

The structure of the OFET-sensor proposed within this work, in the following termed "SensFET", possible sensing mechanisms and the advantages of the concept are described in the chapter below.

5.2. The SensFET Concept

The gate dielectric strongly determines the device operation of a field-effect transistor. As mentioned in chapter 4, we have identified mobile Na^+ ions resulting from sodium acetate to be responsible for the hysteresis found in OFETs including PVA as gate dielectric. By reduction of the ion concentration via dialysis hysteresis was reduced and by deliberately adding NaPSS hysteresis was increased again, making such PVA-based OFETs quasi sensitive to Na^+ ions. Moreover, as discussed in section 2.2.1.3, when ions contained in electrolyte gate dielectrics move to the interfaces or even into the semiconductor, they can induce charge carrier densities $>10^{14}\,cm^{-2}$ in an OFET channel by the formation of electric double layers or due to electrochemical doping. Such effects have already been used in light-emitting electrochemical cells (LECs)[325] or in organic electrochemical transistors.[326] Furthermore, space charge polarization in ion-dispersed gate dielectrics has also been applied for tuning the threshold voltage of an OFET.[327]

These findings were a motivation to combine the ion-conducting abilities of electrolyte gate dielectrics with a sensing functionality in one layer and test this concept in a corresponding OFET device. Generally, the SensFET contains an organic dielectric material as active-sensing matter which is chemically adapted to change its electronic properties upon contact with an analyte. Transistor parameters should be easily influenced by chemical interaction between the analyte and an appropriately designed active-sensing dielectric, yielding a corresponding sensor response.

Figure 5.1 depicts the basic proposed sensor architecture based on the top-gate/bottom-contact configuration. In order to enable direct contact between the analyte and the sensitive dielectric, the top-gate electrode may be structured laterally in a comb- or meander-like shape, which allows for optimized access of the analyte to the organic dielectric layer, in particular over the channel region. Alternatively or in combination, a thin top-gate electrode could be used or the electrode may be made of an analyte-permeable material, not interacting with the analyte.[x]

[x] Generally, also analyte diffusion from the substrate side to the sensitive dielectric layer could be provided for by realization with appropriate analyte-permeable materials or by employing a permeable structure with channels for analyte diffusion.

Structuring the electrode has the advantage of leading to reduced sensor response times, as the active dielectric layer is directly exposed and analyte penetration through various inactive layers is not required.

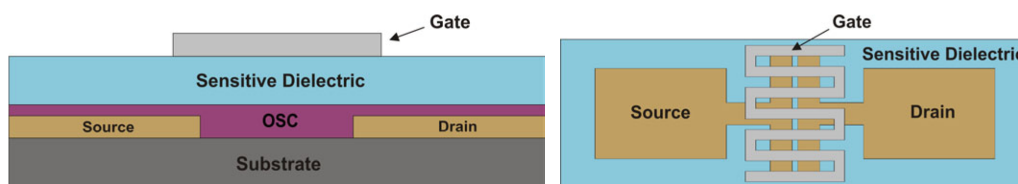

Figure 5.1: Principle SensFET-device architecture (left: cross-section, right: top-view) with meander-shaped top-gate for direct contact between analyte and sensitive gate dielectric; OSC… organic semiconductor.

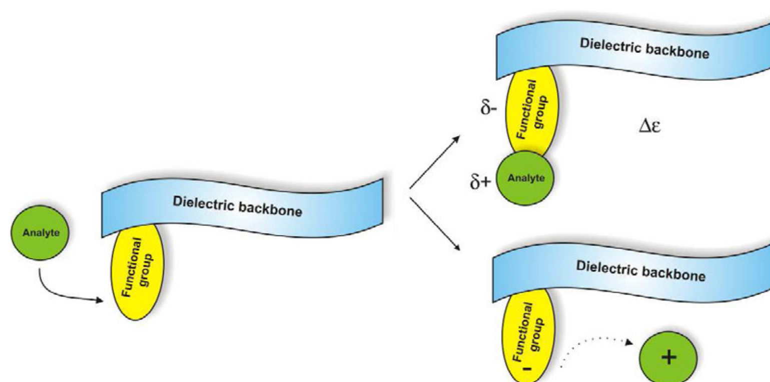

Figure 5.2: Possible reaction mechanisms between a target analyte and a dielectric material containing an active-sensing functional group.

When exposed to the target analyte, the sensitive dielectric material will undergo certain specific responses. Figure 5.2 schematically illustrates two possible reaction mechanisms between an analyte and a sensitive dielectric, which consists of a non-conjugated backbone and an active-sensing functional group. The analyte may dock to the functional group and induce direct charge transfer processes or charge displacements caused by complex formation, resulting in a microscopic change of the dielectric constant of the material. Alternatively, the analyte might be ionized by the interaction with the functional group, resulting in the generation of mobile ions and immobile counter-ions. As mentioned above, in an OFET under operation the mobile ions move within an ion-conducting dielectric (depending on the sign and mobility of the charges) due to the applied electric fields, contributing - together with the immobile counter-ions - to an enhanced polarization and thereby leading - possibly in combination with the formation of electric double layers - to an increase of the mobile charge carrier density within the channel.

Moreover, when reaching the interface to or even moving into the organic semiconductor, the mobile ions may change the concentration of free charge carriers within the channel by doping, trapping or de-trapping mechanisms. Both reactions illustrated in Figure 5.2 will change the electrical properties of the dielectric layer, which in turn modifies the current-voltage characteristics of an OFET in terms of e.g. the on/off-current ratio, the switch-on voltage, the subthreshold slope and/or the magnitude of hysteresis.

The specific sensing functionality can be provided by appropriate chemical design of the dielectric material (e.g. by covalently bonding specific functional groups to the dielectric backbone during synthesis) or by blending a dielectric material (host) with sensing molecules (guest). For both approaches it is important to obtain high sensitivity and selectivity with respect to the target analyte. In order to ensure that the sensor response originates solely from the reaction/interaction of the active-sensing dielectric with the analyte, all other materials constituting the device should be insensitive to the analyte and also to other substances the device will get into contact with during operation. Reversibility of the sensor is obtained by applying suitable procedures which restore the pristine state, e.g. for an oxygen sensor by heating and/or evacuation to remove absorbed oxygen or for a sensor for alkaline gaseous analytes by exposure to an acidic gas. Even if the sensing event cannot be reversed, the sensor could still find its application as cheap disposable device.

One important advantage of this concept, which combines the dielectric with the sensing feature in one layer, is a reduction of the fabrication effort, making the application of an additional sensing layer obsolete. Moreover, by separating the sensing mechanism from the charge-transport functionality of the organic semiconductor, established well-performing semiconductor materials with high mobility can be applied and synthetic effort for optimizing both sensing and charge-transport behavior of a material at the same time is no longer required. In addition, the concept allows for the implementation of device geometries difficult to realize when detecting via the organic semiconductor. Taking into account the top-gate architecture, the semiconducting layer is largely protected against exposure to ambient atmosphere by the dielectric. Therefore particular encapsulation of the semiconductor material, often being sensitive to environmental influences such as oxygen and/or moisture (see chapters 2 and 4), is not necessary and less air-stable, otherwise well-performing organic semiconductors can be used for the channel layer.

For evaluating this concept, within this work various solution-processable, pH-sensitive, ring-opening metathesis polymerized (ROMP) materials were employed as active-sensing gate dielectrics in rr-P3HT- and $PTPA_3$-based bottom-contact OFETs with a meander-shaped top-gate structure and the devices were tested with ammonia as gaseous analyte.

Upon exposure to NH_3 at concentration levels down to 100 ppm, the device response was monitored and compared with OFETs based on a reference dielectric bearing no pH-sensitive groups. Aside from current-voltage OFET-analysis, also UV/VIS-spectroscopy, Fourier transform infrared (FTIR) spectroscopy, capacitance measurements and atomic force microscopy were used to thoroughly investigate the active-sensing dielectrics and to rationalize the underlying sensor mechanism. The applied materials are described in the following section.

5.3. Applied Dielectric Materials

As mentioned, the sensitive dielectrics have to be chosen to ensure high sensitivity and selectivity with respect to the target analyte. Thus, for NH_3, being an alkaline gas, dielectric polymers containing pH-sensitive groups were applied, which were synthesized by the group of Prof. Slugovc.[328] Figure 5.3 depicts the corresponding chemical structures.

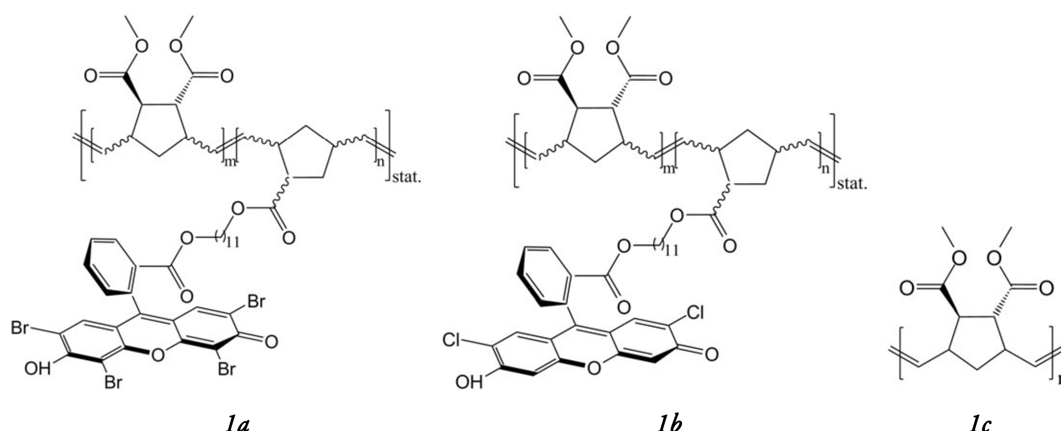

Figure 5.3: Chemical structures of applied dielectric materials: (***1a***) statistic co-polymer with eosin Y as NH_3-sensitive group (m = 300, n = 3); (***1b***) statistic co-polymer with 2,7-dichlorfluorescein as NH_3-sensitive functional group (m = 300, n = 3); (***1c***) reference polymer.

The two active-sensing dielectrics ***1a*** and ***1b*** are composed of xanthene-dye molecules, namely eosin Y or 2,7-dichlorfluorescein (DCF), which were connected to a polymerizable norbonene group and co-polymerized with a chemically inert monomer, namely *endo*,*exo*-bicyclo[2.2.1.]hept-2-ene-5,6-dicarboxylic acid dimethylester, as bulk-monomer using ring-opening metathesis polymerization. As non-sensitive reference material, the homopolymer of *endo*,*exo*-bicyclo[2.2.1.]hept-2-ene-5,6-dicarboxylic acid dimethylester (***1c***) was used. In order to prevent aggregation of the pH-sensitive dyes, for polymers ***1a*** and ***1b*** only 1 mol% of dye-bearing monomers was mixed with the corresponding bulk-monomer. Furthermore, the sensing capabilities of the statistic copolymer ***1d*** (Figure 5.4), comprising the same amount of OH-groups on each active unit as ***1a*** and ***1b***, were also tested, but only in OFET devices.

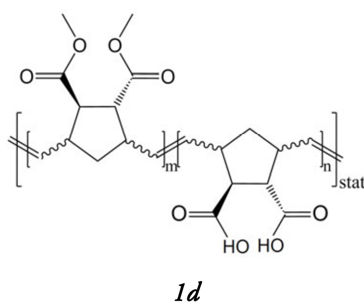

Figure 5.4: Chemical structure of ROM-polymerized statistic co-polymer ***1d*** (m = 300, n = 1.5).

Detailed information about the synthesis and ROMP in general can be found in literature.[329,330,331,332] Basically, ROMP is a polymerization method, which is highly functional group tolerant, very efficient, versatile and well-controllable regarding molecular weight and polydispersity. Xanthene dyes are characterized by high absorption coefficients and high fluorescence quantum yields and have been used e.g. for labeling applications in biology or medicine, as sensitive fluorescent pH-indicators, as photosensitizers or photoinitiators.
Table 8 provides information about relevant material parameters of the applied dielectrics, including values for two different batches of polymers ***1a*** and ***1c***.

Table 8: Relevant ROMP material parameters: M_n... number average molecular weight; *PDI*… polydispersity index; (data determined by the group of Prof. Slugovc with gel permeation chromatography)

ROMP Material	*M_n [g/mol]*	*PDI*
*Eosin Y-based ROM-polymer **1a** - batch 1*	*35430*	*1.78*
*Eosin Y-based ROM-polymer **1a** - batch 2*	*44700*	*1.24*
*DCF-based ROM-polymer **1b***	*40480*	*1.11*
*Dimethylester-homo-polymer **1c** - batch 1*	*46100*	*1.14*
*Dimethylester-homo-polymer **1c** - batch 2*	*53370*	*1.07*
*ROM-polymer **1d***	*62990*	*1.17*

The proposed reaction mechanism between the dielectric and NH_3 is schematically depicted for the eosin Y-based polymer ***1a*** in Figure 5.5. Ammonia deprotonates the dye's OH-group by capturing the hydrogen atom, thus creating mobile ammonium ions (NH_4^+) and immobile counter-ions, which should lead to a change of the electrical behavior and thereby result in a detectable sensor signal.

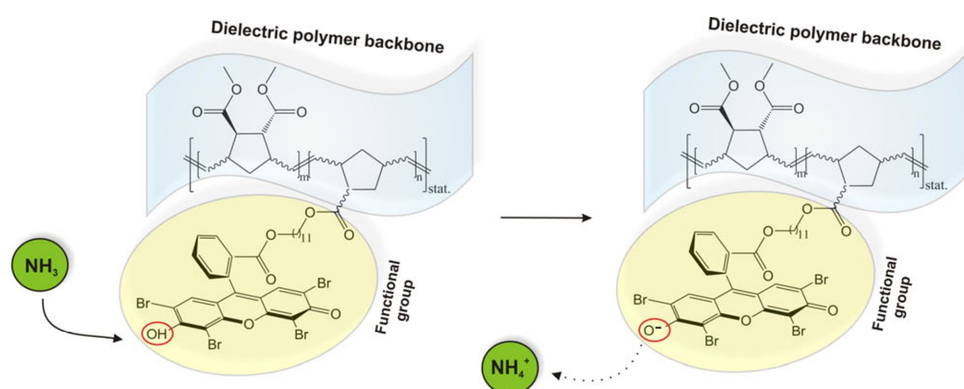

Figure 5.5: Deprotonation reaction between ammonia and ROM-polymerized statistic co-polymer ***1a*** with eosin Y as NH_3-sensitive group (m = 300, n = 3).

Sandholzer and co-workers have already proven a deprotonation reaction of ROMP materials upon exposure to triethylamine (NEt_3) vapor.[329]

5.3.1. Preparation of ROM-Polymer Solutions

An amount of each polymer ***1a-d*** was dissolved in spectrally clean chloroform ($CHCl_3$) to a concentration of 60 mg/ml in argon atmosphere. The solutions were heated at 50°C for 5-10 min to facilitate dissolution. While ***1a***- and ***1b***-based solutions appeared in an orange color, those containing ***1c*** and ***1d*** were yellow (Figure 5.6). The rather high solution concentration (60 mg polymer/ml) was chosen in order to obtain dielectric films thick enough for low gate-leakage currents and high signal-to-noise ratios of later fabricated OFET-sensors.

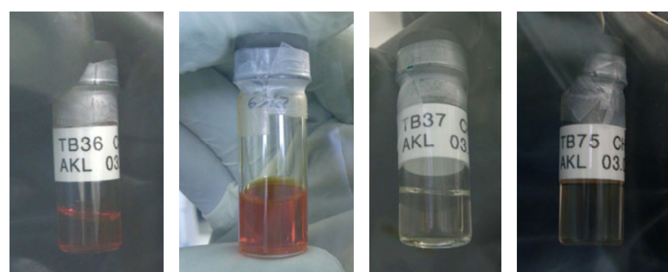

Figure 5.6: Typical solutions of ROMP dielectrics in spectrally clean $CHCl_3$ (60 mg/ml); from left to right: eosin Y-based polymer ***1a***, DCF-based polymer ***1b***, reference polymer ***1c*** and polymer ***1d***.

5.3.2. UV/VIS-Absorption Spectroscopy

In order to verify the disposition of the dye-bearing dielectrics to deprotonate in solid state, the change of optical properties of polymers ***1a-c*** upon exposure to NH_3 and hydrochloric acid (HCl) vapor was studied by UV/VIS spectroscopy of corresponding films under ambient conditions.

As already shown in [329], the reaction of the active-sensing polymers with alkaline substances is expected to lead to an increase of the absorption intensity due to deprotonation.

Glass substrates (microscope slides, dimensions: ~25 mm x ~25 mm) were cleaned in the same way as the wafer pieces described in chapter 3.1.3.1. After a vacuum bake ($p < 5x10^{-6}$ mbar, 150°C, 1 h) to remove residual surface water, the substrates were spin-cast with spectrally clean $CHCl_3$ (1500 rpm, 40 s) in argon and then dried for 10 min at room temperature. Finally films of ***1a-c*** (batch 1) were spin-cast from $CHCl_3$ solutions (1500 rpm, 40 s) and then dried for 10 min at 130°C on a hot plate in argon. AFM measurements revealed a film thickness of ~990 nm for polymer ***1a***, ~880 nm for polymer ***1b*** and ~1070 nm for ***1c***. UV/VIS-absorption measurements were performed under ambient conditions using a SHIMADZU UV-1800 UV-VIS-Spectrophotometer.[y] After optically analyzing the as-prepared films, they were exposed to 100% ammonia gas for 30 min, then to fumes of a 37% HCl solution for 1 min and finally to 100% NH_3 gas for 30 min for a second time, each exposure followed by a corresponding UV/VIS-absorption measurement.

Figure 5.7 depicts the obtained film spectra of reference polymer ***1c*** and eosin Y-bearing polymer ***1a***. As expected, ***1c*** did not show any response to NH_3 and HCl in the investigated spectral range between 300 nm and 700 nm. Polymer ***1a***, in the as-prepared state, displayed a vibronically resolved absorption spectrum with peak maxima centered at 453 nm, 478 nm, 505 nm and 539 nm, in good agreement with the results in [329]. The peak at 539 nm of the pristine film might have resulted from a small amount of already deprotonated eosin Y moieties. Upon NH_3 exposure the intensities of the two peaks at 505 nm and 539 nm were strongly increased, while they were suppressed when exposed to HCl fumes. The peaks appear again upon the second NH_3 exposure, proving the deprotonation and protonation reactions of the active-sensing group. Figure 5.8 shows sample pictures illustrating the color change of the corresponding films due to NH_3 and HCl exposure.

[y] The UV/VIS spectrometer is situated at the Institute for Chemistry and Technology of Materials, Graz University of Technology.

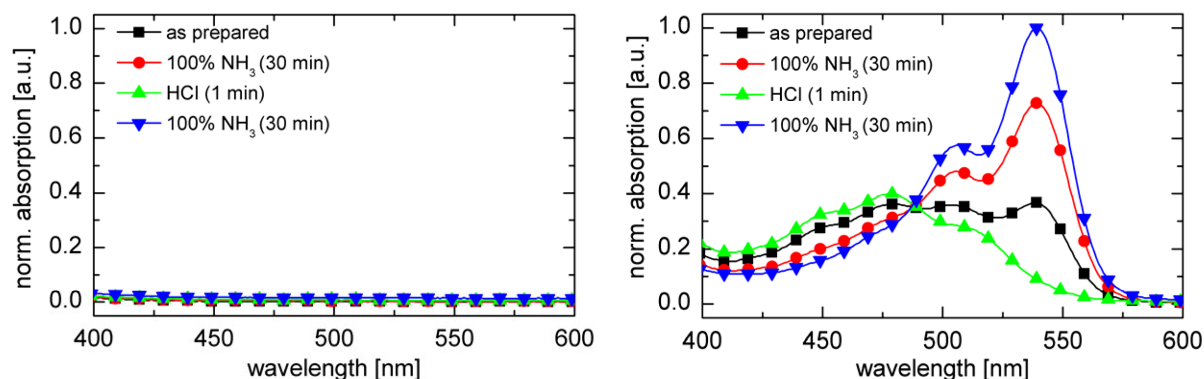

Figure 5.7: UV/VIS-absorption film spectra of reference polymer ***1c*** (batch 1, left) and active-sensing eosin Y-based polymer ***1a*** (batch 1, right) upon exposure to gaseous NH_3 and HCl; all curves normalized to maximum peak of ***1a*** at 539 nm.

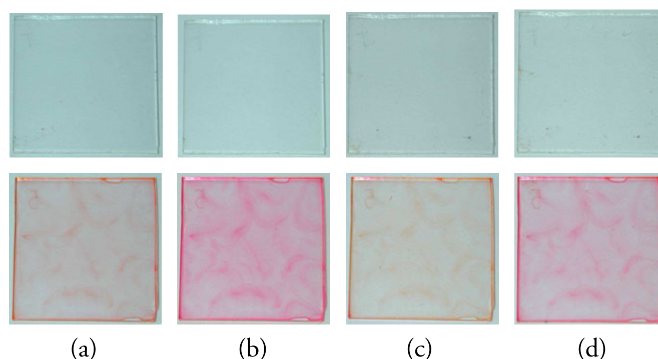

Figure 5.8: UV/VIS-sample pictures with films of the reference polymer ***1c*** (top, batch 1) and the eosin Y-based polymer ***1a*** (bottom, batch 1) on glass substrates; (a) as prepared; (b) after 100% NH_3 exposure for 30 min; (c) after exposure to 37% HCl vapor for 1 min; (d) after 2nd exposure to 100% NH_3 for 30 min.

The spectra of the DCF-based polymer ***1b*** did not reveal such a distinct response to NH_3 as found with polymer ***1a*** and in [329] (Figure 5.9). Possibly, the DCF-dyes of this material have already been deprotonated to a larger extent by alkaline gases in the laboratory atmosphere.

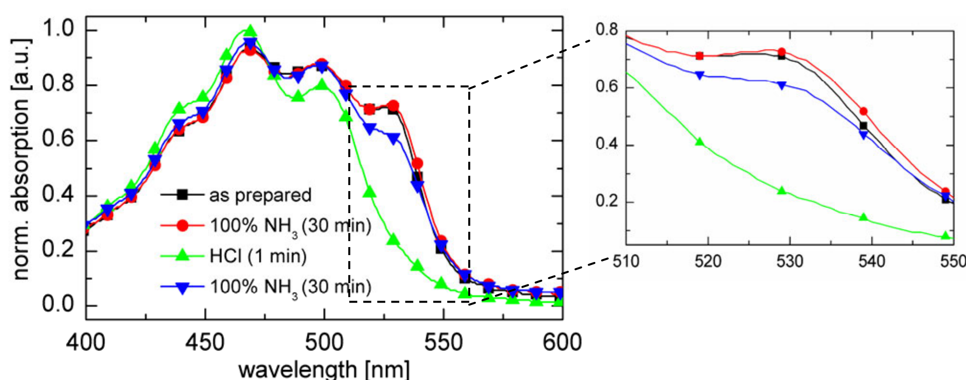

Figure 5.9: UV/VIS-absorption film spectra of active-sensing DCF-based polymer ***1b*** upon exposure to gaseous NH_3 and HCl; all curves normalized to maximum peak at 467 nm.

Still, there was a small response in the region around the peak at 528 nm, which becomes more obvious by calculating the relative change of the spectra with the following equation:

$$\frac{\Delta A}{A}[\%] = \left(\frac{A(\lambda,n+1)}{A(\lambda,n)} - 1\right)\cdot 100 \tag{5.1}$$

$A(\lambda)$… measured absorption intensity at a specific wavelength λ, n… film condition (n = 1: as prepared, n = 2: exposed to 100% NH_3 for 30 min, n = 3: exposed to HCl fumes for 1 min, n = 4: 2nd exposure to 100% NH_3 for 30 min).

This relates a spectrum of the film in a specific state to the one measured in advance and the reaction to ammonia and HCl is now distinctly recognizable for polymer ***1b*** (Figure 5.10).

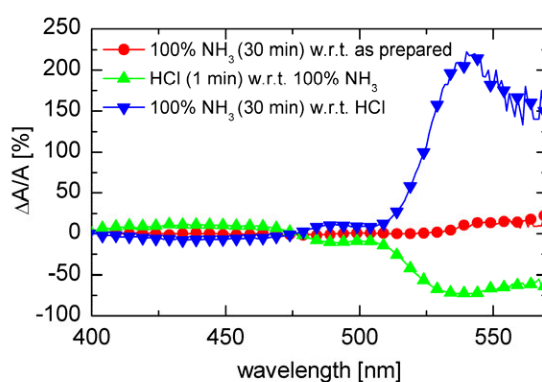

Figure 5.10: Relative change of UV/VIS-absorption film spectra of DCF-based polymer ***1b*** upon exposure to gaseous NH_3 and HCl; each curve represents a spectrum related to the one measured in advance.

5.3.3. FTIR Spectroscopy

The proposed reaction mechanism is also supported by the results of the FTIR analysis. For these measurements native silicon wafer pieces (dimensions: ~15 mm x ~15 mm) were used as substrates, being transparent for the investigated mid-infrared region between 4000 cm^{-1} and 400 cm^{-1}. The samples were prepared similar to those used for UV/VIS-absorption spectroscopy. The film layer thickness, determined by AFM, was ~590 nm for polymer ***1a***, ~500 nm for ***1b*** and ~520 nm for ***1c***. Figure 5.11 illustrates the already NH_3- and HCl-exposed samples.

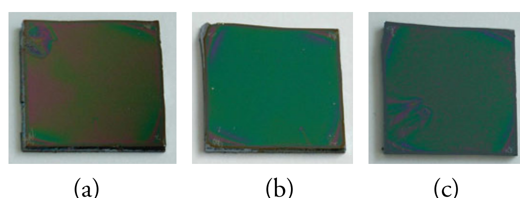

(a) (b) (c)

Figure 5.11: FTIR-sample pictures with films of the eosin Y-based polymer ***1a*** (a), the DCF-based polymer ***1b*** (b) and the reference polymer ***1c*** (c) on native Si substrates after analyte exposure.

FTIR investigation was performed using a Bruker IFS 66v/S FTIR spectrometer[z] in standard normal incidence transmission mode. The equipment comprises a silicon carbide MIR source (spectral range: 7500 cm^{-1} - 30 cm^{-1}) and a liquid-N_2 cooled mercury-cadmium-telluride (MCT) detector, the latter exhibiting an intrinsically low noise level and allowing for a high read-out rate (60 kHz). For each recorded film spectrum 2048 sample scans were performed for averaging, the resolution was set to 4 cm^{-1} and the number of background scans to 1. A cleaned native silicon wafer piece was applied as reference. The samples with the polymer films were measured and exposed to NH_3 and HCl as described for the UV/VIS spectroscopy.[aa] Before each measurement the sample chamber was evacuated for 30 min to a pressure below 4 mbar. Figure 5.12 depicts the obtained transmittance T as a function of wavenumber $\tilde{\nu}$ for polymers ***1c*** and ***1a*,** calculated as follows:

$$T(\tilde{\nu}) = \frac{I(\tilde{\nu})}{I_0(\tilde{\nu})} \tag{5.2}$$

Here I is the intensity of the sample with the ROM-polymer film and I_0 the intensity of the pristine native silicon substrate without the film.

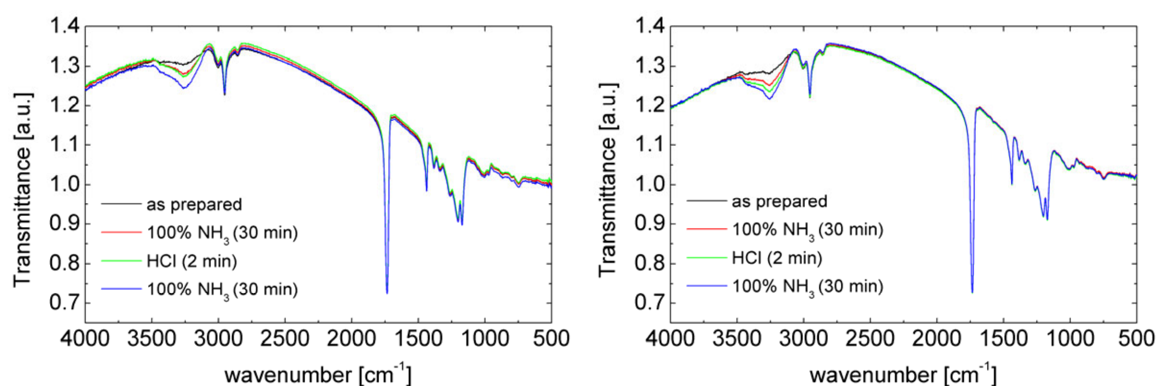

Figure 5.12: FTIR-transmittance film spectra of reference polymer ***1c*** (batch 1, left) and active-sensing eosin Y-based polymer ***1a*** (batch 1, right); all spectra are referenced against a cleaned pristine substrate.

No strong difference can be observed between both graphs. The film spectra of polymer ***1b*** were similar as well (not shown). This is attributed to the fact that only 1 mol% of dye-bearing groups were implemented in polymers ***1a*** and ***1b*** (see above) and hence the absorption is dominated by the bulk material common to all three polymers.

[z] The FTIR spectrometer is situated at the Institute of Solid State Physics, Graz University of Technology.

[aa] HCl exposure was performed for 2 min instead of 1 min, which, however, should have no large influence on the qualitative reaction behavior.

The broad increasing peak centered at ~3260 cm^{-1} resulted from the increasing contamination of the sample chamber and the liquid-N_2 cooled detector by condensation water each time the chamber was opened. Further peak intensities were observed at the following wavenumbers (cm^{-1}), in good agreement with the results in [329]: 3004-2860 with main peak at 2954 (s, $\nu_{ar,CH}$), 1734 (s, $\nu_{C=O}$), 1437 (s), 1382 (m), 1337 (m), 1263 (w), 1201 (m), 1171 (m), 1003 (w), 971 (w, $\nu_{trans,C=C}$), 746 (w).

In both graphs the transmittance T is larger than 1 in a broad wavenumber range, which would correspond to a seemingly larger IR-beam absorption of the pristine substrate without additional polymer film. This is a result of mainly two effects: first, the rougher surface of the samples with the polymer films and multiple reflections also at the interface between the silicon surface and the ROMP dielectric most probably deflect more IR intensity to the detector than the pristine substrate. Second, only one background scan of the native silicon substrate was recorded compared to 2048 scans of the ROMP samples, resulting in a reduced accuracy. However, for material characterization and verification of the deprotonation reaction absolute transmittance values are not as relevant as peak positions and their intensity changes upon analyte exposure.

Unfortunately, due to the small amount of NH_3-sensitive dye-bearing units in polymers ***1a*** and ***1b***, there is also not much difference between the FTIR spectra of a ROM-polymer in the various states. In the standard normal incidence transmission spectroscopy the IR beam only travels a short way through the sample and so the signal change after exposure to NH_3 and HCl was not much pronounced. Remedy for increasing the optical pathway and hence the signal response would be found e.g. with Brewster angle spectroscopy, reflection absorption infrared spectroscopy or attenuated total reflection infrared spectroscopy.[333,334]

Nonetheless, similar as with the UV/VIS-absorption film spectra of polymer ***1b*** (Figure 5.10), an FTIR-transmittance spectrum of a ROM-polymer recorded in a specific state was related to the one measured in the state before by calculating the relative change $\frac{\Delta T}{T}$ with the following equation:

$$\frac{\Delta T}{T}[\%] = \left(\frac{T(\lambda, n+1)}{T(\lambda, n)} - 1 \right) \cdot 100 \tag{5.3}$$

$T(\lambda)$… measured transmittance intensity at a specific wavelength λ, n… film condition ($n = 1$: as prepared, $n = 2$: exposed to 100% NH_3 for 30 min, $n = 3$: exposed to HCl fumes for 2 min, $n = 4$: 2nd exposure to 100% NH_3 for 30 min).

Figure 5.13 displays the corresponding results for the active-sensing polymer ***1a***. According to literature,[335] characteristic vibrations of ammonium ions should be recognizable by very strong intensities in the range 3335-3030 cm^{-1} and strong intensities in the region 1490-1325 cm^{-1}. The former range was covered by the peak resulting from the increasing amount of condensation water within the chamber and on the detector. However, for ***1a*** a change of the peak found around 1353 cm^{-1} could indeed be identified, not being present in the IR data of the reference material ***1c***.[bb] Although the response is rather small, which is again ascribed to the low concentration of eosin Y-dyes (1 mol%) within polymer ***1a*** and the short pathway of the IR-beam through the sample, it still provides another indication for the proposed reaction mechanism described above.

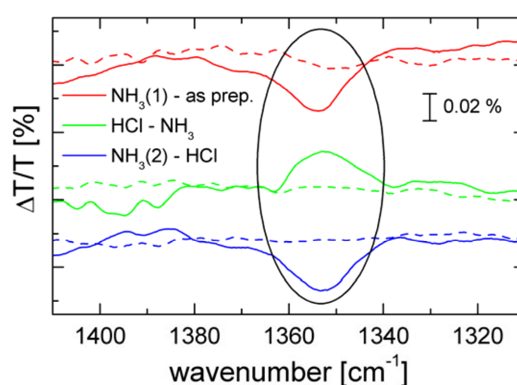

Figure 5.13: Relative change of the FTIR-transmittance spectra of ROMP dielectrics (batch 1) upon NH_3 and HCl exposure; dashed lines: reference polymer ***1c***; solid lines: eosin Y-based polymer ***1a***; each curve represents a spectrum related to the one measured in advance.

5.4. Equipment for Electrical Device Characterization

For the electrical characterization of capacitors and OFETs under inert conditions and upon NH_3 exposure a similar sealable probe chamber as for the stability measurements (see section 4.3.2.1) was fabricated, including appropriate switch boxes with BNC plugs for connecting the feed-through connectors of the chamber with an LCR-meter or parameter analyzer and for switching the individual devices on a sample.[cc] The pictures in Figure 5.14 give an impression.

[bb] For polymer ***1b*** the IR data did not reveal such a distinct response to NH_3 and HCl and are therefore not shown.
[cc] This was in fact the first-generation chamber and did not include a humidity sensor.

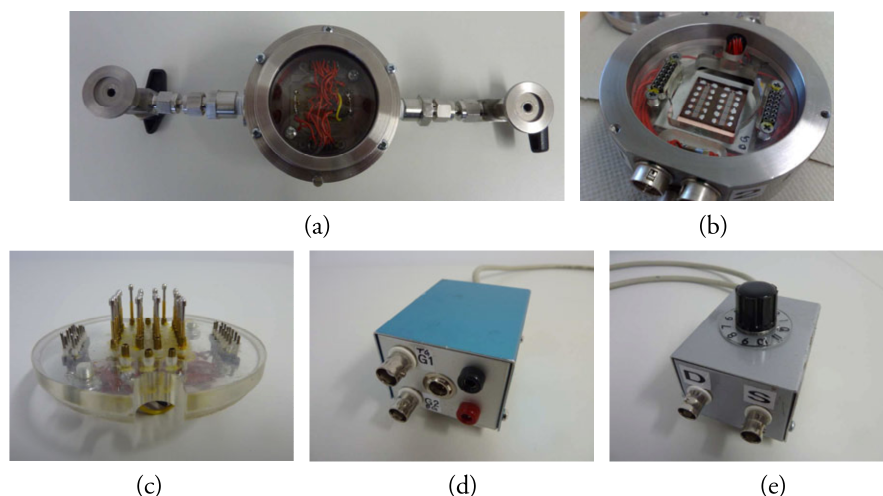

Figure 5.14: a) Sealable gas-measurement chamber for electrical characterization of capacitors and OFETs under various conditions; b) interior with SensFET sample on Peltier element; c) probe head with pogo pins for device contacting; d) & e) switch boxes for connecting the devices to be tested with an LCR-meter or parameter analyzer.

The probe chamber was integrated into a simple gas measurement plant (Figure 5.15) with ¼″ tubing and two gas bottles, one containing argon, one pure or diluted NH_3 (100 ppm or 1%). The gas flow into the chamber and the setting of the NH_3 concentration was controlled via appropriate valves and two manually adjustable rotameters. Moreover, a rotary vane pump was applied for probe chamber evacuation.

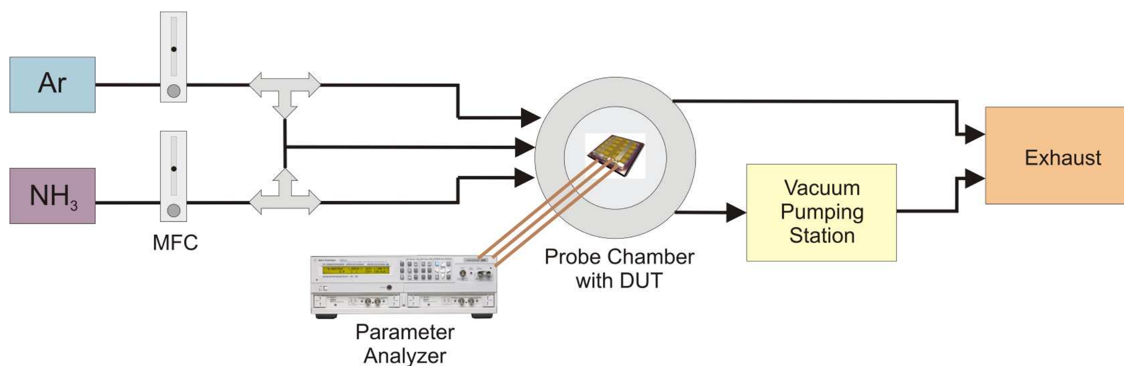

Figure 5.15: Scheme of gas measurement plant integrated in a fume hood at the Institute of Solid State Physics, Graz University of Technology; MFC… Mass Flow Controller.

5.5. Capacitors based on ROMP Dielectrics

Each polymer ***1a-c*** was electrically characterized in capacitor structures, consisting of 125 nm thick, patterned indium tin oxide (ITO) bottom-electrodes on a glass substrate, a spin-cast 600-1000 nm thick ***1a***-, ***1b***- or ***1c***-polymer film and ~100 nm thick aluminum comb-shaped top-electrodes.

In addition, capacitors with PVA (Mowiol 5-88, see chapter 4.4) as dielectric were fabricated and analyzed. Figure 5.16 schematically depicts the sample architecture.

Figure 5.16: Scheme of sample with eight ITO/dielectric/aluminum-capacitor structures with comb-shaped top-electrodes.

5.5.1. Device Fabrication

Glass substrates (dimensions: 1″ x 1″) with a structured[dd] ITO layer (sheet resistance: 15 Ω/sq, KINTEC) were cleaned and then coated with the ROMP dielectrics (batch 1) in the same way as described for the UV/VIS samples. For the PVA-capacitors a dialyzed PVA-hydrogel (9-10 wt%, Figure 4.16) was spin-cast (2500 rpm, 60 s), then dried for 1 h at 110°C on a hot plate in argon and afterwards baked for 3 h at 60°C in vacuum ($p < 5x10^{-6}$ mbar). The corresponding layer thicknesses determined with AFM are shown in Table 9 in the next section. The aluminum comb-shaped top electrodes were thermally evaporated ($p < 5x10^{-6}$ mbar, deposition rate: 8 Å/s) through a shadow mask. A typical sample is depicted in Figure 5.17. For good contacts with the pogo pins of the probe chamber conductive silver paste was applied.

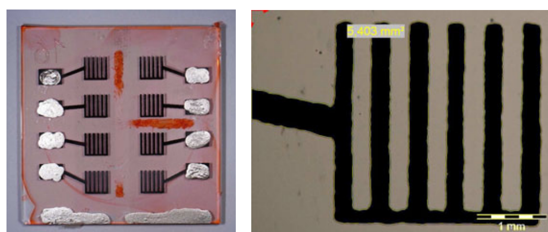

Figure 5.17: Typical sample with eight ITO/dielectric/aluminum-capacitors based on polymer ***1a*** with comb-shaped top-electrodes (left) and optical micrograph of a single device (right).[ee]

The samples were then individually assembled in the sealable probe chamber (see section 5.4) under argon atmosphere and capacitance measurements were performed with an Agilent E4980A LCR-meter.

[dd] Fully ITO-covered glass substrates were masked with two stripes of adhesive tape and then structured by etching in 37% HCl acid, applying also tin powder for reaction enhancement.

[ee] The pronounced polymer structures in the middle of the sample resulted from excess material being sucked to the substrate backside by the vacuum chuck of the spincoater.

5.5.2. Device Characteristics

5.5.2.1. Frequency Dependence

At first absolute impedance $|Z|$ and phase angle Θ data were recorded as a function of frequency at a test-signal amplitude level of $1V_{RMS}$. Figure 5.20 depicts the obtained values of typical capacitors on the four samples in a frequency range between 200 Hz and 100 kHz. An ideal capacitor exhibits a phase angle of -90°, an ideal resistor 0°.[336,337] Obviously the PVA dielectric contained the largest ohmic contribution, which will be explained below.

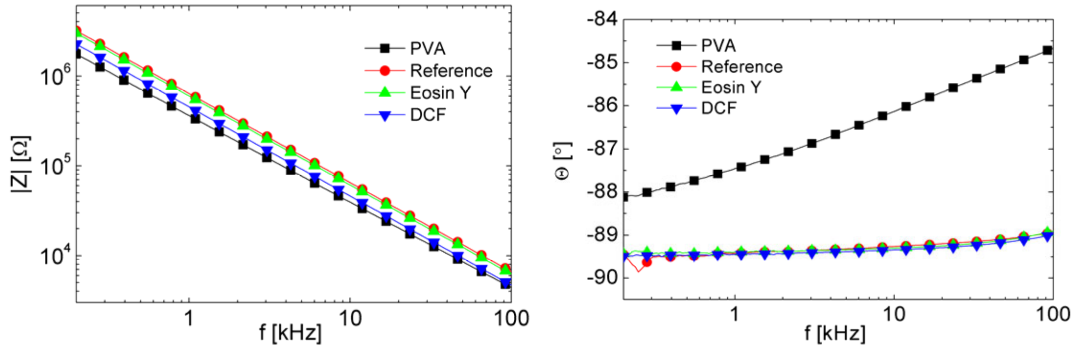

Figure 5.18: Absolute impedance $|Z|$ and phase angle Θ as a function of frequency of a typical ITO/dielectric/aluminum-capacitor with comb-shaped top-electrode on each sample.

For the devices an equivalent circuit model consisting of a capacitance C_P and a resistance R_P in parallel is assumed.[336,337] The corresponding values are obtained from $|Z|$ and Θ by coefficient comparison of equations (5.4) and (5.5), also applying Euler's equation and leading to eqn. (5.6). Z is the impedance, X_C the capacitive reactance and ω the angular frequency of the applied test signal.

$$\frac{1}{Z} = \frac{1}{R_P} + \frac{1}{X_C} = \frac{1}{R_P} + j\omega C_P \tag{5.4}$$

$$\frac{1}{Z} = \frac{1}{|Z|} e^{-j\Theta} = \frac{1}{|Z|} \cdot (\cos\Theta - j\sin\Theta) \tag{5.5}$$

$$C_P = -\frac{1}{\omega \cdot |Z|} \cdot \sin\Theta\,;\; R_P = \frac{|Z|}{\cos\Theta} \tag{5.6}$$

Figure 5.19 shows the extracted C_P and R_P values as a function of frequency of typical capacitors based on the four tested dielectric materials. The capacitance is rather constant for the ROM-polymers in the investigated frequency range. As expected, R_P is reduced with increasing frequency, proving that the dielectric becomes more conductive.

PVA also exhibits a frequency-dependence of C_P and in addition lower R_P values compared to the ROMP dielectrics, which most likely can be ascribed to residual mobile Na^+ ions not removed by dialysis (see also chapter 4.4).

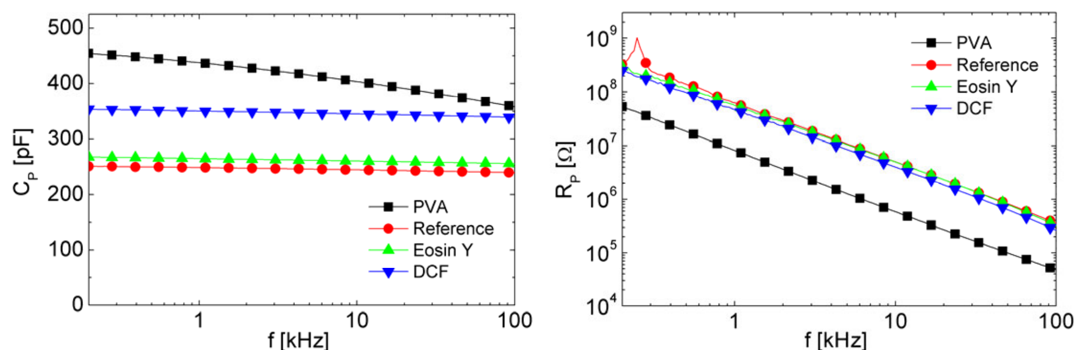

Figure 5.19: Parallel capacitance C_P and parallel resistance R_P as a function of frequency of a typical ITO/dielectric/aluminum-capacitor with comb-shaped top-electrode on each sample; values calculated from measured absolute impedance and phase angle.

From the C_P values of all capacitors on each sample the relative permittivity ε_r of the corresponding dielectric was calculated according to eqn. (5.7), with d_i being the dielectric layer thickness, A the capacitor area and ε_0 the vacuum permittivity:

$$\varepsilon_r = \frac{C_P \cdot d_i}{\varepsilon_0 \cdot A} \tag{5.7}$$

The layer thickness was determined with AFM measurements and the capacitor area with optical microscopy. Table 9 summarizes the average ε_r values for all materials at 1 kHz. The value obtained for PVA is well in accordance with literature values between 6 and 10 (see chapter 4.4). Polymer ***1b*** seems to be less polar than the other two ROMP dielectrics.

Table 9: Average relative permittivity ε_r of ROMP dielectrics and PVA (average values of eight capacitors on each sample); extracted from C_P values according to eqn. (5.7).

ROMP Material	d_i *[nm]*	ε_r *at 1 kHz*
Eosin Y-based ROM-polymer ***1a*** *- batch 1*	*1000*	*5.6*
DCF-based ROM-polymer ***1b***	*600*	*4.5*
Dimethylester-homo-polymer ***1c*** *- batch 1*	*1020*	*5.5*
PVA	*840*	*8.4*

5.5.2.2. DC-Bias Dependence

In order to test for the operational stability of the capacitors, also DC-bias measurements were performed by sweeping a DC-bias voltage, superimposed by the AC test signal (test-signal amplitude: $1V_{RMS}$, test-signal frequency: 1 kHz), and recording the absolute impedance $|Z|$ and phase angle Θ. The DC voltage was swept from 0V to +40V, then to -40V and back to 0V with 1V steps. Again, the corresponding C_p and R_p values as a function of DC-bias voltage were calculated using eqn. (5.6) (Figure 5.20).

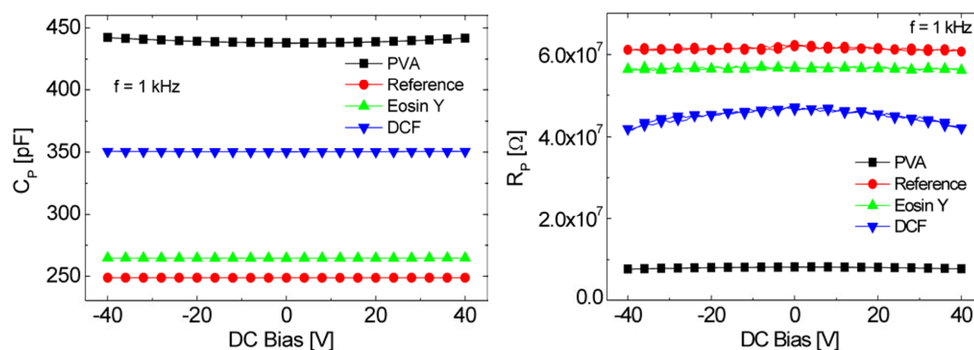

Figure 5.20: Parallel capacitance C_P and parallel resistance R_P as a function of DC-bias voltage of a typical ITO/dielectric/aluminum-capacitor with comb-shaped top-electrode on each sample; values calculated from measured absolute impedance and phase angle.

Obviously, the devices were rather stable. No large hysteresis between the forward and reverse sweep was obtained. PVA shows a slight voltage-dependence of the capacitance and a lower resistance compared to the other materials, again ascribed to residual sodium acetate within the material. Also DCF-based polymer ***1b*** seems to contain mobile ions, as the corresponding resistance shows a distinct voltage-dependence. This will be investigated more in detail in the next section.

5.5.2.3. Exposure to Ammonia

Finally each of the samples was exposed to 100% ammonia. In detail, after 110 s of argon-flushing, the chamber was flushed with 100% NH_3 for 200 s, then sealed for 1200 s and finally flushed again with argon for 500 s. One capacitor on each sample was selected and corresponding impedance and phase angle data were recorded during NH_3 exposure (test-signal frequency: 1 kHz, test-signal amplitude: $1V_{RMS}$, no DC bias, time interval: 10 s). Figure 5.21 depicts the calculated C_P and R_P values and Figure 5.22 the parallel capacitance and resistance normalized to their value at 110 s, the start time of NH_3 inlet.

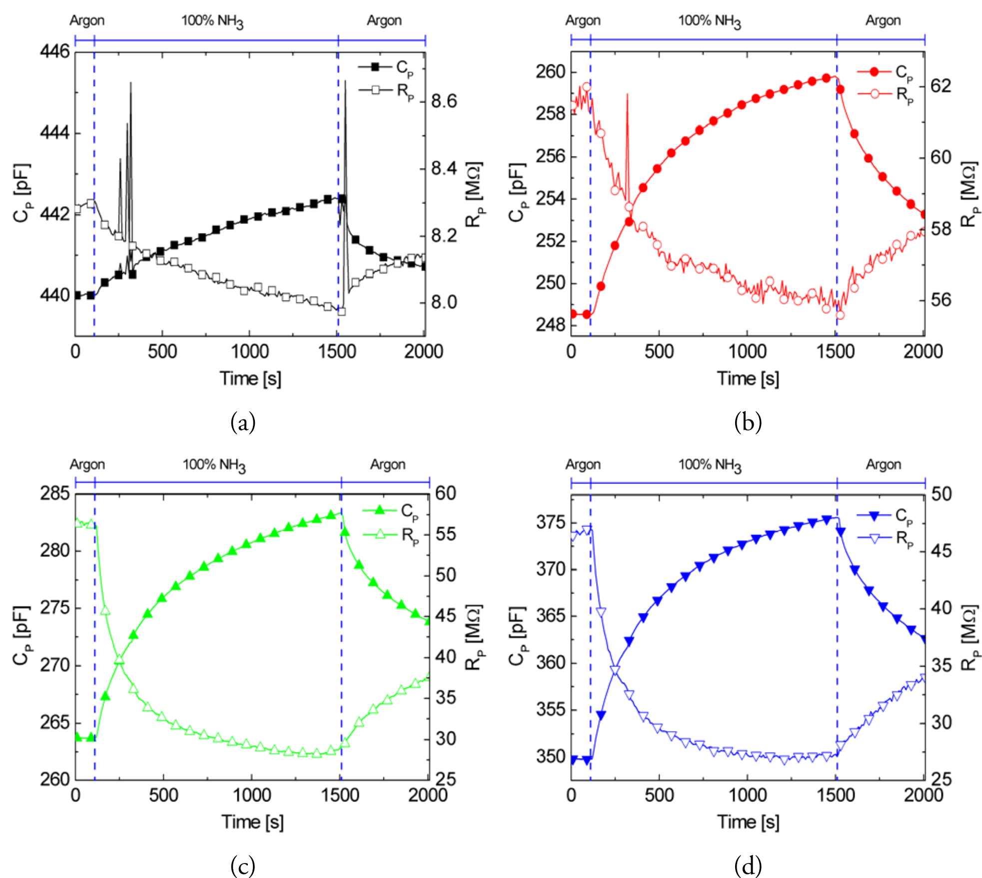

Figure 5.21: Parallel capacitance C_P and parallel resistance R_P of a typical ITO/dielectric/aluminum-capacitor with comb-shaped top-electrode upon exposure to argon and 100% NH_3 gas; a) PVA; b) reference polymer ***1c***; c) eosin Y-based polymer ***1a***; d) DCF-based polymer ***1b***.

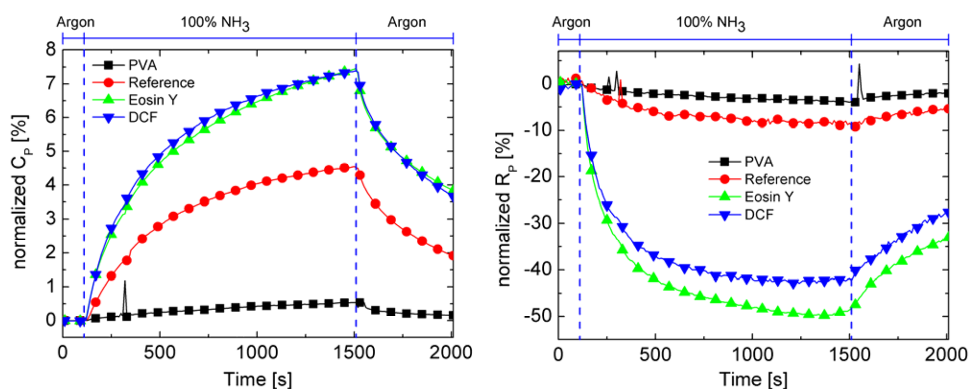

Figure 5.22: Parallel capacitance C_P and parallel resistance R_P (normalized to their values at 110 s) of typical ITO/dielectric/aluminum-capacitors with comb-shaped top-electrodes upon exposure to argon and 100% NH_3 gas.

The active-sensing polymers revealed the strongest response to ammonia exposure, leading to a capacitance increase of ~8% and a resistance decrease of ~50%, which was ascribed to the creation of mobile NH_4^+ ions by the deprotonation of the corresponding pH-sensitive groups.

The small change of the capacitance when using reference polymer ***1c*** is most probably a consequence of minor amounts of COOH groups present in the material, which do apparently not lead to the creation of a large amount of mobile ions upon NH_3 exposure, as the low relative decrease of R_P in Figure 5.22 right suggests. PVA-capacitors showed hardly any response.

The creation of mobile ions within the active-sensing dielectrics becomes even more evident, when investigating the effect of ammonia exposure on the normalized C_P and R_p values as a function of DC-bias voltage (Figure 5.23).

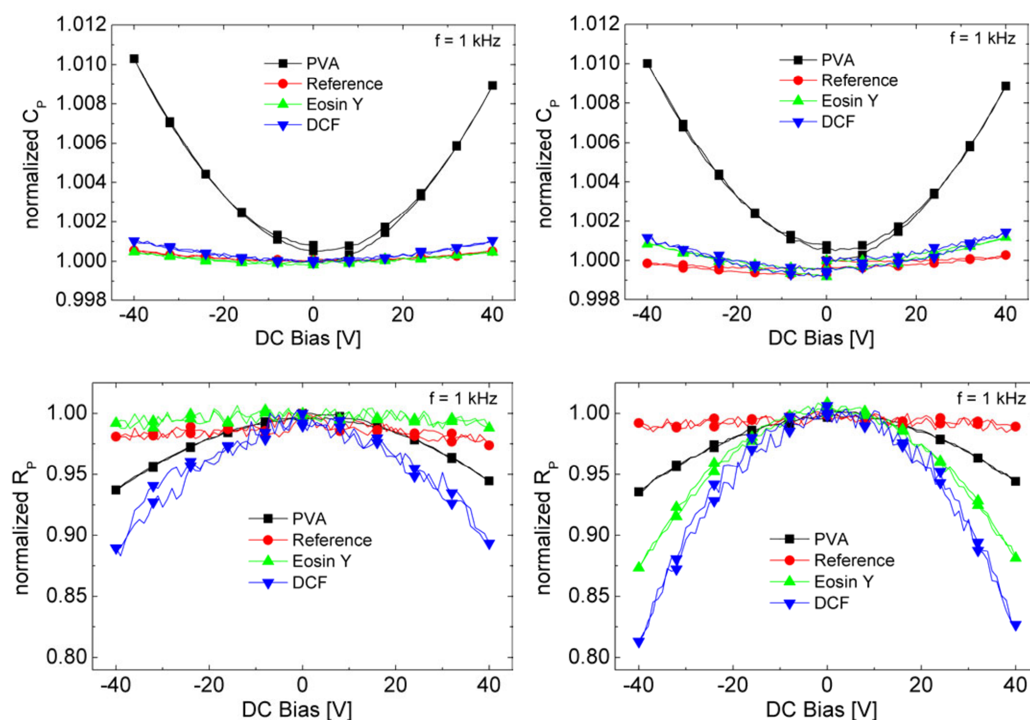

Figure 5.23: Parallel capacitance C_P and parallel resistance R_P (normalized to their values at 0V) as a function of DC-bias voltage of a typical ITO/dielectric/aluminum-capacitor with comb-shaped top-electrode on each sample before (left) and after (right) NH_3 exposure.

The $C_p(V)$-curves are rather similar before and after NH_3 exposure. PVA exhibits the strongest $C_p(V)$-dependence, which is ascribed to the orientation of the rather polar molecules of this material upon DC-voltage application and the formation of space-charges due to moving ions. Before NH_3 exposure the parallel resistances of reference polymer ***1c*** and eosin Y-based polymer ***1a*** only depend slightly on the DC-bias voltage. For PVA and DCF-based polymer ***1b*** R_P is distinctly reduced with increasing voltage. As mentioned, this is most probably due to mobile ions contained in the pristine materials, corresponding also to the presumably larger amount of already deprotonated active-sensing dyes observed in the UV/VIS-absorption spectra of polymer ***1b*** (Figure 5.9).

However, after NH_3 exposure the situation changes: while PVA and the reference polymer show a similar *$C_p(V)$*-behavior, indicating that the same amount of ions is present in the material, the reduction of R_p with increasing DC voltage is much more pronounced for the active-sensing polymers. This clearly demonstrates the reaction with ammonia, leading to an increased concentration of mobile (most probably NH_4^+) ions within polymers ***1a*** and ***1b***.

5.6. NH_3-SensFETs

With the findings of the UV/VIS-, FTIR- and capacitance measurements, top-gate/bottom-contact OFETs including the investigated ROM-polymers were to be fabricated. The following sections show the relevant results.

5.6.1. Preliminary Work - OFETs with Comb-shaped Top-Gate Electrode

In order to verify proper functioning of devices comprising a laterally structured top-gate electrode, two OFET samples including PVA as gate dielectric were prepared as described in chapter 4.4.2,[ff] one comprising a solid-shaped and one a comb-shaped aluminum common top-gate electrode.[296] Both architectures are schematically depicted in Figure 5.24, together with pictures of typical realizations.

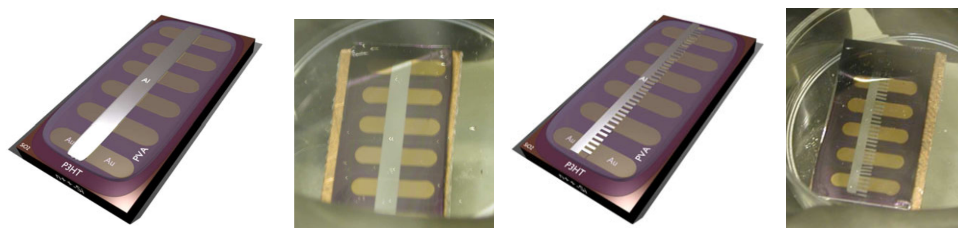

Figure 5.24: Schematic architectures and typical realizations of top-gate/bottom-contact OFET-samples based on PVA and rr-P3HT, one with a solid-shaped and one with a comb-shaped aluminum common top-gate electrode.

Figure 5.25 compares the transfer characteristics of two corresponding OFETs, showing that both perform comparably well, with the device including the solid-shaped top-gate electrode exhibiting slightly larger maximum source-to-drain currents, which most likely might be due to the effectively larger channel area covered by aluminum. With these results the architecture based on a laterally structured top-gate electrode was positively evaluated and could be applied to fabricate OFETs including active-sensing ROMP dielectrics.

[ff] With this device series PVA was dried at ~90°C in argon overnight after spin-casting.

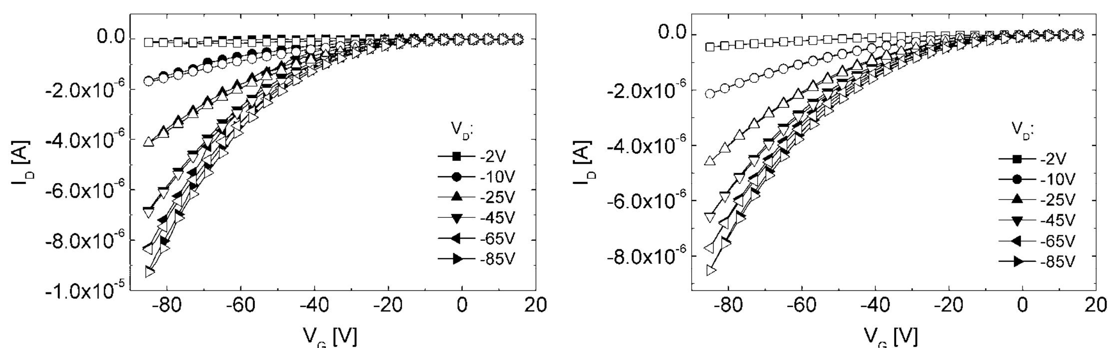

Figure 5.25: Transfer characteristics of typical top-gate/bottom-contact OFETs ($L \approx 20$ µm, $W \approx 2$ mm) based on PVA and rr-P3HT with solid-shaped (left) and comb-shaped (right) aluminum top-gate electrode; measured in argon; filled symbols: sweeps from positive to negative voltages; open symbols: reverse sweep.

5.6.2. First OFET-based Sensors

The applied ROM-polymers could only be dissolved in organic solvents such as $CHCl_3$ or THF. Accordingly, a semiconductor film of rr-P3HT or PTPA would have been dissolved by the subsequent deposition of a ROM-polymer layer. As a consequence, first devices including the ROMP dielectrics were prepared at Graz University of Technology with thermally evaporated pentacene as organic semiconductor, which, however, was also detached during ROM-polymer layer deposition in most OFETs.[324] Therefore first top-gate/bottom-contact OFETs containing the active-sensing ROM-polymers were realized according to the schemes depicted in Figure 5.26a and b.

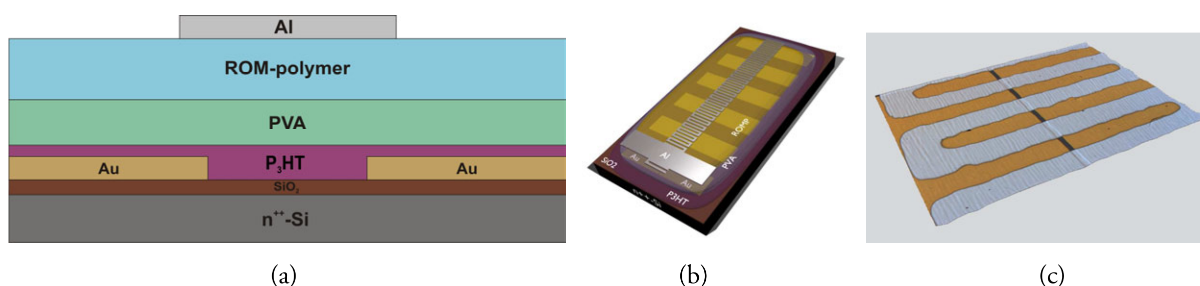

(a) (b) (c)

Figure 5.26: a) Scheme of SensFET device cross-section; b) 3D-scheme of 1st-generation SensFET samples (substrate dimensions: 0.5″x 1″, SiO_2-layer thickness: 200 nm); c) 3D-optical micrograph of a device with a meander-shaped aluminum top-gate in the channel region.

Because of the mentioned solution-incompatibility, water-based polyvinyl alcohol (Mowiol 5-88, see chapter 4.4) was applied as intermediate layer material, so that adjacent layers were deposited by orthogonal solvents. Due to the hydrophilic nature of PVA corresponding coatings are known to be highly resistant and impermeable to most organic solvents.[311]

Moreover, as found with the capacitance measurements, PVA does not react with ammonia, but conducts ions (even when dialyzed), in accordance with the results in chapter (4.4).

Source/drain-electrode definition and rr-P3HT-layer deposition of the presented devices were performed similar as described in chapter 4.4.2. PVA was spin-cast (2500 rpm, 60 s) from a ~9 wt% dialyzed hydrogel, dried for 1 h at 110°C in argon and then for several hours at 60°C in vacuum. ROMP dielectrics[gg] were spin-cast (1500 rpm, 40 s) from 60 mg/ml $CHCl_3$ solutions and dried for 10 min at 130°C on a hotplate. Finally, a ~100 nm thick meander-shaped common top-gate aluminum electrode covering six source/drain structures[hh] was thermally evaporated ($p < 3x10^{-5}$ mbar) through a shadow mask and devices were contacted with conductive silver paste. Figure 5.26c shows a 3D-optical micrograph of a device. The samples were then individually assembled in the sealable probe chamber (see section 5.4) under argon atmosphere and electrical device characterization was performed with an Agilent E5262A parameter analyzer.

The OFETs were alternately exposed to 100% argon and 1% and 3% ammonia (time interval: 2 min), respectively, during which the best-performing device was measured in active operation mode, meaning that the source-to-drain channel current at fixed V_G = -85V and V_D = -100V was recorded as a function of time. Figure 5.27 shows the sensor response in terms of the relative change of the channel current, normalized to the I_D value at 480 s, the start time of NH_3 inlet.

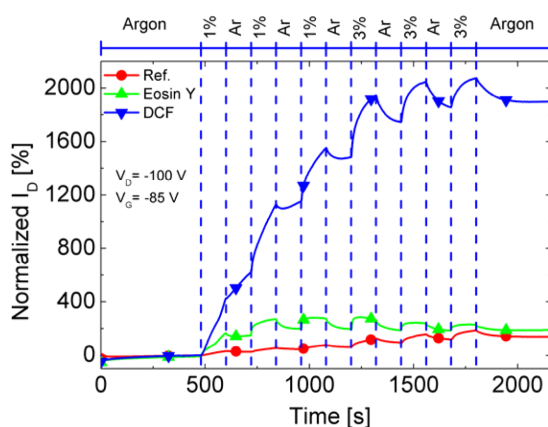

Figure 5.27: Relative change of source-to-drain channel current I_D (at V_D = -100V, V_G = -85V, normalized to I_D value at 200 s) as a function of time of first OFETs ($L \approx 50$ µm, $W \approx 2$ mm) based on various ROMP dielectrics upon exposure to argon, 1% and 3% NH_3.

[gg] For this device series an older batch of reference polymer ***1c*** (M_n: 54110 g/mol, *PDI*: 1.12), eosin Y-based polymer ***1a*** (M_n: 49050 g/mol, *PDI*: 1.12) and DCF-based polymer ***1b*** (M_n: 55350 g/mol, *PDI*: 1.13) was applied.

[hh] One source/drain structure is fully covered by the top-gate electrode for easy contacting within the probe chamber.

The devices based on the active-sensing ROMP dielectrics exhibited a distinct response to ammonia, in particular the DCF-based OFET with an overall increase of >2000% with respect to the start value at 480 s. At first the response was an accumulated one, meaning that the sensor signal resembles the total integrated analyte concentration exposed to the sensitive dielectric so far, which, however, saturated later on, most probably due to the limited number of "deprotonate-able" active dyes in these materials. Figure 5.28 depicts the output and transfer characteristics of typical devices containing the three ROMP dielectrics before and after NH_3 exposure.

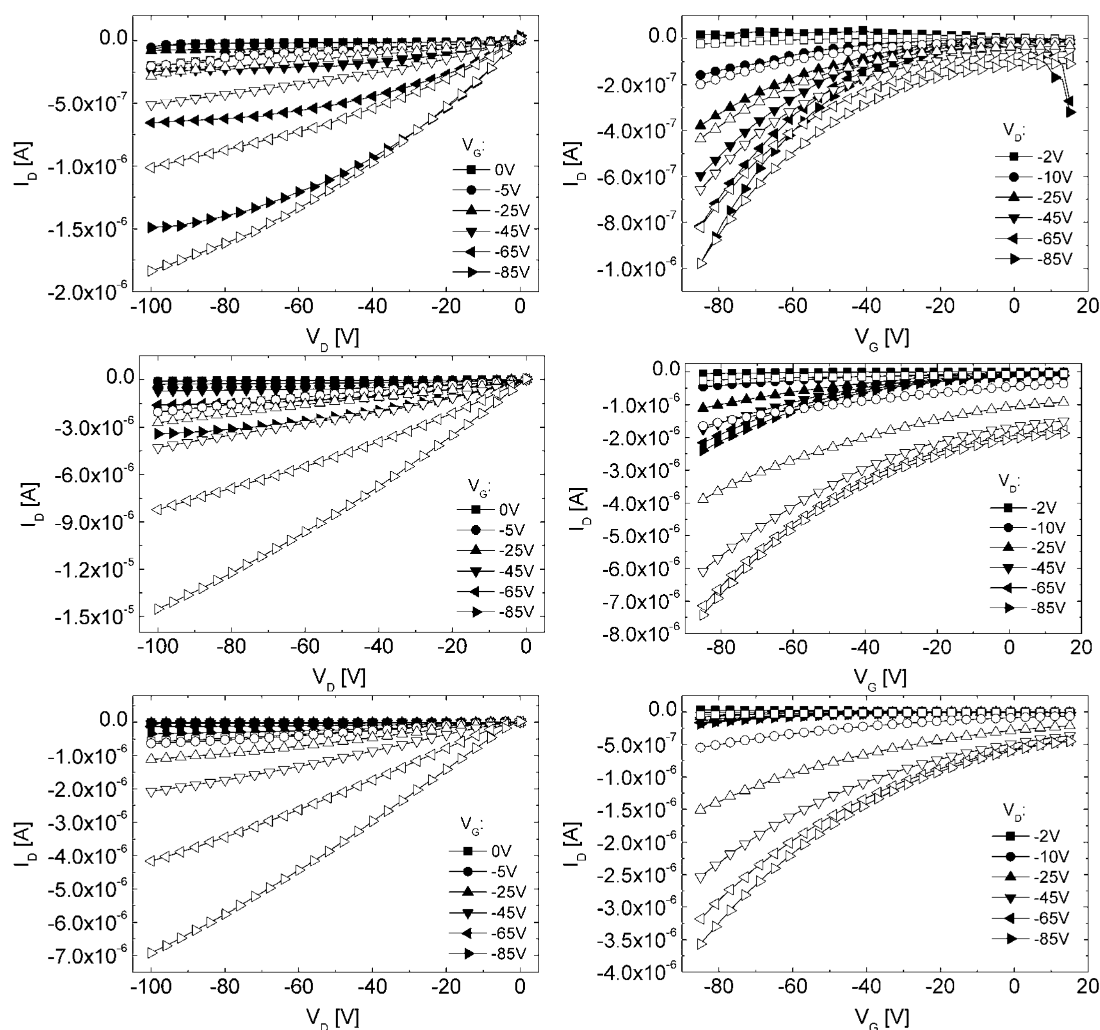

Figure 5.28: Output (left) and transfer (right) characteristics of typical OFETs ($L \approx 50$ µm, $W \approx 2$ mm) based on reference polymer ***1c*** (top), eosin Y-based polymer ***1a*** (middle) and DCF-based polymer ***1b*** (bottom) before (filled symbols) and after (open symbols) NH_3 exposure.

While the OFET including reference polymer ***1c*** showed a small change of the characteristics after analyte exposure, the devices containing the active-sensing dielectrics exhibited highly increased off- and on-currents afterwards.

A detailed possible response explanation will be given in section 5.6.6. Generally these OFETs showed high gate-leakage currents, a large device-to-device variation and poor reproducibility. Therefore, after the establishment of the new OFET fabrication line described in chapter 3.1, the sensor concept was realized and brought to demonstrator level with the new and highly sophisticated equipment within the cleanroom environment at NTC Weiz GmbH. The results are presented in the sections below.

5.6.3. Second-Generation SensFETs

Figure 5.29 schematically illustrates the 2nd-generation SensFET architecture with twelve devices on an n^{++}-Si wafer substrate (dimensions: 1″x 1″) with a thermally evaporated, 200 nm thick SiO_2 layer.

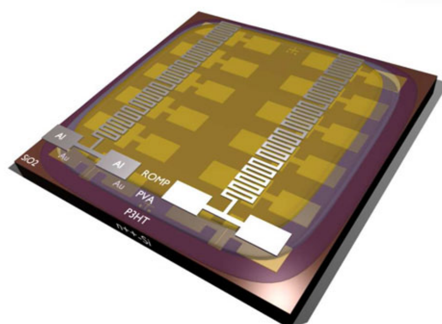

Figure 5.29: 2nd-generation SensFET sample architecture.

5.6.3.1. Device Fabrication and Microscope Analysis

Substrate pre-treatment (without HMDS application), source/drain-electrode structuring ($L \approx 25$ µm, $W \approx 2.85$ mm) and deposition and dedoping of the organic semiconductor film (rr-P3HT: M_n: 26900 g/mol, M_w: 37600 g/mol, layer thickness: 15-20 nm) was performed as described in chapter 3.1.3. A ~700 nm thick PVA intermediate layer was then deposited onto the organic semiconductor by spin-casting (2500 rpm, 60 s) from a 9-10 wt% dialyzed hydrogel. The samples were dried for 1 h at 110°C on a hot plate in argon and for 3 h at 60°C in vacuum ($p < 5x10^{-6}$ mbar). Afterwards a ~700 nm thick ***1a***-, ***1b***-, ***1c***- or ***1d***-ROM-polymer layer (batches 1 and 2) was spin-cast (1500 rpm, 40 s) from 60 mg/ml $CHCl_3$-solutions in argon and dried at 130°C for 10 min on a hot plate.

Devices were completed by thermal (shadow mask) evaporation of two ~100 nm thick, meander-shaped aluminum top-gate electrodes (p < 5x10^{-6} mbar, deposition rate: 8 Å/s), each of which covered six source/drain structures[ii] and enabled direct contact between analyte and ROMP dielectric. The samples were fixed on a single-sided copper board using conductive silver paste, which was also applied to the top-gate and source/drain-electrode pads[jj] for good contacts with the pogo pins of the probe chamber. For comparison, PVA-based OFETs without an additional active-sensing ROMP dielectric were prepared as well (PVA-layer thickness: ~850 nm, spin parameters: 1500 rpm, 60 s). Figure 5.30 shows typical samples in various preparation stages.

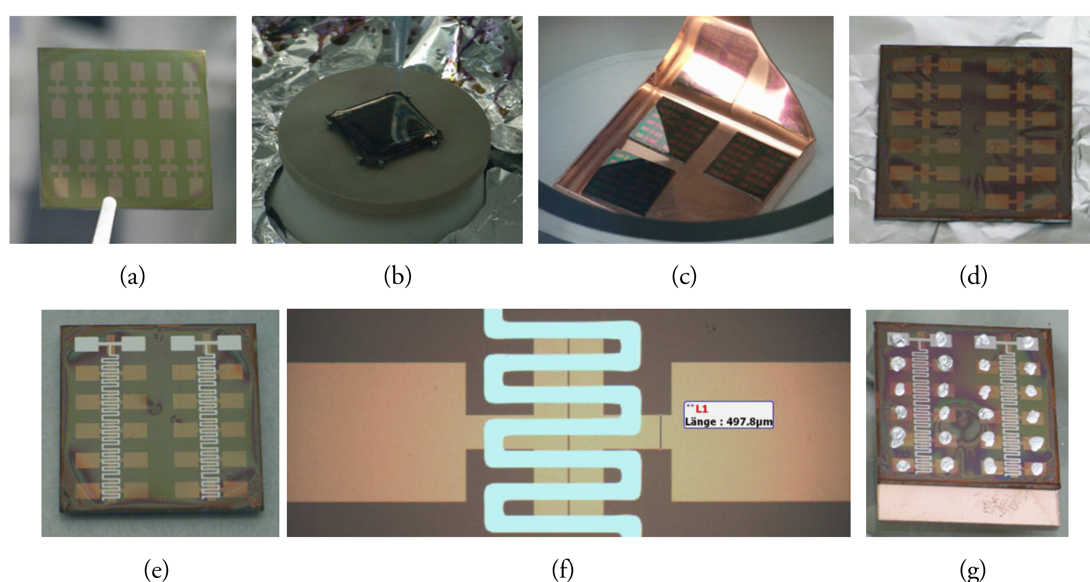

Figure 5.30: Typical SensFET samples in various preparation stages; a) after spin-casting rr-P3HT and device separation; b) spin-casting of PVA; c) curing of PVA layers; d) after spin-casting and drying ROM-polymer film; e) after evaporation of 100 nm aluminum top gate; f) single OFET-sensor; g) sample fixed on copper board and pads contacted with conductive silver paste.

[ii] One source/drain structure is fully covered by each gate electrode for easy contacting within the probe chamber.
[jj] ROMP and PVA layer were scratched with a manipulator needle for electrical contact to source/drain electrodes.

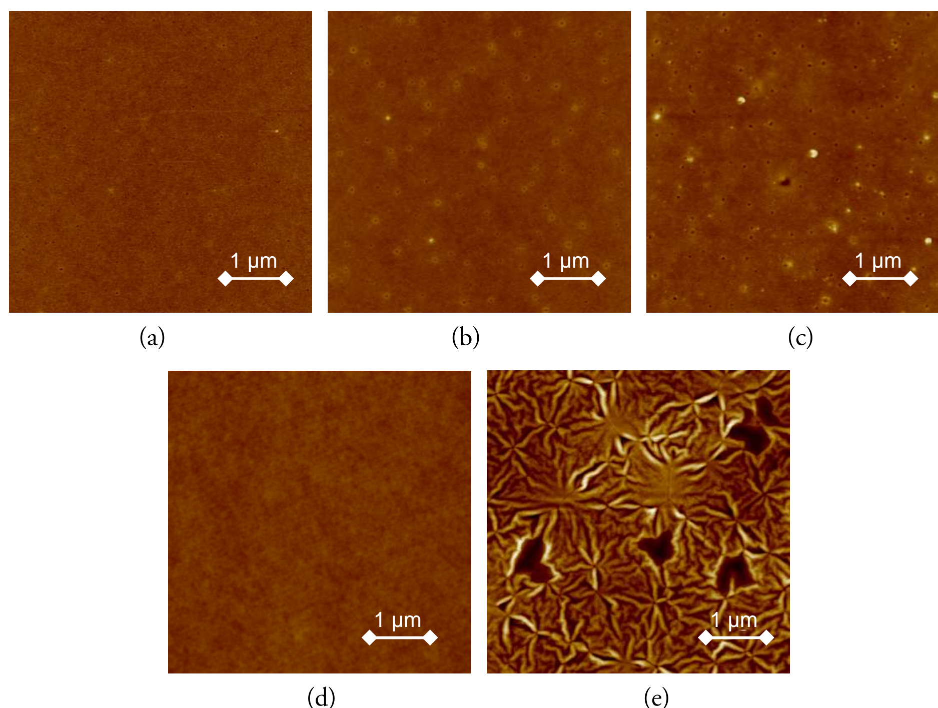

Figure 5.31: AFM-height images of various PVA/ROM-polymer dielectric films in OFET-devices: a) PVA + reference polymer ***1c*** ($d \approx$ 1360 nm); b) PVA + eosin Y-based polymer ***1a*** ($d \approx$ 1440 nm); c) PVA + DCF-based polymer ***1b*** ($d \approx$ 1350 nm); d) PVA solely ($d \approx$ 850 nm); e) PVA + eosin Y-based polymer ***1a*** ($d \approx$ 1360 nm, other sample); scan size: 5 µm; color code from black to white corresponds to a z-data range of 20 nm (for e: 50 nm).

Figure 5.31 illustrates AFM-height images of various PVA/ROM-polymer films in OFET devices, showing similar layer thickness for all dielectrics. While most films were rather smooth, few samples exhibited similar surface morphology as shown in Figure 5.31e. This might have resulted from a partial crystallization within some PVA layers due to mutual orientation of the polar polymer chains,[311,338,339] which can also influence the morphology of the ROM-polymer film deposited on top. Heat treatment might have been responsible for the formation of such crystalline regions. However, the reason, why some layers revealed such morphology and some did not, could not be completely identified. Nevertheless, the sensor response was similarly observed for both smooth and structured surface morphologies.

5.6.3.2. Electrical Characteristics of Sensor-OFETs

After their fabrication the samples were transported to Graz University of Technology under sealed conditions, where they were individually assembled in the sealable probe chamber described in section 5.4 under argon atmosphere. Electrical device characterization was performed with an Agilent E5262A Parameter Analyzer.

a) Before ammonia exposure

Figure 5.32 shows the output and transfer characteristics of typical OFETs based on the ROM-polymers and PVA before NH_3 exposure, measured in argon. Table 10 below summarizes important device parameters. The OFETs exhibited good performance with well-defined saturation behavior, on/off-current ratios between 10^2 and 10^3 and low gate-leakage currents. The device including eosin Y-based polymer ***1a*** showed the largest difference between the channel current values at a particular V_D and (high) V_G (e.g. at $V_D = V_G = -85V$) in the transfer and output characteristics, which is a sign for charge-trapping behavior (see also chapter 3.2.3). This is also confirmed by the large hysteresis and the rather large subthreshold slope, the latter being linked to the maximum interfacial trap density (see chapter 2.2.2.4). For the OFET with DCF-based polymer ***1b*** hysteresis is negligible and channel currents at e.g. $V_D = V_G = -85V$ are similar in the output and transfer characteristics, which indicates that charge-trapping is not an issue and probably results from already present ions in the material, corresponding to the results of the UV/VIS- and capacitance measurements (see also chapter 4.4). This will be made clearer in section 5.6.6.

The devices based on PVA alone exhibited the largest off- and on-currents, the largest field-effect mobility values and positive switch-on voltages, which is ascribed to the thinner dielectric layer in combination with semiconductor doping by the hydrogel[340] and possibly a space charge polarization and/or formation of an electric double layer due to residual mobile Na^+ ions, effects, which seem to be reduced by the addition of a ROM-polymer dielectric. The device-to-device variation on each sample will be shown later.

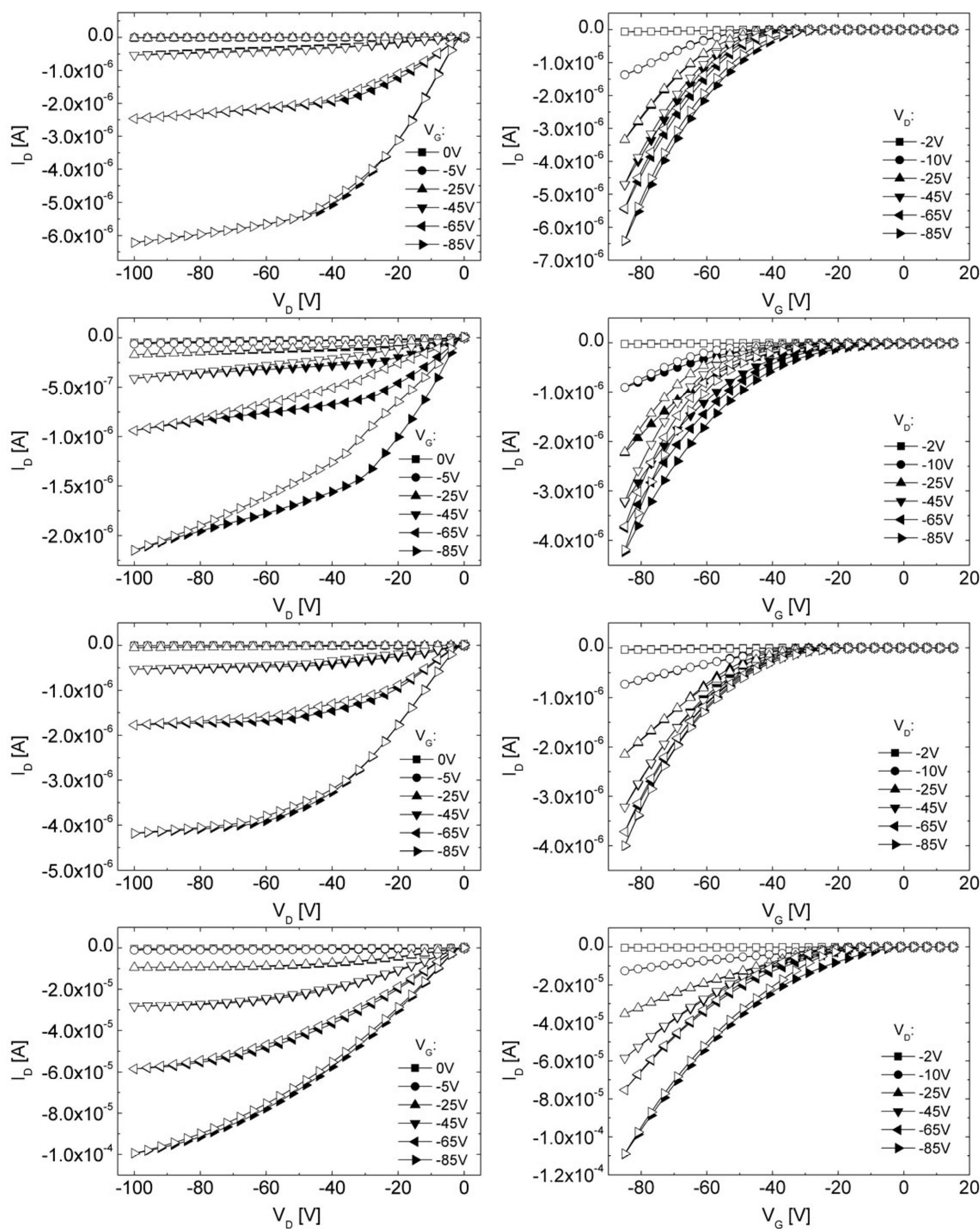

Figure 5.32: Output (left) and transfer (right) characteristics of typical OFETs ($L \approx 25$ µm, $W \approx 2.85$ mm) based on ROMP dielectrics (batch 1) and PVA before NH_3 exposure; from top to bottom: reference polymer ***1c***, eosin Y-based polymer ***1a***, DCF-based polymer ***1b*** and PVA-solely; filled symbols: sweeps from positive to negative voltages; open symbols: reverse sweep.

b) During ammonia exposure

For a single device the source-to-drain channel current I_D at V_D = -100V and V_G = -85V was then monitored upon exposure to 1% ammonia at a flow rate of 10 l/h.

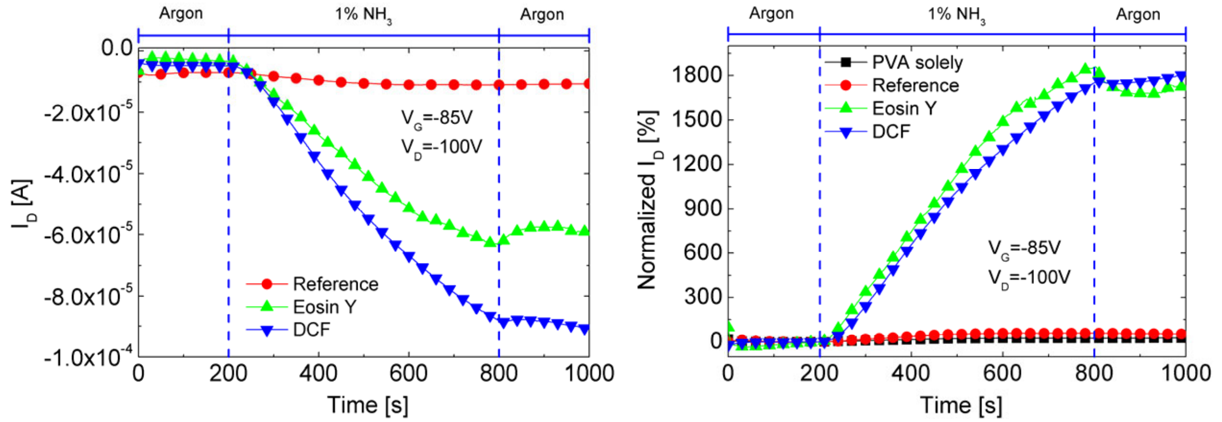

Figure 5.33: Left: source-to-drain channel current I_D (at V_D = -100V, V_G = -85V) as a function of time of OFETs based on various ROMP dielectrics (batch 1) upon exposure to argon and 1% NH_3; right: corresponding sensor response in terms of the relative change of channel current (normalized to I_D value at 200 s) including also a device based on PVA solely; for all: $L \approx 25$ µm, $W \approx 2.85$ mm.

Figure 5.33 left illustrates the corresponding I_D(t)-curves for OFETs including either ROM-polymer ***1a***, ***1b*** or ***1c***. While devices containing reference material ***1c*** showed hardly any response, there is an immediate increase of I_D of OFETs including the two active-sensing dielectrics ***1a*** and ***1b***. When calculating the relative change of the channel current, normalized to the I_D value at 200 s, the start time of NH_3 inlet, and plotting it as a function of time (as done in Figure 5.33 right), the channel current was found to increase to ~1800% after 600 s of NH_3 exposure. After stopping the analyte exposure, the sensor signal remained almost constant. The corresponding gate-leakage currents did not change significantly during NH_3 exposure (Figure 5.34).

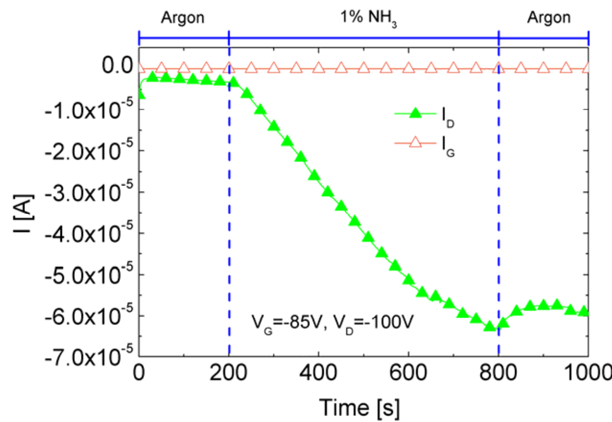

Figure 5.34: Source-to-drain channel current I_D and gate-leakage current I_G (at V_D = -100V, V_G = -85V) as a function of time of an OFET-sensor ($L \approx 25$ µm, $W \approx 2.85$ mm) comprising eosin Y-based polymer ***1a*** upon exposure to argon and 1% NH_3.

c) After ammonia exposure

Figure 5.35 illustrates the corresponding output and transfer characteristics after exposure to 1% NH_3 for 600 s. Note the different scale on the y-axes compared to Figure 5.32, in particular for the devices including the active-sensing dielectrics.

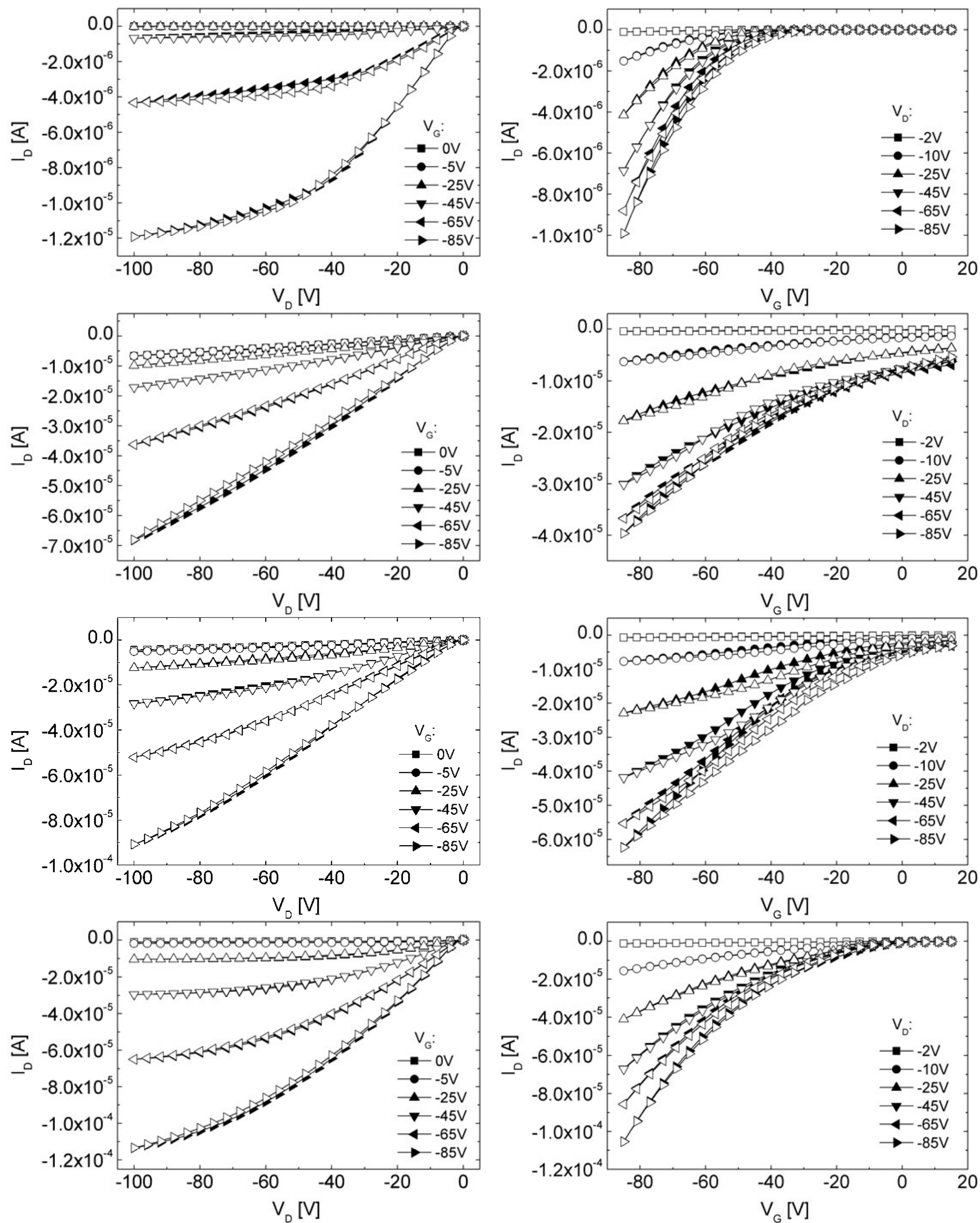

Figure 5.35: Output (left) and transfer (right) characteristics of typical OFETs ($L \approx 25$ µm, $W \approx 2.85$ mm) based on ROMP dielectrics (batch 1) and PVA after exposure to 1% NH_3; from top to bottom: reference polymer ***1c***, eosin Y-based polymer ***1a***, DCF-based polymer ***1b*** and PVA-solely; filled symbols: sweeps from positive to negative voltages; open symbols: reverse sweep.

The sensor response becomes even more evident in the graphs shown in Figure 5.36, where the semi-logarithmic transfer curves at V_D = -85V of several devices on each sample are compared before and after 1% NH_3 exposure for 600 s. They also reveal the low device-to-device variation on each sample. The comparison in Figure 5.37 proves that the response is obvious even at small drain voltages.

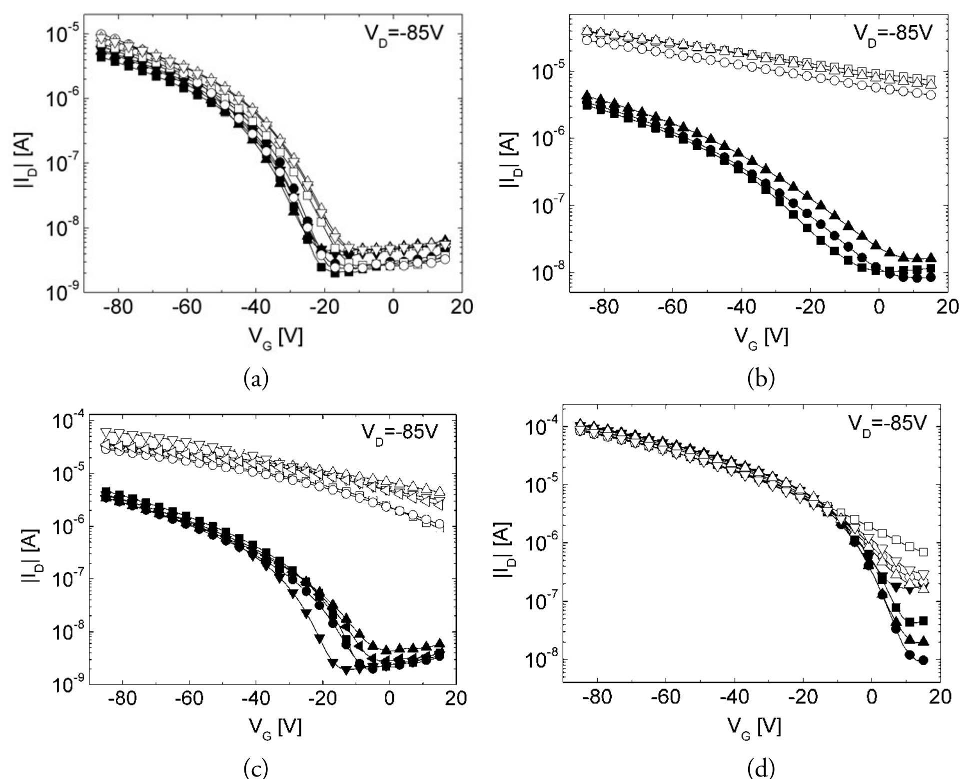

Figure 5.36: Semi-logarithmic transfer curves at V_D = -85V of several OFETs ($L \approx 25$ µm, $W \approx 2.85$ mm) based on ROMP dielectrics (batch 1) and PVA before (filled symbols) and after (open symbols) exposure to 1% NH_3; a) reference polymer ***1c***; b) eosin Y-based polymer ***1a***; c) DCF-based polymer ***1b***; d) PVA solely.

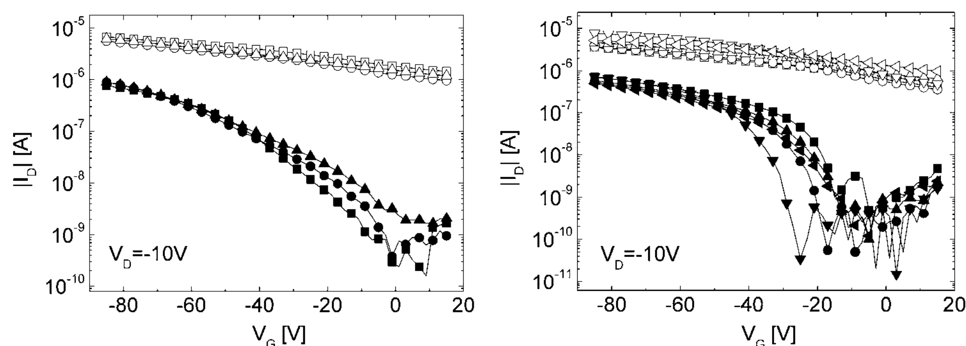

Figure 5.37: Semi-logarithmic transfer curves at V_D = -10V of several OFETs ($L \approx 25$ µm, $W \approx 2.85$ mm) based on ROMP dielectrics (batch 1) before (filled symbols) and after (open symbols) exposure to 1% NH_3; left: eosin Y-based polymer ***1a***; right: DCF-based polymer ***1b***.

While the characteristics of PVA-only devices and OFETs including reference polymer ***1c*** exhibited rather small changes after NH_3 exposure, the OFETs based on the active-sensing polymers ***1a*** and ***1b*** showed a distinct response, reflected by a large increase of on-currents, off-currents[kk] and field-effect mobility values as well as a large shift of the switch-on- and threshold voltages to more positive values. Table 10 summarizes the relevant device parameters. When comparing the channel current values at a particular working point (e.g. $V_D = V_G = -85V$) in the output and transfer characteristics after NH_3 (Figure 5.35), they are distinctly larger in the former, in particular for the active-sensing devices. Also the hysteresis of OFET-sensors in the transfer characteristics is much reduced (polymer ***1a***) or even exhibits an increasing channel current between forward and reverse sweep (polymer ***1b***). Similar behavior has also been observed in chapter 4.4. A detailed explanation for these changes will be given in section 5.6.6.

Table 10: Relevant device parameters of OFETs ($L \approx 25$ mm, $W \approx 2.85$ mm) before (1st value in a field) and after (second value in a field) exposure to 1% NH_3; C_i was calculated assuming a dual layer dielectric with relative permittivity values from Table 9 and a layer thickness d_i of 680 nm for the ROM-polymer and PVA layer, respectively; for the device including PVA solely d_i was 850 nm; μ_{Lin} (at V_D = -10V, V_G = -60V) and μ_{Sat} (at V_D = -85V, V_G = -30V) were calculated with equations (2.14) and (2.15), V_{SO}, V_{th}, S and I_{on}/I_{off} (I_{on}: V_G = -85V, I_{off}: V_G = 0V) were extracted from the transfer curves at V_D = -85V; gate-leakage currents I_G were determined at $V_G = V_D$ = -85V.

OFET / SensFET based on	C_i [nF/cm²]	μ_{Lin} [cm²/Vs]	μ_{Sat} [cm²/Vs]	V_{SO} [V]	V_{th} [V]	S [V/dec]	I_{on}/I_{off}	I_G [nA]
*Reference polymer **1c** - batch 1*	4.33	6.0×10^{-3} 5.8×10^{-3}	3.2×10^{-3} 2.1×10^{-3}	-19 -19	-27 -31	8.1 9.0	2×10^{3} 4×10^{3}	~20 ~8
*Eosin Y-based ROM-polymer **1a** - batch 1*	4.37	3.6×10^{-3} 1.4×10^{-2}	1.5×10^{-3} 6.8×10^{-3}	+5 >+20	-14 +54	26.7 n.e.	2×10^{2} 5	~16 ~30
*DCF-based ROM-polymer **1b** – batch 1*	3.82	3.5×10^{-3} 2.2×10^{-2}	2.4×10^{-3} 2.1×10^{-2}	-15 >+20	-21 +18	8.4 n.e.	2×10^{3} 1×10^{1}	~20 ~10
PVA solely	8.75	1.8×10^{-2} 2.2×10^{-2}	2.1×10^{-2} 1.8×10^{-2}	+11 +11	+1 +2	8.7 16.6	3×10^{2} 1×10^{2}	~280 ~300

d) Determination of detection limit and sensor response as a function of concentration

The graphs in Figure 5.38 illustrate the sensor response of OFETs including ROM-polymers ***1a***, ***1c*** (both from batch 2) and ***1d***, indicating that it is easily possible to detect ammonia concentrations as low as 100 ppm with such a SensFET device. Moreover, when monitoring the change of the slope of the $I_D(t)$-curves, response times on the order of seconds can be obtained. Compared to the device with polymer ***1a***, the OFET including ***1d*** exhibited a slightly smaller response.

[kk] The off-current was increased relatively more than the on-current, resulting in a reduced on/off-current ratio.

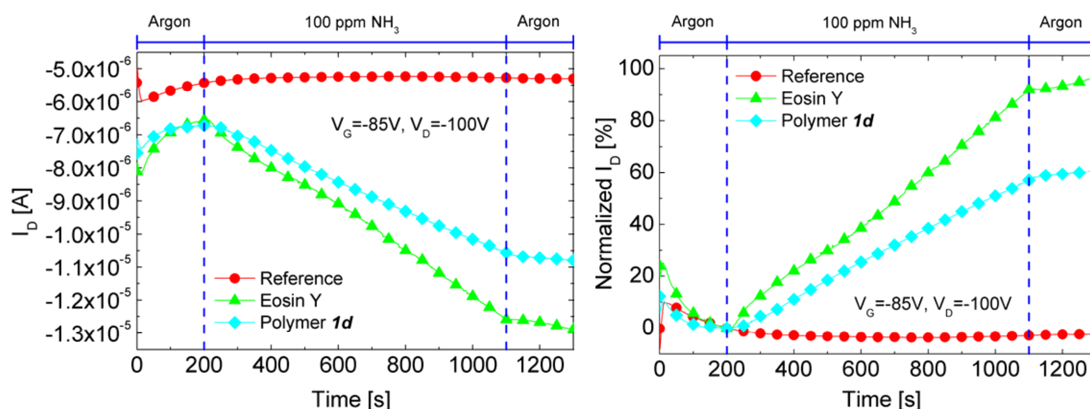

Figure 5.38: Left: source-to-drain channel current I_D (at V_D = -100V, V_G = -85V) as a function of time of OFETs based on various ROMP dielectrics (batch 2) upon exposure to argon and 100 ppm NH_3; right: corresponding sensor response in terms of the relative change of channel current (normalized to I_D value at 200 s); for all: $L \approx 25$ µm, $W \approx 2.85$ mm.

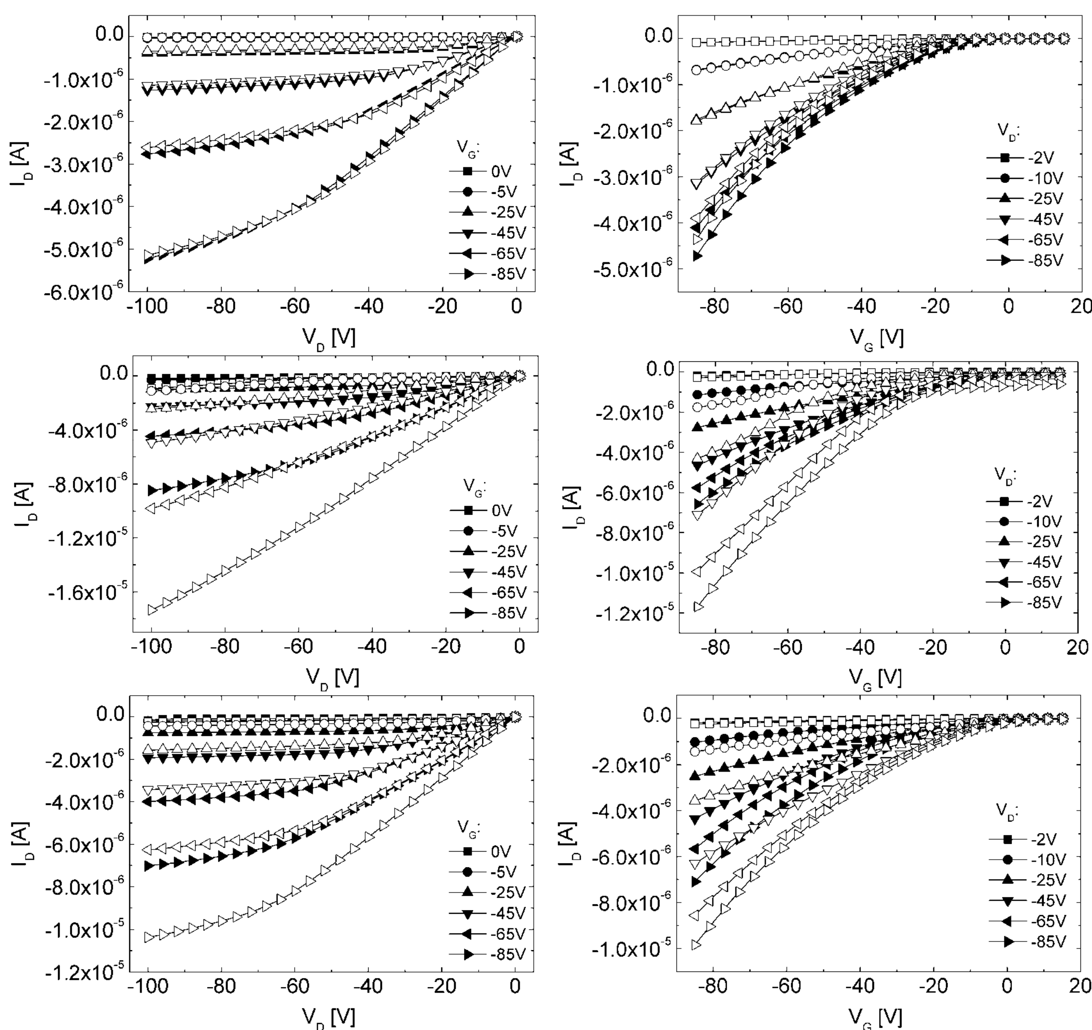

Figure 5.39: Output (left) and transfer (right) characteristics of typical OFETs ($L \approx 25$ µm, $W \approx 2.85$ mm) based on ROMP dielectrics (batch 2) before (filled symbols) and after (open symbols) exposure to 100 ppm NH_3; from top to bottom: reference polymer ***1c***, eosin Y-based polymer ***1a*** and polymer ***1d***.

Figure 5.39 again confirms the capability of the OFET-sensors by comparing the corresponding output and transfer characteristics before and after exposure to 100 ppm NH_3 for 900 s.

Figure 5.40 left shows an I_D(t)-curve of an OFET-sensor with eosin Y-based polymer ***1a*** upon exposure to increasing concentrations of NH_3, also including linear fits of the channel current increase. While no significant difference is observable between the current increase rates during 0.66 ppm and 10 ppm NH_3 exposure, exposure to 100 ppm reveals a distinct change, confirming that the current increase rate is associated with the NH_3 concentration and also revealing a detection limit of 100 ppm at this particular working point. Figure 5.40 right shows the transfer curves of the corresponding device before and after analyte exposure.

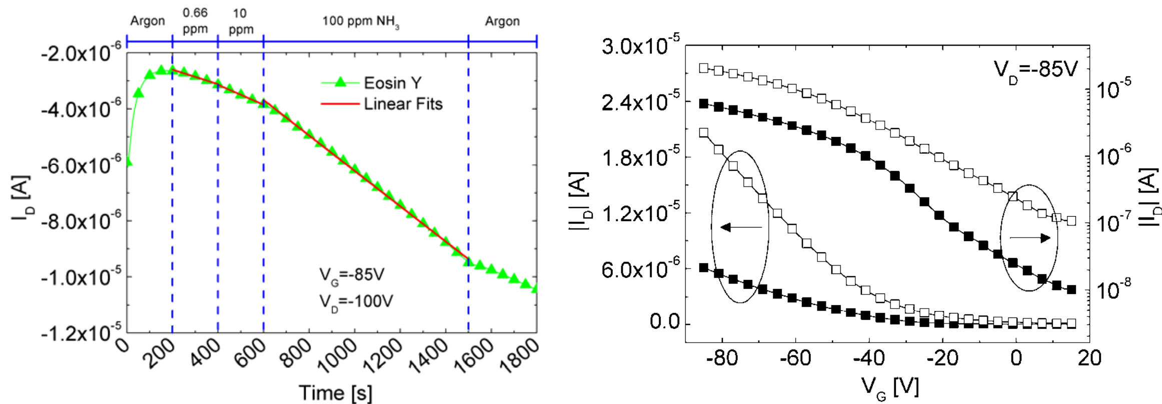

Figure 5.40: Left: source-to-drain channel current I_D (at V_D = -100V, V_G = -85V) as a function of time of an OFET-sensor ($L \approx 25$ µm, $W \approx 2.85$ mm) with eosin Y-based polymer ***1a*** (batch 1) upon exposure to argon and increasing NH_3 concentrations; right: corresponding transfer curves (linear and semi-logarithmic) before and after NH_3 exposure.

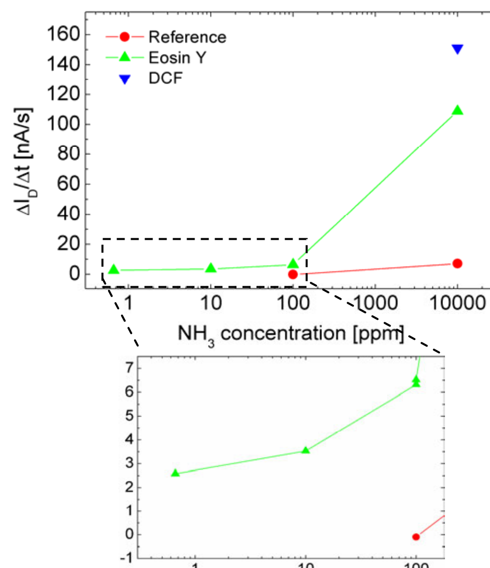

Figure 5.41: Increase rate of the source-to-drain channel current I_D (at V_D = -100V, V_G = -85V) as a function of NH_3 concentration of various ROMP-based OFETs ($L \approx 25$ µm, $W \approx 2.85$ mm); determined by linear fits of the corresponding I_D(t)-curves.

The plot in Figure 5.41 shows the channel current increase rates (at V_D = -100V, V_G = -85V) of several ROMP-based OFETs as a function of NH_3 concentration, calculated from linear fits of the corresponding I_D(t)-curves. Obviously, the rates exhibit a distinct concentration-dependence. However, at least the value at 0.66 ppm must be interpreted with care, as it may just be ascribed to a drift of a small amount of ions already present within the PVA/ROM-polymer layers.

e) Sensor behavior after storage in air

The output and transfer characteristics of an OFET-sensor including eosin Y-based polymer ***1a*** (batch 1) in Figure 5.42 were also recorded before and after exposure to 1% ammonia. However, the devices of this sample were stored under ambient conditions for ~16 h before,[ll] still showing a distinct sensor response afterwards.

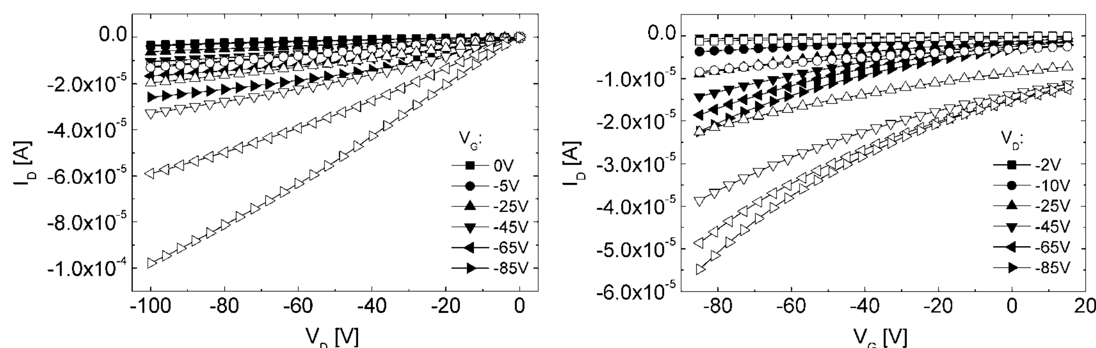

Figure 5.42: Output (left) and transfer (right) characteristics of a typical OFET-sensor ($L \approx 25$ µm, $W \approx 2.85$ mm) with eosin Y-based polymer ***1a*** (batch 1) before (filled symbols)[mm] and after (open symbols) exposure to 1% NH_3 for 10 min; stored in air for ~16 h.

5.6.4. OFETs based on ROM-Polymers and $PTPA_3$ as Organic Semiconductor

In order to test for the influence of the organic semiconductor on the sensing behavior, top-gate/bottom-contact OFETs including the ROMP dielectrics were prepared with $PTPA_3$ (M_n: 15300 g/mol, M_w: 71200 g/mol, $CHCl_3$ solution concentration: 2 mg/ml, see Figure 4.1) as organic semiconductor and investigated upon exposure to 1% NH_3. The device fabrication was similar as for the rr-P3HT-based devices. Figure 5.43 and Figure 5.44 show the corresponding results. Obviously, the devices did not exhibit a very distinct response to gaseous NH_3. Although the channel current of the $PTPA_3$-OFET including active-sensing polymer ***1a*** showed an increase of I_D at the beginning of NH_3 exposure, it soon started to decrease again.

[ll] The sample was also assembled in the probe chamber under ambient conditions (see Figure 5.14b).
[mm] The curves before 1% ammonia exposure (filled symbols) were recorded after the device had already been exposed to 100 ppm NH_3 for three times (in total 480 s).

Overall, the channel current reduction observed with $PTPA_3$-based OFETs is ascribed to charge-trapping behavior. Thus, it seems that only an appropriate material combination of active-sensing ROMP dielectric and organic semiconductor leads to the desired sensing behavior. This will become clearer in section 5.6.6, where a detailed possible explanation for the sensor response will be given.

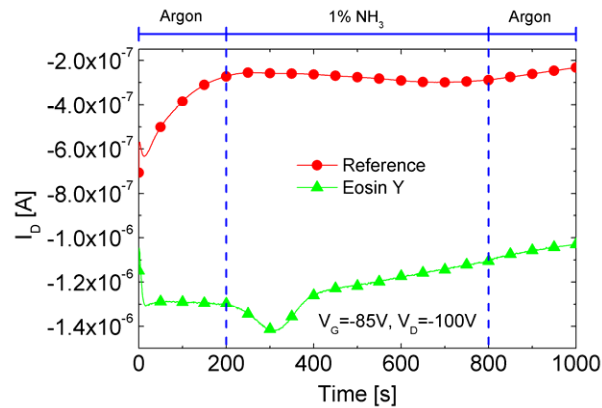

Figure 5.43: Source-to-drain channel current I_D (at V_D = -100V, V_G = -85V) as a function of time of OFETs ($L \approx 25$ µm, $W \approx 2.85$ mm) based on ROMP dielectrics ***1a*** and ***1c*** (batch 2) and $PTPA_3$ as organic semiconductor upon exposure to argon and 1% NH_3.

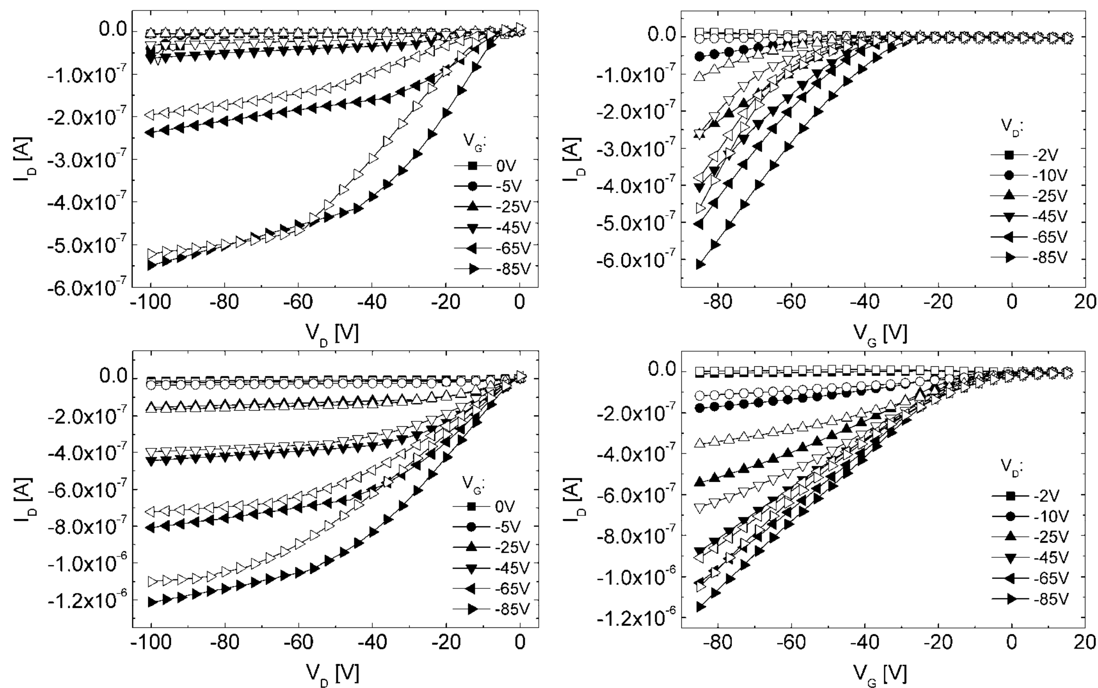

Figure 5.44: Output (left) and transfer (right) characteristics of typical OFETs ($L \approx 25$ µm, $W \approx 2.85$ mm) based on ROMP dielectrics (batch 2) and $PTPA_3$ as organic semiconductor before (filled symbols) and after (open symbols) exposure to 1% NH_3; top: reference polymer ***1c***; bottom: eosin Y-based polymer ***1a***.

5.6.5. Direct Interaction between rr-P3HT and Ammonia

Assadi and co-workers have already observed that mobility and conductivity of P3HT-OFETs *decrease* upon exposure to NH_3 gas, which was ascribed to changes in the hopping conditions for charge transfer between the polymer chains.[322] Similar results were also obtained by other groups.[341,342] As the SensFETs presented above exhibited a channel-current *increase* during NH_3 exposure, this proves that the sensor response can not be ascribed to a direct interaction between rr-P3HT and NH_3. Nevertheless, due to the results of the previous section and in order to verify the findings of Assadi and co-workers with our materials and device configuration, corresponding bottom-gate/bottom-contact OFETs were fabricated according to the procedure described in chapter 3.1.3. The scheme is depicted in Figure 5.45 left.

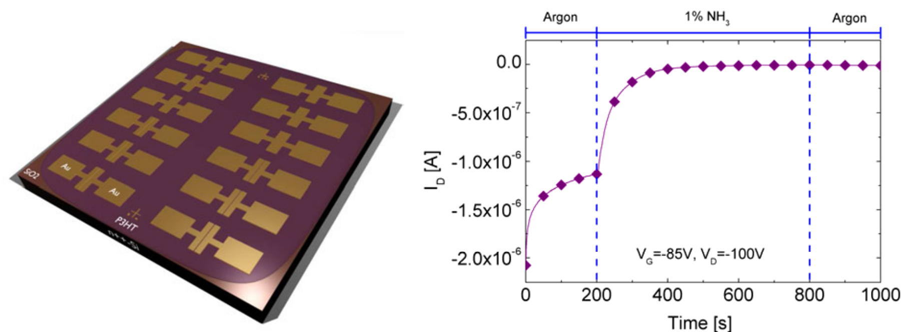

Figure 5.45: Left: scheme of a sample with twelve bottom-gate/bottom-contact OFETs based on rr-P3HT; right: source-to-drain channel current I_D as a function of time of a corresponding device ($L \approx 25$ µm, $W \approx 2.85$ mm) upon exposure to argon and 1% NH_3.

The I_D(t)-curve in Figure 5.45 right proves that also our devices revealed the expected reduction of the channel current upon NH_3 exposure.[nn] The electrical device characteristics in Figure 5.46 show a reduction of the maximum channel current to ~1/3 of the values before analyte exposure.

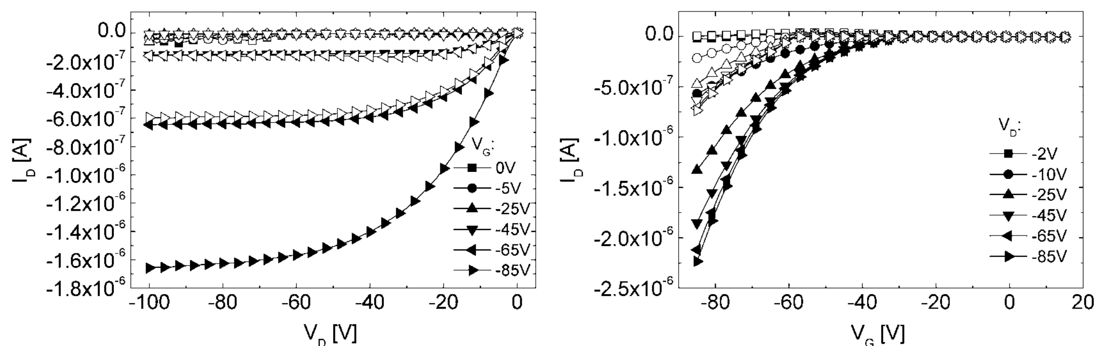

Figure 5.46: Output (left) and transfer (right) characteristics of a typical bottom-gate/bottom-contact OFET ($L \approx 25$ µm, $W \approx 2.85$ mm) based on rr-P3HT before (filled symbols) and after (open symbols) exposure to 1% NH_3 for 10 min.

[nn] The I_D reduction during the first 200 s is ascribed to charge-carrier trapping at the rr-P3HT/SiO_2-interface.

5.6.6. Explanation of the Sensor Response

5.6.6.1. Qualitative Explanation

Analyzing the results above, an interaction between aluminum and NH_3 can be excluded to be responsible for the obtained sensor signal, since this metal was applied as top-gate electrode in all devices. Moreover, PVA-based OFETs without an additional active-sensing ROMP dielectric did not show any response to NH_3, corresponding to the results of the capacitance measurements. As for a possible interaction between analyte and organic semiconductor, we observed the expected channel-current reduction in rr-P3HT-based bottom-gate/bottom-contact OFETs upon ammonia exposure, hence excluding this mechanism in the top-gate OFET-sensors as well. Therefore, taking also into account UV/VIS-, FTIR- and capacitor analyses, the sensor response is most likely induced by NH_4^+ ions and corresponding counter-ions, which are created by the chemical interaction between ammonia and the dye-bearing, pH-sensitive groups of the active-sensing ROM-polymers. The mobile NH_4^+ ions are assumed to move within the dielectric materials into the direction of the drain electrode. During ammonia exposure and recording of the corresponding I_D(t)-curves the devices were operated in the saturation regime at V_G = -85V and V_D = -100V, resulting in a potential difference between top-gate and drain electrode of 15V and hence a corresponding electric field ($E_{GD} = V_G$-V_D/d_i) with a field strength of ~10^5 V/cm, taking into account a total dielectric layer thickness of ~1400 nm. This certainly leads to the described movement of the ions. They localize near the drain region at the PVA/semiconductor interface or even in the rr-P3HT layer, where they increase the density of mobile positive polarons in the semiconductor by several possible interactions (Figure 5.47).

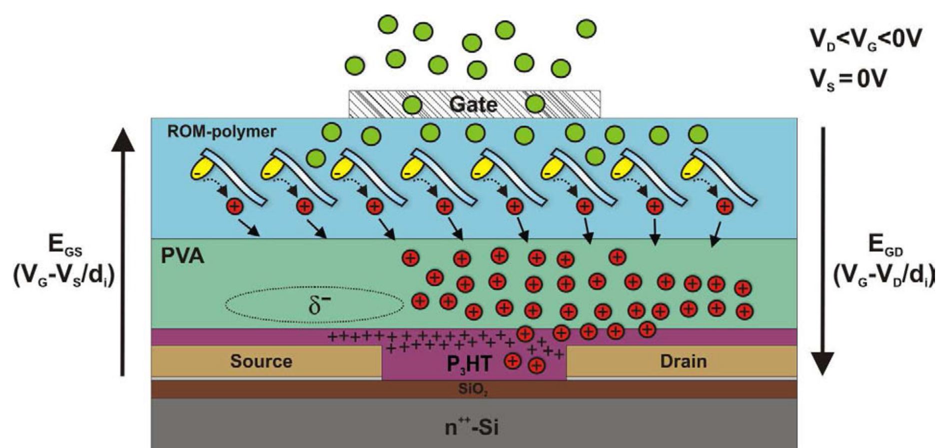

Figure 5.47: SensFET response explanation (green circles = NH_3 molecules, red circles = NH_4^+ ions, δ^- = space charge resulting from immobile (or less mobile) negatively charged counter-ions, + = positive polarons in the channel.

As pointed out in chapter 4.4, the ions might reduce the charge-*ejection* barrier between gold and rr-P3HT and thus the associated contact resistance by the formation of a thin electric double layer or by electrochemical doping as found in an LEC.[315,316] The width of the depletion region is most likely also reduced by the presence of positive ions near the drain side, which would explain the observed non-saturated channel currents for $|V_D| > |V_G|$ after NH_3 exposure (Figure 5.35). Moreover, trapped charges within rr-P3HT, at the PVA/rr-P3HT interface or within PVA might be released due to the positive space charge of the NH_4^+ ions.

Near the source electrode the density of positive ions is most likely reduced due to an electric field between source and gate (E_{GS}) pointing into the direction of the gate (the source potential was always kept at 0V). Therefore a space charge (δ^-) resulting from immobile negatively charged counter-ions may enhance E_{GS}[128] and/or reduce the charge-*injection* barrier between gold and rr-P3HT, accordingly increasing the charge carrier density in the channel. Possibly, also mobile negative ionic impurities are contained within the dielectrics, leading to an electric double layer near the source side or even to electrochemical doping of the semiconductor (see also chapter 2.2.1.3).[343,344] In fact, doping of rr-P3HT was only excluded for direct interaction with gaseous NH_3 (chapter 5.6.5).

The fact that devices including $PTPA_3$ did not reveal a pronounced sensing response, which apparently depends on an appropriate material combination, might be associated with its larger ionization potential compared to rr-P3HT (see also chapter 4), making the material more "resistant" against e.g. electrochemical doping.

All these interactions, electrochemical doping of the contacts and/or the semiconductor, formation of electric double layers near the interfaces, reduction of the depletion width near the drain electrode, charge-carrier de-trapping and space charge polarization of the dielectric, would result in the observed increase of on-currents, off-currents and field-effect mobility values, the degraded saturation behavior and the large shift of the switch-on voltages (and accordingly of the threshold voltages) to more positive values.

However, an additional interface-related effect at the PVA/ROM-polymer boundary layer, resulting in e.g. a release of fixed Na^+ ions also contributing to the charge carrier increase in the rr-P3HT layer, cannot be rigorously excluded. Furthermore, a possible intermixing of PVA with the ROMP-dielectric during film drying at elevated temperatures might have had an influence, too.

In order to test for the reversibility of the sensors some samples were also evacuated after NH_3 exposure. However, since induced ions are not very likely to be removed by evacuation, no large difference was found in the corresponding device characteristics before and after evacuation (not shown). Exposure to HCl vapor for sensor resetting was not performed, as it most likely would have also harmed the aluminum top-gate electrodes.

With the proposed explanation of the sensor response the larger channel-current values observed in the output characteristics after NH_3 exposure at a particular working point compared to the corresponding values in the transfer characteristics (Figure 5.35, Figure 5.39) can be rationalized similar as in chapter 4.4.3. Mobile NH_4^+ ions within the dielectric move to the different interfaces depending on the applied voltage difference between drain and gate. During the first V_D sweeps in the output characteristics the drain voltage is more negative than V_G for a longer time and hence NH_4^+ ions are forced to move to the drain. Only in the last two output curves (V_G = -65V and V_G = -85V) V_G becomes more negative than V_D for a longer time, but the short timescale of the sweeps and the finite mobility of the ions "confine" them near the drain electrode. Accordingly, positive ions are more pushed away from the drain electrode during the measurement of the transfer curves. Therefore effects resulting from NH_4^+ ions are more pronounced in the output characteristics and the corresponding channel current at a particular working point is larger after NH_3 exposure. Before ammonia treatment bias-induced charge-carrier trapping seems to be predominant, in particular for the OFET including eosin Y-based polymer ***1a***, where the transfer characteristics exhibit larger I_D values compared to the output curves and hysteresis with lower channel currents in the reverse sweep (Figure 5.32).

The interaction with NH_4^+ ions is also responsible for the fact that the hysteresis of OFET-sensors in the transfer characteristics was much reduced (polymer ***1a***) or even showed larger channel currents in the reverse sweep (polymer ***1b***) after NH_3 exposure (Figure 5.35).

According to the proposed explanation, making V_D even more negative with respect to V_G would more strongly attract the induced ions to the drain, thus enhancing the effects of the described interactions. This is in fact the case, as shown in Figure 5.48, where transfer curves of an NH_3-exposed OFET-sensor are compared before and after 40 s of bias stress at V_D = -100V and V_G = +85V (V_{GD} = +185V!). As expected, the stress results in a distinctly increased channel current.

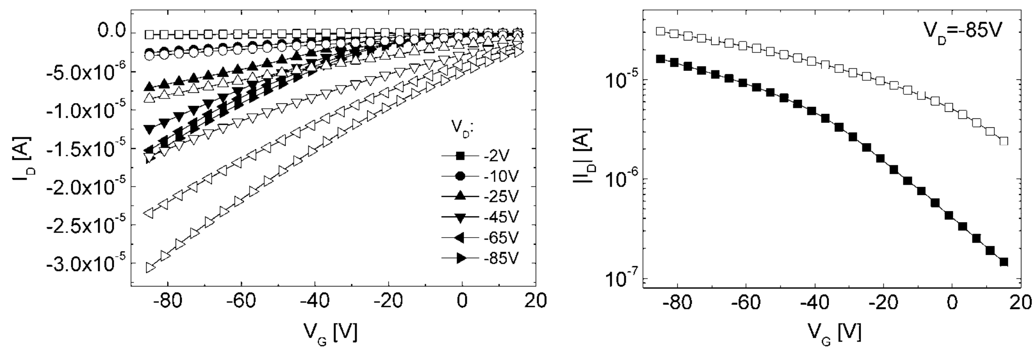

Figure 5.48 Transfer characteristics (left) and semi-logarithmic transfer curves at V_D = -85V (right) of a typical NH_3-exposed OFET-sensor ($L \approx 25$ µm, $W \approx 2.85$ mm) with eosin Y-based polymer ***1a*** (batch 1) before (filled symbols) and after (open symbols) 40 s bias stress at V_D = -100V and V_G = +85V.

The graphs in Figure 5.49 might also be an indication for moving ions, which interact with the organic semiconductor. They were recorded right after the bias stress measurements at V_D = -100V and V_G = +85V, which most likely had resulted in a large NH_4^+ ion density close to the drain electrode. A subsequent application of V_D = -100V and V_G = -85V resulted in a small but distinct further increase of I_D, as more NH_4^+ ions were attracted to the drain (Figure 5.49 left). When immediately afterwards the channel is depleted by applying V_D = +100V and V_G = +85V, the I_D(t)-curves resemble a current of positive polarons moving from the drain to the source. The fact that I_D is at first decreasing might be ascribed to NH_4^+ ions that are leaving the drain region, heading towards the source electrode. Due to their finite mobility, the rearrangement is delayed and only after ~50 s "travel time" contact doping, possibly in combination with other described mechanisms, becomes effective again and the depletion current is slightly increased.

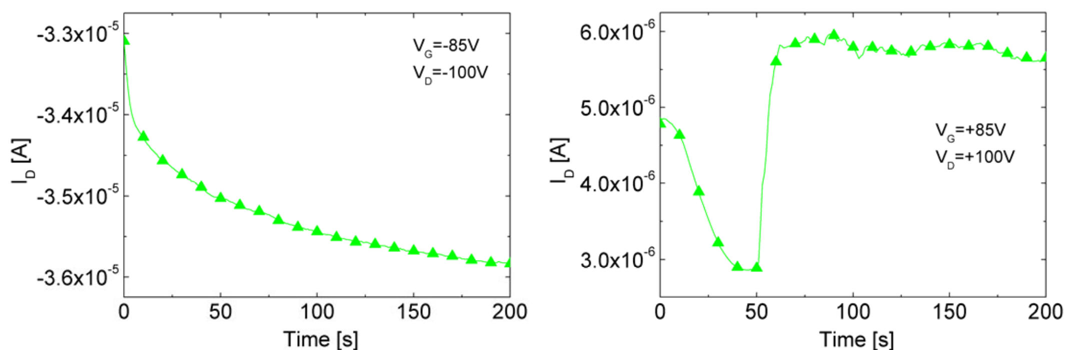

Figure 5.49 Consecutively measured I_D(t)-curves (left: V_D = -100V, V_G = -85V, right: V_D = +100V, V_G = +85V) after bias stress at V_D = -100V and V_G = +85V of a typical NH_3-exposed OFET-sensor ($L \approx 25$ µm, $W \approx 2.85$ mm) with eosin Y-based polymer ***1a*** (batch 1).

Similar effects have been observed by Bäcklund and co-workers,[116] who explained such current reductions by the pinch-off region growing near the source electrode faster than the (doping) ions can move (drift/diffusion) from drain to source.

Another interesting effect could be observed with the SensFETs, in particular when they were also operated in bottom-gate mode, meaning that the n^{++}-Si and SiO_2 of the substrate were used as common bottom-gate electrode and gate dielectric, respectively, with the top-gate left unbiased. Figure 5.50 depicts the transfer curves of several devices on a sample including DCF-based polymer ***1b*** measured in bottom-gate operation mode before and after NH_3 exposure, with the latter being recorded immediately after top-gate operation.

Although all devices had similar channel dimensions, they exhibited decreasing channel currents in the order that they were measured (indicated by the arrow), with the first measured after top-gate operation showing the largest values. Most likely, by consecutively measuring several devices the channel formed near the PVA/rr-P3HT interface during top-gate operation was gradually moved to the rr-P3HT/SiO_2 interface, at which charge-carrier trapping (e.g. due to SiOH groups) is dominant, thus leading to the gradually observed reduction of on- and off- currents and the shift of the switch-on voltages to more negative values.

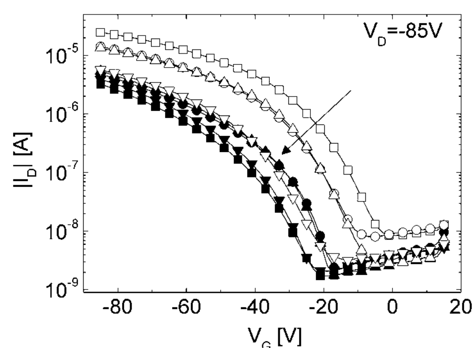

Figure 5.50: Semi-logarithmic transfer curves at V_D = -85V of several OFET-sensors ($L \approx 25$ µm, $W \approx 2.85$ mm) with the DCF-based polymer ***1b*** measured in *bottom-gate operation mode* (SiO_2 is dielectric) before (filled symbols) and after (open symbols) exposure to 1% NH_3; arrow indicates order in which devices were consecutively measured after NH_3 exposure.

Similarly, when several transfer characteristics of a single NH_3-exposed OFET were consecutively recorded in bottom-gate operation mode immediately after top-gate operation, the channel moving gradually to the rr-P3HT/SiO_2 interface was mirrored by a reduction particularly of the off-current (Figure 5.51). The decrease, however, is not much pronounced, because, as mentioned, during the recording of the transfer characteristics the gate voltage is only for a short time at high negative values, hence being not very "effective" in charge-carrier trapping.

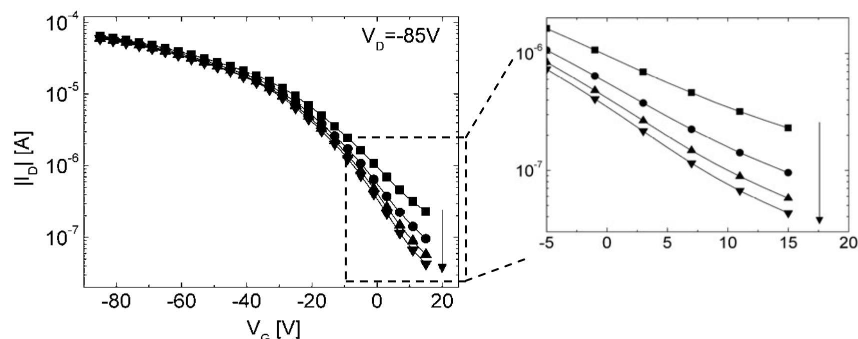

Figure 5.51: Semi-logarithmic transfer curves at V_D = -85V of an NH_3-exposed OFET-sensor ($L \approx 25$ µm, $W \approx 2.85$ mm) with the DCF-based polymer ***1b*** measured consecutively in *bottom-gate operation mode* (SiO_2 is active dielectric) immediately after top-gate operation.

Accordingly, when changing from bottom-gate operation mode (SiO_2 = dielectric) back to top-gate operation (PVA/ROMP = dielectric), the channel is moved back to the PVA/rr-P3HT interface and the effects described above become dominant again, leading to increased on- and off-currents (Figure 5.52).

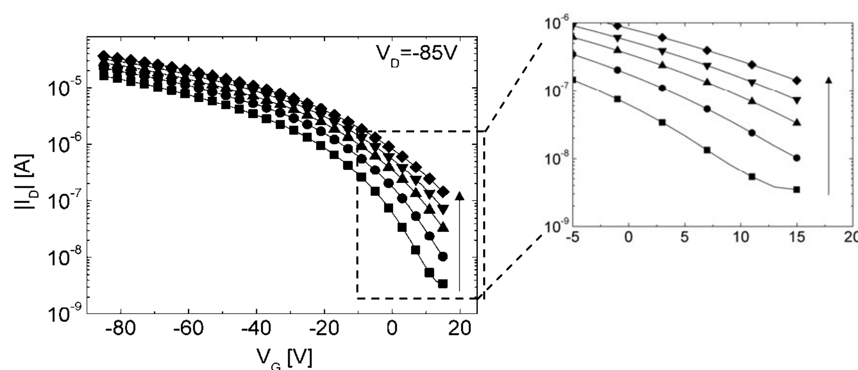

Figure 5.52: Semi-logarithmic transfer curves at V_D = -85V of an NH_3-exposed OFET ($L \approx 25$ µm, $W \approx 2.85$ mm) with the DCF-based polymer ***1b*** measured consecutively in *top-gate operation mode* (ROM-polymer is dielectric) immediately after bottom-gate operation.

Finally, the graph in Figure 5.53 indicates that the DCF-based polymer ***1b*** apparently contained a small amount of ions already before NH_3 exposure, because the consecutively measured transfer curves (filled symbols) shift to more positive switch-on voltages and channel current is increased. However, exposure to ammonia leads to a much stronger change in device characteristics.

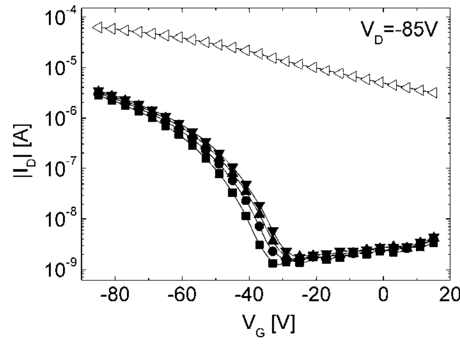

Figure 5.53: Semi-logarithmic transfer curves at V_D = -85V of an OFET-sensor ($L \approx 25$ µm, $W \approx 2.85$ mm) with the DCF-based polymer ***1b*** measured in *top-gate operation mode* before (filled symbols, several consecutively performed measurements) and after (open symbols) exposure to 1% NH_3.

5.6.6.2. Quantitative Estimations

In this section standard device equations will be applied to model the transfer curves in the saturation regime (at V_D = -85V) of an OFET-sensor with DCF-based polymer ***1b*** before and after exposure to 1% ammonia. Although extracted device parameters in combination with rough but reasonable assumptions will be used, this will, on a quantitative level, provide an even better idea of the possible mechanisms leading to the sensor response. The electrical characteristics and parameters of the modeled device are depicted in Figure 5.32, Figure 5.35 and Table 10.

The field-induced charge within an OFET and the corresponding charge carrier density p_{FE} can be derived from:

$$Q = e \cdot p_{FE} = C_i \cdot (V_G - V_{th}) \tag{5.8}$$

For instance, with C_i = 3.82 nF/cm² and V_{th} = -21 V (see Table 10) eqn. (5.8) yields a density of positive field-induced charge carriers of ~1.5×10^{12} cm^{-2} at $V_G = V_D$ = -85V.

With this equation the source-to-drain channel current in the saturation regime can be expressed by eqn. (5.9), assuming a combination of a bulk current I_{off} (at V_G = 0V), resulting from the pristine doping level within the semiconductor, and an additional field-induced current (see also chapter 2.2.2):

$$I_{Dsat} = I_{off} + \left(\frac{W}{2L} \cdot \mu_{FE} \cdot e \cdot p_{FE} \cdot (V_G - V_{th}) \right) \tag{5.9}$$

Equation (5.9) is only valid for (V_G - V_{th}) < 0, as it would else yield I_{off} at $V_G = V_{th}$ and not at V_G = 0V. Moreover, as already mentioned in chapter 2.2.2, it does not take into account the gate-voltage dependence of the field-effect mobility and also neglects contact resistance.

From the extracted off-current at V_G = 0V (2.4 nA) an off-conductivity of 2.5x10^{-13} S/sq can be calculated using eqn. (5.10) (L = 25 µm, W = 2.85 mm).

$$\sigma_{off} = e \cdot p_{Off} \cdot \mu_{Off} = \frac{I_{off}}{V_D} \cdot \frac{L}{W} \tag{5.10}$$

With an extracted mobility in the off-state μ_{off} (V_G = 0V) of 1.3x10^{-6} cm^2/Vs a pristine doping level of ~1.2x10^{12} carriers per cm^2 can be estimated. When taking into account also an extracted saturation field-effect mobility of 4x10^{-3} cm^2/Vs before NH_3 exposure, the transfer curve at V_D = -85V could be well reproduced with eqn. (5.9) in the region between V_{th} and V_G = -85V (Figure 5.54), which is of course expected, as only extracted parameters were applied.

Now let the device be exposed to 1% ammonia. ~500 µl of the solution with the active-sensing ROM-polymer (concentration: 60 mg/ml) was applied by spin-casting, thus containing ~30 mg solid content. Assuming that 20 mg of the material formed the ROM-polymer film, with the rest not remaining on the substrate due to centrifugal forces, the number of polymer chains within the film can be calculated by using the number average molecular weight of the DCF-based polymer ***1b*** (M_n: 40840 g/mol) and Avogadro's constant N_A, leading to a value of ~3x10^{17} chains. As 1 mol% of dye-bearing monomers was mixed with the corresponding bulk-monomer, this leads to ~3x10^{15} active-sensing groups within the film. If they are homogenously distributed within the film and an area of 10 mm^2 would actively contribute to the sensor response during operation of a single device, then ~1.6% (substrate dimensions: 25.4 mm x 25.4 mm) of active groups would be found within this area, in numbers ~4.6x10^{13}. All active groups are assumed to be ionized upon 1% NH_3 exposure and presumably 1 ppm (~4.6x10^7) NH_4^+ ions per second reach the rr-P3HT/PVA interface near the channel region at V_G = -85V and V_D = -100V ($E_{GD} \approx 10^5$ V/cm). If each of those ions would "create" only one positive charge carrier, 4.6x10^7 new charge carriers per channel area (2.85 mm x 25 µm) per second would result in a charge-carrier density increase rate $\Delta p/\Delta t$ of ~6.5x10^{10} positive polarons per cm^2 per second. Accordingly, a channel-current increase rate of ~150 nA/s at V_G = -85V and V_D = -100V is then estimated from eqn. (5.11), corresponding to the measured I_D-increase rate (Figure 5.41).

$$\frac{\Delta I_{Dsat}}{\Delta t} = \frac{W}{2L} \cdot \mu_{FE} \cdot e \cdot \frac{\Delta p}{\Delta t} \cdot \left(V_G - V_{th}\right) \tag{5.11}$$

This value is obtained with the field-effect mobility and threshold voltage values of the pristine device before NH_3 exposure. For sure mobility will increase and V_{th} will shift to more positive values already during NH_3 exposure.

Therefore, the assumed values for the number of ions reaching the interface per second and their "carrier-creation" efficiency have to be seen as rough estimations. For instance, assuming average mobility and threshold-voltage values of 1x10^{-2} cm^2/Vs and 0V, respectively (in the following termed "other values"), would result in about the same I_D current increase rate with a $\Delta p/\Delta t$ of ~2x10^{10} charge carriers per cm^2 per second.

With the estimated $\Delta p/\Delta t$, after 600 s NH_3 exposure this would lead to a total charge-carrier density increase due to interaction with NH_4^+ ions of ~3.9x10^{13} cm^{-2} (other values: ~1.2x10^{13} cm^{-2}), adding to the pristine doping level of ~1.2x10^{12} cm^{-2}, which is only ~3% (other values: ~10%). Accordingly, the channel-current increase rate of ~150 nA/s leads to a total I_D increase of ~90 µA at V_G = -85V and V_D = -100V after 600 s NH_3 exposure, as was observed also in the measurements (Figure 5.33 left).

Using eqn. (2.17), the maximum interfacial trap density calculated from the subthreshold slope of the device before ammonia exposure is $N_{T,max} \approx$ 3.4x10^{12} cm^{-2} eV^{-1} When comparing this value with the estimated total increase of the mobile charge carrier density due to interaction with NH_4^+ ions, it might be concluded that the increase cannot be ascribed to de-trapping alone.

Assuming a new larger off-state mobility (at V_G = 0V) of 8x10^{-5} cm^2/Vs (other values: 2.5x10^{-4} cm^2/Vs) after exposure to NH_3 (due to the higher charge carrier density), the new off-conductivity, resulting from the pristine doping level plus the charge carrier density induced by NH_4^+ ions, would be ~5.1x10^{-10} S/sq (other values: 5.3x10^{10} S), corresponding to a new off-current of ~5 µA (same for other values) derived from eqn. (5.10), which corresponds to the measured value.

Taking into account the new threshold voltage value after NH_3 exposure according to Table 10, the field-induced charge carrier density p_{FE} at V_G = V_D = -85V is modified to ~2.5x10^{12}/cm^2. In combination with the new larger saturation field-effect mobility of 2.0x10^{-2} cm^2/Vs in the on-state after NH_3 exposure (due to the higher charge carrier density), the corresponding transfer curve at V_D = -85V could again be well reproduced with eqn. (5.9). Figure 5.54 compares the measured and modeled curves before and after NH_3 exposure.

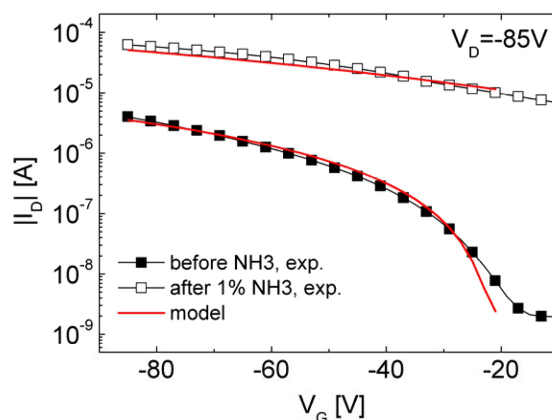

Figure 5.54: Semi-logarithmic transfer curves at V_D = -85V of an OFET-sensor ($L \approx 25$ µm, $W \approx 2.85$ mm) with the DCF-based polymer ***1b*** measured before (filled symbols) and after (open symbols) exposure to 1% NH_3, including modeled curves.

Of course, for the modeled transfer curves many parameters extracted from the measured data were applied so that in fact the good agreement between model and experiment is not surprising. Moreover, rough assumptions were made and possible interactions with immobile (or less mobile) counter-ions were not taken into account. Nevertheless, the estimations in this section provide a more detailed picture of the possible mechanisms in a SensFET when exposed to NH_3.

5.7. Summary and Conclusions

A novel OFET-sensor concept based on the application of a sensitive gate dielectric was proposed, which could be successfully realized by the application of solution-processable, pH-sensitive ROM-polymers in bottom-contact OFETs with meander-shaped top-gate electrodes. Upon exposure to NH_3 at concentration levels down to 100 ppm, the devices exhibited a distinct irreversible source-to-drain current increase, while OFETs comprising a reference dielectric without pH-sensitive groups showed negligible response. The sensor mechanism was thoroughly investigated, also including UV/VIS-, FTIR- and capacitance measurements. It was ascribed to the deprotonation of OH-groups in the active-sensing dielectrics, leading to the creation of mobile ammonium ions, which, upon application of an electric field, move to the dielectric/semiconductor interface or even into the semiconductor. By electrochemical doping of the contacts and/or the semiconductor, the formation of electric double layers near the interfaces, the reduction of the depletion width near the drain electrode, charge-carrier de-trapping and/or by space charge polarization of the dielectric, the mobile ions induce an increase of the charge carrier density within the semiconductor, resulting in the observed sensor response.

The sensing behavior was shown to depend on an appropriate material combination of active-sensing dielectric and organic semiconductor and could be observed even after storage in air.

The fact that capacitors based on the sensitive dielectrics showed minor response to the analyte underlines the potential of the OFET as sensor element.
Even if the sensors were irreversible (at least reversibility could not be demonstrated), they could still be applied as cheap single-use detection elements e.g. for monitoring fish freshness or meat spoilage.
As the sensor response only depends on the applied potential difference, the operating voltage can easily be reduced and lower concentrations of ammonia, possibly even in the ppb region, could be detected at response times on the order of seconds, when monitoring the slope of the $I_D(t)$-curves.
Expensive source/drain-electrode structuring via photolithography could be replaced by the application of efficient large-scale structuring techniques such as inkjet printing or soft lithography, possibly also in combination with flat or cylindrical flexible substrates, enabling SensFETs to be implemented e.g. into textiles.
Furthermore, the application of solvent-compatible active-sensing dielectrics and organic semiconductors will reduce costs and processing effort, as PVA would not be required. The device performance may, however, also be enhanced by including additional intermediate layers to increase selectivity (e.g. upon application of semi-permeable membranes), ambient and operational stability or charge-carrier transport and injection.
By using appropriate dielectrics the concept could be extended to other analytes such as ions or bioactive materials even in aqueous environments. Multiple analyte detection could be enabled, when a number of SensFETs comprising individually adapted dielectric materials is integrated into an array.
For sure, the presented devices leave room for improvement. Nevertheless, the results in this chapter will hopefully contribute in paving the way to all-solution-processed, integrated, smart and flexible (bio)sensor systems.

6. Appendix

6.1. List of Publications

6.1.1. Jounal Papers

- *Direct Ink-Jet Printing of Ag–Cu Nanoparticle and Ag-Precursor Based Electrodes for OFET Applications*; S. Gamerith, A. Klug, H. Scheiber, U. Scherf, E. Moderegger, E. J. W. List, *Adv. Funct. Mater.* **2007**, *17*, 3111.

- *Micromolding in capillaries and microtransfer printing of silver nanoparticles as soft-lithographic approach for the fabrication of source/drain electrodes in organic field-effect transistors;* A. Blümel, A. Klug, S. Eder, U. Scherf, E. Moderegger, E. J. W. List, *Org. Electron.* **2007**, *8*, 389.

- *Organic field-effect transistor based sensors with sensitive gate dielectrics used for low-concentration ammonia detection;* Andreas Klug, Martin Denk, Thomas Bauer, Martina Sandholzer, Ullrich Scherf, Christian Slugovc, Emil J. W. List, *in preparation*.

- *Air-stable polytriphenylamine derivative as active layer material in organic thin-film transistors;* Andreas Klug, Gerhild Wurzinger, Raphael Pfattner, Matthias Baumann, Benjamin Souharce, Michael Forster, Ullrich Scherf, Emil J. W. List, *in preparation*.

- *The role of ionic impurities in PVA gate dielectrics for organic field-effect transistors*; Stefan Brandstätter, Stefan Gamerith, Andreas Klug, Ullrich Scherf, Emil J. W. List, *in preparation*.

- *On the Deconvolution of Kelvin Probe Force Microscopy Data;* A. Blümel, A. Klug, E. J.W. List, H. Plank, E. Fisslthaler, M. Sezen, W. Grogger, submitted to *Review of Scientific Instruments*.

6.1.2. Conference Contributions

- *Solution-Processed Electrodes for Organic Field Effect Transistors*, Stefan Gamerith, Andreas Klug, Ullrich Scherf, Emil J. W. List, MRS 2006 Spring Meeting, San Francisco, CA, USA (17.04-21.04.2006), Poster.

- *PVA Gate Dielectrics in Organic Field Effect Transistors - Improvement of Device Characteristics by Material Purification*, Stefan Brandstätter, Stefan Gamerith, Andreas Klug, Ullrich Scherf, Emil J. W. List, MRS 2006 Spring Meeting, San Francisco, CA, USA (17.04-21.04.2006), Poster.

- *Air-stable Active Layer Materials for Organic Field-Effect Transistors*, Andreas Klug, Raphael Pfattner , Benjamin Souharce, Ullrich Scherf, Emil J.W. List; MRS 2006 Fall Meeting, Boston, MA, USA, (27.11-01.12.2006), Poster.

- *Stability Issues of Organic Field-Effect Transistors,* Andreas Klug, Raphael Pfattner, Matthias Baumann, Benjamin Souharce, Michael Forster, Ullrich Scherf, Emil J. W. List, The 8th International Symposium of Functional π-Electron Systems, Graz, Austria (21.07.-25.07.2008), Poster.
- *Influence of Ambient Conditions on Organic Semiconductors*, Gerhild Wurzinger, Andreas Klug, Arno Meingast, Martin Denk, Michael Forster, Ullrich Scherf, Emil J. W. List, Nano and Photonics 2009, Mauterndorf, Austria (11.03.-14.03.2009), Poster.
- *Stability Issues of Organic Field-Effect Transistors,* Andreas Klug, Raphael Pfattner, Matthias Baumann, Benjamin Souharce, Michael Forster, Ullrich Scherf, Emil J. W. List, Nano and Photonics 2009, Mauterndorf, Austria (11.03.-14.03.2009), Poster.
- *Stability Issues of Organic Field-Effect Transistors,* Andreas Klug, Gerhild Wurzinger, Raphael Pfattner, Matthias Baumann, Arno Meingast, Benjamin Souharce, Michael Forster, Ullrich Scherf, Emil J. W. List, MRS Spring Meeting 2009, San Francisco, CA, USA (13.04.-17.04.2009), Poster.
- *All Solution-Processed Organic Field-Effect Transistors*, Andreas Klug, Emil J. W. List, National Science Network – Winterschool on Organic Electronics – "Interface Controlled and Functionalised Thin Organic Films", Planneralm, Austria (27.01.-02.02.2007), Talk.
- *Organic thin-film transistor based sensors used for low-concentration ammonia detection*, Andreas Klug, Martin Denk, Martina Sandholzer, Thomas Bauer, Christian Slugovc, Ullrich Scherf, Emil J. W. List, MRS Spring Meeting 2009, San Francisco, CA, USA (13.04.-17.04.2009), Talk.
- *Organic thin-film transistor based sensors used for low-concentration ammonia detection*, Andreas Klug, Martin Denk, Martina Sandholzer, Thomas Bauer, Christian Slugovc, Ullrich Scherf, Emil J. W. List, EPF'09 - European Polymer Congress, Graz Austria, (12.07.-17.07.2009), Talk.

6.1.3. Patent Applications

- *OFET-based Sensor for Detecting an Analyte;* E. J. W. List, A. Klug, C. Slugovc, M. Denk, UK patent application No. 0906204.3, **2009**.

6.2. Bibliography

[1] M. Pope, C. E. Swenberg, *Electronic Processes in Organic Crystals and Polymers*, Second Edition, Oxford University Press, New York **1999**.

[2] H. Mette, H. Pick, *Z. Physik* **1953**, *134*, 566.

[3] R. G. Kepler, *Phys. Rev.* **1960**, *119*, 1226.

[4] M. Pope, H. Kallman, P. Magnante, *J. Chem. Phys.* **1963**, *38*, 2042.

[5] H. Hoegl, *J. Phys. Chem.* **1965**, *69*, 755.

[6] D. M. Pai, B. E. Springett, *Rev. Mod. Phys.* **1993**, *65*, 163.

[7] H. Shirakawa, E. J. Louis, A. G. MacDiarmid, C. K. Chiang, A. J. Heeger, *J. Chem. Soc. Chem. Commun.* **1977**, 578.

[8] C. K. Chiang, C. R. Fincher, Jr., Y. W. Park, A. J. Heeger, H. Shirakawa, E. J. Louis, S. C. Gau, A. G. MacDiarmid, *Phys. Rev. Lett.* **1977**, *39*, 1098.

[9] A. J. Heeger, *Angew. Chem.* **2001**, *113*, 2660.

[10] C. W. Tang, S. A. Van Slyke, *Appl. Phys. Lett.* **1987**, *51*, 913.

[11] C. W. Tang, S. A. Van Slyke, *Appl. Phys. Lett.* **1989**, *65*, 3610.

[12] H. Koezuka, A. Tsumura, Y. Ando, *Synth. Met.* **1987**, *18*, 699.

[13] A. Tsumura, H. Koezuka, Y. Ando, *Synth. Met.* **1988**, *25*, 11.

[14] G. Horowitz, D. Fichou, X. Z. Peng, Z. Xu, F. Garnier, *Sol. Stat. Comm.* **1989**, *72*, 381.

[15] F. Garnier, G. Horowitz, X. Z. Peng, D. Fichou, *Adv. Mater.* **1990**, *2*, 592.

[16] J. H. Burroughes, D. D. C. Brandley, A. R. Brown, R. N. Marks, M. Mackay, R. H. Friend, P. L. Burns, A. B. Holmes, *Nature* **1990**, *347*, 539.

[17] A. R. Brown, C. P. Jarrett, D. M. de Leeuw, M. Matters, *Synth. Met.* **1997**, *88*, 37.

[18] G. Horowitz, *Adv. Mater.* **1998**, *10*, 365.

[19] C. D. Dimitrakopoulos, P. R. L. Malenfant, *Adv. Mater.* **2002**, *14*, 99.

[20] P. F. Baude, D. A. Ender, M. A. Haase, T. W. Kelley, D. V. Muyres, S. D. Theiss, *Appl. Phys. Lett.* **2003**, *85*, 3964.

[21] H. Klauk, M. Halik, U. Zschieschang, F. Eder, D. Rohde, G. Schmid, C. Dehm, *IEEE Trans. On Electron Dev.* **2005**, *52*, 618.

[22] H. Sirringhaus, *Adv. Mater.* **2005**, *17*, 2411.

[23] H. Klauk, *Organic Electronics*, Wiley VCH, Weinheim **2006**.

[24] Z. Bao, J. Locklin, *Organic Field-Effect Transistors*, CRC Press **2007**.

[25] I. Kymissis, *Organic Field Effect Transistors - Theory, Fabrication and Characterization*, Springer, New York **2009**.

[26] C. W. Tang, *Appl. Phys. Lett.* **1986**, *48*, 183.

[27] C. J. Brabec, N. S. Sariciftci, J. C. Hummelen, *Adv. Funct. Mater.* **2001**, *11*, 15.

[28] B. Lamprecht, R. Thünauer, M. Ostermann, G. Jakopic, G. Leising, *phys. stat. sol. (a)* **2005**, *202*, R50-R52.

[29] M. Gaal, C. Gadermaier, H. Plank, E. Moderegger, A. Pogantsch, G. Leising, E. J. W. List, *Adv. Mater.* **2003**, *15*, 1165.

[30] I. D. W. Samuel, G. A. Turnbull, *Chem. Rev.* **2007**, *107*, 1272.

[31] J. A. Rogers, Z. Bao, K. Baldwin, A. Dodabalapur, B. Crone, V. R. Raju, V. Kuck, H. Katz, K. Amundson, J. Ewing, P. Drzaic, *PNAS* **2001**, *98*, 4835.

[32] C. D. Sheraw, L. Zhou, J. R. Huang, D. J. Gundlach, T. N. Jackson, *Appl. Phys. Lett.* **2002**, *80*, 1088.

[33] J. E. Lilienfeld, U.S. Patent 1,745,175, **1930**.

[34] M. Shur, *Physics of Semiconductor Devices*, Prentice Hall, Englewood Cliffs, NJ **1990**.

[35] S. M. Sze, *Physics of Semiconductor Devices*, Third Edition, John Wiley and Sons **2007**.

[36] D. Kahng, M. M. Atalla, *IRE Solid-State Devices Research Conference*, Carnegie Institute of Technology, Pittsburgh, PA **1960**.

[37] J. Bardeen, W. H. Brattain, *Phys. Rev.* **1948**, *74,* 230.

[38] W. Shockley, *Bell Syst. Techn. J.* **1949**, *28*, 435.

[39] G. H. Heilmeier, L. A. Zanoni, *J. Phys. Chem. Solids* **1964**, *25*, 603.

[40] D. F. Barbe, C. R. Westgate, *J. Phys. Chem. Solids* **1970**, *31*, 2679.

[41] H. Sirringhaus, N. Tessler, R. H. Friend, *Science* **1998**, *280*, 1741.

[42] A. Dodabalapur, Z. Bao, A. Makhija, J. G. Laquindanum, V. R. Raju, Y. Feng, H. E. Katz, J. Rogers, *Appl. Phys. Lett.* **1998**, *73*, 142.

[43] H. E. A. Huitema, G. H. Gelinck, J. B. P. H van der Putten, K. E. Kuijk, K. M. Hart, E. Cantatore, D. M. de Leeuw, *Adv. Mater.* **2002**, *14*, 1201.

[44] B. Crone, A. Dodabalapur, A. Gelperin, L. Torsi, H. E. Katz, A. J. Lovinger, Z. Bao, *Appl. Phys. Lett.* **2001**, *78*, 2229.

[45] Z.-T. Zhu, J. T. Mason, R. Dieckmann, G. G. Malliaras, *Appl. Phys. Lett.* **2002**, *81*, 4643.

[46] C. Bartic, B. Palan, A. Campitelli, G. Borghs, *Sens. Actuators, B* **2002**, *83*, 115.

[47] K. Müller, W. Bär, K. Henkel, A. Jahnke, C. Schwiertz, D. Schmeißer, *TM* **2003**, *70*, 565.

[48] C. J. Drury, C. M. J. Mutsaers, C. M. Hart, M. Matters, D. M. de Leeuw, *Appl. Phys. Lett.* **1998**, *73*, 108.

[49] F. Eder, H. Klauk, M. Halik, U. Zschieschang, G. Schmid, C. Dehm, *Appl. Phys. Lett.* **2004**, *84*, 2673.

[50] A. Klug, Diploma Thesis, Graz University of Technology **2005** (and references therein).

[51] E. Riedel, *Anorganische Chemie*, 3. Aufl., Walter de Gruyter Berlin, New York **1994**.

[52] L. C. Pauling, "London's paper. General ideas on bonds." **1928**. http://osulibrary.oregonstate.edu/specialcollections/coll/pauling/bond/notes/sci3.001.21.html

[53] R. E. Peierls, *Quantum Theory of Solids*, Clarendon Press, Oxford **1955**.

[54] M. Grell, *Organic semiconductors and devices, Course notes*, University of Sheffield; http://www.shef.ac.uk/physics/teaching/phy411c/phy411.pdf

[55] Ch. Weißmantel, C. Hamann, *Grundlagen der Festkörperphysik*, 4. Aufl., Johann Ambrosius Barth Verlag, Heidelberg, Leipzig **1995.**

[56] L.-L. Chua, J. Zaumseil, J.-F. Chang, E. C.-W. Ou, P. K.-H. Ho, H. Sirringhaus, R. H. Friend, *Nature* **2005**, *434*, 194.

[57] W. Warta, N. Karl, *Phys. Rev. B* **1985**, *32*, 1172.

[58] N. Karl, J. Marktanner, R. Stehle, W. Warta, *Synth. Met.* **1991**, *42*, 2473.

[59] N. Karl, K.-H. Kraft, J. Marktanner, M. Münch, F. Schatz, R. Stehle, H.-M. Uhde, *J. Vac. Sci. Technol. A* **1999**, *17*, 2318.

[60] N. Karl, J. Marktanner, *Mol. Cryst. Liq. Cryst.* **2001**, *355*, 149.

[61] R. W. I. de Boer, M. E. Gershenson, A. F. Morpurgo, V. Podzorov, *phys. stat. sol. (a)* **2004**, *201*, 1302 and references therein.

[62] V. C. Sundar, J. Zaumseil, V. Podzorov, E. Menard, R. L. Willett, T. Someya, M. E. Gershenson, J. A. Rogers, *Science* **2004**, *303*, 1644.

[63] O. D. Jurchescu, J. Baas, T. T. M. Palstra, *Appl. Phys. Lett.* **2004**, *84*, 3061.

[64] M. E. Gershenson, V. Podzorov, A. F. Morpurgo, *Rev. Mod. Phys.* **2006**, *78*, 973.

[65] T. Minari, T. Nemoto, S. Isoda, *J. Appl. Phys.* **2004**, *96*, 769.

[66] T. Minari, T. Nemoto, S. Isoda, *J. Appl. Phys.* **2006**, *99*, 034506.

[67] H. Sirringhaus, P. J. Brown, R. H. Friend, M. M. Nielsen, K. Beechgaard, B. M. W. Langeveld-Voss, A. J. H. Spiering, R. A. J. Janssen, E. W. Meijer, P. T. Herwig, D. M. de Leeuw, *Nature* **1999**, *401*, 685.

[68] H. Sirringhaus, N. Tessler, R. H. Friend, *Synth. Met.* **1999**, *102*, 857.

[69] G. Wang, J. Swensen, D. Moses, A. J. Heeger, *J. Appl. Phys.* **2003**, *93*, 6137.

[70] H. Sirringhaus, M. Bird, T. Richards, N. Zhao, *Adv. Mater.* **2010**, *22*, 1.

[71] J. Yamashita, T. Kurosawa, *J. Phys. Chem. Solids* **1958**, *5*, 34.

[72] T. Holstein, *Ann. Phys.* **1959**, *8*, 325.

[73] T. Holstein, *Ann. Phys.* **1959**, *8*, 343.

[74] D. Emin, *Adv. Phys.* **1975**, *24*, 305.

[75] E. A. Silinsh, G. A. Shlihta, A. J. Jurgis, *Chem. Phys.* **1989**, *138*, 347.

[76] G. Horowitz, *J. Mater. Chem.* **1999**, *9*, 2021.

[77] E. M. Conwell, *Phys. Rev.* **1956**, *103*, 51.

[78] N. F. Mott, *Can. J. Phys.* **1956**, *34*, 1356.

[79] D. Pines, *Can. J. Phys.* **1956**, *34*, 1367.

[80] A. Miller, E. Abrahams, *Phys. Rev.* **1960**, *120*, 745.

[81] P. G. Le Comber, W. E. Spear, *Phys. Rev. Lett.* **1970**, *25*, 509.

[82] G. Horowitz, R. Hajlaoui, P. Delannoy, *J. Phys. III France* **1995**, *5*, 355.

[83] G. Horowitz, M. E. Hajlaoui, R. Hajlaoui, *J. Appl. Phys.* **2000**, *87*, 4456.

[84] G. Horowitz, M. E. Hajlaoui, *Adv. Mater.* **2000**, *12*, 1046.

[85] G. Horowitz, *Adv. Funct. Mater.* **2003**, *13*, 53.

[86] S. F. Nelson, Y.-Y. Lin, D. J. Gundlach, T. N. Jackson, *Appl. Phys. Lett.* **1998**, *72*, 1854.

[87] E. J. Meijer, PhD Thesis, Technische Universiteit Delft, Netherlands **2003**.

[88] W. F. Pasveer, PhD Thesis, Technische Universiteit Eindhoven, Netherlands **2004**

[89] C. Tanase, PhD Thesis, University of Groningen, Netherlands **2005**.

[90] D. Emin, *Phys. Rev. Lett.* **1974**, *32*, 303.

[91] R. A. Marcus, *J. Chem. Phys.* **1984**, *81*, 4494.

[92] N. F. Mott, *J. Non-Cryst. Solids* **1968**, *1*, 1.

[93] N. F. Mott, *Phil. Mag.* **1969**, *19*, 835.

[94] N. F. Mott, E. A. Davis, *Electronic processes in non-crystalline materials*, 2nd ed., Oxford University Press, London **1979**.

[95] P. M. Borsenberger, L. Pautmeier, H. Bässler, *J. Chem. Phys.* **1991**, *94*, 5447.

[96] P. M. Borsenberger, L. Pautmeier, R. Richert, H. Bässler, *J. Chem. Phys.* **1991**, *94*, 8276.

[97] W. D. Gill, *J. Appl. Phys.* **1972**, *43*, 5033.

[98] H. Bässler, *phys. stat. sol. (b)* **1993**, *175*, 15.

[99] P. W. M. Blom, M. C. J. M. Vissenberg, *Mat. Sci. Eng.* **2000**, *27*, 53 and references therein.

[100] Y. N. Gartstein, E. M. Conwell, *Chem. Phys. Lett.* **1995**, *245*, 351.

[101] S. V. Novikov, D. H. Dunlap, V. M. Kenkre, P. E. Parris, A. V. Vannikov, *Phys. Rev. Lett.* **1998**, *81*, 4472.

[102] M. C. J. M. Vissenberg, M. Matters, *Phys. Rev. B* **1998**, *57*, 12964.

[103] C. Tanase, E. J. Meijer, P. W. M. Blom, D. M. de Leeuw, *Phys. Rev. Lett.* **2003**, *91*, 216601.

[104] M. S. Lee, H. S. Kang, H. S. Kang, J. Joob, A. J. Epstein, J. Y. Lee, *Thin Solid Films* **2005**, *477*, 169.

[105] R. Pfattner, Diploma Thesis, Graz University of Technology **2007**.

[106] J. Lee, V. Subramanian, *IEEE Int. Elect. Dev. Meeting Tech. Dig.* **2003**, 8.3.1.

[107] J. B. Lee, V. Subramanian, *IEEE Trans. Electron Devices* **2005**, *52*, 269.

[108] M. Maccioni, E. Orgiu, P. Cosseddu, S. Locci, A. Bonfiglioa, *Appl. Phys. Lett.* **2006**, *89*, 143515.

[109] J. Veres, S. Ogier, G. Lloyd, D. de Leeuw, *Chem. Mater.* **2004**, *16*, 4543.

[110] A. Facchetti, M.-H. Yoon, T. J. Marks, *Adv. Mater.* **2005**, *17*, 1705.

[111] X. Peng, G. Horowitz, D. Fichou, F. Garnier, *Appl. Phys. Lett.* **1990**, *57*, 2013.

[112] R. Parashkov, E. Becker, G. Ginev, T. Riedl, H.-H. Johannes, W. Kowalsky, *J. Appl. Phys.* **2004**, *95*, 1594.

[113] K.-J. Baeg, Y.-Y. Noh, J. Ghim, B. Lim, D.-Y. Kim, *Adv. Funct. Mater.* **2008**, *18*, 3678.

[114] J. Veres, S. D. Ogier, S. W. Leeming, D. C. Cupertino, S. M. Khaffaf, *Adv. Funct. Mater.* **2003**, *13*, 199.

[115] H. G. O. Sandberg, T. G. Bäcklund, R. Österbacka, H. Stubb, *Adv. Mater.* **2004**, *16*, 1112.

[116] T. G. Bäcklund, H. G. O. Sandberg, R. Österbacka, H. Stubb, *Appl. Phys. Lett.* **2004**, *85*, 3887.

[117] M. J. Panzer, C. R. Newman, C. D. Frisbie, *Appl. Phys. Lett.* **2005**, *86*, 103503.

[118] M. J. Panzer, C. D. Frisbie, *Adv. Funct. Mater.* **2006**, *16*, 1051.

[119] A. S. Dhoot, J. D. Yuen, M. Heeney, I. McCulloch, D. Moses, A. J. Heeger, *PNAS* **2006**, *103*, 11834.

[120] M. J. Panzer, C. D. Frisbie, *J. Am. Chem. Soc.* **2007**, *129*, 6599.

[121] J. D. Yuen, A. S. Dhoot, E. B. Namdas, N. E. Coates, M. Heeney, I. McCulloch, D. Moses, A. J. Heeger, *J. Am. Chem. Soc.* **2007**, *129*, 14367.

[122] M. J. Panzer, C. D. Frisbie, *Adv. Mater.* **2008**, *20*, 3177.

[123] S. Brandstätter, Diploma Thesis, Graz University of Technology **2007**.

[124] S. Brandstätter, S. Gamerith, A. Klug, U. Scherf, E. J. W. List, *publication in preparation*.

[125] C. A. Lee, D.-W. Park, S. H. Jin, I. H. Park, J. D. Lee, B.-G. Park, *Appl. Phys. Lett.* **2006**, *88*, 252102.

[126] Y. H. Noh, S. Y. Park, S.-M. Seo, H. H. Lee, *Org. Electron.* **2006**, *7*, 271.

[127] C. A. Lee, D.-W. Park, K.-D. Jung, B. Kim, Y. C. Kim, J. D. Lee, B.-G. Park, *Appl. Phys. Lett.* **2006**, *89*, 262120.

[128] C. Erlen, F. Brunetti, M. Fiebig, G. Scarpa, B. Nickel, A. Di Carlo, P. Lugli, *Mater. Res. Soc. Symp. Proc.* **2007**, 1003-O11-10.

[129] M. Egginger, M. Irimia-Vladu, R. Schwödiauer, A. Tanda, I. Frischauf, S. Bauer, N. S. Sariciftci, *Adv. Mater.* **2008**, *20*, 1018.

[130] S. H. Kim, J. Jang, H. Jeon, W. M. Yun, S. Nam, C. E. Park, *Appl. Phys. Lett.* **2008**, *92*, 183306.

[131] M. Egginger, S. Bauer, R. Schwödiauer, H. Neugebauer, N. S. Sariciftci, *Monatsh. Chem.* **2009,** *140*, 735.

[132] H. E. Katz, X. M. Hong, A. Dodabalapur, R. Sarpeshkar, *J. Appl. Phys.* **2002**, *91*, 1572.

[133] Th. B. Singh, N. Marjanović, G. J. Matt, N. S. Sariciftci, R. Schwödiauer, S. Bauer, *Appl. Phys. Lett.* **2004**, *85*, 5409.

[134] R. C. G. Naber, M. Mulder, B. de Boer, P. W. M. Blom, D. M. de Leeuw, *Org. Electron.* **2006**, *7*, 132.

[135] L. A. Majewski, J. W. Kingsley, C. Balocco, A. M. Song, *Appl. Phys. Lett.* **2006**, *88*, 222108.

[136] J. C. Scott, *J. Vac. Sci. Technol. A* **2003**, *21*, 521.

[137] T. van Woudenbergh, PhD Thesis, University of Groningen, Netherlands **2005**.

[138] N. Koch, A. Kahn, J. Ghijsen, J.-J. Pireaux, J. Schwartz, R. L. Johnson, A. Elschner, *Appl. Phys. Lett.* **2003**, *82*, 70.

[139] S. Gamerith, A. Klug, H. Scheiber, U. Scherf, E. Moderegger, E. J. W. List, *Adv. Funct. Mater.* **2007**, *17*, 3111.

[140] S. Gamerith, PhD thesis, Graz University of Technology **2006**.

[141] H. Sirringhaus, T. Kawase, R. H. Friend, T. Shimoda, M. Inbasekaran, W. Wu, E. P. Woo, *Science* **2000**, *290*, 2123.

[142] P. J. Smith, D.-Y. Shin, J. E. Stringer, B. Derby, *J. Mater. Sci.* **2006**, *41*, 4153.

[143] Z. Bao, Y. Feng, A. Dodabalapur, V. R. Raju, A. J. Lovinger, *Chem. Mater.* **1997**, *9*, 1299.

[144] G. Horowitz, R. Hajlaoui, H. Bouchriha, R. Bourguiga, M. Hajlaoui, *Adv. Mater.* **1998**, *10*, 923 and references therein.

[145] E. J. Meijer, C. Tanase, P. W. M. Blom, E. van Veenendaal, B.-H. Huisman, D. M. de Leeuw, T. M. Klapwijk, *Appl. Phys. Lett.* **2002**, *80*, 3838.

[146] A. Rolland, J. Richard, J. P. Kleider, D. Mencaraglia, *J. Electrochem. Soc.* **1993**, *140*, 3679.

[147] M. McDowell, I. G. Hill, J. E. McDermott, S. L. Bernasek, J. Schwartz, *Appl. Phys. Lett.* **2006**, *88*, 073505.

[148] P. Cosseddu, A. Bonfiglio, *Thin Solid Films* **2007**, *515*, 7551.

[149] G. Horowitz, R. Hajlaoui, D. Fichou, A. El Kassmi, *J. Appl. Phys.* **1999**, *85*, 3202.

[150] R. A. Street, A. Salleo, *Appl. Phys. Lett.* **2002**, *81*, 2887.

[151] P. V. Necliudov, M. S. Shur, D. J. Gundlach, T. N. Jackson, *Solid-State Electron.* **2003**, *47*, 259.

[152] H. Klauk, G. Schmid, W. Radlik, W. Weber, L. Zhou, C. D. Sheraw, J. A. Nichols, T. N. Jackson, *Solid-State Electron.* **2003**, *47*, 297.

[153] J. Zaumseil, K. W. Baldwin, J. A. Rogers, *J. Appl. Phys.* **2003**, *93*, 6117.

[154] L. Bürgi, T. J. Richards, R. H. Friend, H. Sirringhaus, *J. Appl. Phys.* **2003**, *94*, 6129.

[155] G. Horowitz, P. Lang, M. Mottaghi, H. Aubin, *Adv. Funct. Mater.* **2004**, *14*, 1069 and references therein.

[156] E. J. Meijer, G. H. Gelinck, E. van Veenendaal, B. H. Huisman, D. M. de Leeuw, T. M. Klapwijk, *Appl. Phys. Lett.* **2003**, *82*, 4576.

[157] S. Luan W. Neudeck, *J. Appl. Phys.* **1992**, *72*, 766.

[158] B. Stadlober, U. Haas, H. Gold, A. Haase, G. Jakopic, G. Leising, N. Koch, S. Rentenberger, E. Zojer, *Adv. Funct. Mater.* **2007**, *17*, 2687.

[159] M. L. Chabinyc, J.-P. Lu, R. A. Street, Y. Wu, P. Liu, B. S. Ong, *J. Appl. Phys.* **2004**, *96*, 2063.

[160] J. N. Haddock, X. Zhang, S. Zheng, Q. Zhang, S. R. Marder, B. Kippelen, *Org. Electron.* **2006**, *7*, 45.

[161] A. Assadi, C. Svensson, M. Willander, O. Inganäs, *Appl. Phys. Lett.* **1988**, *53*, 195.

[162] Z. Bao, A. Dodabalapur, A. J. Lovinger, *Appl. Phys. Lett.* **1996**, *69*, 4108.

[163] R. H. M. van de Leur, B. de Ruiter, J. Breen, *Synth. Met.* **1993**, *54*, 203.

[164] M. S. A. Abdou, F. P. Orfino, Z. W. Xie, M. J. Deen, S. Holdcroft, *Adv. Mater.* **1994**, *6*, 838.

[165] M. S. A. Abdou, F. P. Orfino, Y. Son, S. Holdcroft, *J. Am. Chem. Soc.* **1997**, *119*, 4518.

[166] E. J. Meijer, C. Detcheverry, P. J. Baesjou, E. van Veenendaal, D. M. de Leeuw, T. M. Klapwijk, *J. Appl. Phys.* **2003**, *93*, 4831.

[167] B. A. Mattis, P. C. Chang, V. Subramanian, *Mat. Res. Soc. Symp. Proc.* **2003**, *771*, L10.35.1.

[168] E. J. Meijer, A. V. G. Mangnus, B.-H. Huisman, G. W. ′t Hooft, D. M. de Leeuw, T. M. Klapwijk, *Synth. Met.* **2004**, *142,* 53.

[169] L. Lüer, H.-J. Egelhaaf, D. Oelkrug, G. Cerullo, G. Lanzani, B.-H. Huisman, D. de Leeuw, *Org. Electron.* **2004**, *5*, 83.

[170] J. Ficker, H. von Seggern, H. Rost, W. Fix, W. Clemens, I. McCulloch, *Appl. Phys. Lett.* **2004**, *85*, 1377.

[171] S. Hoshino, M. Yoshida, S. Uemura, T. Kodzasa, N. Takada, T. Kamata, K. Yase, *J. Appl. Phys.* **2004**, *95*, 5088.

[172] H.-H. Liao, C.-M. Yang, C.-C. Liu, S.-F. Horng, H.-F. Meng, J.-T. Shy, *J. Appl. Phys.* **2008**, *103*, 104506.

[173] B. S. Ong, Y. Wu, P. Liu, S. Gardner, *J. Am. Chem. Soc.* **2004**, *126*, 3378.

[174] R.P. Mikalo, D. Schmeißer, *Synth. Met.* **2002**, *127*, 273.

[175] I. McCulloch, C. Bailey, M. Giles, M. Heeney, I. Love, M. Shkunov, D. Sparrowe, S. Tierney, *Chem. Mater.* **2005**, *17*, 1381.

[176] J. Ficker, A. Ullmann, W. Fix, H. Rost, W. Clemens*, J. Appl. Phys.* **2003**, *94*, 2638.

[177] H. Rost, J. Ficker, J. S. Alonso, L. Leenders, I. McCulloch, *Synth. Met.* **2004**, *145*, 83.

[178] A. Schoonveld, PhD Thesis, University of Groningen, Netherlands **1999**.

[179] M. Matters, D. M. de Leeuw, P. T. Herwig, A. R. Brown, *Synth. Met.* **1999**, *102*, 998.

[180] A. Salleo, R. A. Street, *J. Appl. Phys.* **2003**, *94*, 471.

[181] C. Goldmann, C. Krellner, K. P. Pernstich, S. Haas, D. J. Gundlach, B. Batlogg, *J. Appl. Phys.* **2006**, *99*, 034507.

[182] D. Bernards, R. M. Owens, G. G. Malliaras (eds.), *Organic Semiconductors in Sensor Applications*, Springer, Berlin, Heidelberg **2008**.

[183] H. E. Katz, *Electroanalysis*, **2004**, *16*, 1837 and references therein.

[184] J. T. Mabeck, G. G. Malliaras, *Anal. Bioanal. Chem.* **2006**, *384*, 343 and references therein.

[185] C. Bartic, G. Borghs, *Anal. Bioanal. Chem.* **2006**, *384*, 354 and references therein.

[186] M. Berggren, A. Richter-Dahlfors, *Adv. Mater.* **2007**, *19*, 3201.

[187] L. Torsi, A. Dodabalapur, L. Sabbatini, P. G. Zambonin, *Sens. Actuators, B* **2000**, *67*, 312.

[188] W. Hu, Y. Liu, Y. Xu, S. Liu, S. Zhou, D. Zhu, B. Xu, C. Bai, C. Wang, *Thin Solid Films* **2000**, *360*, 256.

[189] M. Bouvet, A. Leroy, J. Simon, F. Tournilhac, G. Guillaud, P. Lessnick, A. Maillard, S. Spirkovitch, M. Debliquy, A. de Haan, A. Decroly, *Sens. Actuators, B* **2001**, *72*, 86.

[190] M. Bouvet, G. Guillaud, A. Leroy, A. Maillard, S. Spirkovitch, F.-G. Tournilhac, *Sens. Actuators, B* **2001**, *73*, 63.

[191] T. Someya, H. E. Katz, A. Gelperin, A. J. Lovinger, A. Dodabalapur, *Appl. Phys. Lett.* **2002**, *81*, 3079.

[192] L. Torsi, A. J. Lovinger, B. Crone, T. Someya, A. Dodabalapur, H. E. Katz, A. Gelperin, *J. Phys. Chem. B* **2002**, *106*, 12563.

[193] L. Torsi, M. C. Tanese, N. Cioffi, M. C. Gallazzi, L. Sabbatini, P. G. Zambonin, G. Raos, S. V. Meille, M. M. Giangregorio, *J. Phys. Chem. B* **2003**, *107*, 7589.

[194] L. Torsi, A. Tafuri, N. Cioffi, M.C. Gallazzi, A. Sassella, L. Sabbatini, P. G. Zambonin, *Sens. Actuators, B* **2003**, *93*, 257.

[195] L. Wang, D. Fine, A. Dodabalapur, *Appl. Phys. Lett.* **2004**, *85*, 6386.

[196] L. Torsi, A. Dodabalapur, N. Cioffi, L. Sabbatini, P.G. Zambonin, *Sens. Actuators, B* **2001**, *77*, 7.

[197] C. Bartic, A. Campitelli, S. Borghs, *Appl. Phys. Lett.* **2003**, *82*, 475.

[198] T. Someya, T. Sekitani, S. Iba, Y. Kato, H. Kawaguchi, T. Sakurai, *PNAS* **2004**, *101*, 9966.

[199] T. Someya, Y. Kato, T. Sekitani, S. Iba, Y. Noguchi, Y. Murase, H. Kawaguchi, T. Sakurai, *PNAS* **2005**, *102*, 12321.

[200] http://www.ntc-weiz.at

[201] A. Meingast, Diploma Thesis, Graz University of Technology **2009**.

[202] manufactured by Goller Reinraumtechnik GmbH, Münsingen, Germany; http://www.goller-reinraum.de

[203] http://www.millipore.com; resistivity of product water > 5 MΩcm; TOC typically < 30 ppb.

[204] Martin Walter Ultraschalltechnik AG, Straubenhard, Germany; http://www.walter-ultraschall.de

[205] Suss MicroTec Lithography GmbH, Garching, Germany; http://www.suss.com

[206] Sister Semiconductor Equipment GmbH (SSE, now ATMsse GmbH), Singen, Germany; www.sse-semi.com

[207] EV Group (EVG), St. Florian am Inn, Austria; http://www.evgroup.com

[208] GS GLOVEBOX Systemtechnik GmbH, Malsch, Germany; http://www.glovebox-systemtechnik.de; http://www.jacomex.com

[209] S. Sax, PhD thesis, Graz University of Technology **2009**.

[210] GaLa Gabler Labor Instrumente GmbH, Bad Schwalbach, Germany; http://www.gala-instrumente.de

[211] http://www.plasma.de

[212] http://www.olympus.de/microscopy

[213] http://www.veeco.com

[214] http://www.kruss.de

[215] C. Koch, T. J. Rinke, *Lithography - Theory and Application of Photoresists, Developers, Solvents and Etchants*, MicroChemicals **2007**.

[216] K. Suzuki, B. W. Smith, *Microlithography: Science and Technology*, 2nd edition, CRC Press, **2007**.

[217] Photronics MZD GmbH, Dresden, Germany; http://www.photronics.com

[218] micro resist technology GmbH, Berlin, Germany; http://www.microresist.de

[219] J. Daggett, S. Villareal, R. Robbins, J. Goodnight, HMDS Process Setup, University of Texas **2003**. http://www.utdallas.edu/research/cleanroom/tools/HMDS.htm

[220] D. J. Durian, C. Franck, *Phys. Rev. Lett.* **1987**, *59*, 555.

[221] T. Yamada, T. Hasegawa, M. Hiraoka, H. Matsui, Y. Tokura, G. Saito, *Appl. Phys. Lett.* **2008**, *92*, 233306.

[222] D. H. Kim, Y. D. Park, Y. Jang, H. Yang, Y. H. Kim, J. I. Han, D. G. Moon, S. Park, T. Chang, C. Chang, M. Joo, C. Y. Ryu, K. Cho, *Adv. Funct. Mater.* **2005**, *15*, 77.

[223] R. J. Kline, M. D. McGehee, M. F. Toney, *Nat. Mater.* **2006**, *5*, 222.

[224] I. Yagi, K. Tsukagoshia, Y. Aoyagi, *Appl. Phys. Lett.* **2005**, *86*, 103502.

[225] W. Kalb, P. Lang, M. Mottaghi, H. Aubin, G. Horowitz, M. Wuttig, *Synth. Met.* **2004**, *146*, 279.

[226] R. Ruiz, D. Choudhary, B. Nickel, T. Toccoli, K.-C. Chang, A. C. Mayer, P. Clancy, J. M. Blakely, R. L. Headrick, S. Iannotta, G. G. Malliaras, *Chem. Mater.* **2004**, *16*, 4497.

[227] S. Y. Yang, K. Shin, C. E. Park, *Adv. Funct. Mater.* **2005**, *15*, 1806.

[228] J. B. Koo , S. H. Kim, J. H. Lee, C. H. Ku, S. C. Lim, T. Zyung, *Synth. Met.* **2006**, *156*, 99.

[229] A. S. Killampalli, J. R. Engstrom, *Appl. Phys. Lett.* **2006**, *88*, 143125.

[230] Figure taken from manual of SSE Optihot VB20.

[231] http://www.sigmaaldrich.com

[232] S. Grecu, M. Roggenbuck, A. Opitz, W. Brütting, *Org. Electron.* **2006**, 7, 276.

[233] C. N. C. Lam, R. Wu, D. Li, M. L. Hair, A. W. Neumann, *Adv. Colloid Interface Sci.,* **2002**, *96*, 169.

[234] C. Bourgès-Monnier, M. E. R. Shanahan, *Langmuir* **1995**, *11*, 2820.

[235] C. W. Extrand, *Langmuir* **2002**, *18*, 7991.

[236] S. E. Fritz, T. W. Kelley, C. D. Frisbie, *J. Phys. Chem. B* **2005**, *109*, 10574.

[237] C. D. Dimitrakopoulos, A. R. Brown, A. Pomp, *J. Appl. Phys.* **1996**, *80*, 2501.

[238] I. P. M. Bouchoms, W. A. Schoonveld, J. Vrijmoeth, T. M. Klapwijk, *Synth. Met.* **1999**, *104*, 175.

[239] C. C. Mattheus, A. B. Dros, J. Baas, G. T. Oostergetel, A. Meetsma, J. L. de Boer, T. T. M. Palstra, *Synth. Met.* **2003**, *138*, 475.

[240] I. Yagi, K. Tsukagoshi, Y. Aoyagi, *Thin Solid Films* **2004**, *467*, 168.

[241] P. Parisse, S. Picozzi, M. Passacantando, L. Ottaviano, *Thin Solid Films* **2007**, *515*, 8316.

[242] Prof. Ullrich Scherf, Macromolecular Chemistry, University of Wuppertal, Germany.

[243] A. Syekeres, S. Alexandrova, K. Kirov, *phys. stat. sol. (a)* **1980**, *62*, 727.

[244] J. Kassabov, E. Atanassova, E. Goranova, *Solid-State Electron.* **1984**, *27*, 13.

[245] S. Rentenberger, A. Vollmer, E. Zojer, R. Schennach, N. Koch*, J. Appl. Phys.* **2006**, *100*, 053701.

[246] W.-K. Kim, J.-L. Lee, *Appl. Phys. Lett.* **2006**, *88*, 262102.

[247] B. H. Hamadani, C. A. Richter, D. J. Gundlach, R. J. Kline, I. McCulloch, M. Heeney, *J. Appl. Phys.* **2007**, *102*, 044503.

[248] S. C. Lim, S. H. Kim, J. H. Lee, M. K. Kim, D. J. Kim, T. Zyung, *Synth. Met.* **2005**, *148*, 75.

[249] Y. Xia, G. M. Whitesides, *Angew. Chem. Int. Ed.* **1998**, *37*, 550.

[250] Y. Xia, G. M. Whitesides, *Annu. Rev. Mater. Sci*. **1998**, *28*, 153.

[251] F. Zhang T. Nyberg, O. Inganäs, *Nano Lett.* **2002**, *2*, 1373.

[252] Y. Koide, M. W. Such, R. Basu, G. Evmenenko, J. Cui, P. Dutta, M. C. Hersam, T. J. Marks, *Langmuir* **2003**, *19*, 86.

[253] A. Takakuwa, M. Misaki, Y. Yoshida, K. Yase, *Thin Solid Films* **2009**, *518*, 555.

[254] J. A. Rogers, Z. Bao, V. R. Raju, *Appl. Phys. Lett.* **1998**, *72*, 2716.

[255] J. A. Rogers, Z. Bao, A. Makhija, P. Braun, *Adv. Mater.* **1999**, *11*, 741.

[256] J. Tate, J. A. Rogers, C. D. W. Jones, B. Vyas, D. W. Murphy, W. Li, Z. Bao, R. E. Slusher, A. Dodabalapur, H. E. Katz, *Langmuir* **2000**, *16*, 6054.

[257] P. Cosseddu, A. Bonfiglio, *Appl. Phys. Lett.* **2006**, *88*, 023506.

[258] A. Benor, D. Knipp, *Org. Electron.* **2008**, *9*, 209.

[259] R. S. Kane, S. Takayama, E. Ostuni, D. E. Ingber, G. M. Whitesides, *Biomaterials* **1999**, *20*, 2363.

[260] E. Kim, Y. Xia, G. M. Whitesides, *J. Am. Chem. Soc.* **1996**, *118*, 5722.

[261] A. Blümel, Diploma Thesis, Graz University of Technology **2005**.

[262] M. Cavallini, C. Albonetti, F. Biscarini, *Adv. Mater.* **2009**, *21*, 1043.

[263] J. L. Wilbur, A. Kumar, H. A. Biebuyck, E. Kim, G. M. Whitesides, *Nanotechnology* **1996**, *7*, 452.

[264] Y. Xia, N. Venkateswaran, D. Quin, J. Tien, G. M. Whitesides, *Langmuir* **1998**, *14*, 363.

[265] http://www.cabot-corp.com

[266] http://www.rohmhaas.com; http://www.microresist.de

[267] http://www.dowcorning.com

[268] http://www.austriamicrosystems.com

[269] C. R. Martin, I. A. Aksay, *J. Mater. Res.* **2005**, *20*, 1995.

[270] http://en.wikipedia.org/wiki/Silver

[271] F. Carpi, D. De Rossi, *IEEE Trans. Inf. Technol. Biomed.* **2005**, *9*, 295.

[272] http://www.sensatex.com; http://www.mp3blue.de; http://enlighted.com, http://www.lumalive.com

[273] M. Hamedi, R. Forchheimer, O. Inganäs, *Nat. Mater.* **2007**, *6*, 357.

[274] M. R. Lee, R. D. Eckert, K. Forberich, G. Dennler, C. J. Brabec, R. A. Gaudiana, *Science* **2009**, *324*, 232.

[275] http://www.goodfellow.com

[276] M. Heeney, C. Bailey, K. Genevicius, M. Shkunov, D. Sparrowe, S. Tierney, I. McCulloch, *J. Am. Chem. Soc.* **2005**, *127*, 1078.

[277] I. McCulloch, M. Heeney, C. Bailey, K. Genevicius, I. MacDonald, M. Shkunov, D. Sparrowe, S. Tierney, R. Wagner, W. Zhang, M. L. Chabinyc, R. J. Kline, M. D. McGehee, M. F. Toney, *Nat. Mater.* **2006**, *5*, 328.

[278] J. Veres, S. Ogier, S. Leeming, B. Brown, D. Cupertino, *Mat. Res. Soc. Symp. Proc.* **2002**, *708*, B8.7.1.

[279] L. A. Majewski, M. Grell, S. D. Ogier, J. Veres, *Org. Electron.* **2003**, *4*, 27.

[280] R. Kisselev, M. Thelakkat, *Macromolecules* **2004**, *37*, 8951.

[281] D. Zielke, A. C. Hübler, U. Hahn, N. Brandt, M. Bartzsch, U. Fügmann, T. Fischer, J. Veres, S. Ogier, *Appl. Phys. Lett.* **2005**, *87*, 123508.

[282] H. Kempa, K. Reuter, M. Bartzsch, U. Hahn, A. C. Huebler, D. Zielke, M. Forster, U. Scherf, *IEEE Polytronic Conference Proc.* **2005**, 67.

[283] A. Das, R. Dost, T. Richardson, M. Grell, J. J. Morrison, M. L. Turner, *Adv. Mater.* **2007**, *19*, 4018.

[284] S. Allard, M. Forster, B. Souharce, H. Thiem, U. Scherf, *Angew. Chem. Int. Ed.* **2008**, *47*, 4070.

[285] I. Dumsch, C. J. Kudla, U. Scherf, *Macromol. Rapid Commun.* **2009**, *30*, 840.

[286] M. Stolka, J. F. Yanus, D. M. Pai, *J. Phys. Chem.* **1984**, *88*, 4707.

[287] M. Thelakkata, J. Hagen, D. Haarer, H.-W. Schmidt, *Synth. Met.* **1999**, *102*, 1125.

[288] M. Thelakkat, *Macromol. Mater. Eng.* **2002**, *287*, 442.

[289] Y. Shirota, *J. Mater. Chem.* **2005**, *15*, 75.

[290] S. Jungermann, N. Riegel, D. Müller, K. Meerholz, O. Nuyken, *Macromolecules* **2006**, *39*, 8911.

[291] P. Zacharias, M. C. Gather, M. Rojahn, O. Nuyken, K. Meerholz, *Angew. Chem. Int. Ed.* **2007**, *46*, 4388.

[292] C. Jäger, R. Bilke, M. Heim, D. Haarer, H. Karickal, M. Thelakkat, *Synth. Met.* **2001**, *121*, 1543.

[293] K. R. Haridas, J. Ostrauskaite, M. Thelakkat, M. Heim, R. Bilke, D. Haarer, *Synth. Met.* **2001**, *121*, 1573.

[294] J. Cremer, P. Bäuerle, *J. Mater. Chem.* **2006**, *16*, 874.

[295] C. S. Karthikeyan, H. Wietasch, M. Thelakkat, *Adv. Mater.* **2007**, *19*, 1091.

[296] M. Baumann, Diploma Thesis, Graz University of Technology **2007**.

[297] G. Wurzinger, Diploma Thesis, Graz University of Technology **2009**.

[298] B. Souharce, PhD Thesis, Bergische Universität Wuppertal **2008**.

[299] R. S. Loewe, S. M. Khersonsky, R. D. McCullough, *Adv. Mater.* **1999**, *11*, 250.

[300] L. J. A. Koster, V. D. Mihailetchi, P. W. M. Blom, *Appl. Phys. Lett.* **2006**, *88*, 093511.

[301] N. Koch, J. Ghijsen, R. L. Johnson, J. Schwartz, J.-J. Pireaux, A. Kahn, *J. Phys. Chem. B* **2002**, *106*, 4192.

[302] S. Yoo, B. Domercq, B. Kippelen, *Appl. Phys. Lett.* **2004**, *85*, 5427.

[303] http://www.sensirion.ch

[304] Y. Qiu, Y. Hu, G. Dong, L. Wang, J. Xie, Y. Ma, *Appl. Phys. Lett.* **2003**, *83*, 1644.

[305] R. Ye, M. Baba, K. Suzuki, Y. Ohishi, K. Mori, *Thin Solid Films* **2004**, *464-465*, 437.

[306] D. Li, E.-J. Borkent, R. Nortrup, H. Moon, H. Katz, Z. Bao, *Appl. Physl. Lett.* **2005**, *86*, 042105.

[307] S. Ogawa, T. Naijo, Y. Kimura, H. Ishii, M. Niwano, *Appl. Phys. Lett.* **2005**, 86, 252104.

[308] A Benor, A. Hoppe, V. Wagner, D. Knipp, *Org. Electron.* **2007**, *8*, 749.

[309] D. Kumaki, M. Yahiro, Y. Inoue, S. Tokito, *Appl. Phys. Lett.* **2007**, *90*, 133511.

[310] S. D. Wang, T. Minari, T. Miyadera, K. Tsukagoshi, J. X. Tang, *Appl. Phys. Lett.* **2009**, *94*, 083309.

[311] Mowiol PVA datasheet **1999**, Clariant GmbH, Sulzbach, Germany.

[312] Y. Zhang, P. C. Zhu, D. Edgren, *J. Polym. Res.* **2009**, DOI 10.1007/s10965-009-9362-z.

[313] http://www.clariant.com

[314] http://www.spectrapor.com

[315] D. B. A. Rep, A. F. Morpurgo, W. G. Sloof, T. M. Klapwijk, *J. Appl. Phys.* **2003**, *93*, 125.

[316] L. Edman, J. Swensen, D. Moses, A. J. Heeger, *Appl. Phys. Lett.* **2004**, *84*, 3744.

[317] S. Lee, B. Koo, J. Shin, E. Lee, H. Park, H. Kim, *Appl. Phys. Lett.* **2006**, *88*, 162109.

[318] K. G. Falk, G. McGuire, *J. Biol. Chem.* **1919**, *37*, 547.

[319] K. G. Newton, C. O. Gill, *Appl. Environ. Microbiol.* **1978**, *36*, 375.

[320] Colin L. Honeybourne, *J. Chem. Educ.*, **2000**, *77*, 338.

[321] B. Timmer, W. Olthuis, A. van den Berg, *Sens. Actuators, B* **2005**, *107*, 666.

[322] A. Assadi, G. Gustafsson, M. Willander, C. Svensson, O. Inganäs, *Synth. Met.* **1990**, *37*, 123.

[323] P. Pacher, A. Lex, V. Proschek, H. Etschmaier, E. Tchernychova, M. Sezen, U. Scherf, W. Grogger, G. Trimmel, C. Slugovc, E. Zojer, *Adv. Mater.* **2008**, *20*, 3143.

[324] M. Denk, Diploma Thesis, Graz University of Technology **2009**.

[325] Y. Yang, Q. Pei, *J. Appl. Phys.* **1997**, *81*, 3294.

[326] H. S. White, G. P. Kittlesen, M. S. Wrighton, *J. Am. Chem. Soc.* **1984**, *106*, 5375.

[327] H. Sakai, K. Konno, H. Murataa, *Appl. Phys. Lett.* **2009**, *94*, 073304.

[328] Prof. Christian Slugovc, Institute for Chemistry and Technology of Materials (ICTM), Graz University of Technology, Austria.

[329] M. Sandholzer, A. Lex, G. Trimmel, R. Saf, F. Stelzer, C. Slugovc, *J. of Polymer Science, Part A* **2007**, *45*, 1336.

[330] K. Stubenrauch, M. Sandholzer, F. Niedermair, K. Waich, T. Mayr, I. Klimant, G. Trimmel, C. Slugovc, *Eur. Polym. J.* **2008**, *44*, 2558.

[331] C. Slugovc, S. Demel, S. Riegler, J. Hobisch, F. Stelzer, *Macromol. Rapid Commun.* **2004**, *25*, 475.

[332] C. Slugovc, *Macromol. Rapid Commun.* **2004**, *25*, 1283.

[333] K. Yamamoto, H. Ishida, *Vibrational Spectroscopy* **1994**, *8*, 1.

[334] P. Pacher, PhD Thesis, Graz University of Technology **2008**,

[335] G. Socrates, *Infrared and Raman Characteristic Group Frequencies: Tables and Charts*, 3rd ed., John Wiley & Sons Ltd., West Sussex, England **2001**, Ch. 22.

[336] *Agilent Solutions for Measuring Permittivity and Permeability with LCR Meters and Impedance Analyzers*, Application Note 1369-1, Agilent Technologies **2008**.

[337] *Agilent E4980A Precision LCR Meter User's Guide*, Seventh Edition, Manufacturing No. E4980-90070, Agilent Technolgies **2008**.

[338] K. E. Strawhecker, E. Manias, *Macromolecules* **2001**, *34*, 8475.

[339] H. S. Mansur , C. M. Sadahira, A. N. Souza, A. A. P. Mansur, *Mater. Sci. Eng., C* **2008**, *28*, 539.

[340] H. G. O. Sandberg, T. G. Bäcklund, R. Österbacka, M. Shkunov, D. Sparrowe, I. McCulloch, H. Stubb, *Org. Electron.* **2005**, *6*, 142.

[341] P. Foot, T. Ritchie, F. Mohammad, *J. Chem. Soc. Chem. Commun.* **1988**, 1536.

[342] F. Mohammad, *J. Phys. D* **1998**, *31*, 951.

[343] H. Shimotani, G. Diguet, Y. Iwasa, *Appl. Phys. Lett.* **2005**, *86*, 022104.

[344] M. Taniguchi, T. Kawai, *Appl. Phys. Lett.* **2004**, *85*, 3298.